A Measurement of the Self-Coupling of Electroweak Bosons

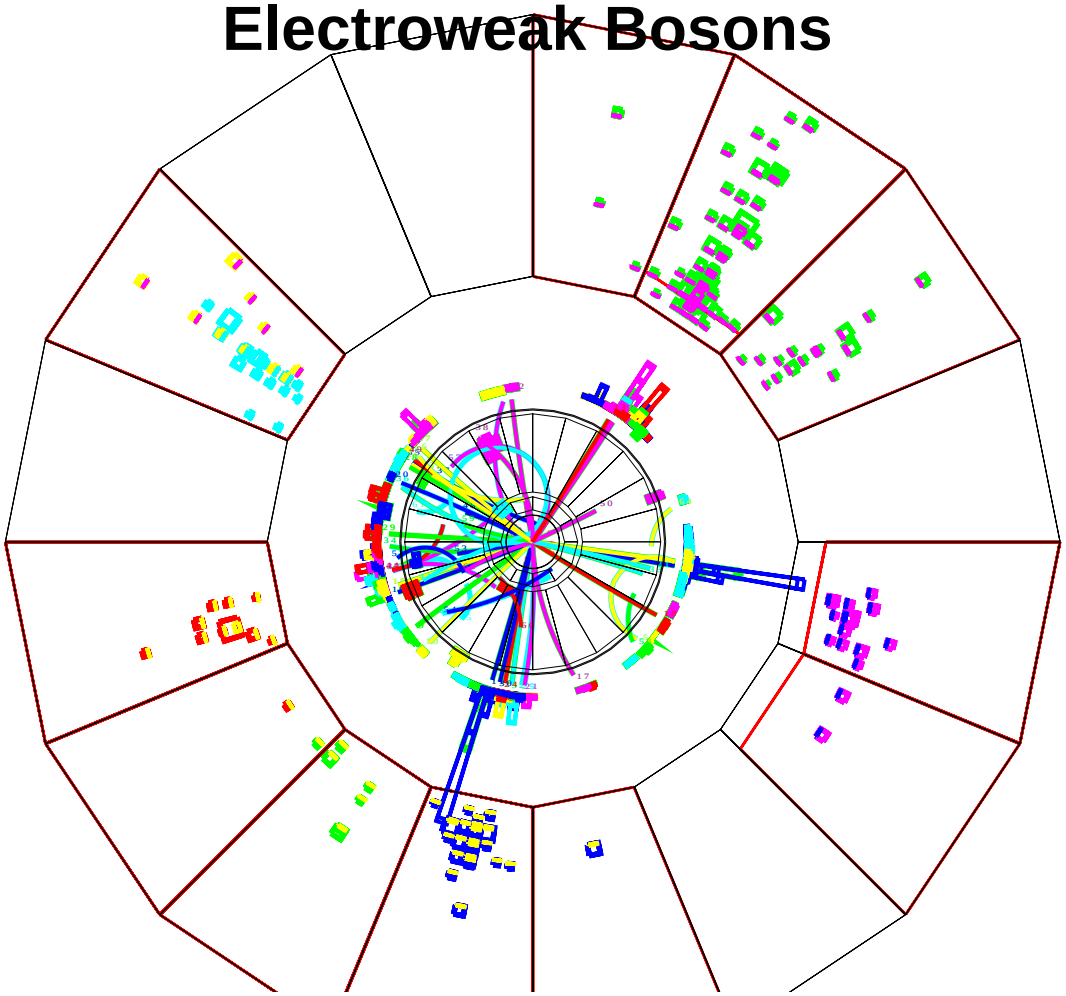

Peter Molnár

1999

A Measurement of the Self-Coupling of Electroweak Bosons

D I S S E R T A T I O N

zur Erlangung des akademischen Grades

d o c t o r r e r u m n a t u r a l i u m

(Dr. rer. nat.)

im Fach Physik

eingereicht an der

Mathematisch-Naturwissenschaftlichen Fakultät I

der Humboldt-Universität zu Berlin

von

Peter Molnár

geboren am 15 Mai 1973 in Zossen

Präsident der Humboldt-Universität zu Berlin
Prof. Dr. Dr. h.c. Hans Meyer

Dekan der Mathematisch-Naturwissenschaftlichen Fakultät I
Prof. Dr. Jürgen Rabe

Gutachter:
Prof. Dr. Thomas Hebbeker
Prof. Dr. Martin Pohl
Prof. Dr. Paul Söding

Tag der mündlichen Prüfung: 26. November 1999

Abstract

The couplings between the bosons of the electroweak interaction, γ, Z^0 and $W^{\pm}$, is one of the fundamental building blocks of the Standard Model, which was not yet tested with high precision.
Indirect hints for the existence of boson self-coupling have been obtained by analysing Z^0 pole data with respect to radiative corrections. This analysis uses for the first time all available electroweak precision data obtained at LEP 1, SLC, TEVATRON and at low energy experiments. The coupling strength between the electroweak gauge bosons is obtained by a global fit to all these data, leading to

$$g_1^Z = 0.983 \pm 0.018^{+0.018}_{-0.003} \quad \text{and} \quad \kappa_\gamma = 1.016 \pm 0.019^{+0.009}_{-0.013},$$

where the first error includes statistical and systematic effects and the second error reflects the variation of the Higgs mass between 90 and 1000 GeV. The first parameter describes the coupling strength of the ZWW and the second of the γWW interaction.
A precise direct measurement of triple gauge boson couplings became possible in 1996 at LEP 2, where W bosons could be produced in pairs, $e^+e^- \rightarrow W^+W^-$. In addition single-resonant W production, $e^+e^- \rightarrow We\nu_e$, and single photon production, $e^+e^- \rightarrow \nu\bar{\nu}\gamma(\gamma)$, are evaluated with respect to boson self-couplings. In total a luminosity of 77 pb^{-1} was collected with the **L3** detector at 161, 172 and 183 GeV centre-of-mass energy in the years 1996 and 1997. The couplings are measured to be

$$g_1^Z = 1.11^{+0.19}_{-0.18} \pm 0.10 \qquad \kappa_\gamma = 1.11^{+0.26}_{-0.25} \pm 0.17 \qquad \text{and}$$
$$\lambda_\gamma = 0.10^{+0.22}_{-0.20} \pm 0.10,$$

where the first error is statistical and the second systematic. The parameter λ_γ describes contributions to the γWW interaction. The Standard Model expectations of one for g_1^Z and κ_γ and zero for λ_γ show good agreement with this measurement. The measurement of g_1^Z is the first proof of the existence of a ZWW vertex. The

LEP 2 data were further used to limit violation of parity and C-parity at the ZWW vertex expressed through

$$g_5^Z = -0.44^{+0.23}_{-0.22} \pm 0.12.$$

The Standard Model expects no P- or C-violation, thus a value of zero for g_5^Z. The results of the measurement for the three different channels, corresponding to three different regions of momentum transfer Q^2, showed no Q^2 dependence of the coupling measurement. Thus the magnetic dipole moment μ_{W} and electric quadrupole moment q_{W} are measured to be

$$\mu_{\mathrm{W}} = (1.33 \pm 0.27) \times 10^{-5} \ \ \mu_B \qquad\qquad q_{\mathrm{W}} = (5.6 \pm 2.5) \times 10^{-36} \ \ \mathrm{m}^2$$

These two static properties of the W give information on the size and the geometrical form of the W, such that the W radius could be limited to

$$R_{\mathrm{W}} < 2 \times 10^{-18}\mathrm{m} \ \ (95\%\ C.L.)$$

and the deformation parameter δ was restricted by

$$\delta \cdot R_{\mathrm{W}}^2 = (3.3^{+30}_{-31}) \times 10^{-37}\ \mathrm{m}^2.$$

In addition the coupling constants were used to limit the phase space of the extension of the Standard Model with a sequential Z$'$ boson in terms of mixing angle and Z$'$ mass. The unified matter theory by Klein is ruled out with more than ten standard deviations.

Zusammenfassung

Ein fundamentaler Baustein des Standardmodels, des heute am weitesten akzeptierten Models der Elementarteilchenphysik, ist die Selbstkopplung der elektroschwachen Eichbosonen γ, Z^0 und $W^{\pm}$. Während andere Vorhersagen des Standardmodels mit hoher Präzision getestet wurden, ist über die Stärke der Selbstkopplung der Bosonen wenig bekannt.
Erste indirekte Hinweise über solche Kopplungen wurden aus präzisen Messungen der Fermionpaarproduktion auf dem Z^0-Pol gewonnen. Diese Messungen sind sensitiv auf Strahlungskorrekturen. In dieser Analyse werden zum ersten Mal alle verfügbaren elektroschwachen Präzisionsdaten, die unter anderen bei LEP 1, am SLAC und am TEVATRON gewonnen wurden, benutzt, um in einer globalen Anpassung die Kopplungsstärken der elektroschwachen Eichbosonen zu ermitteln. Die Anpassung ergibt

$$g_1^Z = 0.983 \pm 0.018^{+0.018}_{-0.003} \quad \text{und} \quad \kappa_\gamma = 1.016 \pm 0.019^{+0.009}_{-0.013}.$$

Der erste Fehler ist die Summe aus statistischen und systematischen Fehlern und der zweite Fehler ergibt sich aus einer Variation der Higgsmasse zwischen 90 und 1000 GeV. Der erste Parameter beschreibt die Kopplungsstärke der ZWW und der zweite der γWW Wechselwirkung. Präzise direkte Messungen der Kopplungsstärke wurden durch die Erhöhung der Schwerpunktsenergie am LEP-Beschleuniger im Jahre 1996 möglich, die die Paarproduktion von W-Bosonen, $e^+e^- \rightarrow W^+W^-$, erlaubte. Zusätzlich zu diesem Kanal wurde auch noch die Kopplungsabhängigkeit des Wirkungsquerschnitts der einfach-resonanten W-Produktion, $e^+e^- \rightarrow We\nu_e$, und der Photonproduktion, $e^+e^- \rightarrow \nu\bar{\nu}\gamma(\gamma)$, benutzt, um die Selbstkopplung der Bosonen zu bestimmen. Zur Analyse wurden Daten, die einer Gesamtluminosität von 77 pb^{-1} entsprechen und bei Schwerpunktsenergien von 161, 172 und 183 GeV in den Jahren 1996 und 1997 mit dem **L3** Detektor aufgezeichnet wurden, benutzt. Die Kopplungsstärken ergeben sich zu

$$g_1^Z = 1.11^{+0.19}_{-0.18} \pm 0.10 \qquad \kappa_\gamma = 1.11^{+0.26}_{-0.25} \pm 0.17 \qquad \text{und}$$
$$\lambda_\gamma = 0.10^{+0.22}_{-0.20} \pm 0.10.$$

Der erste Fehler ist statistischer und der zweite systematischer Natur. Der Parameter λ_γ beschreibt Beiträge zur γWW Wechselwirkung. Die Vorhersagen des

Standardmodels von Eins für g_1^Z und κ_γ sowie von Null für λ_γ sind in guter Übereinstimmung mit allen Messungen. Insbesondere mit der Messung von g_1^Z konnte zum ersten Mal die Existenz des ZWW Vertex experimentell nachgewiesen werden. Zusätzlich fordert das Standardmodel die Erhaltung der C- und P-Parität am ZWW Vertex. Diese Vorhersage wurde durch die Messung der Kopplungskonstante g_5^Z zu

$$g_5^Z = -0.44^{+0.23}_{-0.22} \pm 0.12.$$

getestet und es wurde gute Übereinstimmung mit ihrer Standardmodelvorhersage gefunden. Die Messung der Kopplungsstärken in drei unterschiedlichen Kanälen entspricht der Messung in unterschiedliche Regionen von Impulsüberträgen Q^2. Die Messungen zeigen keine Q^2-Abhängigkeit, so dass sowohl das magnetische Dipolmoment μ_W als auch das elektrische Quadrupolmoment q_W des W-Bosons aus den Kopplungen hervorgehen

$$\mu_\mathrm{W} = (1.33 \pm 0.27) \times 10^{-5} \ \ \mu_B \qquad\qquad q_\mathrm{W} = (5.6 \pm 2.5) \times 10^{-36} \ \ \mathrm{m}^2.$$

Diese statischen Eigenschaften des W-Bosons geben Informationen über dessen Grösse und geometrische Struktur. So ergeben sich Radius und Deformationsparameter des W-Bosons zu

$$R_\mathrm{W} < 2^{-18}\mathrm{m} \ \ (95\%\ C.L.) \quad \text{und} \qquad\qquad \delta \cdot R_\mathrm{W}^2 = (3.3^{+30}_{-31}) \times 10^{-37}\ \mathrm{m}^2.$$

Zusätzlich zu diesen Informationen über das W-Boson, konnte der Parameterbereich einer Erweiterung der Standardmodels durch ein sequentielles Z′-Boson eingeschränkt werden. Ein Model von Klein das die Vereinigung von Kräften und Materie beschreibt wurde mit 10 Standardabweichungen ausgeschlossen.

Contents

I From motivation to measurement **1**

II From Standard Model of electroweak interactions to physics at LEP 2 **3**

2.1 Forces 4
2.2 Particles 8
2.3 e^+e^- physics 9
2.4 Three boson couplings in the electroweak sector 13
2.5 W pair production 14
2.6 A more fundamental approach 19
2.7 Selected models beyond the SM 28
2.8 Four-fermion final states 31
2.9 TGCs from $e^+e^- \to \nu\bar{\nu}\gamma(\gamma)$ 35
2.10 Bremsstrahlung process $e^+e^- \to W^+W^-\gamma$ 37
2.11 Is an e^+e^- collider the best place to study TGCs ? 38

III From past to presence **41**

3.1 Indirect bounds from Z^0 pole data 41
3.2 Direct bounds from Z^0 pole data 50
3.3 Do we need LEP 2? 52

IV From detector to data **53**

4.1 Large Electron Positron Collider 53
4.2 **L3** detector 56
4.3 Simulation 69
4.4 Reconstruction 70

4.5 Kinematic constraints 81
4.6 Is the experimental apparatus sufficient ? 82

V From data to selected events 83
5.1 Selection of W pairs 83
5.2 Selection of single Ws 91
5.3 Selection of $\nu\bar{\nu}\gamma(\gamma)$ events 94
5.4 Summary of selections 96

VI From selected events to physics parameters 99

From selected events to physics parameters 99
6.1 Choice of observables 100
6.2 Model independent presentation of data 105
6.3 Theory prediction 109
6.4 Principle of measurement 114
6.5 Measuring the couplings 120
6.6 Test of fit result 126
6.7 Tests of fit method 128
6.8 Fit result 140

VII From numbers to model comparison 141
7.1 Standard Model and W substructure 141
7.2 Non-standard models 144

VIII From this measurement to the world 147

IX From present to future studies of TGCs 151
9.1 TGCs from electroweak precision data 151
9.2 Rare B and K decays 151
9.3 Direct measurements of TGCs 152

X From beginning to end 155

A Boson self-coupling in the SM 159

B The linear extension 161

C The selection cuts 163

D Optimalness of optimal observables 169

E Some words about likelihood curves and statistics 173

F Contour curves and distributions 175

Abbreviations

ADC	**A**nalog to **d**igital **c**onverter
ALEPH	**A** detector for **LE**P **ph**ysics, experiment at LEP
ALR	**A**ctive **l**ead **r**ing, forward calorimeter of **L3**
BE	**B**ose-**E**instein effect
BGO	**B**ismuth **G**ermanium **O**xide = Bismuth Germanate, material of the **L3**-ECAL
BGO-MIP	MIP which is identified by its signature in the **L3**-electromagnetic calorimeter
CDF	**C**ollider **d**etector at **F**ERMILAB, experiment at the TEVATRON $p\bar{p}$ collider
CERN	European Laboratory for Particle Physics in Geneva, Switzerland
CKM	**C**abibbo-**K**obayashi-**M**askawa mixing matrix
C.L.	**C**onfidence **l**evel
CR	**C**olour **r**econnection
DØ	experiment at TEVATRON
DCA	**D**istance of **c**losest **a**proach
DELPHI	**De**tector with **l**epton, **p**hoton and **h**adron **i**dentification, experiment at LEP
DESY	**D**eutsches **E**lectronen **S**ynchrotron, accelerator center in Hamburg, Germany
DL	**D**etector **l**evel
ECAL	**E**lectromagnetic **cal**orimeter
FSR	**F**inal **s**tate **r**adiation
FermiLab	**Fermi** national accelerator **lab**oratory, Batavia, Illinois, USA
GL	**G**enerator **l**evel
HCAL	**H**adronic **cal**orimeter
HCAL-MIP	MIP which is identified by its signature in the **L3**-hadron calorimeter
ID (Id)	**Id**entity, used as synonym for the identification process of a particle
IP	**I**nteraction **p**oint
ISR	**I**nitial **s**tate **r**adiation
KEK	accelerator center in Tsukuba , Japan
L3	experiment at LEP
LC	**L**inear **c**ollider

LED	**L**ight **e**mitting **d**iode
LEP	**L**arge **e**lectron **p**ositron collider at CERN
LHC	**L**arge **h**adron **c**ollider
MC	**M**onte **C**arlo, technique for simulation of probabilistic processes
MIP	**M**inimum **i**onising **p**article
Ndf	**n**umber of **d**egrees of **f**reedom
NMR	**N**uclear **m**agnetic **r**esonance
NN	**N**eural **n**etwork
OO	**O**ptimal **o**bservables
OPAL	**O**mni-**p**urpose **a**pparatus at **L**EP, experiment at LEP
pdf	**P**robability **d**ensity **f**unction
SLAC	**S**tanford **l**inear **a**ccelerator **c**enter
SLD	**S**tanford **l**inear accelerator **d**etector
SM	**S**tandard **M**odel
SMD	**S**ilicon **m**icrovertex **d**etector
SPACAL	**Spa**ghetti **cal**orimeter, the **L3**-SPACAL covers the region between BGO-barrel and BGO-endcap
SRC	**S**mallest **r**esolvable **c**luster
TDC	**T**ime to **d**igital **c**onverter
TGC	**T**riple **g**auge boson **c**oupling
TGV	**T**riple **g**auge boson **v**ertex
TEC	**T**ime **e**xpansion **c**hamber, drift chamber of **L3**
TEVATRON	**TeV** **a**ccelerating synchro**tron**, $p\bar{p}$ collider at FermiLab
VSAT	**V**ery **s**mall **a**ngle **t**agger, forward detector of **L3**
WvW	**W**eyl van der **W**aerden, algorithm for matrix element computation using single helicity amplitudes
ZCH	**Z-ch**amber, drift chamber constructed to measure especially the z-coordinate in **L3**

Research is what I'm doing when I don't know what I'm doing.
W.v. Braun

I

From motivation to measurement

Physics as science derives from the rationalistic materialism that emerged in classical Greece and is closely connected to the questions of our existence and the existence of our surrounding. The scientific way of understanding is based upon the measurement, as its source of information. In a measurement test objects are brought in interaction with the object of interest and the reaction is observed. This process of understanding things goes back to the beginning of mankind. These studies evolved finally to the picture that the interaction of the test objects is governed by forces of different origin. It was only in the beginning of this century that models were introduced which explained the existence of forces as the process of the exchange of mediator particles. The study of the strength with which the mediator particles couple to matter resulted as the main objective of physics ever since. It needed until 1989 to discover experimentally that also mediator particles couple to each other, namely it was found that the mediator particle of the strong force, the gluon has this property [?, ?, ?] At the same time, the world physics community started to operate an electron-positron collider near Geneva. The discovery of the self-interaction of the mediator particles of the weak interaction was one of the important objectives of this project.
The goal was reached in 1996 as pairs of W Bosons, the charged mediator of the weak interaction, were produced in significant amounts at this collider. The exact measurement of this self-coupling is explained in the following chapters.
Theoretical guidance to today's understanding of particle physics is given in chapter two. It starts from the basics of the most accepted model and shows how the self-

interaction is embedded in this model. Extensions and alternative models are discussed with respect to different predictions about the self-coupling in the weak sector.
Proofs for the existence of the self-interaction of the weak bosons from existing data are discussed in the successive chapter. Numerical results for the coupling strength within a special model are presented.
The measurement of the self-interaction was carried out with the **L3** detector. The device is discussed in detail in chapter four. In addition the potential of the detector to measure self-couplings is discussed in terms of detector resolutions.
The selection of data events is explained in chapter five, followed by a view to the coupling extraction in chapter six. In the end the limitations of the measurement process are discussed.
In the next chapter models which are already introduced in chapter two are compared to the extracted coupling information and are evaluated with respect to their agreement to the measurement.
An outlook to promising experiments in the sector of self-interaction of weak bosons is given in the last chapter. The potential of the different projects is compared and it is shown that the field of the study of the self-interaction of mediator particles attracts more and more attention.

People prefer usually hunting for particles
and do not study interactions
- I guess that's materialism.
F. Jegerlehner

This isn't right. This isn't even wrong.
Wolfgang Pauli

II

From Standard Model of electroweak interactions to physics at LEP 2

The current theoretical understanding of the nature of fundamental particles and forces is called the Standard Model (SM) of particle physics [**?**]. In this theory the fundamental particles are spin-one-half fermions while the fundamental forces are mediated due to spin-one bosons. The only yet non-observed particle of this model is the spin-zero Higgs boson [**?**, **?**, **?**], responsible for the mass of bosons and fermions. Models with extended particle spectra like the non-minimal SM (a SM with more than one Higgs particle) or Supersymmetry (SUSY) [**?**, **?**] are constrained by experimental data.

In this chapter a short introduction into the structure of the SM is given, followed by a detailed discussion of its prediction of the boson self-coupling. Several final states of electron-positron interactions having relevance for the study of bosonic self-interaction are identified. One of these channels, the W pair production, is then used to discuss in great detail the SM prediction as well as the influence of alternative models and extensions to the SM. After this the other channels are discussed. The chapter finishes with a short comparison of the potential to study boson self-couplings at proton-anti-proton and electron-positron colliders.

2.1 Forces

The interaction of particles is distinguished into four different forces

- the gravitational force, responsible *e.g.* for the movement of the earth around the sun or the movement of galaxies,
- the electromagnetic force, responsible for the movement of the electron in the atomic orbit and the emission of light,
- the strong force, responsible for the stability of the nucleus and
- the weak force, responsible for the β-decay of nuclei and the fusion process in the sun.

While the gravitational force is not yet included in the framework of the SM the other three forces are. Within the SM they can be interpreted as interactions resulting from local phase transformations $U(x)$ in the space of the particle wave functions $\Psi(x)$

$$\Psi(x) \rightarrow \tilde{\Psi}(x) = U(x)\Psi(x), \tag{2.1}$$

where x is the local phase space coordinate. In the SM it is assumed that physics is invariant under such transformations. This is called the gauge principle. One representation of a local phase transformation is

$$U(x) = e^{\alpha_i(x)T_i}, \tag{2.2}$$

where T_i are called generators of the transformation and they determine the nature of the interaction.
In the case of the electromagnetic force the generator is the electromagnetic charge Q. The application of the gauge principle to the equation of motion of a particle with charge Q leads to relations consistent with the description of an electromagnetic wave - in the following called photon γ. The corresponding field potential is A_μ. Thus it is interpreted that the use of the gauge principle with the electromagnetic charge leads to the existence of the massless photon, understood as mediator particle of the related interaction. As the photon is a single element it is group-theoretically described by a local Abelian group $U(1)$.

The strong interaction is described due to the utilisation of the gauge principle to the SU(3)-colour charge leading to the existence of an octet of massless vector boson fields - the eight gluon fields $(\vec{G}_\mu)^i$ (i=1..8). Since the SU(3) group is non-Abelian the mediator particles of the strong interaction are also carriers of colour charge and thus interact with each other.
The application of the gauge principle in the case of the SU(2)-weak isospin results in the existence of a triplet of massless vector bosons $(\vec{W}_\mu)^i$ (i=1,2,3). The non-Abelian character of the SU(2) group causes self-interaction of these three bosons. However, it is experimentally known [?, ?] that the weak interaction is very short ranged. Thus the mediator particles of the weak interaction must have large masses. This mismatch is resolved by the Higgs mechanism of spontaneous symmetry breaking, the only known mechanism to have a renormalisable [?] theory with massive mediator particles. The mass which is given to the massless mediator particles results from the interaction of these particles with the Higgs background field, which is a complex scalar doublet field

$$\Phi = \frac{1}{\sqrt{2}} \begin{pmatrix} \phi_1 + i\phi_2 \\ \phi_3 + i\phi_4 \end{pmatrix}. \tag{2.3}$$

The number of possible Higgs fields is unlimited. Theories with only one Higgs field Φ are called minimal and only those are considered in the following.
The consideration of the process of pair production of weak bosons [?, ?] revealed that the photon field has to be included in the Higgs mechanism, in order to obtain a production rate which respects the unitarity bound [?]. This necessity leads to an unified picture of the electroweak interaction, group theoretically expressed by $SU(2)_L \times U(1)$. Here L denotes the coupling of the weak part only to left-handed fermions (those where the spin projection to its direction of motion is negative), later referred to as parity violation [?]. The generators of these groups are the weak isospin T_i (i=1,2,3) and the weak hypercharge Y, the corresponding gauge fields are the massless vector boson triplet $(\vec{W}_\mu)^i$ (i=1,2,3) and the singlet B_μ. The vector bosons observed in experiments [?] ($W^\pm$, Z^0, γ) are linear combinations of these four vector fields. This linear combination leads also to a relation between the generators of these fields, which is

$$Q = T_3 + Y. \tag{2.4}$$

Summarising the last paragraphs one can express high-energy particle physics described by the SM as resulting from the symmetry group $SU(3) \times SU(2)_L \times U(1)$. Each of the parts can be identified with a coupling constant, so that one finds three independent couplings g_i (i=1,2,3).
With these definitions the gauge field part of the Lagrangian of the SM consisting of the kinetic energy of all vector fields is

$$L = -\frac{1}{4}(\vec{W}_{\mu\nu}\vec{W}^{\mu\nu} + B_{\mu\nu}B^{\mu\nu} + \vec{G}_{\mu\nu}\vec{G}^{\mu\nu}). \tag{2.5}$$

The field strength tensors of the electroweak interaction $B_{\mu\nu}$ and $\vec{W}_{\mu\nu}$ and the one of the strong interaction $\vec{G}_{\mu\nu}$ are defined as

$$B_{\mu\nu} = \partial_\mu B_\nu + \partial_\nu B_\mu \tag{2.6}$$

$$(\vec{W}_{\mu\nu})^i = \partial_\mu(\vec{W}_\nu)^i - \partial_\nu(\vec{W}_\mu)^i - g_2\epsilon^{ijk}(\vec{W}_\mu)_j(\vec{W}_\nu)_k \tag{2.7}$$

$$(\vec{G}_{\mu\nu})^i = \partial_\mu(\vec{G}_\nu)^i - \partial_\nu(\vec{G}_\mu)^i - g_3 f^{ijk}(\vec{G}_\mu)_j(\vec{G}_\nu)_k, \tag{2.8}$$

where ϵ^{ijk} and f^{ijk} are the SU(2) and SU(3) structure constants, respectively. The terms which are containing these constants are the self-coupling terms, arising from the non-Abelian structure of the gauge groups. The Lagrangian terms arising from the scalar Higgs field are

$$L = T - V = [(D_\mu\Phi)^*(D^\mu\Phi)] - [\frac{1}{2}\mu^2\Phi^*\Phi - \frac{1}{4}\lambda(\Phi^*\Phi)^2], \tag{2.9}$$

where the first term is the kinetic energy term and the second describes the Higgs potential. The extremum of this potential is at

$$v = \sqrt{-\frac{\mu^2}{\lambda}}. \tag{2.10}$$

The structure of this potential allows that the minimum is not at $\Phi = 0$. In this case one finds two minima at $+v$ and at $-v$. The choice of the ground state is the process of spontaneous symmetry breaking, not only giving masses to the weak bosons but also creating a new scalar particle - the Higgs boson. To achieve invariance of the Lagrangian under local $\mathrm{SU}(2)_L$ gauge transformation the covariant derivative D_μ must be defined as

$$D_\mu = \partial_\mu + ig_1 Y B_\mu + ig_2\frac{\tau_i}{2}W_\mu^i, \tag{2.11}$$

where τ_i (i=1,2,3) represents the generators of the $SU(2)_L$. The covariant derivative leads to mass terms for the weak bosons, because one identifies the following terms in the Lagrangian

$$\left|\left(ig_2\frac{\tau_i}{2}W_\mu^i + ig_1 Y B_\mu\right)\Phi\right|^2 = \frac{1}{8}v^2 g_2^2\left[(W_\mu^1)^2 + (W_\mu^2)^2\right] + \frac{1}{8}v^2 (W_\mu^3, B_\mu)\begin{pmatrix} g_2^2 & -g_2 g_1 \\ -g_2 g_1 & g_1^2 \end{pmatrix}\begin{pmatrix} W^{3\mu} \\ B^\mu \end{pmatrix}, \quad (2.12)$$

as mass terms, where the first term is the mass term of the $W^\pm$ due to

$$\begin{pmatrix} W_\mu^+ \\ W_\mu^- \end{pmatrix} = \sqrt{\frac{1}{2}}\begin{pmatrix} 1 & -1 \\ 1 & 1 \end{pmatrix}\begin{pmatrix} W_\mu^1 \\ iW_\mu^2 \end{pmatrix} \quad (2.13)$$

and the second is the mass term for photon field A_μ and the Z^0 field Z_μ resulting from

$$\begin{pmatrix} A_\mu \\ Z_\mu \end{pmatrix} = \frac{1}{\sqrt{g_1^2 + g_2^2}}\begin{pmatrix} g_1 & g_2 \\ g_2 & -g_1 \end{pmatrix}\begin{pmatrix} W_\mu^3 \\ B_\mu \end{pmatrix}. \quad (2.14)$$

The masses of the vector bosons are thus proportional to the vacuum expectation value of the Higgs field v according to

$$m_{\mathrm{W}} = \frac{1}{2}v g_2, \quad (2.15)$$

$$m_{\mathrm{Z}^0} = \frac{1}{2}v\sqrt{g_1^2 + g_2^2} \quad \text{and} \quad (2.16)$$

$$m_\gamma = 0 \text{ GeV}. \quad (2.17)$$

These equations relate the coupling constants of the electroweak interaction with the masses of the mediating bosons in the form of

$$\frac{m_{\mathrm{W}}}{m_{\mathrm{Z}^0}} = \frac{g_2}{\sqrt{g_1^2 + g_2^2}} = \cos\theta_w, \quad (2.18)$$

where θ_w is called the weak mixing angle. The vacuum expectation value is computed from the ratio of the W mass and the weak coupling constant, which is accurately known from measurements of the muon life time [**?**]. Its value is $v = 246.2$ GeV.

2.2 Particles

Particles in the SM are understood as fundamental, thus not built up from other particles. The nature of particles can be classified according to their couplings in the interactions described above. All known matter particles are spin-half fermions. Mass terms like $m\bar{\Psi}\Psi$ cannot be included easily into the Lagrangian, since these

Generations			$U(1)[Y]$	$SU(2)_L[T_3]$	$SU(3)$ [colour]
$\begin{pmatrix}\nu_e\\ e^-\end{pmatrix}_L$	$\begin{pmatrix}\nu_\mu\\ \mu^-\end{pmatrix}_L$	$\begin{pmatrix}\nu_\tau\\ \tau^-\end{pmatrix}_L$	$-\frac{1}{2}$	$+\frac{1}{2}$ $-\frac{1}{2}$	–
e_R	μ_R	τ_R	-1	0	–
$\begin{pmatrix}u\\ d\end{pmatrix}_L$	$\begin{pmatrix}c\\ s\end{pmatrix}_L$	$\begin{pmatrix}t\\ b\end{pmatrix}_L$	$+\frac{1}{6}$	$+\frac{1}{2}$ $-\frac{1}{2}$	r,g,b
u_R	c_R	t_R	$+\frac{2}{3}$	0	r,g,b
d_R	s_R	b_R	$-\frac{1}{3}$	0	r,g,b

Table 2.1: *The periodic table of Particle Physics : Y is the weak hypercharge, T_3 is the third component of the electroweak isospin, r,g and b symbolise the three colours of the strong interaction and L and R denote left-handed and right-handed fermions.*

violate gauge invariance. As for bosons the coupling to the Higgs field is responsible for the masses of the fermions. Only with this field one can achieve combinations of right- and left-handed fields as needed for mass terms, such as

$$\begin{aligned} L &= G_e \left[(\bar{\nu}_e, \bar{e})_L \Phi e_R + \bar{e}_R \Phi^* \begin{pmatrix}\nu_e\\ e\end{pmatrix}_L \right] \\ &= \frac{G_e}{\sqrt{2}} v(\bar{e}_L e_R + \bar{e}_R e_L) + \frac{G_e}{\sqrt{2}}(\bar{e}_L e_R + \bar{e}_R e_L)h, \end{aligned} \tag{2.19}$$

where h is the remainder of the Higgs field after expansion at its vacuum expectation value v and G_e is the Higgs electron coupling constant. The first term is identified as mass term, as coming from a Yukawa like coupling [**?**] with

$$m_e = \frac{G_e v}{\sqrt{2}} \tag{2.20}$$

and the second term as an interaction term of the Higgs scalar and the electron with the coupling

$$\tilde{g} = \frac{m_e}{v} = 2 \times 10^{-6}. \tag{2.21}$$

Quark masses are generated similarly.

2.3 e^+e^- physics

In e^+e^- physics electrons and positrons are brought into interaction, leading either to the scattering of these particles or to the production of different particles. The electroweak part of the SM is suited to describe the interaction of electrons and positrons. This interactions is distinguished into s-channel scattering displayed in figure 2.1-a and t-channel scattering shown in figure 2.1-b. In s-channel scattering the electron and positron annihilate to an intermediate state which could be a photon γ, a Z^0 boson or a Higgs h.

Figure 2.1: **a***: The Annihilation of* e^+e^- *into a* Z^0 *boson, a* γ *or a Higgs is called s-channel production of these particles.* **b***: The scattering of the incoming* e^+e^- *is the exchange of a particle in the t-channel. The t-channel contribution to the Bhabha scattering* $e^+e^- \rightarrow e^+e^-$ *is used for the measurement of the luminosity.*

The t-channel scattering is characterised by the exchange of a particle between electron and positron. This particle could be a photon, a $W^\pm$, a Z^0, an electron $e^\pm$, a neutrino ν_e or a Higgs h. While in the s-channel case the final states are decay products of the virtual intermediate state one finds the final state for the t-channel defined by the initial state and the exchanged particle. The most prominent of these interactions is the t-channel photon exchange in $e^+e^- \rightarrow e^+e^-$ and is used for the measurement of the luminosity at LEP.

While at LEP 1 the main focus was the study of the Z^0 in the s-channel production, at LEP 2 it is used for the detector calibration.

2.3.1 The Bhabha scattering at small angles

The Bhabha scattering $e^+e^- \to e^+e^-$ is dominated by the t-channel exchange of a photon between the initial electron and positron. This process is an electromagnetic process and as such well known from low energy measurements. In Born approximation the differential cross section for small angles can be described as

$$\frac{d\sigma(e^+e^- \to e^+e^-)}{d\cos\theta} \propto \frac{1}{\theta^3 \sin\theta}, \tag{2.22}$$

thus the cross section rises strongly in the very forward (backward) direction. This is a typical behaviour of t-channel processes. The e^+e^- final state arises also from s-channel Z^0 and γ exchange, as well as from t-channel Z^0 exchange. However, their contribution to the total production rate is small compared to the t-channel photon exchange. At LEP 1 the s-channel Z^0 production was used to study the properties of this boson.

2.3.2 The Z^0 production and the Z^0 resonance

The Z^0 formation in e^+e^- collisions proceeds via the annihilation of the initial state particles into a Z^0 boson, as pictured in figure 2.1-a. The probability amplitude of this process in the following called matrix element is obtained by translating this pictorial representation using Feynman's rules [**?**]. This results into

$$\begin{aligned} M &= M_{e.m.} + M_{weak} \\ &= \frac{\imath}{s}\bar{v}(p_2)\gamma^\mu q_e u(p_1)\bar{u}(p_3)\gamma_\mu q_f v(p_4) \\ &+ \frac{\imath}{s}\, a(s) 4\bar{v}(p_2)\gamma_\mu(g_e^V + g_e^A\gamma^5)u(p_1)\bar{u}(p_3)\gamma^\mu(g_f^V + g_f^A\gamma^5)v(p_4) \ , \end{aligned} \tag{2.23}$$

where u and v are the spinors of the initial and final state particles, with the corresponding momenta p_i (i=1...4), γ_μ are Dirac's gamma matrices, s is the square of the centre-of-mass energy, and $a(s)$ is

$$a(s) = \frac{1}{4\sin^2\theta_w \cos^2\theta_w} \ \ \frac{s}{s - m_{Z^0}^2 + \imath m_{Z^0}\Gamma_Z} \tag{2.24}$$

the relative strength of the photon and the Z^0 graph. The properties of the initial and final state fermions enter via their axial vector (g_f^A) and vector couplings (g_f^V) and their electromagnetic charges (q_f). This equation can be used to compute

the differential and total cross section. For unpolarised beams and with fermion masses neglected one finds

$$\frac{d\sigma}{d\cos\theta} = \frac{3}{8} N_f^C \left[A\left(1+\cos^2\theta\right) + B\cos\theta \right] \frac{2\pi\alpha^2}{3s}, \tag{2.25}$$

with

$$A = \overbrace{q_e^2\, q_f^2}^{\text{Photon exchange}} + \overbrace{2q_e\, q_f\, g_e^V g_f^V \Re(a(s))(1-h_f)}^{\text{Interference}} + \overbrace{\left[(g_e^V)^2+(g_e^A)^2\right]\left[(g_f^V)^2 - 2h_f g_f^V g_f^A + (g_f^A)^2\right]|a(s)|^2}^{\text{Z}^0\text{ exchange}}, \tag{2.26}$$

$$B = \overbrace{4q_e q_f g_e^A g_f^V (1-h_f)\Re(a(s))}^{\text{Interference}} - \overbrace{4g_e^V g_e^A\left[h_f (g_f^V)^2 - 2g_f^V g_f^A + h_f (g_f^A)^2\right]|a(s)|^2}^{\text{Z}^0\text{ exchange}} \tag{2.27}$$

and N_f^C the number of QCD colours, which is one for leptons and three for quarks. For the total cross section equation 2.25 has to be integrated. This leads to

$$\sigma = N_f^C A \frac{4\pi\alpha^2}{3s} \tag{2.28}$$

If the final state particle helicity h_f cannot be determined, the sum of all possible helicity states has to be taken. Figure 2.2 displays the dependence of the cross section on the square root of the centre-of-mass energy, showing the typical resonance behaviour of the cross section close to the Z^0 mass.

For small centre-of-mass energies the terms with $a(s)$ are small and can be neglected. Only the cross section of pure photon exchange remains

$$\sigma(s \ll m_{Z^0}^2) = q_e^2\, q_f^2 \frac{4\pi\alpha^2}{3s}. \tag{2.29}$$

If the centre-of-mass energy is close to the Z^0 mass the Z^0 exchange will dominate the photon exchange term as well as the interference term, while if the energy is equal the Z^0 mass the interference term will vanish, because

$$a(s) = -\frac{1}{4\sin^2\theta_w \cos^2\theta_w} \cdot \frac{m_{Z^0}}{\Gamma_Z} i \tag{2.30}$$

has no real part anymore. This leads to

$$\sigma(s = m_{Z^0}^2) = \frac{12\pi}{m_{Z^0}^2} \frac{\Gamma_e}{\Gamma_Z} \frac{\Gamma_f}{\Gamma_Z}, \tag{2.31}$$

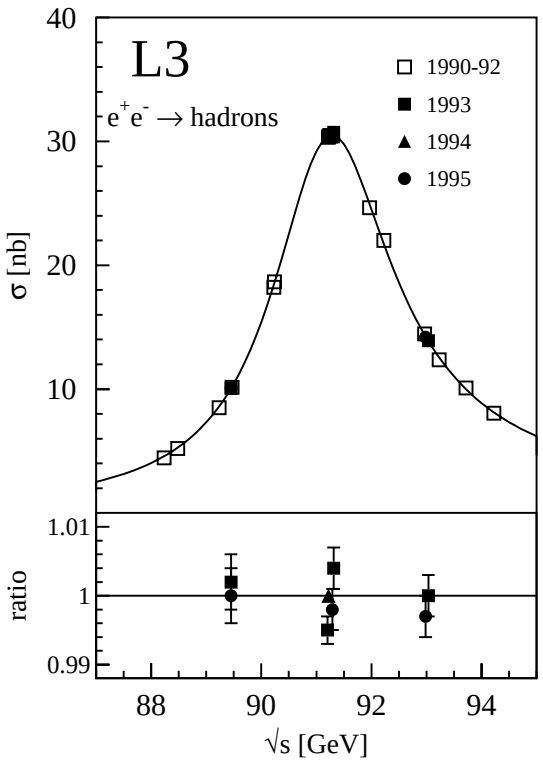

Figure 2.2: *The cross section* $e^+e^- \rightarrow$ *hadrons as a function of the centre-of-mass energy. The line represents the SM while the dots correspond to data taken with the* **L3** *detector in the years 91-95. The lower plot shows the ratio of the measurement and the SM prediction. The peaking structure is explained as the resonance production of a* Z^0 *boson.*

where

$$\Gamma_f = N_f^C \frac{\alpha \, m_{Z^0}}{12 \sin^2\theta_w \, \cos^2\theta_w} \left[(g_f^V)^2 + (g_f^A)^2\right] \tag{2.32}$$

is called partial decay width of the Z^0 into a fermion pair $f\bar{f}$.

For even higher energies both photon and Z^0 exchange contribute almost equally to the cross section, according to formula 2.28.

2.4 Three boson couplings in the electroweak sector

The electroweak part of the SM contains three bosons : the photon γ, the Z^0 and the $W^{\pm}$. Thus the existence of ten three boson vertices and 15 four boson vertices is expected, if these bosons couple to each other. Charge conservation reduces this number to six and nine respectively. Only two of the six possible three boson vertices exist in the SM, namely the γWW and the Z^0WW vertex. The remaining four are the

- $\gamma\gamma\gamma$ vertex which tests the electromagnetic charge of the photon ($q < 5 \times 10^{-5} e$ [?, ?, ?]), the
- $\gamma\gamma Z^0$ vertex testing the weak properties of the photon, the
- $Z^0Z^0\gamma$ vertex which tests the electromagnetic properties of the Z^0 and the
- $Z^0Z^0Z^0$ vertex testing the weak charge of the Z^0,

which do not exist in the SM. In the case of four boson vertices only four of the nine are realised in the SM. Those are WWWW, WWZ^0Z^0 $WW\gamma\gamma$ and $WWZ^0\gamma$ while

- $Z^0Z^0Z^0Z^0$,
- $\gamma\gamma\gamma\gamma$,
- $Z^0Z^0Z^0\gamma$,
- $Z^0\gamma\gamma\gamma$, and
- $Z^0Z^0\gamma\gamma$

do not exist. The SM argument for their non-existence is discussed in more detail in appendix A.
The following sections will now be devoted to the study of the two three boson vertices. Taking just the vertex γWW the construction of four cases by rotation of the time axis is possible, namely an existing γ decays into two Ws, two existing Ws fuse to form a photon γ and an existing W absorbs or emits a γ . These processes

are displayed in figure 2.3. It is obvious by construction that the relevant energy scale Q^2 changes due to rotation and thus that the study of all the combinations will give the most complete understanding of these vertices. All combinations can in fact be studied at e^+e^- machines at Born level and will be discussed in the following. Figure 2.3-a can be studied with W pair production, $e^+e^- \rightarrow W^+W^-$, at $Q^2 = s$, figure 2.3-b with single-resonant W production, $e^+e^- \rightarrow We\nu_e$, at $Q^2 = m_W^2$, figure 2.3-c with single photon production, $e^+e^- \rightarrow \nu\bar{\nu}\gamma(\gamma)$, at $Q^2 = 0$ and figure 2.3-d with WWγ production, $e^+e^- \rightarrow W^+W^-\gamma$, at $Q^2 = 0$. Analogue processes exist for the measurement of the ZWW couplings.

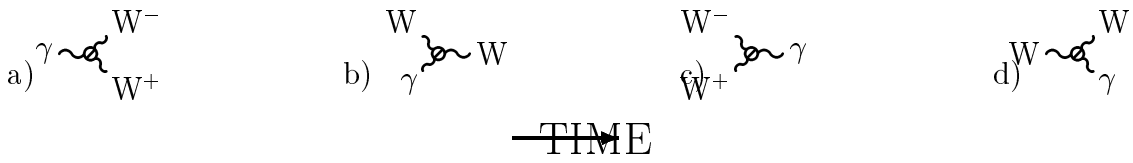

Figure 2.3: *The* γWW *vertex has four representation with respect to the time axis.*

2.5 W pair production

Not only fermions but also bosons are produced in pairs in e^+e^- interactions. This is visualised in figure 2.4 for the W pair production where both s- and t-channel contribute. The s-channel production enables to determine one of the fundamental building blocks of the electroweak part of the SM - the non-Abelian structure of the $SU(2)_L \times U(1)$ gauge group manifested in the self-coupling of the electroweak gauge bosons. In figure 2.4 two of these couplings can be seen. The coupling of the photon to the W bosons in figure 2.4.b is the manifestation of charge of these gauge bosons. But they have also a weak charge which causes the graph in figure 2.4.c where the Z couples to the W boson. In the t-channel graph fermion-W boson couplings can be observed. The three diagrams in figure 2.4 represent all lowest order diagrams in the SM, The Higgs s-channel production diagram is omitted, due to the strong suppression of this diagram by the small coupling of the Higgs to the initial state electron.

Since the t-channel is purely weak, only left-handed electrons can participate and

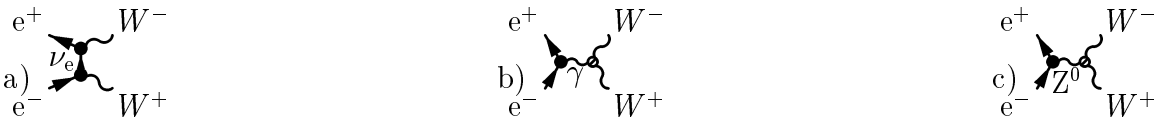

Figure 2.4: W *pair production in* e^+e^- *interactions proceeds via three mechanisms, the t-channel exchange of a* ν_e *(a) and the s-channel exchange of a* γ *(b) or of a* Z^0 *(c). These three charged current diagrams are usually referred to as CC03.*

contribute to the total cross section. The matrix element can be written as [**?**]

$$M_\nu = \frac{e^2}{4\sin^2\theta_w}\frac{1}{t}\,\bar{v}(p_+)\gamma_\mu\epsilon_+^\mu(k_+,\lambda_+)\gamma_\nu(k_+-p_+)^\nu\gamma_\eta\epsilon_-^\eta(k_-,\lambda_-)(1-\gamma^5)u(p_-), \tag{2.33}$$

where u and v are the electron and positron spinors, $\epsilon_\pm$ are the helicity amplitudes of the positive and negative W boson, $p_\pm/k_\pm$ are the momenta of initial/final state particles, $\lambda_\pm$ are the helicities of the outgoing bosons, and t is the four-momentum squared of the exchanged neutrino. The production via the photon in the s-channel can be described with [?]

$$\begin{aligned} M_\gamma = &-\frac{e^2}{s}\bar{v}(p_+)\gamma_\mu u(p_-) \\ &\times\epsilon_-(k_-,\lambda_-)_\nu\left[k_+^\nu g^{\eta\mu}-k_-^\eta g^{\nu\mu}+\frac{(k_+-k_-)^\mu}{2}g^{\nu\eta}\right]\epsilon_+(k_+,\lambda_+)_\eta, \end{aligned} \tag{2.34}$$

while the production via the Z boson can be expressed as [?]

$$\begin{aligned} M_{\mathrm{Z}}^0 = &-\frac{e^2}{s}\,\frac{\cos\theta_w}{\sin\theta_w}\,\frac{1}{2\cos\theta_w\sin\theta_w}\,\frac{s}{s-m_{\mathrm{Z}^0}^2+\imath m_{\mathrm{Z}^0}\Gamma_Z}\times\bar{v}(p_+)\gamma_\mu(g_{\mathrm{e}}^V-g_{\mathrm{e}}^A\gamma^5)u(p_-) \\ &\times\epsilon_-(k_-,\lambda_-)_\nu\left[k_+^\nu g^{\eta\mu}-k_-^\eta g^{\nu\mu}+\frac{(k_+-k_-)^\mu}{2}g^{\nu\eta}\right]\epsilon_+(k_+,\lambda_+)_\eta. \end{aligned} \tag{2.35}$$

Combining the matrix elements for the W production with the decay amplitude into a fermion pair [?]

$$D_\lambda(\theta_1,\phi_1) = \begin{pmatrix} \frac{1}{\sqrt{2}}(1-\cos\theta_1)\,e^{-\imath\phi_1} \\ -\sin\theta_1 \\ \frac{1}{\sqrt{2}}(1+\cos\theta_1)\,e^{\imath\phi_1} \end{pmatrix} \begin{matrix} \lambda=+1 \\ \text{for } \lambda=\ \ 0 \\ \lambda=-1 \end{matrix} \tag{2.36}$$

one gets

$$\frac{d^5\sigma(e^+e^- \to W^+W^- \to f_1\bar{f}_2 f_3\bar{f}_4)}{d\cos\theta\, d\cos\theta_1\, d\phi_1\, d\cos\theta_2\, d\phi_2} =$$
$$\frac{9\beta}{8192\pi^3 s} B(W \to f_1\bar{f}_2) B(W \to f_3\bar{f}_4) \times \sum_{\sigma\lambda\bar{\lambda}\lambda'\bar{\lambda}'} M(\sigma\lambda\bar{\lambda}) M^*(\sigma\lambda'\bar{\lambda}')$$
$$\times D_\lambda(\theta_1,\phi_1)\, D^*_{\lambda'}(\theta_1,\phi_1)\, D_{\bar{\lambda}}(\pi-\theta_2,\phi_2+\pi)\, D^*_{\bar{\lambda}'}(\pi-\theta_2,\phi_2+\pi) \qquad (2.37)$$

The sum extends over the helicities λ of the two Ws and over the helicity σ of the electron. The angles θ_i and ϕ_i are the decay angles of the Ws into the fermion-anti-fermion pairs in the W rest frame. They are very well suited to analyse the polarisation of the decaying W. The parity violation [?] of the charged current coupling creates favoured directions for the W decay products as can be seen in figure 2.5. In the case that a W^- of helicity $\lambda = 1$ decays, the electron will mainly be emitted in opposite direction to the W flight direction, while in the case of helicity $\lambda = -1$ the emission occurs parallel to this direction. If the W^- has a helicity of $\lambda = 0$ then the (anti-)parallel emission of the fermion is strongly suppressed, since the parallel emission of the fermion requires left-handed anti-fermions and anti-parallel emission requires right-handed fermions. These arguments lead to the mathematical description of the W decay amplitude shown in equation 2.36. The coordinate system of the W rest frame is defined such, that the z-axis points towards the W flight direction and the y-axis is perpendicular to the z-axis and the direction of the beam. While θ_1 and ϕ_1 are defined from the fermion in the W^- rest frame, θ_2 and ϕ_2 are the angles of the anti-fermion in the W^+ frame.
This is a very simplified approach since the W decays very fast and has a considerable width, such that one has to include the off-shell behaviour of the W into the calculation. The equations above hold only very close to the W production threshold, where they lead in first order approximation to

$$\sigma \approx \frac{\pi\alpha^2}{s} \frac{1}{4\sin^4\theta_w} 4\beta + O(\beta^3). \qquad (2.38)$$

Close to the threshold the W velocity β is small and suppresses the s-channel contribution, since it is proportional to β^3, while the t-channel W pair production, proportional to β, is favoured. The neglect of the W width is called the narrow width scheme, while for the correct computation the width has to be taken into

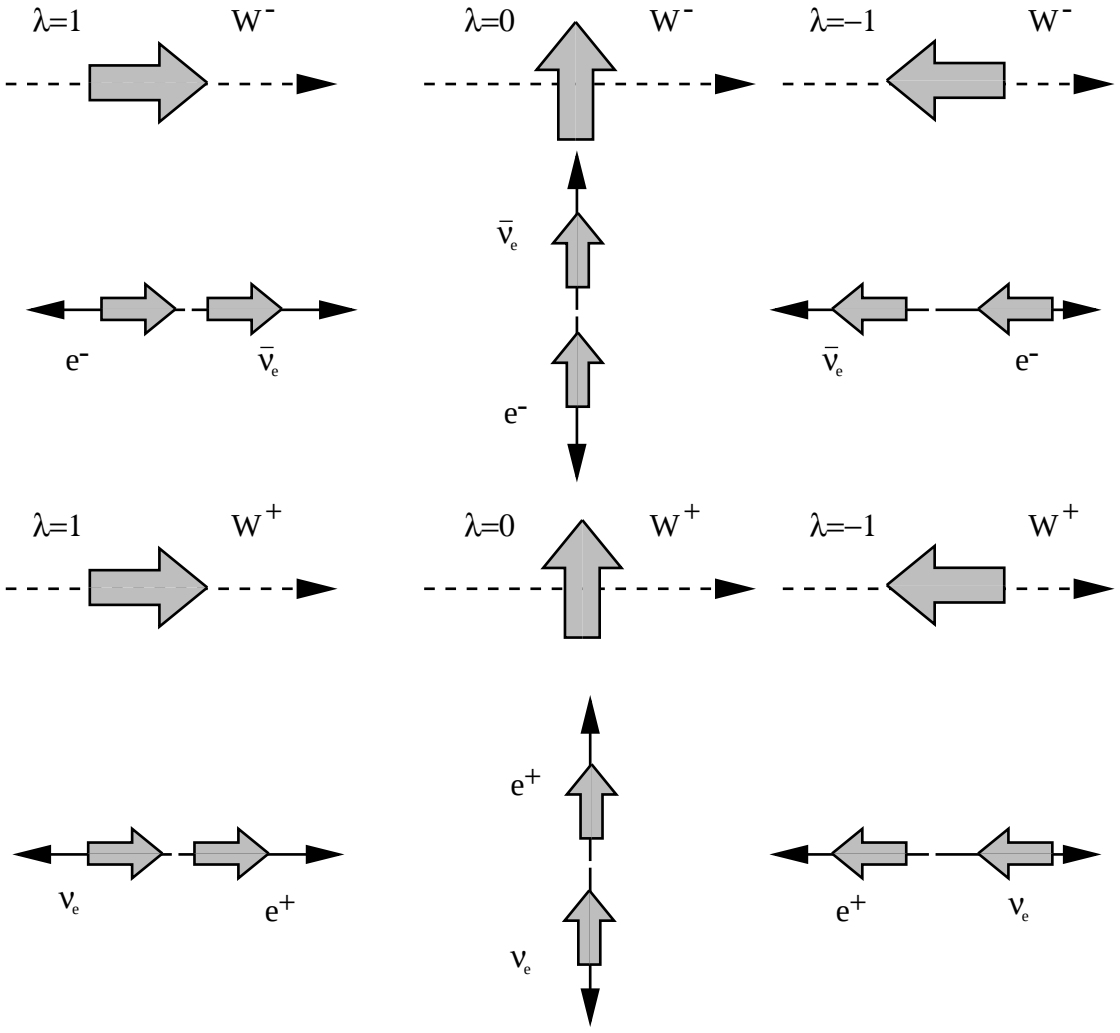

Figure 2.5: *The decay of* W^+ *and* W^- *in* $\mathrm{e}\nu_\mathrm{e}$ *displayed for the different* W *helicity states* $\lambda = \pm 1, 0$. *The shaded arrows indicate the spin direction* $\vec{n}_J$, *while the solid arrows point in the direction of the momentum* $\vec{n}_p$. *Neutrinos* ν_e *are always left-handed* ($\vec{n}_J \cdot \vec{n}_p = -1$), *while anti-neutrinos* $\bar{\nu}_\mathrm{e}$ *are always right-handed. Thus the emission angles of the decay products have favoured values, making the distinction of different helicity states of the* W *by analysing its decay angles possible.*

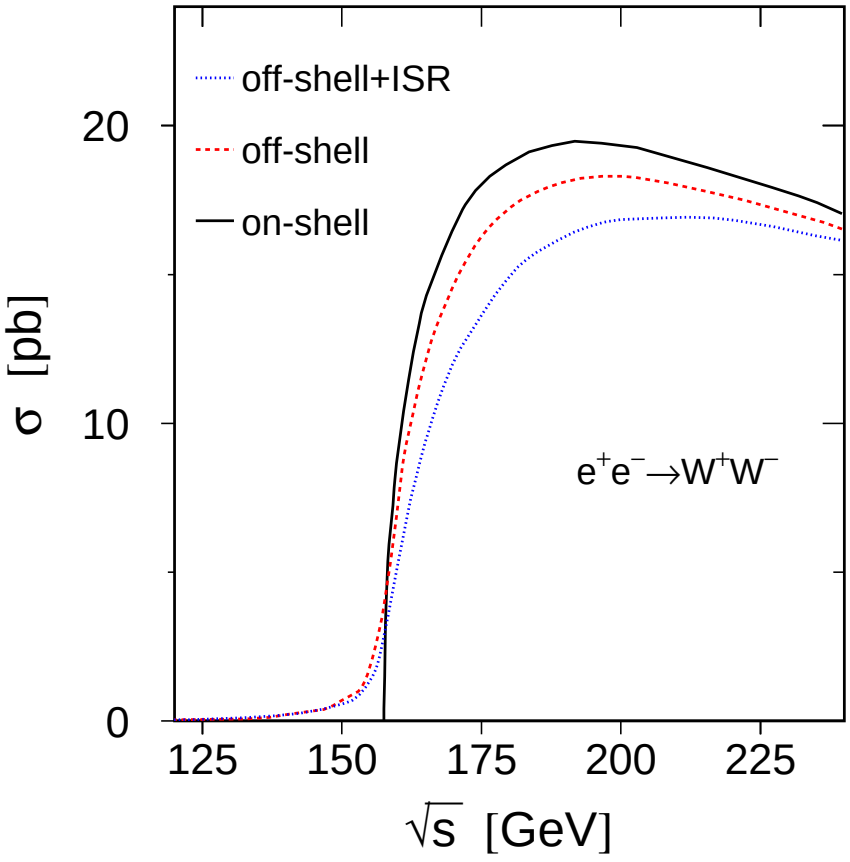

Figure 2.6: *The energy dependence of* W *pair production cross section gets changed by including the* W *width and initial state radiation in the computation.*

account. One possibility is to convolute the total cross section with two Breit-Wigner functions [**?**].

$$\sigma(s) = \int_0^s ds_1 \rho(s_1) \int_0^{(\sqrt{s}-\sqrt{s_1})^2} ds_2 \rho(s_2) \sigma_0(s, s_1, s_2) \quad , \tag{2.39}$$

where

$$\rho(s_i) = \frac{1}{\pi} \frac{m_{\mathrm{W}} \Gamma_{\mathrm{W}}(s_i)}{(s_i - m_{\mathrm{W}}^2)^2 + m_{\mathrm{W}}^2 \Gamma_{\mathrm{W}}^2(s_i)} \quad . \tag{2.40}$$

Here one uses the s-dependent W width $\Gamma_{\mathrm{W}}(s_i)$ which is defined as

$$\Gamma_{\mathrm{W}}(s_i) = \frac{s_i}{m_{\mathrm{W}}^2}\Gamma_{\mathrm{W}}. \tag{2.41}$$

The use of the W width has important influence especially close to the production threshold as can be seen in figure 2.6. The possible off-shell production of the W pair allows production through the CC03 diagrams at centre-of-mass energies below twice the W mass. The cross section at energies far larger than the threshold is decreased slightly due to the inclusion of the width in the computation, as this smears the double resonant behaviour of the CC03 process. In addition the initial electrons and positrons loose energy before they collide due to the emission of photons, in the following called initial state radiation (ISR). Since this means effectively a reduction of the centre-of-mass energy for W pair production the total cross section decreases strongly in regions where it rises steeply with $\sqrt{s}$, as is displayed in figure 2.6.

2.6 A more fundamental approach

In the last section the W pair production was discussed in the framework of the SM. Although the SM celebrated great successes over the last 20 years, a model independent approach is more suitable to discuss the W pair production and to test the predictions of this model.

The most general Lagrangian assuming only Lorentz invariance of the WWV

(V=Z/γ) vertex is [?, ?]

$$\begin{aligned}
\imath\mathcal{L}_{eff}^{\mathrm{WWV}} &= g_{\mathrm{WWV}}\{g_1^V V^\mu \left(W^-_{\mu\nu}W^{+\nu} - W^+_{\mu\nu}W^{-\nu}\right) \\
&+ \kappa_V W^+_\mu W^-_\nu V^{\mu\nu} \\
&+ \frac{\lambda_V}{m^2_{\mathrm{W}}} V^{\mu\nu} W^{+\rho}_\nu W^-_{\rho\mu} \\
&+ \imath g_5^V \epsilon_{\mu\nu\rho\sigma}\left(\left(\partial^\rho W^{-\mu}\right)W^{+\nu} - W^{-\mu}\left(\partial^\rho W^{+\nu}\right)\right)V^\sigma \\
&+ \imath g_4^V W^-_\mu W^+_\nu \left(\partial^\mu V^\nu + \partial^\nu V^\mu\right) \\
&- \frac{\tilde{\kappa}_V}{2} W^-_\mu W^+_\nu \epsilon^{\mu\nu\rho\sigma} V_{\rho\sigma} \\
&- \frac{\tilde{\lambda}_V}{2m^2_{\mathrm{W}}} W^-_{\rho\mu} W^{+\mu}_\nu \epsilon^{\nu\rho\alpha\beta} V_{\alpha\beta}\}
\end{aligned} \tag{2.42}$$

In formula 2.42 one finds the overall coupling constants $g_{WWZ} = e\cos\theta_w$ and $g_{WW\gamma} = e$ as well as fourteen (2×7) constants for each possible combination of the vector fields of V and W. In general all the constants have a real and an imaginary part. The imaginary part is the absorptive part of the vertex function. In a weakly coupled theory, like the SM, these parts go usually with very small couplings. However, if the W boson sector is strongly interacting these terms might be large, but would not only change the treatment of the WWV vertex but change the complete amplitude of the $e^+e^- \to W^+W^-$ process [?]. Since, no large deviation from the SM have been observed yet in other electroweak tests, it is assumed that a weakly coupled theory is realised in nature, thus the imaginary part is omitted in the following. Within the SM the coupling constants are

$$g_1^\gamma = g_1^Z = \kappa_\gamma = \kappa_Z = 1 \tag{2.43}$$

and

$$\lambda_\gamma = \lambda_Z = 0 \tag{2.44}$$

$$g_5^\gamma = g_5^Z = 0 \qquad \text{CP conserving, C and P violating} \tag{2.45}$$

$$g_4^\gamma = g_4^Z = \tilde{\kappa}_\gamma = \tilde{\kappa}_Z = \tilde{\lambda}_\gamma = \tilde{\lambda}_Z = 0\,. \qquad \text{CP violating} \tag{2.46}$$

The consequences for the physics at the WWV vertex in terms of the discrete transformation of space inversion or parity P and particle-antiparticle conjugation C, if

the SM value is not realised in nature, is indicated. Apart from this terminology it is also common to define variables which just parameterise the difference to the SM expectation. Thus if the SM expectation of a coupling constant is non-zero one defines a variable, for which the SM expectation is zero. Therefore Δg_1^Z, $\Delta\kappa_Z$, Δg_1^γ and $\Delta\kappa_\gamma$ are often used instead of g_1^Z, κ_Z, g_1^γ and κ_γ.
The parameters for the photon-W coupling can equivalently be interpreted in terms of electromagnetic multipole moments of the W. These are the electric charge

$$Q_W = g_{WW\gamma} g_1^\gamma = e g_1^\gamma \tag{2.47}$$

the magnetic dipole moment

$$\mu_W = \frac{g_{WW\gamma}}{2m_{\mathrm{W}}}(g_1^\gamma + \kappa_\gamma + \lambda_\gamma) \tag{2.48}$$

and the electric quadrupole moment

$$q_W = -\frac{g_{WW\gamma}}{m_{\mathrm{W}}^2}(\kappa_\gamma - \lambda_\gamma). \tag{2.49}$$

The extension of the Lagrangian compared to the SM leads to changed matrix elements for W pair production.

$$M_\gamma = -\sqrt{2}\sigma e^2 \beta A^\gamma_{\lambda\bar\lambda} d^{J_0}_{\sigma,\lambda,\bar\lambda} \tag{2.50}$$

$$M^0_{\mathrm{Z}} = \sqrt{2}\sigma e^2 \beta A^Z_{\lambda\bar\lambda} \left[1 - \delta_{\sigma,-1}\frac{1}{\sin^2\theta_w}\right] \frac{s}{s - m^2_{\mathrm{Z}^0}} d^{J_0}_{\sigma,\lambda,\bar\lambda} \tag{2.51}$$

$$M_\nu = \delta_{\sigma,-1}\frac{1}{2\beta\sin^2\theta_w}\left[B_{\lambda,\bar\lambda} - \frac{1}{1-\beta^2-2\beta\cos\theta} C_{\lambda,\bar\lambda}\right] d^{J_0}_{\sigma,\lambda,\bar\lambda} \quad , \tag{2.52}$$

where $\delta_{-1,-1} = 1$ and $\delta_{\sigma\neq-1,-1} = 0$ and $A^V_{\lambda,\bar\lambda}$, $B_{\lambda,\bar\lambda}$, $C_{\lambda,\bar\lambda}$ and $d^{J_0}_{\sigma,\lambda,\bar\lambda}$ are defined in table 2.2. The A-functions come from the description of the WWV vertex. The configurations $\lambda\bar\lambda = +-\,,\ -+$, *i.e.* $|\lambda - \bar\lambda| = 2$, are only produced due to the t-channel diagram, since γ and Z^0 have spin-one. Thus s-channel diagrams contribute to seven helicity combinations, which results in the need of seven coupling constants to describe the most general WWV vertex. This was exactly the number found in equation 2.42. The d-functions [?] $d^{J_0}_{\sigma,\lambda,\bar\lambda}$ come from the quantum mechanical description of the decay of a spin-one or spin-two state into two spin-one states. Two examples are sketched in figure 2.7. It is interesting to note that in the SM $A^\gamma_{\lambda\bar\lambda}$ and $A^Z_{\lambda\bar\lambda}$ are equal, as can be read from table 2.2.
Thus the equations 2.50 to 2.52 show the interesting SM-property of gauge cancellation in $\mathrm{e^+e^-}\to\mathrm{W^+W^-}$. The effect of gauge cancellation played a significant

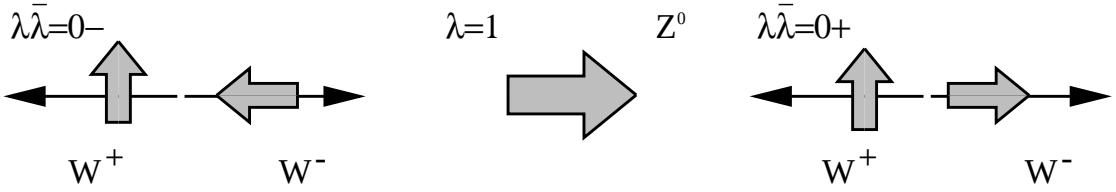

Figure 2.7: *The* Z^0 *decay into* W^+W^- *shown for the* W *helicity combinations* $0-$ *and* $0+$*, where the first has a d-function proportional to* $1-\cos\theta_W$ *and the second one proportional to* $1+\cos\theta_W$*.*

role in the development of the SM. It was noted at the time that the cross section of the process $\nu_e\,\nu_e \rightarrow W^+W^-$ was growing with energy, if only the t-channel exchange of an electron was considered [**?**]. The only way to save unitarity was the introduction of a cut-off energy, thus automatically implying that one deals only with an effective theory. The introduction of the Z^0 solved this problem in a natural way [**?**], since the growing terms cancel and the cross section decreases inversely proportional to energy. In the case of $e^+e^- \rightarrow W^+W^-$ the t-channel and the Z^0 s-channel terms do not cancel their bad high energy behaviour. However, both electromagnetic and weak pair production amplitudes grow with energy and cancel each other in the high energy limit, such that the scattering amplitude decreases inversely proportional to energy if $\sqrt{s} >> 2m_W$ [?]. This argument holds only for massless fermions while for massive ones some energy proportional terms remain [?]. However, the s-channel exchange of the Higgs particle h delivers such terms to finally make the cross section vanish at $\sqrt{s} = \infty$. Going back to equations 2.50 to 2.52 one sees that the two terms in equation 2.51 are the same as M_γ and the first term in M_ν if s is much larger than $m^2_{Z^0}$ and if β is close to one. Only the second term of equation 2.52 survives, but it is inversely proportional to Lorentz-γ, which means it decreases with increasing centre-of-mass energies. Thus the SM cross section vanishes sufficiently fast in the high energy limit. From these matrix elements one can now compute the cross section as it was outlined in the last section for the SM case. The contributions from the different polarisation combinations of the W in the SM can be seen in figure 2.8. The transverse-transverse component (TT) is strongly forward peaked since its only produced via t-channel. However it vanishes at $\cos\theta_W = \pm 1$ due to the d-function d^2_{12}, which is proportional to $\sin\theta_W$. Also the d-function of the longitudinal-longitudinal component (LL) is proportional to $\sin\theta_W$, having the same effect of vanishing contributions from LL

$\lambda\bar{\lambda}$	$A^V_{\lambda,lam\bar{b}da}$	$B_{\lambda,\bar{\lambda}}$	$C_{\lambda,\bar{\lambda}}$	$d^{J_0}_{\sigma,\lambda,\bar{\lambda}}$
$++$	$g_1^V + 2\gamma^2\lambda_V + \frac{i}{\beta}(\tilde{\kappa}_V + \tilde{\lambda}_V(1-2\gamma^2))$	1	$\frac{1}{\gamma^2}$	$-\frac{\sigma\sin\theta}{\sqrt{2}}$
$--$	$g_1^V + 2\gamma^2\lambda_V - \frac{i}{\beta}(\tilde{\kappa}_V + \tilde{\lambda}_V(1-2\gamma^2))$	1	$\frac{1}{\gamma^2}$	$-\frac{\sigma\sin\theta}{\sqrt{2}}$
$+0$	$\gamma(g_1^V + \kappa_V + \lambda_V - g_4^V + \beta g_5^V + \frac{i}{\beta}(\tilde{\kappa}_V - \tilde{\lambda}_V))$	2γ	$\frac{2(1+\beta)}{\gamma}$	$\frac{1+\sigma\cos\theta}{2}$
$0-$	$\gamma(g_1^V + \kappa_V + \lambda_V + g_4^V + \beta g_5^V - \frac{i}{\beta}(\tilde{\kappa}_V - \tilde{\lambda}_V))$	2γ	$\frac{2(1+\beta)}{\gamma}$	$\frac{1+\sigma\cos\theta}{2}$
$0+$	$\gamma(g_1^V + \kappa_V + \lambda_V + g_4^V - \beta g_5^V + \frac{i}{\beta}(\tilde{\kappa}_V - \tilde{\lambda}_V))$	2γ	$\frac{2(1-\beta)}{\gamma}$	$\frac{1-\sigma\cos\theta}{2}$
-0	$\gamma(g_1^V + \kappa_V + \lambda_V - g_4^V - \beta g_5^V - \frac{i}{\beta}(\tilde{\kappa}_V - \tilde{\lambda}_V))$	2γ	$\frac{2(1-\beta)}{\gamma}$	$\frac{1-\sigma\cos\theta}{2}$
$0\,0$	$g_1^V + 2\gamma^2\kappa_V$	$2\gamma^2$	$\frac{2}{\gamma^2}$	$-\frac{\sigma\sin\theta}{\sqrt{2}}$
$+-$	0	0	$2\sqrt{2}\beta$	$\sin\theta * \frac{1-\cos\theta}{2}$
$-+$	0	0	$2\sqrt{2}\beta$	$-\sin\theta * \frac{1+\cos\theta}{2}$

Table 2.2: *Definition of the ingredients for the matrix element computation of* W *pair production [?]. The d-functions [?] are the ones for the decay of a spin-two state ($J_0 = 2$) in the case of $\lambda\bar{\lambda} = +-, -+$, while $J_0 = 1$ for all other cases.*

at $\cos\theta_w = \pm 1$. The local minima for LL shows impressively the effect of the cancellation of γ, Z^0 and ν_e exchange. At this value of the $\cos\theta_W$ the contribution of the second term of equation 2.52 equals the remaining contributions. This is also present for the transversal-longitudinal (TL+LT) case, but the summing over the five configuration with different minima positions makes this effect less visible. Since the d-functions for the TL+LT configurations are proportional to $(1\pm\cos\theta_W)$ they do not vanish at $\cos\theta_W = \pm 1$.

From table 2.2 one can readily see that the cross section depends quadratically from all couplings. This is visualised for the case of g_1^Z in figure 2.9.

Non-SM couplings of the W cannot be accommodated in today's SM as it cannot be made gauge invariant with these couplings. Small changes to the contribution of a single amplitude will completely spoil the gauge cancellation and thus the cross section will violate the unitarity condition. The only way to save unitarity is the introduction of an energy cut-off, making the SM to an effective theory. Thus non-SM couplings imply additional interactions which require the existence of additional gauge bosons [**?**], Goldstone bosons (would-be GB) and Higgs fields [**?**, **?**, ?] or/and imply substructure of the W boson.

In case that all coupling constants are independent, one needs terms in the Lagrangian which contain up to twelve fields or covariant derivatives, in the following

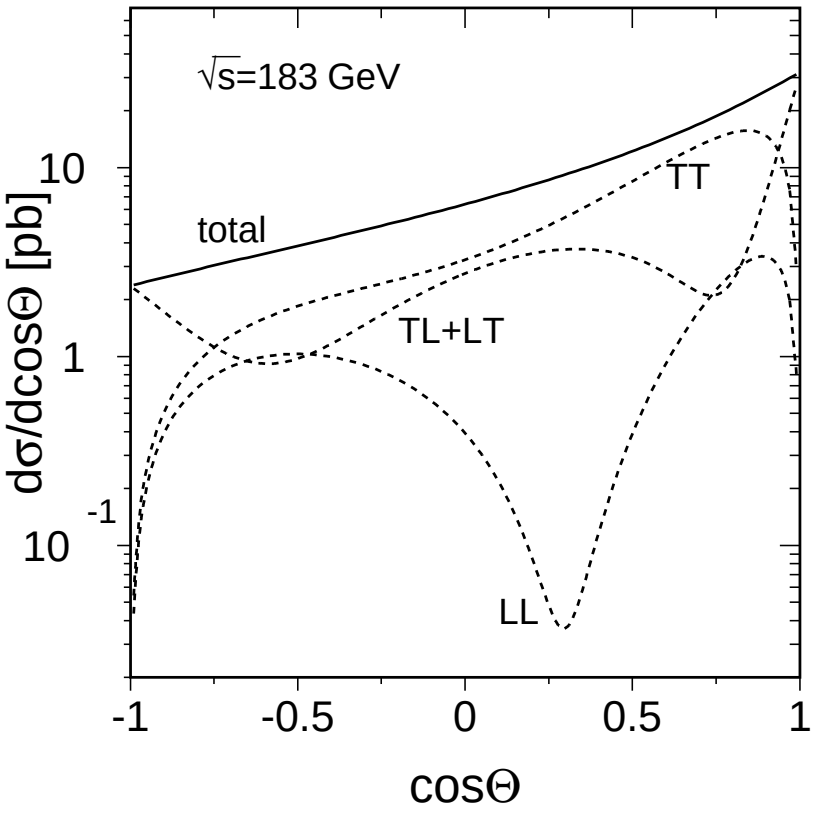

Figure 2.8: *The SM* W *pair production cross section distinguished for the polarisation combinations of* W*s :* TT*=*$(+\,-)+(-\,+)+(+\,+)+(-\,-)$*,* TL*+*LT*=*$(+\,0)+(-\,0)+(0\,+)+(0\,-)$*,* LL*=*$(0\,0)$*, where the numbers represent the polarisation (+1,0,-1) of* W^+ *and* W^- *in* W *pair production.*

called dimension-twelve-operators [?]. If it is desired to have only operators of lower dimensionality, one introduces relations among the different coupling constants.

However also models with higher dimension operators show such relations in their low energy solutions, since the higher order terms are strongly suppressed by terms $(\sqrt{s}/\Lambda_{NP})^{d-4}$ [?], where Λ_{NP} is the new physics mass scale and d is the dimension of the operator. The suppression occurs only if Λ_{NP} is large compared to the centre-of-mass energy.

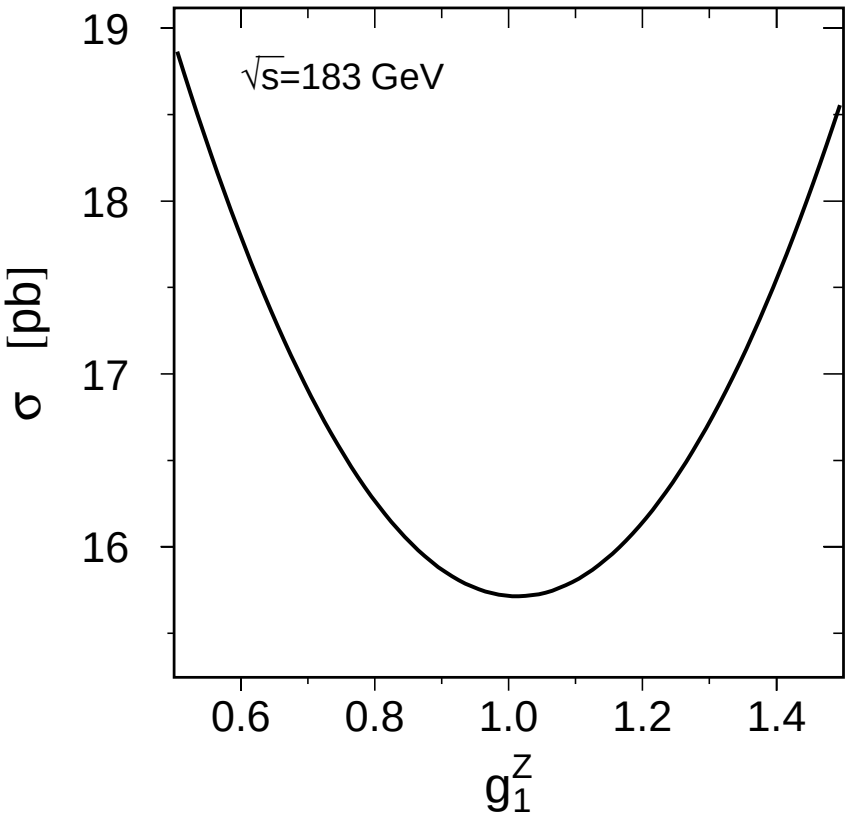

Figure 2.9: *The dependence of the total* W *pair cross section on the TGC parameter* g_1^Z *is quadratic.*

The Higgs Doublet - linear realisations In the minimal SM one has only one physical Higgs particle, which evolves from a Higgs doublet with a vacuum expectation value v. If this value is small ($v \ll \Lambda_{NP}$) compared to the new physics scale, which was discussed earlier, one can decouple the effects coming from the Higgs mechanism and the physics at the new physics scale. Thus the effect on the Lagrangian at the Higgs mass scale would be only in form of the residual effects of the new physics due to an effective low energy theory. If the new physics is restricted in such a way that it conserves the local SU(2)×U(1) symmetry and that this symmetry is exclusively spontaneously broken by the Higgs expectation value only eleven independent operators with their corresponding coupling constants (see appendix B) are found. Four of them affect the Z and W mass, two the Higgs self-

interaction, two give rise to processes like $H \to \mathrm{Z}^0\gamma\gamma$ and three to non-standard TGCs

$$\mathcal{L} = \frac{1}{\Lambda_{NP}^2}\left(f_{B\Phi}\mathcal{O}_{B\Phi} + f_{\mathrm{W}\Phi}\mathcal{O}_{\mathrm{W}\Phi} + f_{\mathrm{W}}\mathcal{O}_{\mathrm{W}}\right), \tag{2.53}$$

where f_i is the form factor for the operator effect of the operator $\mathcal{O}_i$. This equation is usually rewritten in the form where the Λ_{NP} is absorbed in coupling constants. One finds

$$\Delta g_1^Z = \frac{m_{\mathrm{Z}^0}^2}{2\Lambda_{NP}^2} f_{\mathrm{W}\Phi} \tag{2.54}$$

$$\Delta\kappa_Z = \left(f_{\mathrm{W}\Phi} - \sin^2\theta_w(f_{B\Phi} + f_{\mathrm{W}\Phi})\right)\frac{m_{\mathrm{Z}^0}^2}{2\Lambda_{NP}^2} \tag{2.55}$$

$$\Delta\kappa_\gamma = (f_{B\Phi} + f_{\mathrm{W}\Phi})\frac{m_{\mathrm{W}}^2}{2\Lambda_{NP}^2} \tag{2.56}$$

$$\lambda_\gamma = f_{\mathrm{W}}\frac{3m_{\mathrm{W}}^2 g^2}{2\Lambda_{NP}^2} = \lambda_Z \tag{2.57}$$

Thus the above TGC depend on the new physics scale Λ_{NP} and vanish in the limit $\Lambda_{NP} \to \infty$, which is the SM. The equations 2.54 to 2.57 do not only relate λ_Z and λ_γ but it follows also

$$\Delta\kappa_\gamma = \frac{\cos^2\theta_w}{\sin^2\theta_w}(\Delta\kappa_Z - \Delta g_1^Z). \tag{2.58}$$

Equation 2.53 can now be rewritten in a scale independent form

$$\begin{aligned}\mathcal{L} = {} & \imath g'\frac{\Delta\kappa_\gamma - \cos^2\theta_w\Delta g_1^Z}{m_{\mathrm{W}}^2}(D_\mu\Phi)^\dagger B^{\mu\nu}(D_\nu\Phi) + \imath g\frac{\cos^2\theta_w\Delta g_1^Z}{m_{\mathrm{W}}^2}(D_\mu\Phi)^\dagger\vec{\tau}\cdot\hat{\vec{W}}B^{\mu\nu}(D_\nu\Phi) \\ & + g\frac{\lambda_\gamma}{6m_{\mathrm{W}}^2}\hat{\vec{W}}B_\nu^\mu\cdot(\hat{\vec{W}}B_\rho^\nu\times\hat{\vec{W}}B_\mu^\rho)\end{aligned} \tag{2.59}$$

and can be identified with the terms of the effective Lagrangian in equation 2.42. Thus this model constraints the 14 parameters in such a way that only three independent parameters are left. All parameters other than Δg_1^Z, $\Delta\kappa_V$ and λ_V are zero.

Although the last arguments were well received by the LEP 2 community as it reduces significantly the number of free parameters, no argument can be raised why dimension-eight operators are suppressed if Λ_{NP} is only moderately high.

Additional terms like

$$\Delta\mathcal{L} = \imath\frac{f_\lambda^{(8)}}{\Lambda_{NP}^4}\epsilon^{ijk}\hat{W}_\mu^{i\nu}\hat{W}_\nu^{j\rho}\Phi^\dagger\frac{\sigma^k}{2}[D_\rho, D^\mu]\Phi + \imath\frac{f_\kappa^{(8)}}{\Lambda_{NP}^4}(D_\mu\Phi)^\dagger(D_\nu\Phi)\Phi^\dagger[D^\mu, D^\nu]\Phi \quad (2.60)$$

lift the relations between λ_γ and λ_Z (left term) and also relation 2.58 [**?**, ?]. The additional contributions come with a suppression factor of $\frac{v^2}{\Lambda_{NP}^2}$. Also this approach extends the Lagrangian in a linear form.
As mentioned earlier the introduction of higher dimension operators introduces also couplings between the Higgs boson and the photon, namely one can construct terms of the structure [**?**]

$$\Delta\mathcal{L} = g_{H\gamma\gamma}H\,A_{\mu\nu}A^{\mu\nu} + g^{(1)}_{H\mathrm{Z}^0\gamma}A_{\mu\nu}Z^\mu\partial^\nu H + g^{(2)}_{H\mathrm{Z}^0\gamma}H\,A_{\mu\nu}Z^{\mu\nu}. \quad (2.61)$$

With the operators shown in appendix B one finds the connection of the form factors with the Higgs-γ coupling constants to be

$$g_{H\gamma\gamma} = -\frac{g_2\ m_\mathrm{W}\ \sin^2\theta_w}{2\ \Lambda_{NP}^2}(f_{WW} + f_{BB}) \quad (2.62)$$

$$g^{(1)}_{H\mathrm{Z}^0\gamma} = -\frac{g_2\ m_\mathrm{W}\ \sin^2\theta_w}{2\ \cos\theta_w\ \Lambda_{NP}^2}(f_W + f_B) \quad (2.63)$$

$$g^{(2)}_{H\mathrm{Z}^0\gamma} = -\frac{g_2\ m_\mathrm{W}\ \sin^2\theta_w}{\cos\theta_w\ \Lambda_{NP}^2}(\sin^2\theta_w\ f_{BB} - \cos^2\theta_w\ f_{WW}). \quad (2.64)$$

Therefore this model connects the Higgs-γ coupling $g^{(1)}_{H\mathrm{Z}^0\gamma}$ to the TGCs, as can be seen by comparing equation 2.63 with equations 2.54-2.57, leading to

$$g^{(1)}_{H\mathrm{Z}^0\gamma} = \left(2\,\frac{\Delta g_1^Z}{m^2_{\mathrm{Z}^0}} - \frac{\Delta\kappa_\gamma}{m^2_\mathrm{W}}\right)\frac{g_2\ m_\mathrm{W}\ \sin\theta_w}{2\ \cos\theta_w}. \quad (2.65)$$

The no-Higgs model and non-linear realisations The mass of the electroweak bosons in the SM was introduced by a Higgs doublet field causing the spontaneous symmetry breaking of the electroweak SU(2)×U(1). However symmetry breaking can be accommodated differently (Technicolour [**?**], no-Higgs models [**?**, **?**, **?**]). Another problem which was solved due to the introduction of the Higgs field was the violation of unitary *e.g.* in the channel $\mathrm{W}^+\mathrm{W}^-\to\mathrm{W}^+\mathrm{W}^-$ at roughly $\sqrt{s} = 4\,\pi\,v \approx 3$ TeV [?]. This requires either the Higgs or some other new physics to be present at lower energies. Thus if the Higgs is heavier than 3 TeV or does not exist at all, one has to introduce another source for new physics such

that the new physics scale Λ_{NP} is smaller than av. The new physics field Ξ can be expressed by

$$\Xi = e^{i\vec{\omega}\cdot\vec{\tau}/v}, \tag{2.66}$$

where ω_i are the Goldstone bosons of the new physics [**?**] . Ξ is introduced in equation 2.59 instead of the Higgs field, taking also the appropriate SU(2)×U(1) covariant derivative into account. The introduction of this Ξ-field leads to the existence of operators of dimension-six and dimension-eight, thus the extension is non-linear. The coupling constants Δg_1^V and $\Delta\kappa_V$ evolve with $\frac{1}{\Lambda_{NP}^2}$ as it is also the case for the light Higgs model [**?**, ?, ?], in contrary λ_V evolves like $\frac{1}{\Lambda_{NP}^4}$. Thus the λ_V are expected to be much smaller than Δg_1^V or $\Delta\kappa_V$ if Λ_{NP} is sufficiently high [?].

2.7 Selected models beyond the SM

After these general remarks about the extension of the SM, special models are discussed with respect to their influence on TGCs. Technically, the terms of the Lagrangian of these models are compared to those in equation 2.42. Two classes of TGC changes are discussed; the change due to radiative corrections (SUSY, Fourth generation fermions and TECHNICOLOUR) and the change due to introduction of new born level production processes (Z′ and Large extra dimensions).

SUSY The coupling argument of the last sections was dominated from Born-level discussions. In fact non-zero couplings are also present in the SM coming from loop corrections to the WWZ and WWγ vertex. However these loop corrections lead to values in the order of 10^{-3} [**?**, **?**, **?**] which is two orders of magnitude smaller than the precision which is expected from LEP 2. The number of available loop corrections gets increased if SUSY is taken into account, as one finds a larger particle spectrum. However computations in the framework of the Minimal Supersymmetric Standard Model (MSSM) [**?**, **?**, **?**] show only small enhancements of the coupling expectations. In supergravity models where SUSY breaking occurs in a "hidden sector", which is decoupled from the ordinary world, and is mediated to it via gravitational interaction the SUSY breaking scale is the grand

unification scale (SUGRA-GUT) and $|\Delta\kappa_\gamma|$ ($|\Delta\kappa_Z|$) is predicted to be less than 4.4×10^{-3} (7.2×10^{-3}) [?, ?]. In a more general calculation with the goal to maximise the effects on the TGCs, the TGC expectation is $\Delta\kappa_\gamma = 17.5 \times 10^{-3}$ and $\Delta\kappa_Z = 8.4 \times 10^{-3}$ [?].

Z' The particle spectrum can also be extended by the existence of an additional light and weakly coupled boson Z′. The group representation of this model is $SU(3)_C \times SU(2)_L \times U(1)_Y \times U'(1)$. In contrary to the small effects of the MSSM sector one expects significant deviations due to the inclusion of Z^0-Z′ mixing [?, ?, ?, ?]. Limits on Z′ masses and couplings to fermions were already set at LEP 1 [?, ?, ?] and at the TEVATRON [?, ?]. These limits were improved at LEP 2 from measurements of the cross sections in the fermion-pair production [?]. Actually the Z′ does not couple to the W pair because of $SU(2)_L$ gauge symmetry, but the influence comes through the Z^0-Z′ mixing. Thus the Z^0 contribution in the s-channel matrix element shown in equation 2.35 must be replaced by the sum of the contributions from the mass eigenstates Z_1 and Z_2, which are the elements of the diagonalised mass matrix (the Z^0-Z′ mass matrix is not necessarily diagonal). The eigenvalues Z_1 and Z_2 have the coupling constants g_{WWZ_1} and g_{WWZ_2} to the W pair, which can be formulated as

$$g_{\mathrm{WWZ_1}} = e \cot\theta_w \cos\theta_M, \qquad g_{\mathrm{WWZ_2}} = e \cot\theta_w \sin\theta_M, \tag{2.67}$$

where θ_M is the Z_1-Z_2 mixing angle. The usual form of the matrix element can be restored if the additional terms are absorbed into the g_1^γ and g_1^Z coupling constants. Thus non-SM coupling values are expected. This absorption procedure leads to [?]

$$\begin{aligned}
\Delta g_1^\gamma &= \cot\theta_w \, v_\mathrm{e} \, \sin\theta_M \, \cos\theta_M \, g_{\mathrm{Z_1}} \left(\frac{g'^A_\mathrm{e}}{g^A_\mathrm{e}} - \frac{g'^V_\mathrm{e}}{g^V_\mathrm{e}} \right) \left(1 + \frac{s - m^2_{\mathrm{Z^0}}}{s - m^2_{\mathrm{Z'}}} \right) \\
\Delta g_1^Z &= \sin\theta_M \left[\cos\theta_M \, \frac{g_{\mathrm{Z_2}}}{g_{\mathrm{Z_1}}} \, \frac{g'^A_\mathrm{e}}{g^A_\mathrm{e}} \left(1 + \frac{s - m^2_{\mathrm{Z^0}}}{s - m^2_{\mathrm{Z'}}} \right) + \sin\theta_M \, \frac{(m_{\mathrm{Z'}} - m^2_{\mathrm{Z^0}})s}{(s - m^2_{\mathrm{Z'}})(s - m^2_{\mathrm{Z^0}})} \right]
\end{aligned} \tag{2.68}$$

Thus the existence of a Z′ would lead to non-SM values for the TGCs. Equation 2.68 shows that the extend to which non-SM values for the TGCs are expected depends on the mixing angle θ_M, on the Z′-mass $m_{\mathrm{Z'}}$, on the axial vector (g'^A_e) and vector coupling (g'^V_e) of the electron to the Z′ and on the coupling strength of the

Z_1 and Z_2, which is represented by g_{Z_1} and g_{Z_2} respectively. In the sequential SM, in which the Z′ is understood as only different to the Z^0 due to its mass, it has the same couplings to the fermions, *i.e.* $g_1 = g_2$, $g'^V_e = g^V_e$ and $g'^A_e = g^A_e$. Thus its introductions leads to non-SM values of Δg^Z_1, but not of Δg^γ_1.

Fourth generation fermions The particle spectrum of the SM is described in terms of three generations. However the reason for having this number of generations is yet unclear, such that a possible fourth generation may exist. This fourth generation must have a heavy neutrino ($m_\nu > 45$ GeV), which can be concluded from the invisible Z^0 width measured at LEP 1 [**?**]. Loops with these fermions introduce non-SM values for the TGCs [**?**]. In the limit where the up-type quarks are much heavier than the down type ones (which is true for the second and third generation), that the neutrino mass is much larger than the lepton mass (which is not true for all other generations) one can find changes in the TGC of the order of 10^{-3} [?]. Other assumptions about the mass relations lead to TGCs of the same magnitude.

Technihadrons In technicolour models [**?**,**?**,**?**] the particle spectrum is extended with technihadrons. If one assumes that the masses of the technifermions (quarks (U,D) and leptons (L,N)) are degenerate ($m_{T_U} = m_{T_D}$, $m_{T_N} = m_{T_L}$) and in the order of the technicolour scale Λ_{TC}, $\Lambda_{TC} \gg m_W$ one finds TGCs in the order of $10^{-3} \times N_{TC}$, where N_{TC} is the number of technicolours [?].

Large extra dimensions This extension of the SM proposes that the scale M_S at which the strength of gravitational interaction is comparable to the strength of other gauge interactions is close to the weak scale [**?**]. In the SM two extremely different scales have to be incorporated; the weak scale of $M_{weak} = 100$ GeV and the gravitational scale of $M_{Planck} \approx 10^{19}$ GeV. The scale difference requires that *e.g.* radiative corrections are stable by running them over 10^{17} orders of magnitude. It turns out that the radiative corrections to the Higgs mass diverge either quadratically or have to be fine-tuned with the bare Higgs mass. This hierarchy problem [**?**] is solved by the ansatz of this extension, since one is left with only one fundamental scale, which is the weak scale. However to stay consistent with Newtons law and the Planck mass of 10^{19} GeV, it is proposed to introduce $n \geq 2$ extra dimensions of size $R = (M_{Planck}/M_S)^{2/n}/M_S$. If M_S is chosen to be in the

order of 1 TeV and two extra dimensions are assumed the size of the dimensions is in the order of 1 mm, thus large compared to the interaction length of the weak interaction. While the SM particles propagate only in the four-dimensional space-time, the gravitons propagate through all 4+n dimensions. This concept allows to modify the gravitational potential at $r \ll R$, where it is not anymore proportional to $1/r^2$, while it is unchanged at larger distance scales. Since gravitons couple to all SM particles the s- and t-channel exchange of gravitons modifies the W pair production. Modifications of the SM amplitudes by a factor of

$$1+ \frac{4\ s\ t}{\mathrm{M}_S^4}\ \frac{2\sin^2\theta_w}{e^2}\ \frac{1}{\delta_{\sigma,-1}} \tag{2.69}$$

for the t-channel exchange and by a factor of

$$1+ \frac{4s^2}{\mathrm{M}_S^4}\ (1-\beta\cos\theta)\ \frac{1}{2e^2}\ \frac{1}{1-(1-\delta_{\sigma,-1}\frac{1}{2\sin^2\theta_w})\frac{s}{s-m^2_{\mathrm{Z}^0}}} \tag{2.70}$$

for the γ and Z^0 s-channel exchange can be derived [?, ?]. While the second factor can also be interpreted in terms of TGCs, the t-channel modification prohibits the easy mapping from M_S to TGC values. It is interesting to note that finally these factors do not depend on the number of extra dimensions n, but only on M_S, which results from the summation over all graviton states in the computation of the virtual graviton exchange in the s- and t-channel.

2.8 Four-fermion final states

The measurement of the W pair production requires the selection of four-fermion final states, as each of two Ws decays into two fermions. A W can decay into nine final states, namely eν_e, $\mu\nu_\mu$, $\tau\nu_\tau$, ud, cs, us ,cd, cb and ub. The contributions of the last four configurations is very small, since the quark mass eigenstates and their weak eigenstates are almost identical, making their mixing matrix, referred to as Cabibbo-Kobayashi-Maskawa (CKM) mixing matrix [?], almost diagonal. The mixing matrix of the leptonic sector is diagonal and in the following also the CKM-matrix is assumed to be diagonal. Not only the CC03 process can lead to a particular final state configuration but one finds non-separable background contributions and interferences of W pairs and non-resonant contributions. As an example, figure 2.10 shows the graphs which can lead to the qqeν_e final state.

As 20 graphs graphs are contributing and the final state fermion configuration is compatible with coming from W decays, this process is called CC20-process. Table 2.3 summarises the number of graphs for the final states, which may result from decayed W pairs. Some of these final states could also result from neutral current (NC) processes, thus may either be called *e.g.* CC56 or NC56. The notation is such that particle configuration of type $U_i\bar{D}_i\bar{U}_jD_j$ are CC processes and of type $U_i\bar{U}_iD_j\bar{D}_j$ are NC processes, where U and D denote up- and down-type fermions. The fermion family is given by i and j. The "mixed" processes have accordingly the configuration $U_i\bar{U}_iD_i\bar{D}_i$, such as $\mu^-\bar{\nu}_\mu\mu^+\nu_\mu = \mu^-\mu^+\nu_\mu\bar{\nu}_\mu$.

fermions	eν_e	$\mu\nu_\mu$	$\tau\nu_\tau$	ud	cs
eν_e	CC56/NC56	CC18	CC18	CC20	CC20
$\mu\nu_\mu$	CC18	CC19/NC19	CC09	CC10	CC10
$\tau\nu_\tau$	CC18	CC09	CC19	CC10	CC10
ud	CC20	CC10	CC10	CC43/NC43	CC11
cs	CC20	CC10	CC10	CC11	CC43/NC43

Table 2.3: *Four fermion final states are not only produced via double resonant diagrams but have also a contribution from non-resonant diagrams. Diagrams which contain* W *bosons in the intermediate state are from the charge current (CC) class while diagrams with only photons and Zs are neutral current (NC) graphs. The number of diagrams for a particular final state can be read from this table.*

In figure 2.10 on can also find the graphs of the CC03 process already displayed in figure 2.4, of which two (the last two diagrams) contain a TGV. On the other hand two other graphs (the first two diagrams) contain such a vertex too. They are called single-resonant W production.

2.8.1 The single-resonant W production

Until now the TGC measurement was discussed only for the case of W pair production, but also the single-resonant W production [?,?,?,?,?] is sensitive to the TGC as defined in the Lagrangian in equation 2.42. The Feynman diagrams of single W production, where the W is decaying into quarks are the first two processes in figure 2.10. As the W is generated due to a t-channel fusion process the WZ fusion

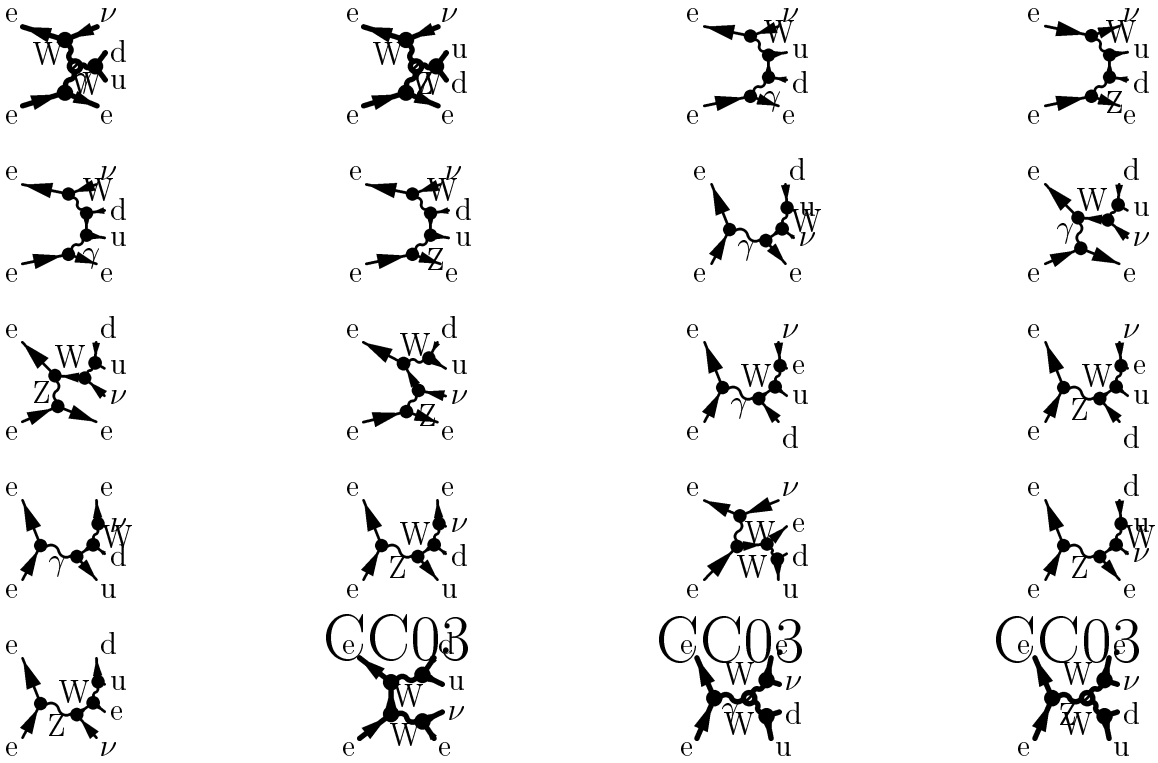

Figure 2.10: *The four-fermion final state* $qqe\nu_e$ *can be produced via 20 charged current processes and is therefore called CC20 process. The first two processes correspond to single* W *production and the last three, marked CC03, to* W *pair production.*

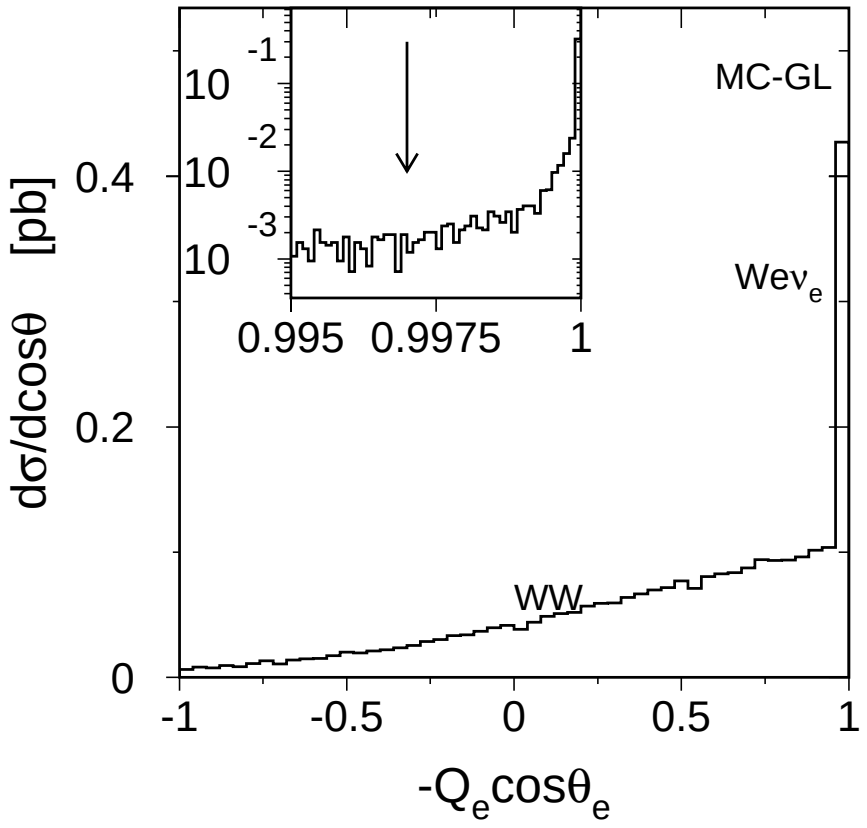

Figure 2.11: *The electron polar angle distribution of* $\mathrm{qqe}\nu_e$ *is used to distinguish the s-channel production of* W *pairs (last two processes in figure 2.10 and the single* W *production in the t-channel fusion of* $\mathrm{W}\gamma$ *(first process in figure 2.10). A value of* $\cos\theta_\mathrm{e} = 0.997$*, indicated by the arrow, is chosen to separate these processes for the single* W *signal definition. The cut is applied to signal events on Monte-Carlo generator level (MC-GL).*

is much suppressed compared to the $\mathrm{W}\gamma$ fusion. This allows to measure only the $\mathrm{WW}\gamma$ couplings without assumptions on the WWZ-vertex. Thus the couplings in the case of single W production are not constraint by the LEP I data, which mainly test the ZWW vertex.

The separation of the four-fermion final state from the non-separable background, thus the enhancement of the single-resonant graph in the CC20 Matrix element can be done by cutting on the electron angle as can be seen in figure 2.11. Single W events, as t-channel production, tend to be forward peaked. This is a delicate

region of the phase space with respect to theoretical calculations, as it includes the region of zero-scattering angle. Theoretical approaches, where the final fermion masses are set to zero (as in most available MC generators) in order to simplify the cross section computation are not suitable in this phase space regime [?] as in this case collinear singularities occur.

2.9 TGCs from $e^+e^- \to \nu\bar{\nu}\gamma(\gamma)$

The process $e^+e^- \to \nu\bar{\nu}\gamma(\gamma)$ is the third process allowing the measurement of TGCs [?, ?, ?, ?, ?]. The process $e^+e^- \to \nu\bar{\nu}Z^0$ is suppressed by the large mass m_{Z^0} . Figure 2.12 shows that the production processes which involves a TGV is accompanied by four background diagrams of the same final state. With respect to the neutrino flavour $\nu\bar{\nu}\gamma(\gamma)$ refers always to the sum of all flavours, ν_e , ν_μ and ν_τ. While $\nu_e\bar{\nu}_e\gamma$ is produced due to all diagrams of figure 2.12, $\nu_\mu\bar{\nu}_\mu\gamma$ and $\nu_\tau\bar{\nu}_\tau\gamma$ are only produced due to the s-channel processes, displayed as the lower two diagrams in figure 2.12.

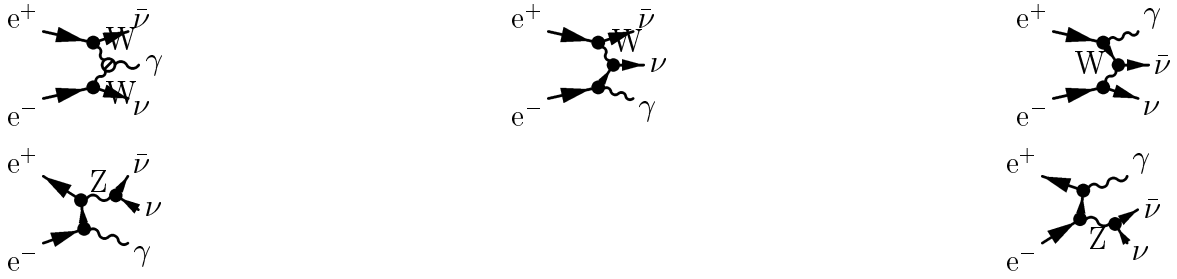

Figure 2.12: *The $\nu\nu\gamma$ final state can be produced via these five processes. The first process is sensitive to TGC.*

The t-channel process with initial state radiation of a photon (ISR) dominates at energies far away from the Z^0 resonance, but still there are significant contributions from the radiative return to the Z. No exact computation of the cross section has yet been published, as processes where the "high" energetic photon is accompanied by two, three or more soft photons have to be taken into account. Therefore two approximate schemes are in today's use. In the first method the Born level matrix elements of the process $\nu\nu n\gamma$ with n=1,2,3 are computed. However, QED-radiative corrections of the same order are neglected in the computation, but are introduced by a correction using a structure function approach [?]. The second

method uses only the differential cross section of invisible neutrino pair production, $e^+e^- \to \nu\bar{\nu}$ and convolutes it with a radiator function to attach photons to it. Several choices of the radiator function have been proposed; an angular dependent radiator function [?, ?], a parton shower algorithm [?] and the Yennie-Frautschi-Suura method [?, ?]. The cross section results of both schemes agree on the O(1%) level [?] for the total $\nu\bar{\nu}\gamma(\gamma)$ cross section. The TGV graph is often omitted in cross section computations, since in the SM its effect to the total cross section is small. The relative contribution of the TGV graph with respect to the total $\nu\bar{\nu}\gamma(\gamma)$ cross section is shown in figure 2.13-a. Although the contribution to the total cross

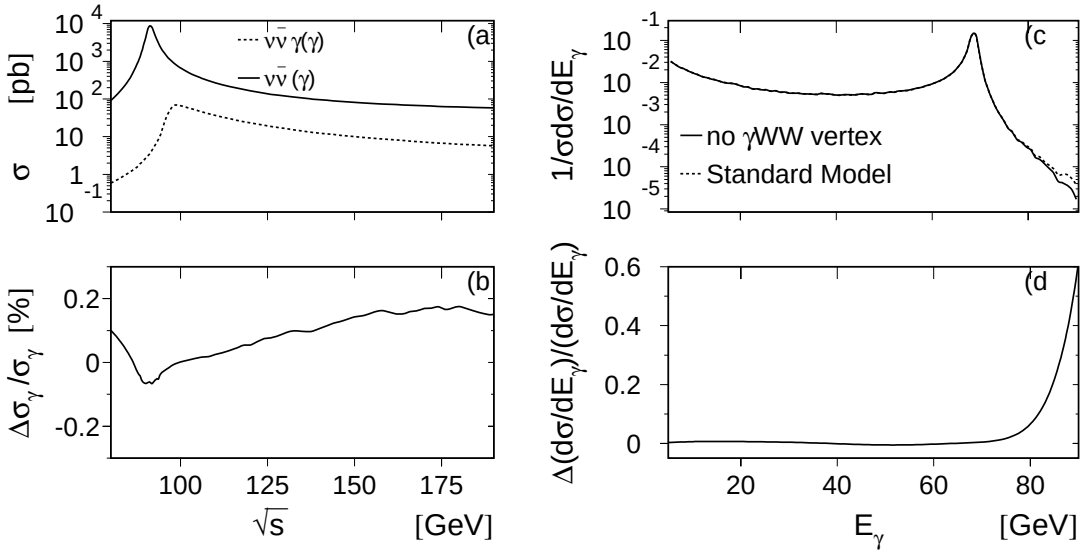

Figure 2.13: *The total neutrino pair production cross section , $e^+e^- \to \nu\nu(\gamma)$, and the cross section where $E_\gamma > 5$ GeV and $|\cos\theta_\gamma| < \cos 10^\circ$, $e^+e^- \to \nu\bar{\nu}\gamma(\gamma)$, (a) and the relative contribution of photon emission by the* W *in the t-channel to the total $\nu\bar{\nu}\gamma(\gamma)$ cross section (b) as function of the centre-of-mass energy. The photon energy distribution for the hypothesis of nonexistence of the γ*WW *vertex and the SM distribution (c) and the relative difference of these two models (d). The theory prediction is computed with KORALZ [?].*

section is small, its effect on differential cross sections, mainly its effect on the photon energy distribution is sizeable. This comes from the fact, that ISR-photons tend to have either low energies or energies, such that the invariant mass of the

neutrino pair corresponds to m_{Z^0} , called the radiative return peak. In contrary to this have photons from the W fusion process a large energy which is not correlated to the Z^0 mass. The energy spectrum of $\nu\bar{\nu}\gamma(\gamma)$ production decomposed into the differential cross section coming from the TGV graph and its interferences with the others and into the one from the other four graphs is shown in figure 2.13-b. Non-SM TGC values are introduced following equation 2.42. By definition the cross section depends also here quadratically on the couplings. The effect of non-SM couplings to cross section and photon energy distribution was already visible in figure 2.13, as the neglect of the process is identical to the case of $\Delta g_1^\gamma = -1$ and $\Delta\kappa_\gamma = -1$.

2.10 Bremsstrahlung process $e^+e^- \rightarrow W^+W^-\gamma$

The last possible configuration is the bremsstrahlung process. Here the W emits a photon or Z^0 but will still be visible in the detector. Z^0 bremsstrahlung is suppressed by the large Z mass. Since this process can be decomposed into W pair production and final state radiation of a photon it is natural to assume that the process is suppress by the coupling constant of the electromagnetic interaction, thus approximately by two order of magnitudes. The final state configuration $U_i\bar{D}_i\bar{U}_jD_j\gamma$ can however also be produced by ISR and final state radiation (FSR) of fermions. So a complete computation of the first order QED radiative correction has do be undertaken (which to my knowledge is not yet available), to describe properly the differential cross section. Methods for approximate solution were already discussed in the section about single γ production. However, this final state has got significant attention due to its capability to study quartic gauge boson couplings [**?**]. Two final states that allow an insight into such quartic couplings (QGC) are displayed in figure 2.14. Since restrictions to the QGC will be weak in the framework of LEP 2 [**?**, ?], they are not considered any longer.

Figure 2.14: *Quartic couplings can be studied in* e^+e^- *collisions. However, the restrictions to the quartic coupling constants are weak [?, ?].*

2.11 Is an e^+e^- collider the best place to study TGCs ?

In the last sections channels were identified which can give a handle on all possible configurations of the VWW vertex, as displayed in figure 2.3, these were W pair, single W, single photon and $W^+W^-\gamma$ production at e^+e^- colliders. Although the discussion focused on processes at e^+e^- colliders, the same channels are found at $p\bar{p}$ colliders replacing the electron-positron-pair with a quark-anti-quark pair, $q\bar{q}$. In addition the bremsstrahlung process of γ or Z^0 seen in figure 2.3-d, can occur from directly produced Ws. These Ws result from annihilation of up-type quarks with down-type antiquarks or vice versa, $U_i\bar{D}_i$ or $D_i\bar{U}_i \rightarrow$ W. The favourable situation of $p\bar{p}$ colliders from the point of accessible channels and from the point of the interaction cross section, *e.g.* $\sigma_{p\bar{p}\rightarrow W}(\sqrt{s} = 1.8 \text{ TeV}) = 7.4$ nb, is spoiled by the fact, that the experimental conditions in terms of event reconstruction and selection are very complicated. The SM cross section of processes which are studied at LEP and at TEVATRON are displayed in table 2.4.

Figure 2.3	$p\bar{p}$ *e.g.* TEVATRON			e^+e^- *e.g.* LEP		
	L	$\approx$	$2 \times 100\text{pb}^{-1}$	L	$=$	$4 \times 500\text{pb}^{-1}$
a)	$\sigma_{p\bar{p}\rightarrow \text{W}^+\text{W}^-}$	$=$	9.5 pb	$\sigma_{\text{e}^+\text{e}^-\rightarrow \text{W}^+\text{W}^-}$	$=$	15.7 pb
b)				$\sigma_{\text{e}^+\text{e}^-\rightarrow \text{We}\nu_e}$	$=$	0.5 pb
c)				$\sigma_{\text{e}^+\text{e}^-\rightarrow \nu\bar{\nu}\gamma(\gamma)}$	$=$	5.5 pb
d)	$\sigma_{p\bar{p}\rightarrow W\gamma}$	$=$	38.5 pb	$\sigma_{\text{e}^+\text{e}^-\rightarrow \text{W}^+\text{W}^-\gamma}$	$\approx$	0.5 pb

Table 2.4: *Comparison of* $p\bar{p}$ *and* e^+e^- *colliders in terms of cross section of the relevant processes with TGC sensitivity [?, ?, ?, ?]. The cross section numbers correspond to* $\sqrt{s} = 1.8$ *TeV for* $p\bar{p}$ *and* $\sqrt{s} = 183$ GeV *for* e^+e^-.

Thus it can be concluded that although a large number of Ws are actually produced at $p\bar{p}$ colliders the cross section of the coupling sensitive channels are compatible to the ones at e^+e^-. From the point of view of reconstruction of the phase space information and the background situation an e^+e^- machine must be preferred.
To study all the processes the centre-of-mass energy has to be chosen such, that one exceeds their kinematic limits. Thus the energy should exceed twice the W mass, $\sqrt{s} > 161$ GeV for the study of the W pair production. The single W and single γ production have lower kinematic limits. The bremsstrahlung process of a photon sets also in at $\sqrt{s} > 2m_{\mathrm{W}}$, while the Z^0 bremsstrahlung starts only at 250 GeV. The existing LEP 1 collider, which was running at $\sqrt{s} \approx 91$ GeV, was thus upgraded to reach and cross the kinematic limit for W pair production. Starting from 1996 the energy was increased from 161 GeV to 200 GeV in 1999. However, the kinematic limit for Z^0 bremsstrahlung will not be crossed, before LEP 2 shuts down in 2000.
The discussion of the this chapter focused on TGC studies from Born-level processes. It was noted that for such a study the energy must be large, but at least larger than 161 GeV. But TGCs have influence on physics already at lower energies, such that in the next chapter constraints to TGCs coming from measurements at LEP 1 and SLAC are discussed, before coming to the experimental apparatus that is used to detect the LEP 2 processes in chapter IV.

This is known as Cardan's Solution, though it was originally given by Tartaglia. He unwisely told Cardan, who promptly published it as his own.
The Math Forum Project

III

From past to presence

Couplings among the four electroweak bosons not only play a role at LEP 2. Already at the Z resonance TGCs have to be taken into account. Here they enter through radiative correction to the $Z^0 f\bar{f}$ vertex, to which LEP 1 was sensitive to. Although, the high precision electroweak data [**?**] where a major footing of arguments in the discussion whether LEP 2 might add valuable information in the TGC sector [?, ?, **?**] or not, they are until now only partly analysed with respect to TGCs [**?**, **?**]. An analysis using all available electroweak precision data is discussed in the first section [**?**]. Apart from this indirect method, also direct TGC information is available at LEP 1. It comes from W pair production, where one W is extremely off-shell. In the second section the treatment of the hadronic Z^0 pole cross section with respect to TGCs is discussed in detail. A comparison of these indirect and direct measurements and conclusions with respect to LEP 2 are given in the last section.

3.1 Indirect bounds from Z^0 pole data

Indirect bounds to TGCs can be obtained from electroweak precision data, since they modify the $Z^0 f\bar{f}$ vertex and the Z^0/γ propagator through radiative correc-

tions. The most prominent example is the computation of R_b, the fraction of pair produced b-quarks, $Z^0 \rightarrow b\bar{b}$, and all hadronic events, $Z^0 \rightarrow$ hadrons [?, ?]. For the computation, corrections to the vertex as illustrated in figure 3.1 have to be taken into account, allowing that the masses of top-quark and Higgs can be determined from those radiative corrections.

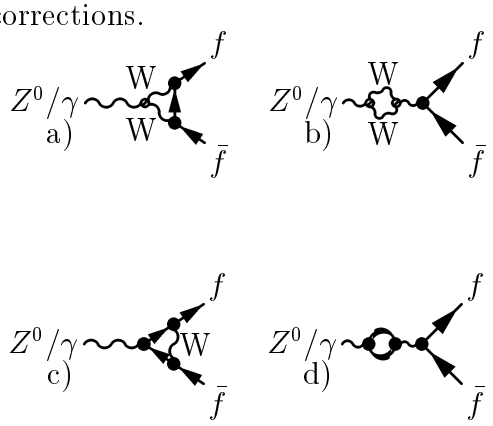

Figure 3.1: *Radiative correction to the decay width of the Z into fermions, $Z \rightarrow f\bar{f}$. This process was used at LEP 1 to determine limits on Higgs and top-quark masses. a) and b) do depend on the* WWV *coupling constants, c) and d) depend only on fermion to boson couplings.*

Looking at figure 3.1-(a) and (b) one realises that graphs involving TGCs are involved. The couplings in these graphs were set to their SM expectation value in the computation of the Higgs and top-quark mass from radiative corrections. But these TGC dependent graphs do not only occur in the case of b-quark production but also for any other fermion-anti-fermion production. This means, that the high precision data available from LEP 1 constrain the three-linear couplings. Following the computation in [?] non-SM values of TGCs lead to non-SM values of the parameters $\epsilon_{1,2,3}$ [?]. The ϵ-parameters are most suitable to see these deviations, as they are designed such, that the leading radiative correction, namely the one by the t-quark is only present in two of these parameters and therefore the others are sensitive to Higgs and new physics effects only. The ϵ-parameters are defined

in [?] as

$$\epsilon_1 = \Delta\rho \tag{3.1}$$

$$\epsilon_2 = \cos^2\theta_w^0\Delta\rho + \frac{\sin^2\theta_w^0\Delta r_W}{\cos^2\theta_w^0 - \sin^2\theta_w^0} - 2\sin^2\theta_w^0\Delta k' \tag{3.2}$$

$$\epsilon_3 = \cos^2\theta_w^0\Delta\rho + (\cos^2\theta_w^0 - \sin^2\theta_w^0)\Delta k' \tag{3.3}$$

$$\epsilon_b = -\frac{g_A^b}{g_A^l} - 1 \tag{3.4}$$

where θ_w^0 denotes θ_w before non-pure QED corrections, given by

$$\sin^2\theta_w^0\cos^2\theta_w^0 = \frac{\pi\alpha(m_{Z^0})}{\sqrt{2}G_F m_{Z^0}^2}. \tag{3.5}$$

The parameters $\Delta\rho$ and $\Delta k'$ parameterise the radiative corrections to the axial and vector current couplings of the charged leptons according to

$$g_A = -\frac{1}{2}\left(1 + \frac{\Delta\rho}{2}\right) \tag{3.6}$$

$$\frac{g_V}{g_A} = 1 - 4\,(1 + \Delta k')\sin^2\theta_w^0 \equiv 1 - 4\sin^2\theta_w^{\text{eff}} \tag{3.7}$$

The parameter Δr_W is understood as weak correction part to the boson masses according to

$$\left(1 - \frac{m_W^2}{m_{Z^0}^2}\right)\frac{m_W^2}{m_{Z^0}^2} = \frac{\pi\alpha(m_{Z^0})}{\sqrt{2}G_F m_{Z^0}^2}\,\frac{1}{1-\Delta r_W}. \tag{3.8}$$

As the fermion coupling constants depend on the ϵ-parameters one can extract these from the Z^0 pole measurements (except the top-quark mass) as reported in table 3.1, which all depend on g_V, g_A and $\sin^2\theta_w^{\text{eff}}$; see [?, ?], for example. The numbers displayed in table 3.1 base on measurements of all four LEP experiments as well as of measurements from SLD [?], the TEVATRON experiments CDF [?] and DØ [?] and low energy measurements [?, ?, ?]. A simultaneous fit to all four parameters and in addition to the electromagnetic coupling constant $\alpha_{em}(m_Z)$, the strong coupling constant $\alpha_s(m_Z)$ and m_Z gives the numbers quoted in table 3.2. The computation of the SM expectations shows that these values are in good agreement with the measured ones, and they are also in good agreement with other recent computations [?, ?]. One finds strong correlations between ϵ_b and α_s as well as for ϵ_1 and ϵ_3. The latter is visible in figure 3.2, showing the two-dimensional contours of each pair of ϵ-parameters. These contour curves are compared with the change of ϵ-parameters as a function of the TGC coupling constants.

parameter	central value	errors
$1/\alpha^{(5)}(m_{\mathrm{Z}^0})$	128.878	0.090
m_{Z^0}	91.1867	0.0021
Γ_Z	2.4939	0.0024
σ_{had}	41.491	0.058
R_e	20.765	0.026
A^e_{FB}	0.01683	0.00096
$\mathcal{P}_e$	0.1479	0.0051
$\mathcal{P}_\tau$	0.1431	0.0045
$\sin^2\theta^{\mathrm{eff}}_w(Q_{\mathrm{fb}})$	0.2321	0.0010
$\sin^2\theta^{\mathrm{eff}}_w(A_{\mathrm{LR}})$	0.23109	0.00029
m_{W} (LEP2)	80.37	0.09
m_{W} ($\mathrm{p\bar{p}}$)	80.41	0.09
R_b	0.21656	0.00074
R_c	0.1735	0.0044
A^b_{FB}	0.0990	0.0021
A^c_{FB}	0.0709	0.0044
A_b	0.867	0.035
A_c	0.647	0.040
m_t	173.8	5.0

Table 3.1: *Preliminary electroweak parameters [?] resulting from averaging measurements done by the LEP experiments, SLD, the TEVATRON experiments and others. The correlations among the observables in the b and c quark sector as well as the one between m_{Z^0}, Γ_Z, σ_{had}, R_e and A^e_{FB} is properly taken into account. m_t is only used in the SM calculation of the ϵ-parameters. For parameter definitions see [?].*

fit parameter	measured	SM
$1/\alpha^{(5)}(m_{Z^0})$	128.878±0.090	-
$\alpha_s(m_{Z^0})$	0.1244±0.0045	-
m_{Z^0}	91.1866±0.0021	-
$\epsilon_1 \times 10^3$	4.2±1.2	4.6 ± 1.1
$\epsilon_2 \times 10^3$	−8.9±2.0	-7.5 ± 0.3
$\epsilon_3 \times 10^3$	4.2±1.2	5.8 ± 0.7
$\epsilon_b \times 10^3$	−4.5±1.9	-5.8 ± 0.5

fit parameter	correlation matrix						
	$\frac{1}{\alpha^{(5)}}$	α_s	m_{Z^0}	ϵ_1	ϵ_2	ϵ_3	ϵ_b
$1/\alpha^{(5)}(m_{Z^0})$	**1.00**	0.00	0.00	0.00	-0.07	0.46	0.00
$\alpha_s(m_{Z^0})$	0.00	**1.00**	0.00	-0.45	-0.22	-0.31	-0.62
m_{Z^0}	0.00	0.00	**1.00**	-0.06	-0.01	-0.02	0.00
$\epsilon_1 \times 10^3$	0.00	-0.45	-0.06	**1.00**	0.44	0.80	-0.01
$\epsilon_2 \times 10^3$	-0.07	-0.22	0.00	0.44	**1.00**	0.26	-0.01
$\epsilon_3 \times 10^3$	0.46	-0.31	-0.02	0.80	0.26	**1.00**	0.00
$\epsilon_b \times 10^3$	0.00	-0.62	0.00	-0.01	-0.01	0.00	**1.00**

Table 3.2: *The ϵ values in the SM and from a fit to the electroweak data summarised in table 3.1 ($\chi^2/Ndf = 11.6/11$, probability 39%).*

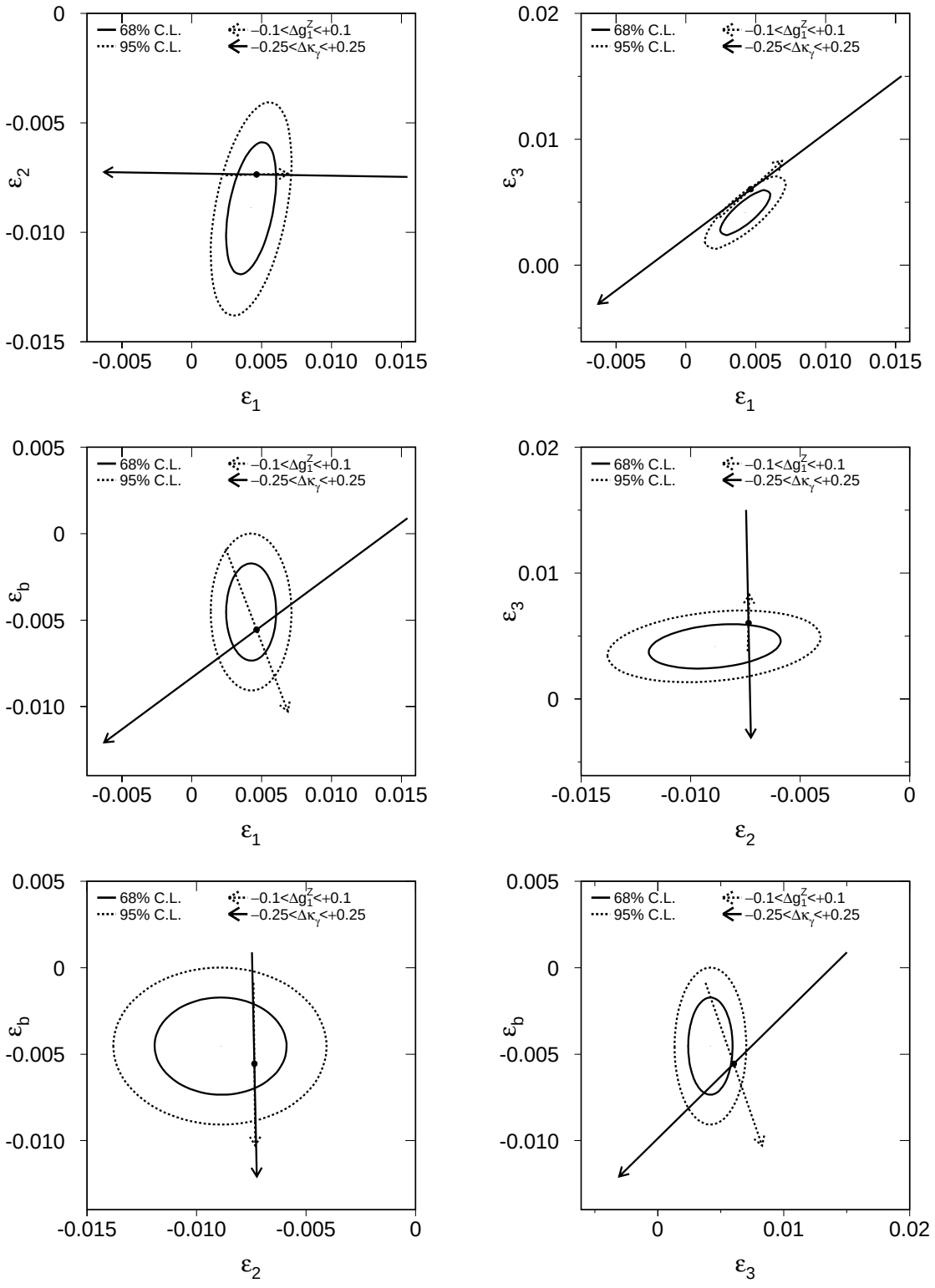

Figure 3.2: *The contours of the ϵ parameters. The arrows indicate the change of the SM prediction if the coupling parameters Δg_1^Z and $\Delta\kappa_\gamma$ are varied according to the combined direct measurements of LEP2 and TEVATRON, displayed in chapter VIII.*

In the second step the subset of table 3.2 concerning the ϵ-parameters is taken and compared to the SM expectations, also listed in this table. The changes of the ϵ-parameters for non-standard couplings in the model of the linear extension of the SM using only additional dimension-six operators are [?, ?, ?]

$$-\frac{12\pi}{\alpha}\Delta\epsilon_1 = \left\{\left[\frac{27}{2} - \tan^2\theta_W\right]\frac{m_{Z^0}^2}{m_W^2}\ln\frac{\Lambda^2}{m_W^2} + \frac{9}{2}\frac{m_{Z^0}^2 m_H^2}{m_W^4}\left[\ln\frac{\Lambda^2}{m_H^2} + \frac{1}{2}\right]\right\}\Delta\kappa_\gamma + \left\{\left[\tan^2\theta_W - \cot^2\theta_W\right] - \frac{9}{2}\frac{m_H^2}{m_W^2}\left[\ln\frac{\Lambda^2}{m_H^2} + \frac{1}{2}\right]\right\}\Delta g_1^Z \tag{3.9}$$

$$\frac{12\pi}{\alpha}\Delta\epsilon_2 = \frac{m_{Z^0}^2}{m_W^2}\sin^2\theta_W\Delta\kappa_\gamma + \cot^2\theta_W\Delta g_1^Z \tag{3.10}$$

$$\frac{12\pi\sin^2\theta_W}{\alpha}\Delta\epsilon_3 = \left\{\left[\cos^4\theta_W - 7\cos^2\theta_W - \frac{3}{4}\right]\frac{m_{Z^0}^2}{m_W^2}\ln\frac{\Lambda^2}{m_W^2} - \frac{3}{4}\frac{m_H^2}{m_W^2}\left[\ln\frac{\Lambda^2}{m_W^2} + \frac{1}{2}\right]\right\}\Delta\kappa_\gamma + \left\{10\cos^2\theta_W + \frac{3}{2}\right\}\ln\frac{\Lambda^2}{m_W^2}\Delta g_1^Z \tag{3.11}$$

$$\Delta\epsilon_b = \frac{m_{Z^0}^2 m_t^2}{64\pi^2 m_W^4}\ln\frac{\Lambda^2}{m_W^2}\Delta\kappa_\gamma - \left[\frac{\cot^2\theta_W}{64\pi^2}\frac{m_{Z^0}^2 m_t^2}{m_H^4}\ln\frac{\Lambda^2}{m_W^2} + \frac{3\cot^2\theta_W}{32\pi^2}\frac{m_t^2}{m_W^2}\ln\frac{\Lambda^2}{m_W^2}\right]\Delta g_1^Z \tag{3.12}$$

These expressions are based on the constraints between TGCs quoted earlier. The effect of deviations of Δg_1^Z and $\Delta\kappa_\gamma$ from their SM value is visualised in figure 3.2. All non-standard contributions are logarithmically divergent. The coupling parameters, that are used here, are defined in dependence on the new physics scale Λ and a form factor f coming from the new physics effect, *e.g.*

$$\Delta g_1^Z = \frac{m_Z^2}{\Lambda^2}f. \tag{3.13}$$

In the following the new physics scale Λ is conservatively set to 1 TeV; higher values of Λ imply tighter constraints on TGCs. In addition the Higgs mass is set to 300 GeV and varied between 90 GeV, the lower limit on the Higgs mass derived from the direct search [**?**], and 1000 GeV, the upper limit coming from computations of the Higgs self-energy [**?**]. Since one looks for effects beyond the SM, one cannot make use of constraints on the Higgs mass derived from a SM analysis of radiative corrections such as [**?**].

A fit using equations 3.9 to 3.12 and the difference of the measured values of the ϵ-parameters and the ones expected in the SM as shown in table 3.2 is used

to determine the TGC coupling parameters g_1^Z and κ_γ. The errors on the SM predictions of the ϵ-parameters are included. The correlation of the ϵ-parameters from the experimental measurement are included in the fit, while the correlation of the SM prediction are neglected. The χ^2 curves of a fit to each of these coupling constants, setting the other to its SM value of zero, is shown in figure 3.3. One finds the following results:

$$g_1^Z = 0.983 \pm 0.018^{+0.018}_{-0.003}(m_H) \tag{3.14}$$

or

$$\kappa_\gamma = 1.016 \pm 0.019^{+0.009}_{-0.013}(m_H). \tag{3.15}$$

If both couplings are allowed to vary in the fit, one finds the contour plot in figure 3.4. The corresponding numerical values of the TGC-parameters are

$$\begin{aligned} g_1^Z &= 0.987 \pm 0.027^{+0.023}_{-0.001}(m_H) \\ \kappa_\gamma &= 1.005 \pm 0.029^{+0.011}_{-0.001}(m_H), \end{aligned} \tag{3.16}$$

with a correlation of 75.5 percent. The SM expectation of one for both TGC parameters agrees well with this measurement. For other values of the new physics scale Λ, both fitted central values and fitted errors of the TGC parameters scale approximately as $1/\ln\Lambda^2$. Thus the significance of the compatibility of the TGC with the SM, *i.e.* value/error, is approximately independent of Λ as is displayed in figure 3.4. The systematic uncertainty arising from the Higgs mass variation is quoted as second error in equations 3.14-3.16. The error of 5 GeV on m_t, as quoted in table 3.1 has a negligible impact on the result [?].

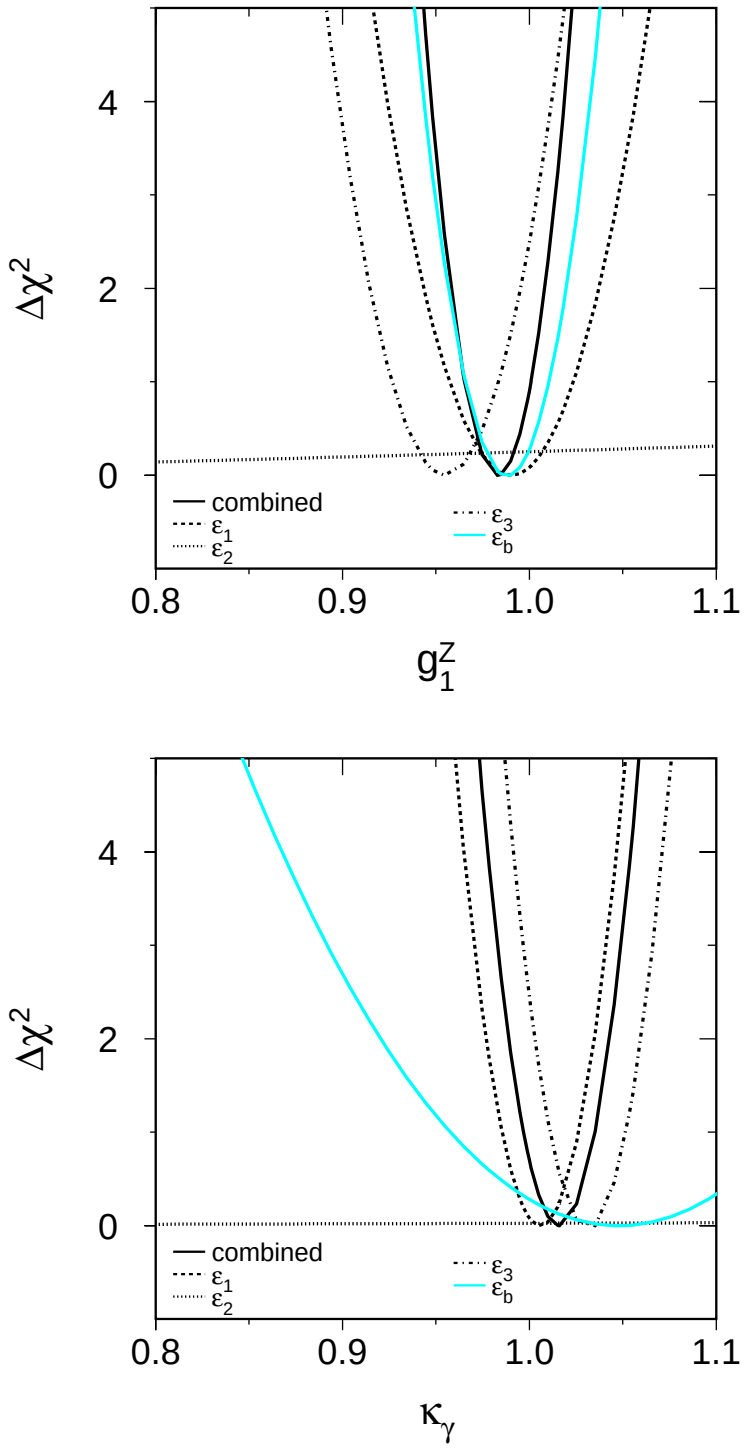

Figure 3.3: *The $\Delta\chi^2$ curves for the couplings and the contributions of the different ϵ parameters. The combined curve is the sum of the single curves taking the correlation coefficients properly into account. The parameter ϵ_2 has no sensitivity to TGCs.*

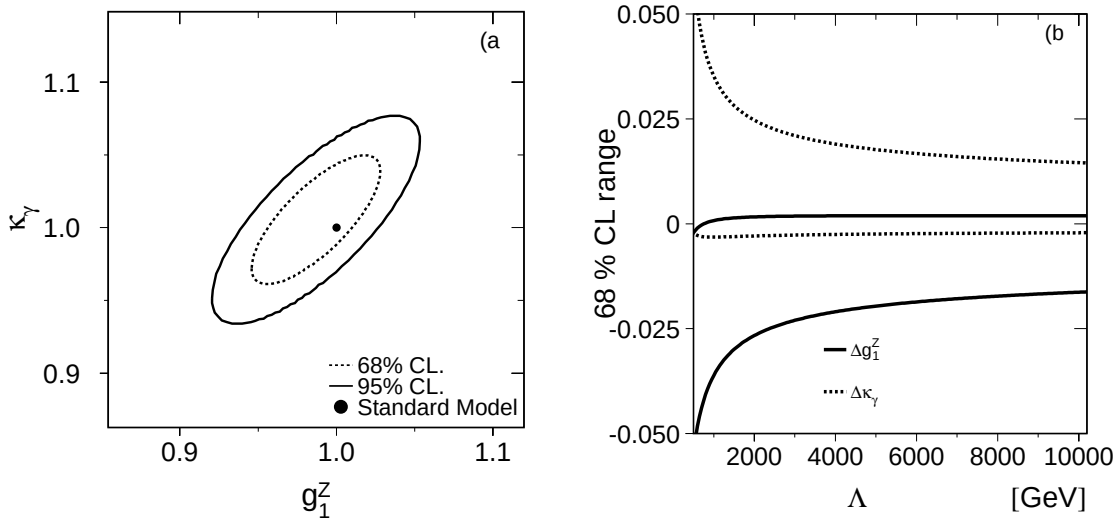

Figure 3.4: *The contour curves for the two dimensional fit, g_1^Z versus κ_γ(a). The dot shows the SM expectation. The bounds on the TGC tighten if higher new physics scales are assumed (b).*

3.2 Direct bounds from Z^0 pole data

Apart from the indirect bounds from radiative corrections one can also obtain direct bounds on the TGCs from LEP 1. W pair production can also occur much below the threshold if one of the Ws is produced off-shell. The same Feynman graphs contribute as for the W pair production above the threshold. The W pair cross section peaks as the fermion-pair production cross section close to the Z^0 mass, as the Z^0 in the s-channel creates a resonance behaviour. The W pair production can be understood as production of an on-shell W and another W which is highly off-shell. Thus if the on-shell W decays hadronically, it mimics a hadronic Z^0 decay and is selected in a hadron selection of LEP 1 data. Thus from the hadronic cross section measurement of LEP 1 one can infer a measurement of TGCs. The hadronic pole cross section was measured at LEP to be 41491 ± 58 pb, while the SM prediction without taking W pair production into account is 41473 pb [?]. The W pair cross section as a function of the couplings was computed with GENTLE [**?**].

The extend of the change of the cross section as function of the couplings is shown in figure 3.5. The likelihood curves for the estimation of the couplings Δg_1^Z and $\Delta\kappa_\gamma$ is displayed in figure 3.5. From this one measures TGCs of

$$g_1^Z = 11.8^{+12.1}_{-35.0} \tag{3.17}$$

$$\kappa_\gamma = -1148^{+3518}_{-1214}. \tag{3.18}$$

This error contains the systematic error of the hadronic cross section measurement. The fit result is stable with respect to changes of the physics parameters in the computation of the WW cross section, thus additional systematic errors are not taken into account. In order to demonstrate the sensitivity of the hadronic cross section to the ZWW couplings only, no correlation between ZWW and γWW couplings is assumed. This means that $\Delta\kappa_Z$ is set to zero in the fit procedure of $\Delta\kappa_\gamma$.

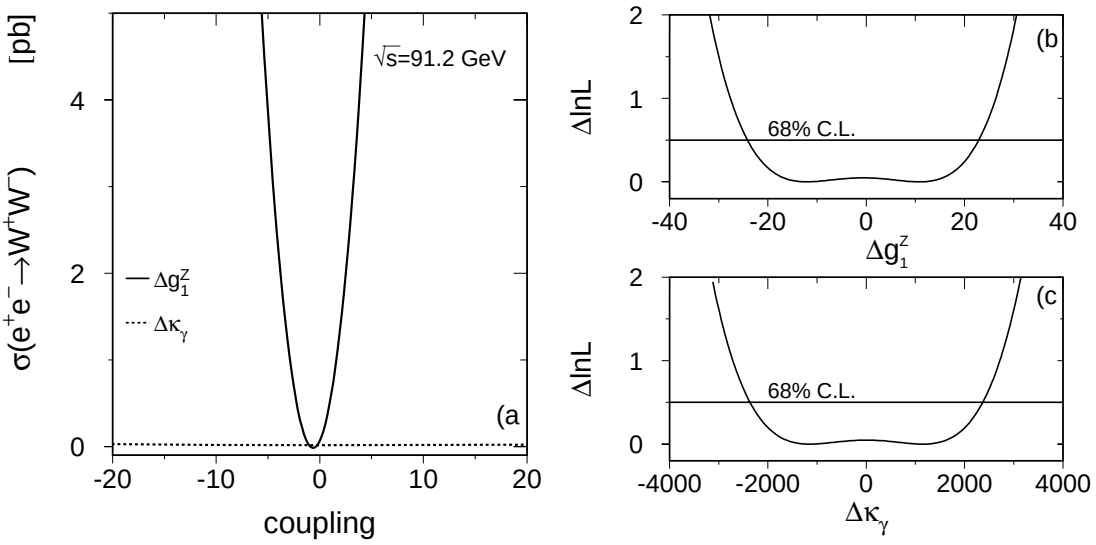

Figure 3.5: *The Z pole cross section for* W *pair production (a) is a function of the TGCs Δg_1^Z (solid line) and $\Delta\kappa_\gamma$ (dashed line). Likelihood curves (b+c) can be obtained for these two cases if one uses the measurement of the hadronic pole cross section.*

3.3 Do we need LEP 2?

Bounds on TGCs where obtained indirectly from their influence on radiative corrections to electroweak precision data and directly from the hadronic Z^0 pole cross section measured by the four LEP experiments. While the indirect measurements give tight bounds on the couplings the direct bounds are far less stringent. However, the indirect measurement relies heavily on the SM, as it is derived from small changes to small corrections, namely the radiative ones, to tree level parameters. The influence and thus existence of other possible physics beyond the SM is completely neglected in the computation. The limits are only valid in a specific model, the linear extension of the SM, while a general approach has not been considered. Assumptions on the physics beyond the SM are less relevant if couplings have influence on tree level processes. The direct limits from LEP 1 are thus interesting. Nevertheless, they give no information on whether the ZWW or γWW vertices are realised in nature or not, since their sensitivity is far too low. The W pair cross section evolution with the centre-of-mass energy, shown in figure 5.14, suggests however, that increasing the energy above the W pair production threshold and at best even further, will provide significant gain in sensitivity of the direct measurement.

This requires that the integrated luminosity at which the electrons and positrons are brought to collision and the efficiency of the detection of the final states, consisting of electrons, muons, taus, jets, and photons, must be large. Thus much effort has been undertaken to design a high energy-high luminosity electron-positron collider and to design detectors with large coverage and excellent resolutions. The result of these efforts, namely the design of the LEP collider and the design of **L3**, one of the four LEP experiments, is discussed in the next chapter.

Experience is that marvellous thing that enables you to recognise a mistake when you make it again.
F.P. Jones

IV

From detector to data

The physics case of measuring triple gauge boson couplings was discussed in the last two chapters. It was concluded that the best place to measure TGCs will be an electron-positron collider running at an energy above the W pair production threshold of $\sqrt{s} = 161$ GeV. A collider fulfilling these requirements was built at the European Laboratory for Particle Physics CERN, located close to Geneva, Switzerland. Its design and its properties will be discussed in the first section. The second section is dedicated to the apparatus, which is used to detect the elementary particles of the final state, the **L3** detector. In the successive sections the first two steps of the analysis chain of high energy physics experiments are discussed. The simulation of the physics reaction of electrons and positrons and the simulation of the detector response to the final state particles in section 4.3 and the extraction of high level physics objects, such as energy and momenta of particles, from the detector response in form of electronic pulses in section 4.4.

4.1 Large Electron Positron Collider

The LEP machine was designed to study the properties of the massive gauge bosons of the electroweak interaction. The detailed study of the properties of these bosons is only possible if a large number of bosons is produced. Since there are two of these bosons, there is a twofold strategy for the LEP collider.

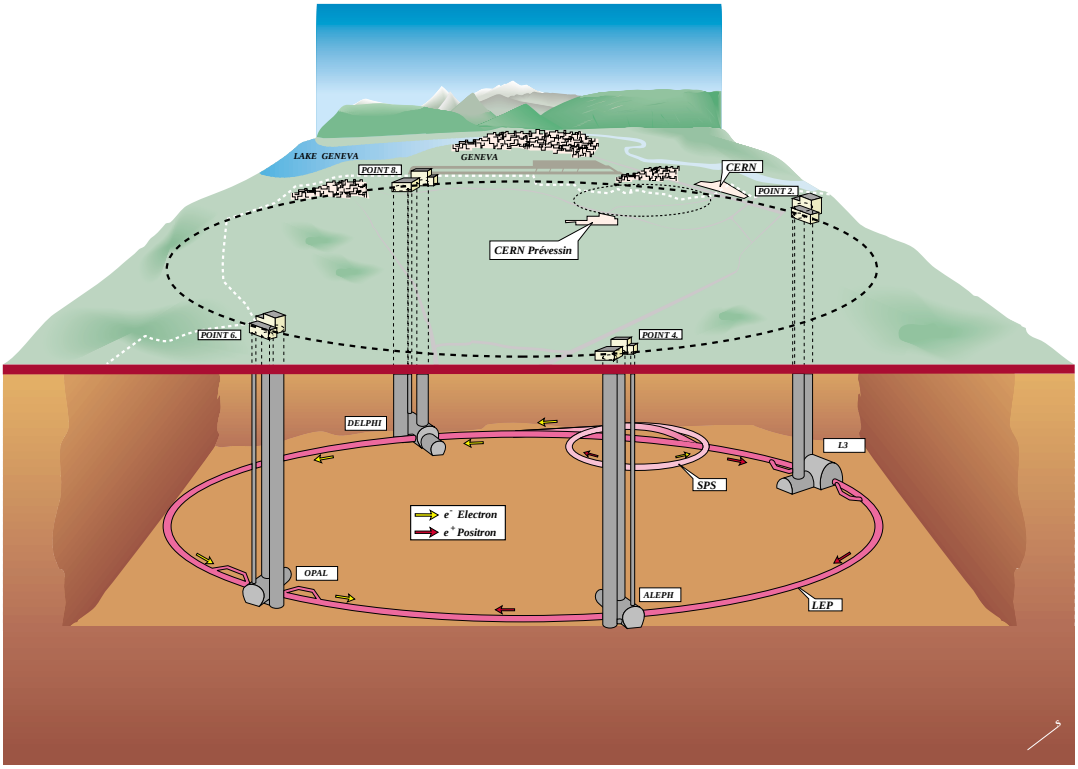

Figure 4.1: *Schematic view of the LEP accelerator with the location of the four LEP experiments ALEPH, DELPHI,* **L3** *and OPAL.*

The best situation to study the neutral weak boson Z^0 is the resonance production of this boson, *i.e.* electron-positron annihilation at a centre-of-mass energy corresponding to the rest mass of the Z^0. At this energy the fermion production due to the Z^0 s-channel diagram dominates the γ s-channel fermion pair production. The interference term of the two vanishes. The resonance behaviour increases the cross section by a factor of $\mathcal{O}(10^3)$. The LEP Z^0 production program started in 1989 and ended in 1995.

Since 1995 until the year 2000 the beam energy of the ring increases. In 1996 the threshold for pair production of the charged weak boson W, the second physics goal of the LEP, was reached and in the afterwards a large number of W bosons were produced.

The underlying physics demanded, that the ring can deliver high energy electrons and positrons (the pair production of Ws requires the beam energy to be larger than

the W mass of about 80 GeV) and a high luminosity (to produce a large amount of bosons). The energy requirements and the limited amount of accelerating power to replace the loss due to synchrotron radiation defined the ring to have the large circumference of 26.7 km, which resulted in a ring beneath the surface in a tunnel extending from the Jura mountains to the Lake Geneva, along the Swiss-French border. The ring is actually not circular, as could be concluded from the sketch in figure 4.1, but consists of eight straight and eight curved sections.
In the LEP 1 phase the ring was equipped with 3304 dipole magnets, to bend the electron and positron path to an approximately circular orbit, delivering a magnetic field up to 0.134 T. The focusing is done with quadrupole magnets. 128 copper cavities in the straight sections at point 2 and 6 were responsible for the acceleration and the replace of the energy loss by synchrotron radiation of about 120 MeV per turn. They supplied 16 MW accelerating power. For the LEP 2 program the copper cavities have successively been replaced with 384 superconducting cavities, now also placed in the straight sections at point 4 and 8.
The electrons and positrons are not accelerated from zero to beam energy in the LEP ring, but a whole chain of pre-accelerators supply LEP with electrons and positrons of about 20 GeV. The chain starts with two linear accelerators of 0.2 and 0.6 GeV, followed by the 0.6 GeV electron-positron accumulator. After this electrons and positron are injected into the proton synchrotron (PS) for an acceleration up to 3.5 GeV and then in the super proton synchrotron (SPS) to get an energy increase up to 20 GeV. Hereafter the beams are injected in the LEP ring where the energy gets ramped up to the desired beam energy.
Electrons and positrons travel in about 90 μs around the ring and are condensed in 8 (4×2) bunches of about 1 cm length, a horizontal extension of 200 μm and a vertical dimension of 20 μm. The revolution time can be translated to an interaction rate of 45 kHz at each interaction region (IP), of which one finds eight at LEP. At four of them the four LEP experiments ALEPH [**?**] (IP4), DELPHI [**?**] (IP 8), OPAL [**?**] (IP 6) and **L3** [**?**] (IP 2) are located, while at the odd numbered IPs the beams are electrostatically separated such that no interaction occurs.

4.1.1 LEP energy calibration

An exact determination of the beam energy is a crucial point in determining the properties of the final state, *e.g.* the measurement of the Z^0 mass at LEP I and the

W mass at LEP II. The resonant depolarisation method was applied at LEP I. This method exploits the Sokolov-Ternov effect [?], which leads to the self-polarisation of an electron beam on a circular orbit due to the emission of synchrotron radiation. On the other hand a beam can be depolarised by applying a periodic external field which is orthogonal to the leading magnetic field and whose frequency is identical to the number of spin oscillations per revolution. These two relations connect the depolarisation frequency f_{depol} with the beam energy E by

$$f_{\text{depol}} = \left| \frac{E}{m_e} \times \frac{g-2}{2} \pm n \right| f_{\text{rev}} \tag{4.1}$$

thus one can extract the beam energy with very high precision by measuring these two frequencies. Here g is the gyro-magnetic constant of the electron and f_{rev} is the revolution frequency.
However, one cannot apply this method at LEP 2, since disturbances to the beam due to machine imperfections, *e.g.* the magnetic field inhomogeneities, which are proportional to the beam energy squared [?], prevent the beam from self-polarisation. Since no accurate absolute measurement of the energy is possible, one employs nuclear magnetic resonance (NMR) and flux loop[1] measurements for monitoring the dipole magnets for a relative energy measurement. These two methods are then calibrated with depolarisation around the Z^0 resonance energy (from 40-65 GeV). These measurements and their uncertainties are then extrapolated to the actual beam energy [?, ?, ?]. In total eight NMR probes are located around LEP and the location of the flux loops with which almost every dipole is equipped, are shown in figure 4.2.
At LEP 2, accuracies of 20 MeV on the beam energy have been reached with the described methods. Luminosities and accuracies of the beam energy as well as its spread is shown in table 4.1.

4.2 L3 detector

The **L3** detector is one of the four multipurpose detectors installed at the LEP storage ring. It is specialised for the measurement of energy and momenta of muons, electrons and photons. To achieve these goals the detector is build according to

[1] Flux loops are electrical loops around the pole tips of the dipoles, measuring changes of the magnetic fields due to the induced voltage.

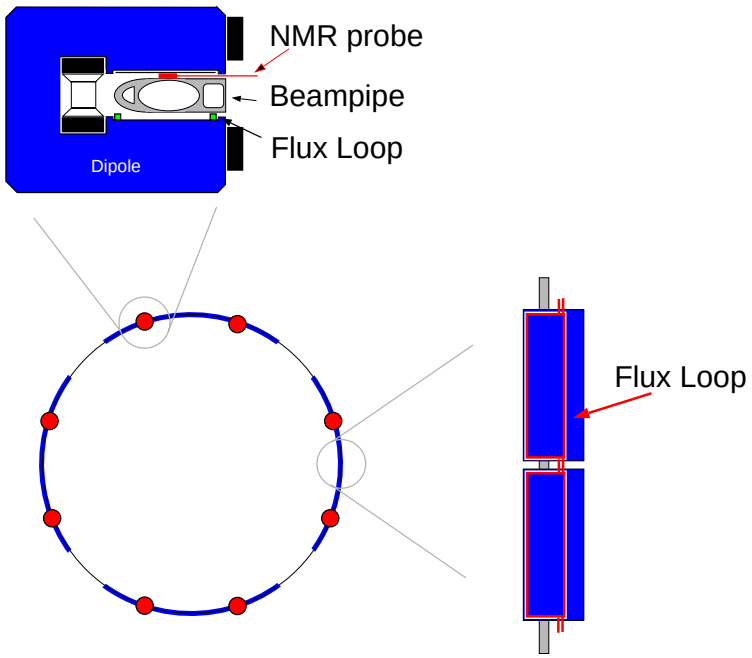

Figure 4.2: *The LEP beam energy is measured by NMR probes. As cross check flux loop measurements are performed if the dipole voltages are raised to the working point. Both methods are calibrated at energies close to the* Z^0 *resonance by resonant depolarisation.*

three main principles : Tracking with high spatial resolution in the inner part of the detector, calorimetry with high resolution in energy and position in the central part and high resolution muon tracking in the outer part.

All detector parts are described in means of the right-handed common **L3** coordinate system. Its origin is defined by the geometrical centre of the detector, which coincides with the nominal interaction point and the z-axis is given by the direction of the LEP electron beam. The x-axis points towards the centre of the LEP ring. Since physics as well as the **L3** detector components are usually symmetric under rotation around the z-axis, polar coordinates are often preferred in the description of detector components. The polar angle θ is the angle with respect to the z-direction and the azimuthal angle ϕ the angle in the x-y plane with respect to the x-direction. The radius r denotes the distance to the origin

year	mean energy [GeV]	energy error [MeV]	energy spread [MeV]	**L3** integrated luminosity [pb^{-1}]
1995(peak)	91.31	5	55.6	13.67
1996	161.34	27	144 ± 7	10.90
1996	172.13	30	165 ± 8	10.25
1997	182.68	25	219 ± 11	55.46
1998	188.64	20	237 ± 12	176.35

Table 4.1: *The measurements at LEP 2 have until 1999 been performed at energies between 161 and 189 GeV with the displayed integrated luminosities [?, ?, ?].*

4.2.1 Inner components

The inner part of the detector consists of a silicon micro-vertex detector (SMD), a time expansion chamber (TEC) and the Z^0 chamber (ZCH).
The SMD [**?**] is a double sided silicon strip detector consisting out of 96 wafers, each providing a measurement of the rϕ and the z coordinate. The principle of the measurement is based on p-n junction diodes [**?**], which results in a resolution of 7.5 μm for the rϕ coordinate and 14.3 μm for z [?]. Four wafers are assembled in a module, 12 of those making up a layer, forming a two layer detector. The layers are positioned at 62 mm and 78 mm radial to the beam axis. The layout is sketched in figure 4.5. Polar angles between 21° and 159° are covered. The readout strips of the outer layer are tilted by 2° with respect to the inner ones, to resolve track reconstruction ambiguities.
The tracking region is extended with drift chambers. **L3** uses a drift chamber working in the time expansion mode [**?**]. In a low, homogeneous field, called the drift region, electrons drift slowly in direction to the anode. Shortly before the anode, the electrons pass a grid of wires. Between the anode and the grid a high field is imposed, such that the electrons get accelerated and perform a large number of ionisations. This amplified signal is then collected by the anode. This method guarantees a high spatial resolution due to the low drift velocity in the drift region and a high, clear signal due to the amplification in the amplification region. A gas consisting out of 80% carbon dioxide and 20% isobutane at 1.2 bar is used, allowing drift velocities as low as 6 μm/ns. Figure 4.5 shows the principle of this

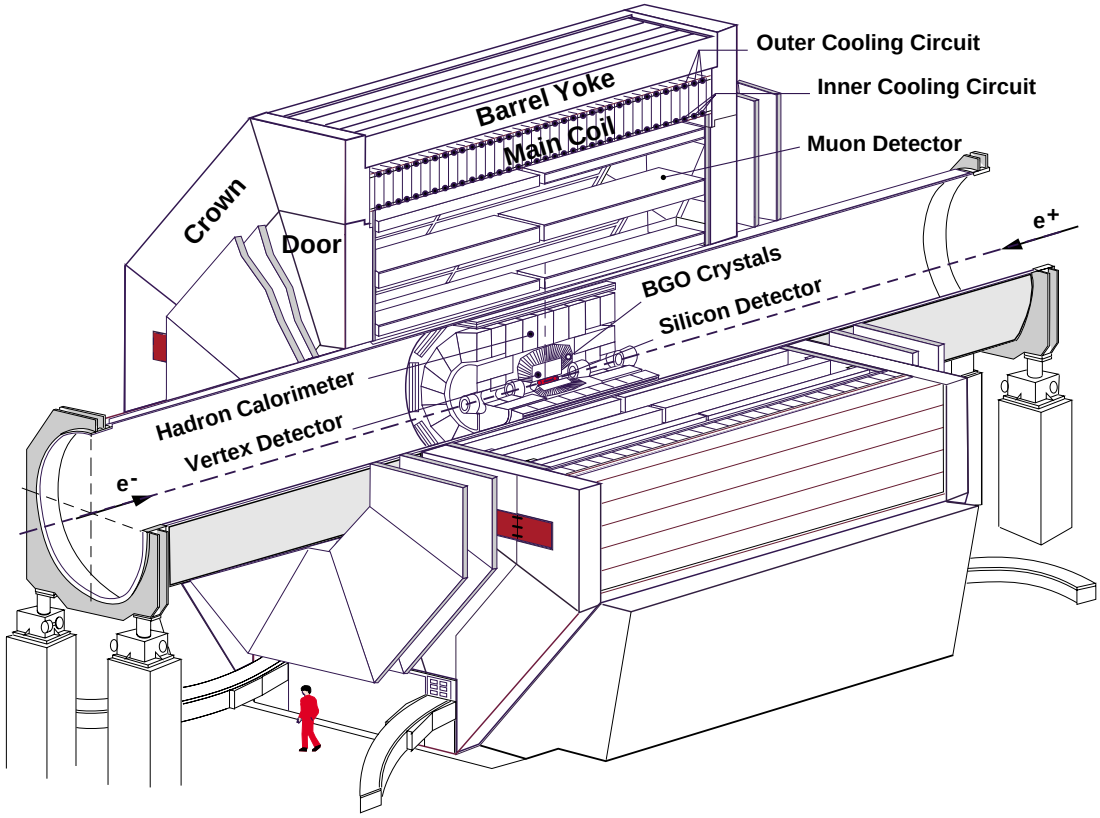

Figure 4.3: *Perspective view to the* **L3** *detector, allowing to distinguish between the detector components (see text).*

detector. The additional focus wires are used to ensure the homogeneity of the field within the drift region. The TEC increases the tracking volume up to a distance of 46 cm from the interaction point. The total lever arm of the TEC is 31.7 cm radially. The volume is subdivided in the inner chamber consisting out of 12 sectors in ϕ direction and the outer chamber with 24 sectors. A particle traversing the TEC can initiate a signal on 62 wires, eight of which are in the inner chamber. For charge identification of a 45 GeV particle with 95% C.L. about 50 TEC-hits are required. The problem of left-right-ambiguity is solved due to the displacement of the outer sectors with respect to the inner ones and the use of pick-up wires in the grid planes of the outer TEC. The solution, after matching the outer with the inner TEC track, is ambiguity free. Since the anode wires are arranged parallel to the beam direction, they can only measure the ϕ coordinate of the traversing particle. Eleven out of 62 anode wires are additionally equipped

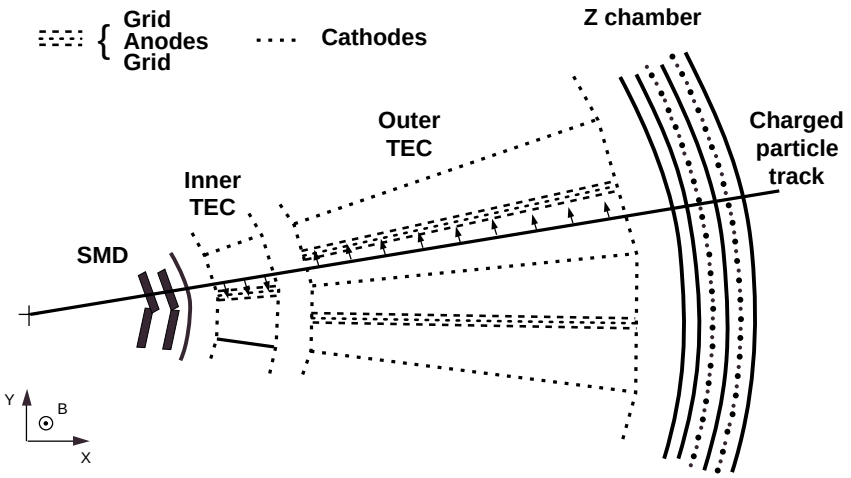

Figure 4.4: *The* **L3** *tracking system consists out of the SMD, the TEC and the* Z^0 *chamber. The* rϕ *view of one sector of the tracking system and the schematic drawing of the processes that occur if a particle crosses the tracking system (for more details see text).*

for measuring also the z coordinate. The measurement is based upon the principle of charge division, where the signal charge is read out at both ends of the anode wire, and the z position is computed with help of the ratio of the collected signals. The resolution of this method is a few centimetres. The drift time for the position determination is measured with respect to the beam crossing time as delivered by the LEP machine. The drift velocity is determined by self-calibration. The minimisation of the distance of a single hit to the fitted track gives the drift time-to-drift distance relation. It is separately obtained for each anode and each half sector. The interaction point is imposed as constraint for this calibration. Since such calibration improves (changes) the track fit, the calibration is an iterative process, which must be repeated until the track fit and the drift time-to-drift distance relation do not improve any more. After this TEC self-calibration, a detector inter-calibration using also SMD and the muon chamber information is performed to improve the single wire resolution even more. For this dimuon events, measured with the SMD and the muon chambers (see section "Outer components") are used. These components allow the exact determination of the track traversing

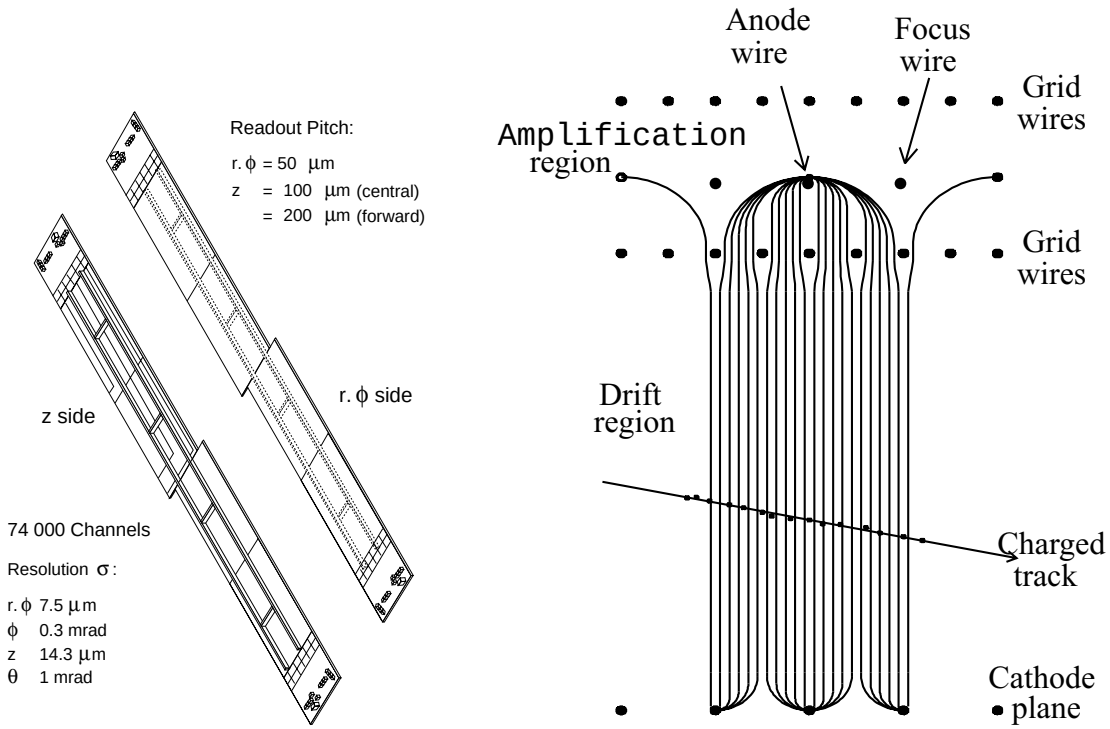

Figure 4.5: **Left:** *The SMD is a double sided silicon strip detector. The ambiguities in the pattern recognitions are resolved by a small tilt between the outer and the inner layer.* **Right:** *The separation of drift and amplification region gives good spatial resolution to the* **L3** *drift chamber.*

the TEC. The time-to-distance relation is corrected by comparing this track with the one measured only by TEC. As the method does not depend only on TEC it reduces significantly the systematics of the calibration.

As a result the TEC can provide a momentum resolution $\sigma(\frac{1}{p_\perp})$ of 0.018 GeV^{-1}, which can be improved by the use of the SMD measurements to 0.010 GeV^{-1}.

The resolution of the z coordinate measured with TEC only is not precise enough. For this reason two cylindrical proportional wire chambers [**?**] are installed between 47 and 49 cm radial distance from the interaction point, covering the angular range of $42° \leq \theta \leq 138°$. The two cathode layers of these detectors are subdivided into strips with a pitch of 4.45 mm, which are read out for measuring the mirror charge of the charge avalanche around the anode. 240 readout strips of one cathode per chamber are oriented perpendicular to the beam axis, whereas the strips of the remaining layers are used as stereo layers forming a helix with an angle of

$\pm 69°$. The stereo layers are needed to match the z-chamber [?] hits measuring the z-coordinate of a track to the track measured in the TEC having only a bad z-measurement. The 576 anode wires are arranged parallel to the beam axis. The resolution of the z-chamber is position dependent. In the centre it is as good as 200 μm while at the edges it reaches only a resolution of 800 μm.
Since the z-chamber does not cover the forward and the backward region an additional detector has to be used to measure θ in those regions. This detector is called forward tracking chamber (FTC) [**?**] and has a spatial resolution of 200 μm.

4.2.2 Central Components

The calorimetry, *i.e.* the energy measurement is done in the central part of the **L3** detector. It consists of a Bismuth Germanate $Bi_4Ge_3O_{12}$ crystal calorimeter (BGO) for the measurement of electromagnetic showers and a calorimeter for the measurement of hadronic showers (HCAL).
The BGO [**?**] is designed to measure the energies of electrons and photons with high precision over a wide range of energies and having sufficient spatial precision. For this reason the BGO is subdivided into 10734 crystals, each having the form of a truncated pyramid. In general, a crystal has a length of 24 cm, which corresponds to 21 radiation lengths and one nuclear interaction length, a front face of 2×2 cm^2 and a rear face of 3×3 cm^2. The BGO covers the angular region from 42.5° to 137.5°, called the barrel region (7680 crystals), and the regions $9.9° \leq \theta \leq 36.4°$ and $143.6° \leq \theta \leq 171.1°$ called the endcap region (1527 crystals each). The distance from the beam line to the barrel is 52 cm radially. An electromagnetic shower produces scintillation light in the crystals, which is read out by two photo diodes glued on the rear face of each crystal. The crystals are tilted by 10 mrad in the azimuthal direction with respect to the IP direction to minimise energy leakage. The BGO is calibrated according to four different methods. Before mounted inside the **L3** detector the BGO was calibrated with an electron test beam of 0.18, 2, 10 and 50 GeV. Based on these measurements the energy resolution is determined to be approximately 5% at 0.1 GeV, less than 2% at 2 GeV and 1.2% at 45 GeV. The linearity is better than 1%. The position of an electromagnetic shower inside the BGO can be measured with a resolution better than 2 mm, if one uses the centre-of-gravity method. For the second method a reference light pulse of a Xenon flash light is injected into the rear face of a crystal and the detector response is monitored.

The third method, called the RFQ [?, ?] (radio-frequency quadrupole) uses a beam of hydrogen ions which are shot on a lithium target within the **L3** detector. The proton capture process releases mono-energetic photons of 17.6 MeV energy which are monitored by the BGO. In addition wide angle Bhabha scattering is used to calibrate the BGO calorimeter.

The region between BGO barrel and endcap is equipped with a spaghetti calorimeter [?] consisting out of lead bricks interlaced with scintillating fibres.

The HCAL [?] encloses the BGO. Its barrel region extends from 35° to 145°, the forward (backward) part covers the angular range $5.5° \leq \theta \leq 35°$ ($145° \leq \theta \leq 174.5$), such that the HCAL covers 99.5% of the full solid angle. The method of the measurement is based on signal sampling, since it is built out of uranium and brass absorber plates as showering material and interleaved proportional chambers as detector material. A particle passing the HCAL has to traverse 6-7 interaction lengths depending on its polar angle. The HCAL-barrel is subdivided into 9 rings, each consisting of 16 modules. The 7968 proportional chambers are grouped in 101088 projective towers pointing towards the beam line. Each of the towers covers an angular range of 2.5° in θ and ϕ, leading to a subdivision of a module into 9 segments in transverse and 8 to 10 in longitudinal direction. An HCAL-endcap is assembled out of 3 rings, one outer and two inner rings. In the endcaps the proportional chambers are collected into 3960 projective towers.

This design leads to an energy resolution of $(55/\sqrt{E/\mathrm{GeV}} \oplus 8)\%$ for a single pion, while the granularity allows the determination of jet directions with a precision of 2.5°.

For both calorimeters together one finds a resolution in total energy of about 10% and in jet direction of about 2° for hadronic two-jet events at the Z^0 pole.

Some hadronic showers are not completely contained within the HCAL. Thus a tail catcher called muon filter is installed between the HCAL and the muon spectrometer to observe the energy leakage. It is subdivided into eight octants, each octant consisting out of six brass absorber plates interleaved with proportional chambers. The thickness corresponds to one interaction length.

A lead shield protecting the tracking chamber from beam related background is installed between BGO and HCAL in forward direction. It is equipped with plastic scintillators making it an active device (active lead ring (ALR) [?]) for energy measurements in the forward direction.

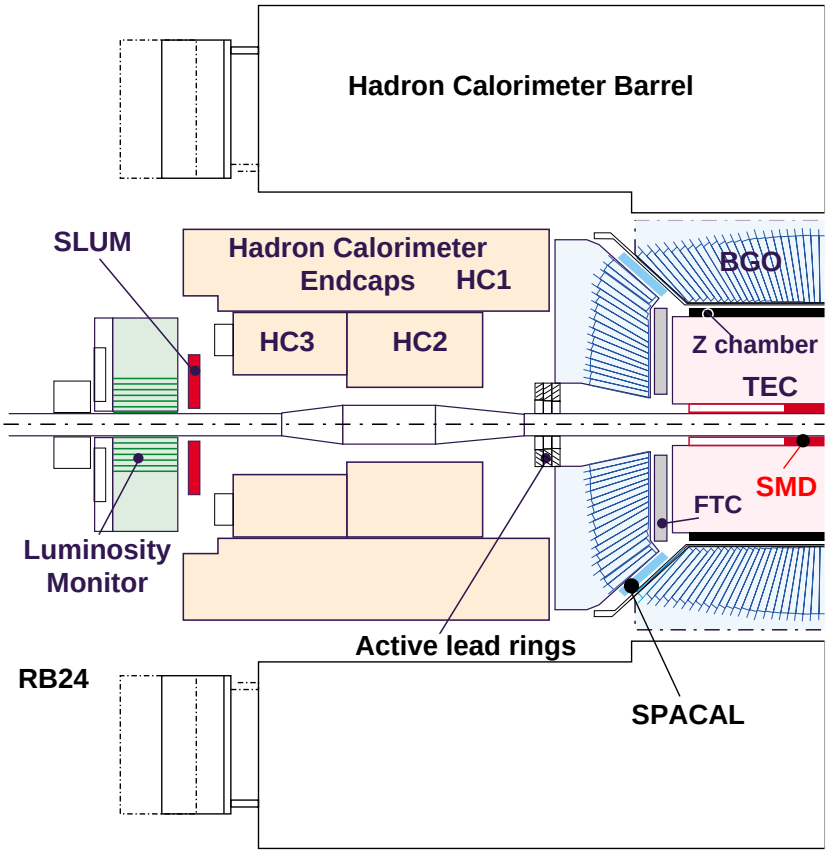

Figure 4.6: *The central and inner components of the left half of the* **L3** *detector. The right half has an identical structure.*

The central part of **L3** houses also a ring of scintillation counters [**?**] which are used for timing purposes. An array of 30 scintillators is situated between barrel part of the BGO and barrel part of the HCAL, covering a region of $34° \leq \theta \leq 146°$ corresponding to 93% of the azimuthal angular range. The endcap is equipped with 16 scintillation counters. The scintillators give time information of traversing particles, which can be used to discriminate dimuon from cosmic muon events. The time information has a resolution of 0.8 ns in the barrel and 1.0 ns in the endcaps.

4.2.3 Outer components

The muon spectrometer and the magnet form the outer part of the **L3** detector. The muon spectrometer [**?**,**?**,**?**] consists of three layers of precision drift chambers

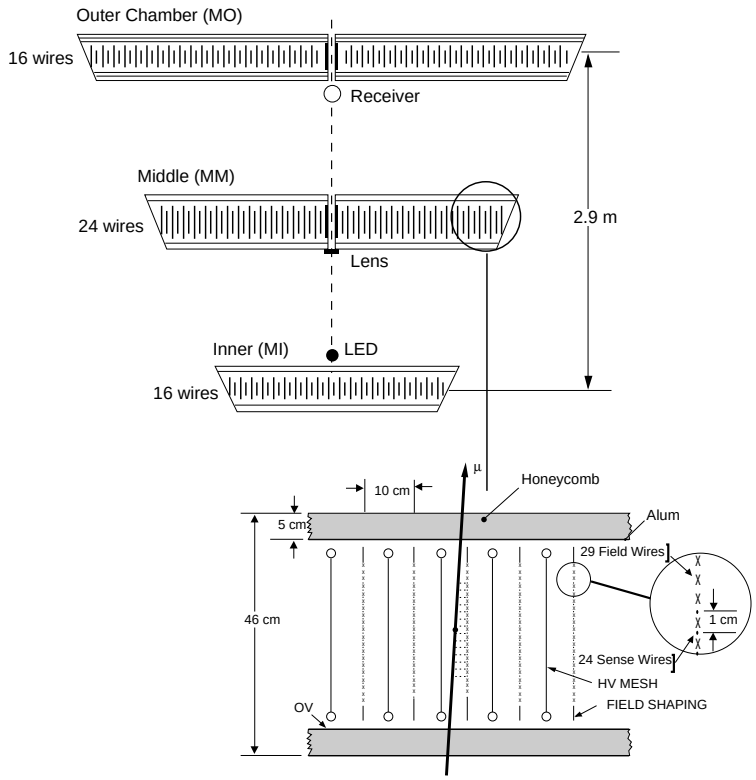

Figure 4.7: *An octant of the* **L3** *muon chamber system, shown in front view, consists of three layers.*

(P chambers), each of which is made of eight octants. This is displayed in figure 4.7. One distinguishes the inner (MI), the middle (MM) and the outer layer (MO), each having a single wire resolution of about 200 μm. MI and MO have 16 signal wires per cell while MM has 24. The wires are strung along the beam line and measure the rϕ coordinate. Additional drift chambers for the measurement of the z-coordinate are installed (Z chambers) at top and bottom of MI and MO. A Z chamber consists of two layers of drift cells offset by half a cell with respect to each other to resolve reconstruction ambiguities. The single wire resolution is 500 μm. The barrel part reaching from 44° to 136° is extended by endcaps down to 24° (156°).

For a 45 GeV particle a momentum resolution of 2.5% could be achieved if one has hits in all three barrel chambers. But also if only two chambers are hit, **L3** can measure the muon momenta, since in one chamber one measures not only the local position but also the slope of the particle trajectory with an accuracy of about

1 mrad, resulting in a momentum resolution of about 20% for a doublet muon.
The magnet is the outermost component of the **L3** detector and houses all the other detector components. It is a solenoid with an inner radius of 6 m and 12 m length, which is surrounded by an iron yoke. A current of 30 kA creates a magnetic field of 0.5 T along the beam axis. The coil is made of aluminium and makes 168 turns around the detector. The large magnetic volume and the magnetic field allow the good muon momentum resolution of the **L3** detector. Before the installation of the detector, a field map of the magnet was determined, such that the field at any point of the magnetic volume is known with high precision. In addition Hall probes, NMR probes and 1000 magneto resistors are installed to continuously monitor the magnetic field.
Muons going in forward direction have their main momentum component parallel to the solenoidal field and are thus only slightly bent. Therefore a toroidal magnet is installed in forward direction, providing a field of 1.2 T perpendicular to the beam axis and allowing muon momentum measurements in the endcap muon chambers.

4.2.4 Other components

The luminosity monitor and the very small angle tagger (VSAT) are positioned far away from the interaction point. Luminosity monitors [?] are located at ±2.7 m

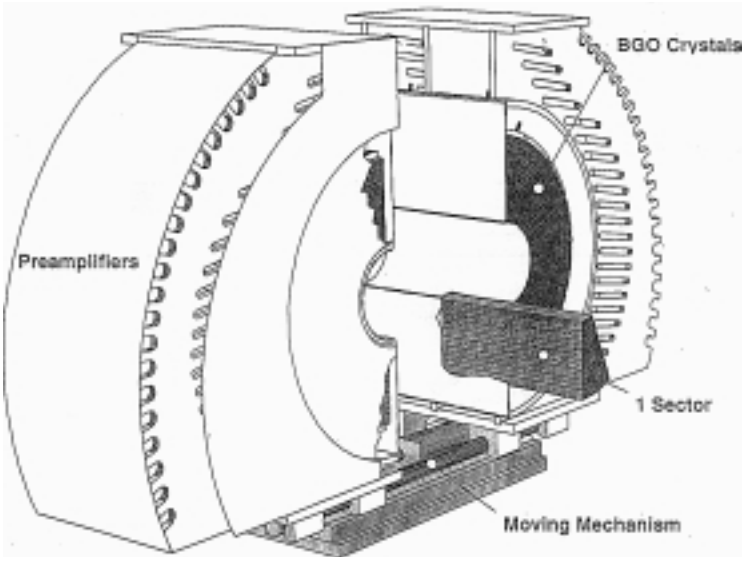

Figure 4.8: *The* **L3** *luminosity monitor [?]*

at either side of the interaction point to measure small angle Bhabha scattering. This process is used to compute the luminosity $\mathcal{L}$ from the measured number of events N_{events} according to

$$\mathcal{L} = \frac{N_{\text{events}}}{\epsilon \ \sigma}, \tag{4.2}$$

since the cross section σ of this electromagnetic process is well understood as pointed out earlier (c.f. section 2.3.1). The efficiency ϵ of the Bhabha event selection is computed on the basis of Monte-Carlo modelling of the Bhabha process and the detector response to it. The simulation techniques are discussed further in section 4.3. The luminosity detector consists of two half cylinders, each having 304 BGO crystals. One half cylinder is displayed in figure 4.8. Every crystal is read out by a photo diode. A LED is glued on each crystal to monitor its functionality. The luminosity monitor covers the angular range $1.4^\circ \leq \theta/(180-\theta) \leq 3.9^\circ$ with a resolution of about 2% in energy. Since the Bhabha cross section changes dramatically with electron polar angle extremely accurate measurements of these angles are required. Thus the position measurement is provided by a silicon strip tracking detector (SLUM), consisting of three layers of which two measure the polar and one the azimuthal angle.
The VSAT [**?**] consists out of four boxes with 24 BGO crystals each of the size of $9 \times 18 \times 220$ mm^3. The depth corresponds to about 20 radiation lengths. It covers the angular region from 5 to 10 mrad in θ. The VSAT is situated 8.17 m up- and down-stream from the interaction point, to monitor electrons scattered under very small angles. Since beam optics elements are sitting between the VSAT and the interaction point it makes only sense to measure in the horizontal plane since the vertical momentum components are disturbed by the corresponding fields.

4.2.5 Trigger

The beam crossing frequency at LEP is about 45 kHz, while the data acquisition system of **L3** is only able to handle data rates of less than 20 Hz, thus one cannot read out the complete detector at each beam crossing but has to take a decision, when an interesting event has occurred. This is done in the level 1 trigger (L1), which decides on the basis of event properties of interesting physics events whether the detector has to be read out or not. One distinguishes the TEC trigger [**?**], the energy trigger [**?**, **?**, **?**, **?**], the ALR trigger [**?**], the muon trigger [**?**], the scintillator

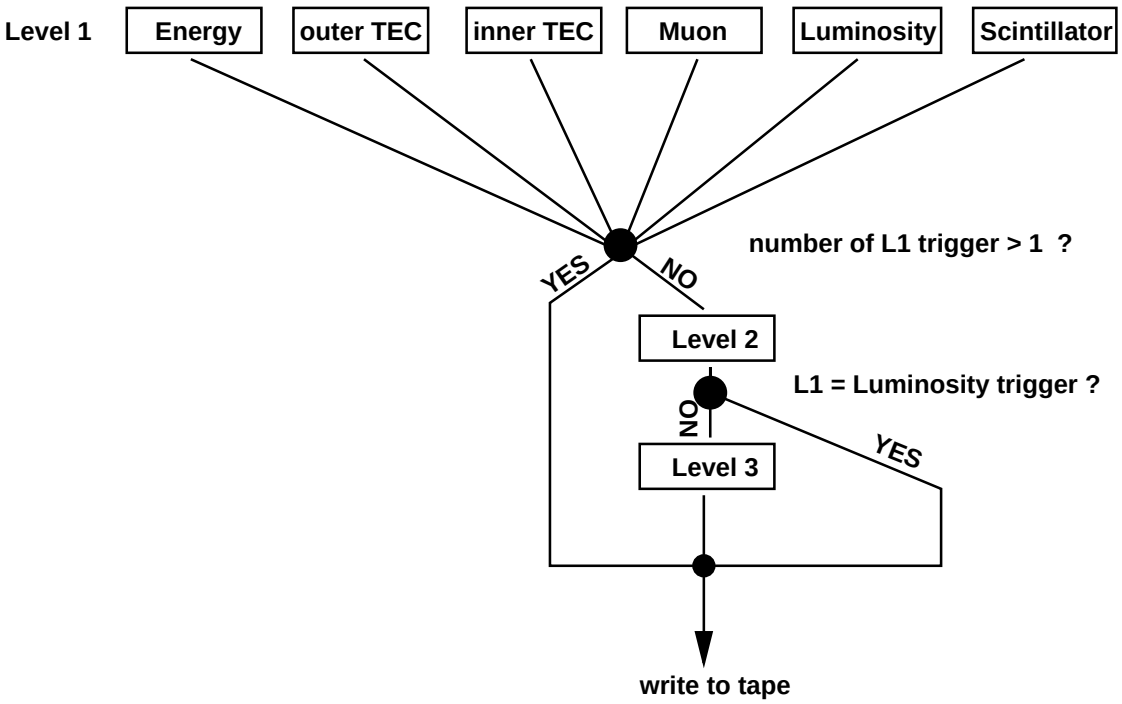

Figure 4.9: *The* **L3** *trigger is based on three levels. The first level trigger (L1) consists out of energy, inner TEC, outer TEC, muon, luminosity and scintillator trigger (see text for details). Triggered events are written to tape as raw data and are reconstructed offline.*

trigger and the luminosity trigger. If only one of these triggers gives a positive decision the event is sent to the level-2 (L2) trigger system [?], which acts to suppress background from electronic noise, synchrotron radiation, beam-gas and beam-wall interactions. Its decision is based on a more complete picture of the event such as approximate vertex reconstruction and BGO-HCAL hit correlation. The event is now send to the level-3 trigger system (L3) [?] which uses the complete detector information for applying tighter cuts to select mostly good physics events. Events having more than one L1-trigger are passed untouched through L2 and L3. Events that have only the L1-luminosity trigger are analysed by L2 but are not rejected by L3.

4.3 Simulation

The analysis chain of modern high-energy physics experiments involves Monte-Carlo (MC) based simulation of events of all possible event classes. The use of this technique allows to compare data with theoretical predictions and to understand the detector performance in any kind of differential event distribution. The simulation is split usually into the simulation of the physics process and the simulation of the detector response.

4.3.1 Physics processes and their simulation

The generation of a physics event in e^+e^- experiments proceeds via two steps. The first step is the electroweak process of electron-positron interaction and the production of the final state fermions and bosons and the second is the decay of these particles, if they do so. In the case of quarks in the final state one has to include the intermediate step of hadronisation which turns the coloured quarks into colourless hadrons, which are then treated in step two.
A list of generators which are used in the analysis of W pair, single-W and $\nu\bar{\nu}\gamma(\gamma)$ events and the simulated processes are listed in table 4.2.

4.3.2 Simulation of the detector response

After the event generation, the detector response to the final state particles is simulated. It results in pulse information of particular readout channels. This means that after a smearing of the e^+e^- interaction point (IP) according to the known real IP-size the particles are tracked through every detector element taking the magnetic field and detector support structures into account [**?**]. Probabilistic methods are used to simulate the interaction of particles with material of sensitive and passive parts of the detector. If a particle enters a sensitive part of the detector (*e.g.* a BGO-crystal) the energy deposition of this particle is stored. The tracking involves also the decay of unstable particles (particles that can decay within the sensitive detector volume). After the complete tracking one transforms the energy depositions in a particular detector part into its response to this deposition in form of *e.g.* ADC and TDC (analog/time-to-digital converter) counts. The transfer uses time dependencies of the detector performance as seen in data. Although this

MC-event generator	simulated process
KORALW [?]	$e^+e^- \to W^+W^- \to ffff$
EXCALIBUR [?]	$e^+e^- \to ffff$
GRC4.F [?]	$e^+e^- \to ffff$
HERWIG [?]	$e^+e^- \to W^+W^- \to ffff$
NUNUGPV [?, ?]	$e^+e^- \to \nu\nu\gamma(n\gamma)$
KORALZ [?]	$e^+e^- \to \nu\nu\gamma(n\gamma)$
PYTHIA [?]	$e^+e^- \to qq(\gamma)$
PYTHIA [?]	$e^+e^- \to Z^0/\gamma^* Z^0/\gamma^* \to ffff$
PHOJET [?]	$e^+e^- \to \gamma^*\gamma^* \to eeqq$
DIAG [?]	$e^+e^- \to \gamma^*\gamma^* \to eell$
LEP4F [?]	$e^+e^- \to \gamma^*\gamma^* \to eell$
KORALZ [?]	$e^+e^- \to \mu\mu(n\gamma), \tau\tau(n\gamma)$
BHAGENE3 [?]	$e^+e^- \to e^+e^-(n\gamma)$
BHWIDE [?]	$e^+e^- \to e^+e^-(n\gamma)$
TEEGG [?]	$e^+e^- \to e^+e^-(n\gamma)$
GGG [?]	$e^+e^- \to n\gamma$

Table 4.2: *MC-generators for* e^+e^-*-physics*

point is logically connected to the simulation it is technically connected to the reconstruction, as this scheme allows the multiple use of simulated events using various kinds of detector imperfections. This "real" detector simulation is based upon the status of each subdetector during data taking, which is compared to the date and time which is given to the simulated event according to the luminosity distribution over the data taking period to be simulated.

4.4 Reconstruction

The formation of high-level physics objects from raw data available as digitised information of the various detector channels is done by the reconstruction. The various detector components suggest different physics objects definition, so one

distinguishes between physics objects of the tracking detectors called tracks, objects in the calorimeters called clusters and objects in the muon spectrometer called muons.

Tracks are reconstructed using the hits in the TEC, Z^0 chamber and in the SMD. The parameters of the tracks, the curvature, the distance of the closest approach (DCA) of the track to the vertex and the θ and ϕ angle of the track at the vertex are obtained by a fit to all hits assigned to the track. The quality of a track is judged on the χ^2 of the fit, the number of hits on the track, the distance between the first and the last hit, the DCA and the track momentum.

Calorimetric information of the BGO and the HCAL is bundled together in a particle definition called (calorimetric) cluster. Groups of BGO-crystals are formed, starting with those crystals which represent local maxima of the energy deposition (bumps). The remaining crystals with lower energy depositions are assigned to the geometrically connected bump. Hits in the HCAL are geometrically matched to these bumps.

4.4.1 Electron and photon identification and the electron charge

The electron is identified combining the information of TEC and BGO. An electromagnetic shower is identified by its shape using the energy deposition in nine and 25 crystals around the shower centre. If the ratio of these energies, E_9/E_{25} is close to one, *i.e.* the shower is well contained within the nine inner crystals, the bump is an electron or photon candidate. The tracking chamber is used for the electron-photon separation. If a track can be matched to the centre of the electron/photon candidate one calls the candidate an electron, while if no track can be matched one has a photon candidate. Since the tracking resolution in the azimuthal angle ϕ is much better than the resolution in the polar direction, one performs the matching in this variable only. The ϕ-resolution of electrons in W pair MC-events is displayed in figure 4.10-a. The central region is described by a Gaussian with a resolution of 2.1 mrad. The tails, containing about one percent of the events, result from forward going electrons and badly reconstructed tracks. Thus the matching criteria changes with $\cos\theta$ as the resolution worsens in forward direction, since the number of possible TEC wires hits per track decreases from 62

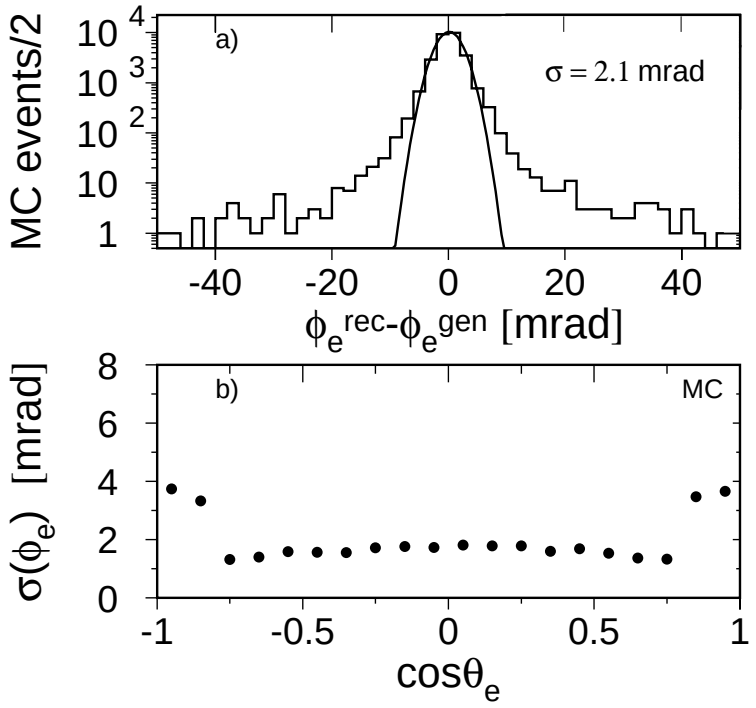

Figure 4.10: *The ϕ-resolution of electrons in $W^+W^- \to qqe\nu_e$ events a) integrated over $\cos\theta_e$ and b) in bins of electron azimuthal angle as seen in MC. The resolution worsens in the very forward direction since the number of hits per track decreases due to the limited TEC polar acceptance.*

in the barrel to zero in the very forward direction. This can be seen in figure 4.10-b where the resolution worsens considerably outside the barrel region, $|\cos\theta_e| > 0.75$. In the barrel a $\Delta\phi$ of 50 mrad is used for electron identification while this criteria softens in the forward direction. The description of the resolution in the MC has been carefully checked with Bhabha events, collected each year in calibration runs at $\sqrt{s} = 91$ GeV [?, ?, ?].

The $\cos\theta$ dependence of the track resolution (see figure 4.10) plays also a significant role in the determination of the electron charge. Thus the charge confusion increases in forward direction, as can be seen in figure 4.11 for 1995 Bhabha and dimuon events. For Bhabhas the charge confusion in forward direction found in MC is lower than that in data, a manifestation of the fact that the detector resolution is underestimated. However, great improvements in the detector description

in MC have been reached since 1995 [?, ?, ?], thus the difference is expected to be much smaller in the 1996-98 data taking periods than the one displayed in figure 4.11. Anyway, this cannot be proven since the data statistics collected in Z^0 calibration runs in each year is to low to draw firm conclusions. This data-MC charge confusion difference is therefore conservatively assumed in the evaluation of systematic error in section 6.7.

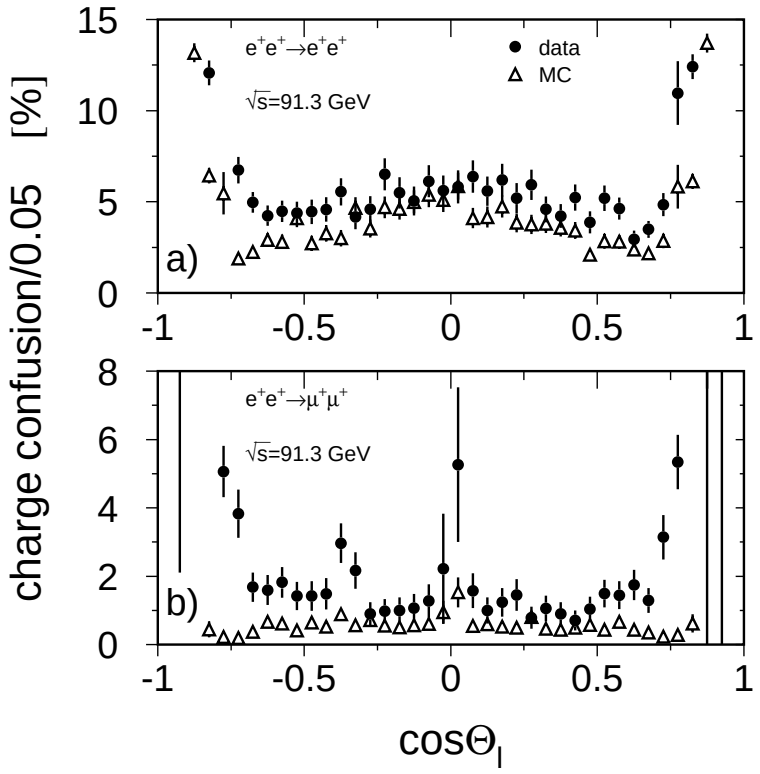

Figure 4.11: *The charge confusion for electrons (a) and muons (b) of about 45 GeV energy as determined by counting Bhabha or dimuon events with equal sign leptons,* $\frac{N_{ll}(|\sum Q|=2)}{2N_{ll}}$. *The energy of these leptons produced at LEP 1 energies (here data collected in 1995 are used) corresponds to that of the leptons resulting from* W *decays at LEP 2. The difference of data and MC is a source of systematic errors in the coupling determination in semileptonic events.*

4.4.2 Muon and MIP identification and the muon charge

Muons are identified as tracks that are reconstructed in the muon spectrometer. For being considered as a muon candidate, the track must have been reconstructed in at least two P-segments (doublet) of the spectrometer. Only then it is possible to assign a momentum to the track. Good quality muons have been tracked through all three P-chambers (triplet), have a low DCA after extrapolation to the IP (using not only θ and ϕ but also the curvature of the muon track) to the vertex and have a time-of-flight measured with the associated scintillators, that corresponds to the hypothesis of being created during a beam collision. In detection regions which are not covered by the muon chambers one uses the minimal ionising particle (MIP) signature of muons in the rest of the detector. A MIP is characterised by a good track in the TEC, a low energy cluster in the BGO, which has only a small number of crystals, and a small energy deposition in the HCAL. The charge of a MIP is obtained from the curvature of the track in the TEC and its charge confusion probability is equal to that of an electron (see figure 4.11).

The angular and momentum resolution in MC for muons resulting from semileptonic W pair decays, $W^+W^- \to q\bar{q}\mu\nu_\mu$, regardless whether they are triplets, doublets or MIPs can be seen in figure 4.12. The central parts are described by Gaussians with resolutions of 4/TeV for the transverse momentum and 1 mrad for the azimuthal angle ϕ. The tails of the distributions result from badly measured muons, *i.e.* doublets and MIPs.

The muon charge is determined from the curvature of the muon track. The charge confusion is smaller than in the case of the electrons, as can be seen in figure 4.11-b, due to the longer lever arm of the tracking. The agreement of MC and data in the 1995 data set is fair. Especially the forward region is not well described by the MC. In contrary to that, the loss in resolution at $\cos\theta_\mu = 0$, resulting from the fact that the right and the left half of the **L3** muon chambers are separated by several millimetres, is well described. Major repairs on the **L3** muon chambers took place in the 1995/96 and 1996/97 shutdown periods, resulting in significant improvement in resolution. Thus also an improved charge determination for the 1996-1998 data taking is expected. The data statistics collected in Z^0 calibration runs is however not large enough to draw a firm conclusion, thus the data-MC difference in charge confusion as displayed in 4.11-b is later assumed in the evaluation of the systematic errors on the TGC measurement.

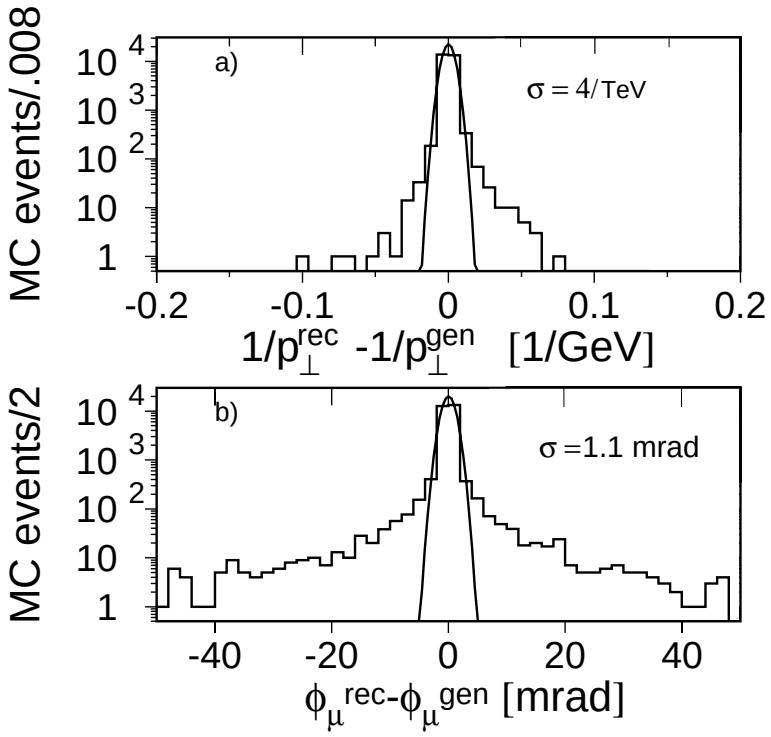

Figure 4.12: *The transverse momentum (a) and the ϕ (b) resolution for muons in $W^+W^- \to qq\mu\nu_\mu$ events regardless whether they are reconstructed due to the triplet, doublet or MIP signature.*

4.4.3 Jets and jet charges

Jets are objects assembling many calorimetric clusters and tracks closely together in space. They are formed to reconstruct quark energies and emission directions, as quarks hadronise and fragment before reaching the detector. Several algorithms to form jets have been proposed, the most important algorithms are the binary algorithms Jade [?, ?] and Durham [?, ?, ?] and the geometrical cone algorithm [?]. Binary algorithms replace two clusters by their sum (jet) if their distance y_{ij} is the smallest in the event. This procedure is repeated until either the wanted number of jets or an upper limit of the distance is reached.
The distance measure of the **Jade** algorithm is

$$y_{ij} = \frac{2E_iE_j(1-\cos\theta_{ij})}{E_{\text{vis}}^2} \tag{4.3}$$

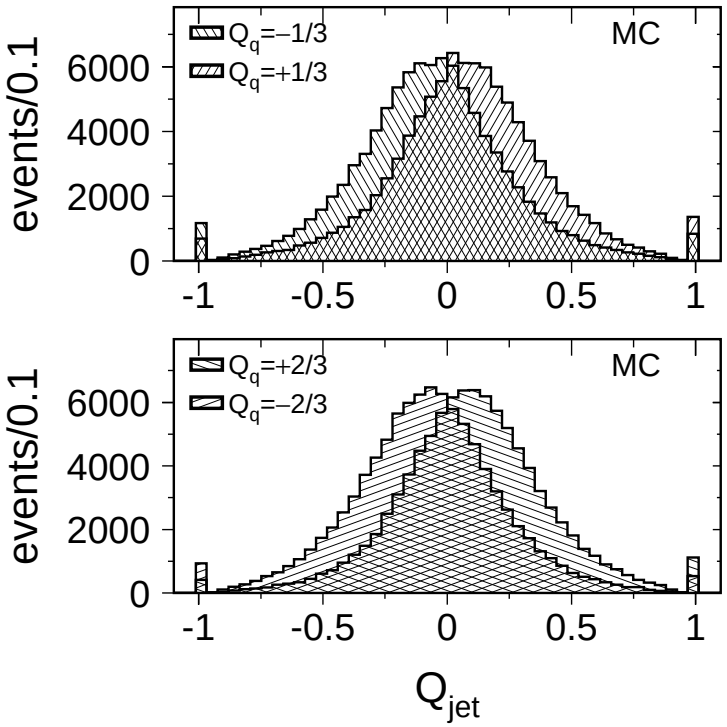

Figure 4.13: *The jet charge of the different quark flavours. The resolution is too poor to distinguish the single quark charges.*

and the one of the **Durham** algorithm is

$$y_{ij} = \frac{2\min(E_i^2, E_j^2)(1-\cos\theta_{ij})}{E_{\text{vis}}^2}, \tag{4.4}$$

where E_{vis} is the visible energy in the event, E_i and E_j are the energies of the two clusters or jets and θ_{ij} is the angle between them. While the distance measure of the Jade algorithm tends to cluster soft particles together even if they are not geometrically close in space, the distance measure of the Durham algorithm corresponds to a more geometrical scale.

The geometrical cone algorithm adds all clusters which fall in a cone defined around each particle. The jet is the sum of the cluster four-momenta. This procedure is repeated with the new jets until no change in number and energy of the jets is observed. This method is mainly used for finding a narrow τ-jet in an hadronic environment, while the binary algorithms are more suitable for events containing only hadronic quark jets.

The quark charge can be estimated using the charge of the particles in the corresponding jet. Since the common picture of hadronisation [?] of quarks suggests that the initial quark ends up in the high momentum hadrons, the most common algorithm uses the sum of the momentum weighted charges

$$Q_{\text{jet}} = \frac{\sum Q_i (\vec{p_i} \cdot \vec{p_{\text{jet}}})^\kappa}{\sum (\vec{p_i} \cdot \vec{p_{\text{jet}}})^\kappa} \tag{4.5}$$

to estimate the quark charge (Q_i is the charge of each particle in the jet, p_i is its momentum and p_{jet} is the jet momentum). Figure 4.13 shows the resolution of the jet charge using a κ value of 0.5 [**?**]. Although the resolution of this method is bad in terms of measuring quarks charges, it will be used to measure W charges in hadronic W pair decays. However, it was used already at LEP 1 to determine the forward-backward asymmetry in $b\bar{b}$ events [**?**, **?**].

4.4.4 τ-lepton identification and τ charge

In both cases, hadronic and leptonic τ-decays, one cannot reconstruct the τ as one cannot measure the one or two neutrinos which are produced in τ-decays. However, the direction of the visible decay products give already information about the approximate τ flight direction, as the τ-mass is much smaller than its momentum. Hadronically decaying τ-leptons show up as one, three or five charged tracks. While they are relatively easy to identify in $\tau\nu l\nu$ production, the identification within an hadronic environment ($qq\tau\nu$) is more complicated. In general an hadronically decaying τ is defined via a low multiplicity jet, with up to five tracks (also even numbers of tracks are allowed to recover loss of tracks due to reconstruction). While this criterion is sufficient in the first case one needs additional angular separation cuts to hadronic jets resulting from quarks in the case of $qq\tau\nu$.
The angular resolution for hadronically and leptonically decaying τ-leptons can be seen in figure 4.14. The problems in reconstructing the τ which have been discussed before lead to much worse resolutions compared to the other leptonic channels. Misidentification of tracks from the two quark-jets as τ-jet, dominate the flat tails.
In the case of leptonically decaying τ-leptons the charge is equal to the one of the muon or the electron. The charge of hadronically decaying τ-leptons is determined

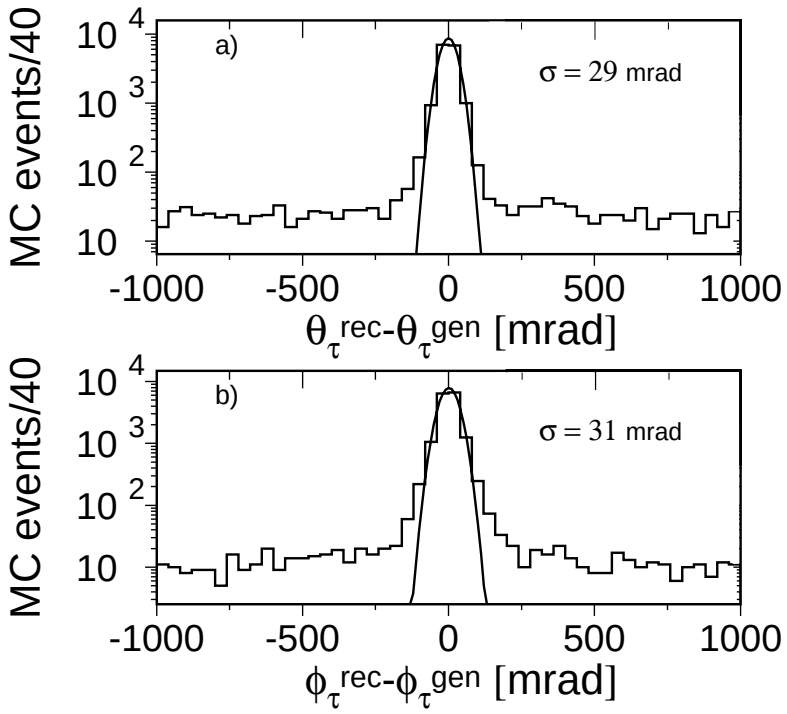

Figure 4.14: *The resolution of the polar angle θ (a) and the azimuthal angle ϕ (b) for τ-leptons in $W^+W^- \to qq\tau\nu_\tau$ events regardless if the τ has decayed hadronically or leptonically.*

by adding the charges of the tracks which are associated to the τ-jet. Zero τ-charge, which might be obtained in the case that the τ-jet contains an even number of tracks allows no distinction between fermion and anti-fermion. The charge confusion probability of a single track corresponds to that of an electron.

4.4.5 Reconstruction of Ws and the W charge

The W direction can be reconstructed from its decay products, if those are measured with the detector. Since the W decays either into two quarks or a lepton-neutrino-pair, where the neutrino escapes detection, full reconstruction is only possible in the case of hadronic W decays. In this case one registers two highly energetic jets. The W charge can be reconstructed using the jet charges of both daughter jets. In case of leptonic W decays the charge of the W corresponds to

that of the lepton.

In case of W pair production, the W reconstruction is improved by the fact of having two decaying Ws. The easiest case is the semileptonic W pair decay, having two quark-jets and a lepton identified in the detector. Assuming four-momentum conservation the neutrino momentum can be computed from the known four-momenta of the two initial electrons and the three registered final state fermions. Technically this is done by a kinematic fit [?, ?], which does not only take the final state four-momenta but also the resolution of the measurement into account. However, ISR imposes an additional energy loss to an event and those losses are assigned to the four momentum of the neutrino, resulting in a worse resolution in the reconstruction of the W four-momentum. The determination of the W charge in semileptonic events is based on the charge of the identified lepton as the charge confusion probability is small compared to those of the hadronic side (c.f. jet, electron, μ and τ identification).

Whereas the reconstruction of single hadronically decaying Ws was easy, it is harder for hadronically decaying W pairs. In this case four jets (j_1, j_2, j_3, j_4) are registered in the detector. This opens three possibilities ($[j_1j_2][j_3j_4]$, $[j_1j_3][j_2j_4]$, $[j_1j_4][j_2j_3]$) to combine two jets to form a W. The jet pairing is done on the basis of the smallest difference of the two W masses, disregarding the case of the smallest sum of the W masses. The right jet pairing is found in 74 percent of the cases. This can be seen *e.g.* in the $\cos\theta_{\mathrm{W}}$ resolution in MC as displayed in figure 4.15-a. The W charge determination exploits the jet charge method and the fact that the two Ws have opposite charges. Thus an events charge $Q_{W^-} - Q_{W^+} = q_{j_1} + q_{j_2} - q_{j_3} - q_{j_4}$ is computed to measure the W charge. The resolution of the charge measurement can be seen in figure 4.15-b. This method allows correct charge assignment in 69 percent of the cases. Thus both the W charge and its direction are correctly assigned in only 51 percent of the events.

In the case of leptonically decaying W pairs one cannot reconstruct the direction of both neutrinos. However, the W direction can be reconstructed with a twofold ambiguity. Assuming that the W mass is known and equal for the two decays and neglecting ISR and FSR one can compute two W four-momenta, which could be responsible for this two-lepton-final state configuration. The construction can be pictured as follows: As one knows the invariant mass of the neutrino and the measured lepton, since it equals the W mass, one knows the angle between neu-

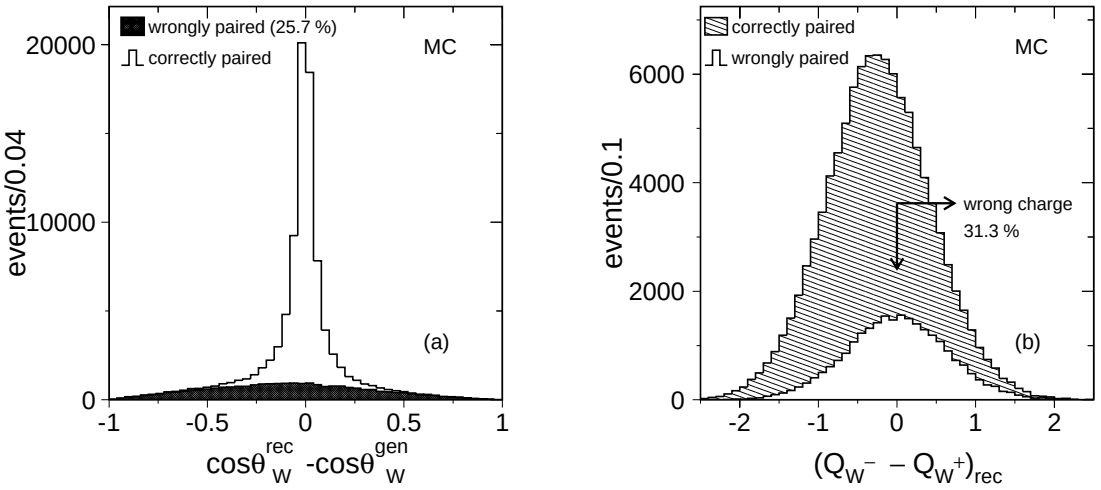

Figure 4.15: *A correct pairing of quark-jets to* W*s is obtained in 74% of the events. In wrongly paired* W*s the reconstructed and the true* W *direction are not correlated, resulting in flat resolution in* $\cos\theta_{\mathrm{W}}$ *(a). The* W *pair event charge (b) is the sum of the jet charges of the four jets. The* W *charge is estimated correctly in about 69% of the events which have a correct pairing.*

trino and lepton. Thus the neutrino direction is fixed to a cone around the lepton momentum vector. Since the W four-momentum is the sum of lepton and neutrino momentum, also the W momentum is fixed to a cone around the lepton direction. This holds for both Ws and thus one finds two cones around the lepton directions. As the Ws are back-to-back the W direction is identical to one of the two intersection lines of the two cones. These relations are visualised in figure 4.16. In about 23 percent of all $\ell\nu_\ell\ell\nu_\ell$ events resolution effects on the measured lepton momentum and W width effects allow that the lepton energy in the W mass frame exceed half the W mass. This configuration leads to two complex solutions for the W momentum. In this case the imaginary part of the momentum is neglected.

The W charge is taken from the corresponding lepton. If the charge of the leptons are measured to be equal, the lepton charge with the smallest charge confusion probability defines the W charge, *i.e.* taking the order μ, e, τ.

In the case of τ-leptons the computed W direction only approximates the direction of

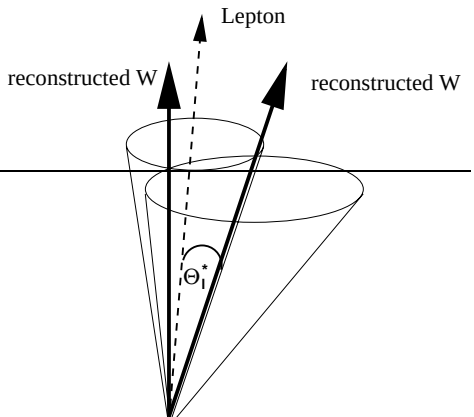

the W, since the two undetected neutrinos from the τ-decay lead to uncertainties in the τ direction. Nevertheless, also the computed $\cos\theta_{\mathrm{W}}$ value for these events shows sensitivity to TGCs and is used later for the determination of the triple boson couplings in chapter V.

4.5 Kinematic constraints

The imposition of kinematic constraints in the event reconstruction of W pair events results in an improvement of the energy, angular and mass (only for hadronic jets) resolutions. Kinematic fits are performed in the channels that contain at most one unmeasured neutrino, which are qqeν_e, qq$\mu\nu_\mu$ and qqqq. In the case of hadronic jets their velocity $|\vec{p}|/E$ is kept constant, as it is assumed that the systematic effects on the momentum and energy measurement cancel in the ratio. Four-momentum conservation and equality of the masses of the two W bosons are imposed as constraints, allowing a 2C[1] fit for qqeν_e and qq$\mu\nu_\mu$ events and a 5C[2] fit for qqqq events.
Kinematic fits are not applicable in the case of qq$\tau\nu_\tau$ and $\ell\nu_\ell\ell\nu_\ell$ events since the number of unknowns (at least two neutrinos - at least six unknowns) exceeds the number of constraints (5). However, the energy of the hadronic jets in qq$\tau\nu_\tau$ is rescaled by a common factor so that their sum equals the beam energy. The τ-direction is approximated by the flight direction of its decay products and the τ energy is

[1] Unknown neutrino three-momentum and five constraints = twice over-constrained
[2] Zero unknowns and five constraints = five times over-constrained

determined together with the neutrino momentum from imposing four momentum conservation. No treatment is applied to the measured four-momenta in $\ell\nu_\ell\ell\nu_\ell$ events.

4.6 Is the experimental apparatus sufficient ?

TGC sensitive channels were identified in chapter II. It was concluded that a e^+e^- collider running above the W pair production threshold would be the ideal place for their study. In the first section of this chapter, it was discussed that the LEP collider is running above this energy and is thus capable to produce events in those channels. The sensitive channels contained photons, electrons, muons, τ-leptons and hadronic jets in the final state. In the last sections it was shown that the **L3** detector is capable of detecting these particles and of measuring their momenta and charges with high precision. The excellent performance in detecting final state fermions allows to reconstruct the momenta of the two W bosons in W pair events, regardless of the W decay topology. In leptonic W pair decays this reconstruction has a twofold ambiguity. The quality of W charge measurement, necessary for the measurement of the forward-backward asymmetry $\cos\theta_{\mathrm{W}}$ ranges from excellent in the case of semileptonic and leptonic W pairs decays to fair in the case of hadronically decaying W pairs.

V

We don't think -
we measure.
S.C.C. Ting

From data to selected events

Coupling measurements at LEP focus one three of the four channels identified in chapter II. These are the W pair, the single W and the single photon production. Events of these event classes are only a small fraction of the events produced at e^+e^- collisions at LEP. The selection of events for each of the channels, will be discussed in the successive sections, starting with W pair events and finishing with single photon production.

5.1 Selection of W pairs

The identification of W pair events is split into five channels: the hadronic channel, three semileptonic channels and the leptonic channel. Each of them will be discussed in detail in the next paragraphs. The selections are outlined for the analysis of data taken at a centre-of-mass energy of 183 GeV [?]. The analyses for the centre-of-mass energies of 172 GeV [**?**] and 161 GeV [**?**] follow along the same principles.

5.1.1 The hadronic channel

A W pair can decay into four quarks which show up as four hadronic jets in the detector, as is visualised in figure 5.1 next to a schematic view to the rϕ-projection of the **L3** detector. The four jets can easily be distinguished from their energy depositions in the BGO and in the HCAL. The identification of those events focuses on the properties of the hadronic jets, one of which is high multiplicity, such

that one requires more than ten tracks reconstructed in the central tracking chamber and at least 30 calorimetric clusters. Since hadronic W decays do not involve neutrinos one expects the missing momentum to be small. This is accounted for in selecting only events with a large visible energy E_{vis} ($> 0.7\sqrt{s}$) and a small longitudinal imbalance ($|\sum \cos\theta_i E_i| < 0.25 E_{\mathrm{vis}}$). These four cuts remove most of the background sources but the $e^+e^- \to qq(\gamma)$ one. To reduce this background the events are clustered into four jets using the Durham cluster algorithm. The four jet topology like in hadronic W pair decays is enhanced by requiring that for selected events the Durham jet resolution parameter y_{34}, where the jet topology changes from four to three jets is larger then 0.0015. Many of the $qq(\gamma)$ background events which are still selected, are accompanied by a high energetic photon.

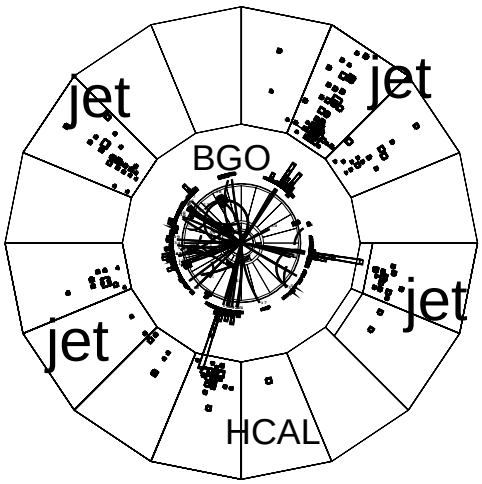

Figure 5.1: *Candidate event for* $W^+W^- \to qqqq$

The cross section of these events is enhanced since initial state radiation leads to the production of an on-shell Z^0 boson ("radiative return"), which results in a resonance behaviour. One requests that jets contain less than 40 GeV of electromagnetic energy and that the highest energetic photon reconstructed in the detector carries less than 80% of the energy of each jet to suppress these events. Events which contain a muon with more than 25 GeV energy are also disregarded, as these events are most probably $qq\mu\nu_\mu$ events. After this preselection 95.6% of signal events were kept, while the $Z^0 \to qq(\gamma)$ background is reduced by a factor of 15, *i.e.* about 430 background events survive in the 183 GeV data set.

The final selection is done using a neural network [**?**]. This network is constructed out of eight input nodes, one hidden layer with 15 nodes and one output node. The net is trained to give an output of one for the signal and of zero for the background. The input variables are the minimal and maximal jet energy, the minimal jet-jet opening angle, the minimal cluster multiplicity of the jets, the Durham jet

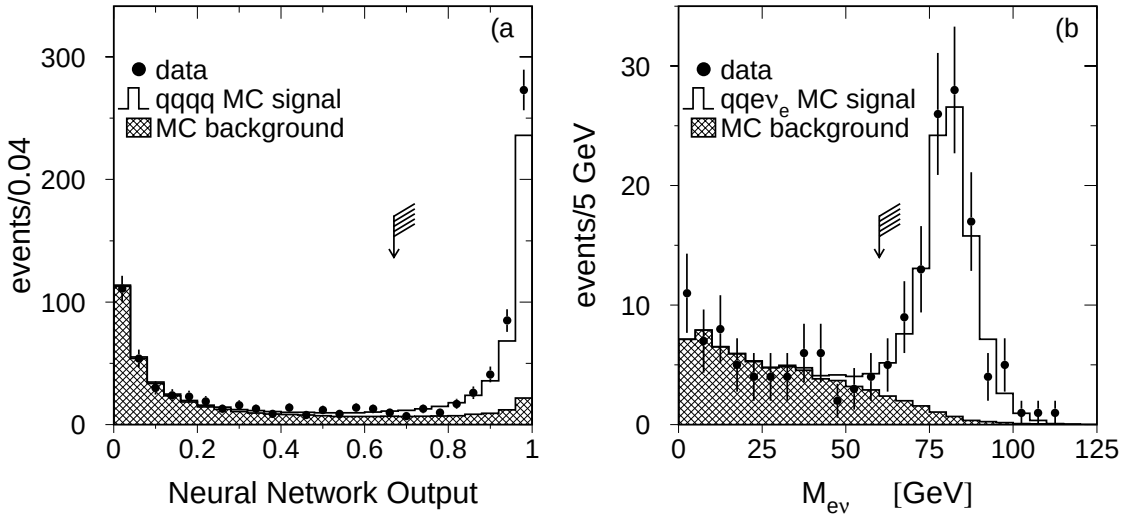

Figure 5.2: *The distribution of the neural network output for the selection of* $W^+W^- \rightarrow qqqq$ *(a) and the* $M_{e\nu}$ *invariant mass distribution for the selection of* $qqe\nu_e$ *events (b). The cuts are indicated by the arrow - all other cuts are already applied.*

resolution parameter y_{34}, the spherocity[1], the mass difference of two W masses and the jet mass average if the event is forcibly reconstructed as two jet event. All variables are used after a kinematic fit imposing energy-momentum conservation, which improved the energy and angular resolution of jets. The distribution of the neural net output is shown in figure 5.2-a. Good agreement has been found in the background region at output values close to zero, whereas in the signal region an excess of data of about 2.4 Gaussian sigmas is observed. From this distribution events are selected with a cut on the neural net output, yielding 473 events selected in the 183 GeV data set. Background and signal expectations are summarised in table 5.1 and a summary of all applied selection criteria can be obtained from appendix C.

5.1.2 The $qqe\nu_e$ channel

In the $qqe\nu_e$ case (CC20) the W pair production (CC03) is accompanied by 17 other graphs of four fermion production as outlined earlier. For this reason the

[1]Spherocity is defined as $\frac{4}{\pi} min \left(\frac{\sum |p_T|}{\sum |p|} \right)^2$, where p_T is the transverse momentum of each particle of momentum p to a unit vector $\vec{n}$, with respect to which the term is minimised.

selection is optimised for the signal definition of

$$E_e, E_\nu > 20 \text{ GeV}$$
$$|\cos\theta_e|, |\cos\theta_\nu| < 0.95$$
$$M_{e\nu}, M_{qq} > 45 \text{ GeV}$$

enriching the CC03 contribution. These cuts are applied to the phase space on generator level and efficiencies and signal expectation are always quoted relating to these phase space cuts.

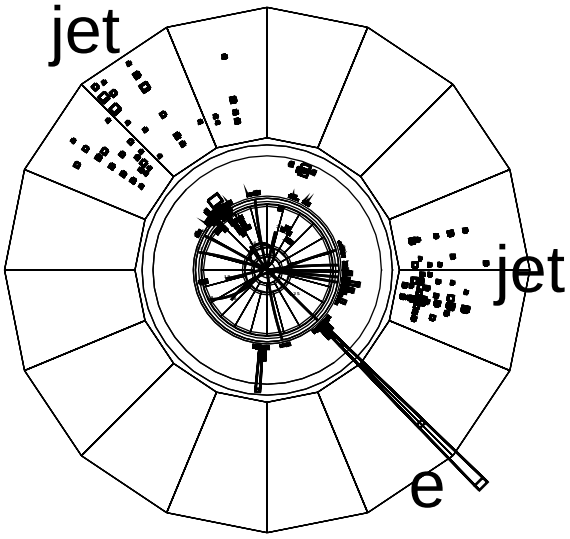

Figure 5.3: *Candidate event for* $W^+W^- \to qqe\nu_e$

The event selection requires a high energetic electron (> 20 GeV) to be detected within the electromagnetic calorimeter. The two hadronic jets leave large particle multiplicity in the detector. One accounts for this property by requiring at least twelve calorimetric clusters. This cut rejects almost all background from purely leptonic final states. In addition the undetected neutrino can be reconstructed due to the missing momentum (imposing energy-momentum conservation). The neutrino is required not to point in the direction of the beam pipe ($|\cos\theta_\nu < 0.94$) to distinguish W pair events from $q\bar{q}(\gamma)$ events where the photon escapes along the beam pipe.

To reduce further the background one applies a cut on the invariant dijet mass (> 33 GeV) accounting for the fact, that W events have always a high dijet-mass (≈ 80 GeV), while this is not the case for the background.

Semileptonic events where one of the Ws has decayed in $\tau\nu_\tau$ are rejected by requiring that the invariant mass formed by the electron and the neutrino is larger than 60 GeV.

The cuts mentioned above are tightened, if the electron is not detected within the BGO-barrel or endcap, but in the SPACAL filling the gap between these two

BGO-parts.

A summary of all selection criteria can be found in appendix C and the distribution of the invariant mass of the electron and the neutrino for the data collected at $\sqrt{s} = 183$ GeV is shown in figure 5.2-b. The signal peaks as expected close to the W mass of 80 GeV, whereas the background peaks at low invariant masses. Data and MC agree well with each other.

In the end 112 events were selected in in the 183 GeV data set.

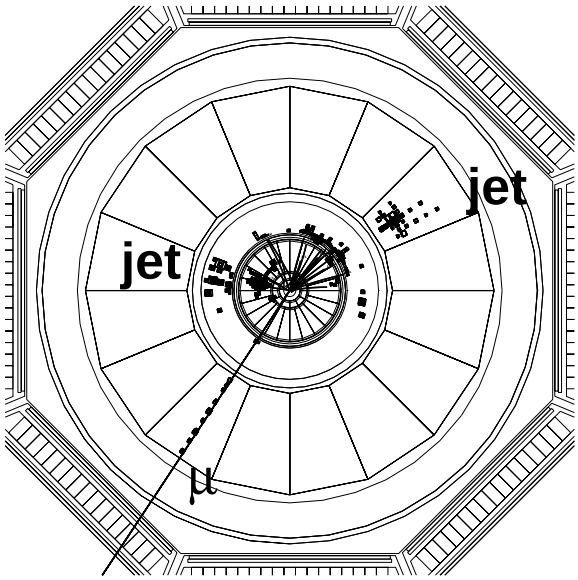

Figure 5.4: *Candidate event for* $W^+W^- \to qq\mu\nu_\mu$

5.1.3 The $qq\mu\nu_\mu$ channel

The event selection in this channel is based on the properties of two hadronic jets and the properties of the muon. The hadronic part of these events leave a high multiplicity in the calorimeter, such that one can suppress purely leptonic events by requiring at least ten calorimetric clusters to be reconstructed. Muons are either identified as a high momentum track ($|\vec{p}| > 15$ GeV) in the muon spectrometer or due to their MIP signature. In the following the selection is only outlined for spectrometer muons contributing with more than 90%, while the selection criteria for MIPs are summarised in appendix C.

After the muon was identified one requires that it is separated from the jets (energy in a 20° cone around the muon is less then 20 GeV) to avoid background originating from hadron decays.

The neutrino is reconstructed as missing momentum (imposing energy-momentum conservation). In $qq(\gamma)$ events, where the photon escapes along the beam pipe and thus could mimic the signal, the reconstructed neutrino polar angle θ_ν is very small. The angle between the reconstructed muon, resulting from hadron decays, to the nearest jet α is also small. This is exactly opposite in signal events, where

the neutrino direction is in most of the cases well within the detector and the muon is well separated from the hadronic jets, thus requiring that $\alpha \sin\theta_\nu$ is larger than 4° rejects a large fraction of the background events.
In W pair events one finds high invariant masses of the dijet system ($20\ \text{GeV} < m_{jj} < 120\ \text{GeV}$) and the muon-neutrino system ($m_{\mu\nu} > 45\ \text{GeV}$), resulting from the mass of the W ($\approx 80\ \text{GeV}$), while the background prefers lower values of the masses.
A summary of all selection criteria can be found in appendix C. The distribution of the μ-momentum is shown in figure 5.5-a. Since the muons of the signal result from W decay, they carry about half of its energy, which corresponds to half of the beam energy. Thus the signal muons show up at about 45 GeV whereas the background muons, resulting mainly from semileptonic decays of bottom or charm hadrons, are mostly low energetic muons.
The application of this selection to data selected 108 events in the 183 GeV data set.

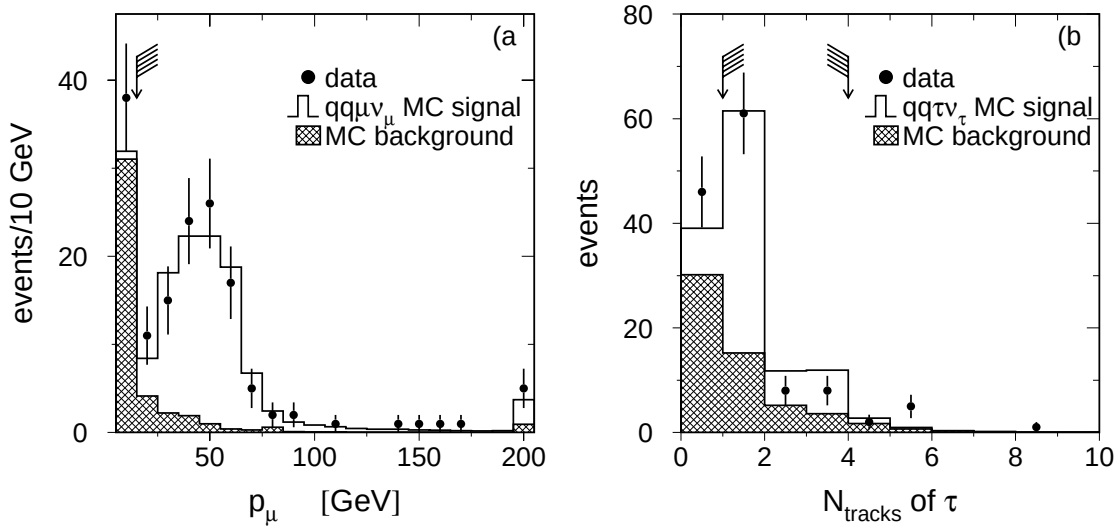

Figure 5.5: *The distribution of the μ-momentum for the selection of $W^+W^- \to qq\mu\nu_\mu$ (a) and the number of tracks of the τ-candidate for the selection of $qq\tau\nu_\tau$ events (b). The cuts are indicated by the arrows - all other cuts are already applied.*

5.1.4 The $\mathrm{qq}\tau\nu_\tau$ channel

Crucial for the selection of $\mathrm{qq}\tau\nu_\tau$ events is the identification of a τ-lepton in a hadronic environment. A τ-lepton can decay either into an electron (17.8% of the cases), into a muon (17.3%), or into hadrons (64.8%).
Purely leptonic background processes are suppressed by requiring high multiplicity events (> 14 calorimetric clusters, > 5 tracks).
Since in $\mathrm{qq}\tau\nu_\tau$ events at least two neutrinos escape undetected, one finds large missing energy, if energy-momentum conservation is assumed. This is accounted for by requesting the events to have a transverse energy imbalance of at least 10 GeV, a sum of missing momentum and visible mass larger than 110 GeV and a difference of visible energy and missing momentum less than 140 GeV. Photons in "return-to-the-Z" events carry approximately 65 GeV of energy and are preferentially emitted parallel to the beam axis. Thus the background coming from $q\bar{q}(\gamma)$ events is reduced by applying an upper cut on the longitudinal energy imbalance (< 40 GeV).
In the case where the τ has decayed in a lepton one identifies these leptons as described earlier, but uses the fact that in $\mathrm{qq}\tau\nu_\tau$ events two neutrinos with large angle to each other escape detection while in $\mathrm{qq}\ell\nu_\ell$ ($l \neq \tau$) events only one neutrino is produced. This property allows to distinguish between original $\mathrm{qq}\ell\nu_\ell$ events and those originating from the signal in terms of the invariant mass of the lepton and the missing momentum vector, which is expected to be lower for signal compared to $\mathrm{qq}\ell\nu_\ell$ events.
If the τ has decayed into hadrons, one tries to reconstruct it using the cone clustering algorithm with 15° opening angle. Among at least three reconstructed jets one identifies the τ-jet by using a neural network. Inputs to this network are jet mass, electromagnetic energy of the jet, its number of tracks and clusters as well as its half-opening angle. Since the overwhelming fraction of hadronic τ-decays are decays in either one or three charged hadrons one requires that the τ-jet candidate must have one or three tracks. The distribution of the number of tracks of the τ-candidate is shown in figure 5.5-b. Only for the hadronic τ-events the constraints on the missing momentum are tightened ($|\cos\theta_{\mathrm{miss}}| < 0.95$). The invariant mass of the τ-jet candidate and the missing momentum is required to be between 40 and 120 GeV and the dijet mass of the remaining hadrons must be between 50 and 110 GeV in order to reduce $\mathrm{qq}(\gamma)$ events.

The list of all applied selection criteria can be obtained from appendix C.
Applying all cuts one finds 77 events in data collected at 183 GeVcentre-of-mass energy.

5.1.5 The $\ell\nu_\ell\ell\nu_\ell$ channel

The $\ell\nu_\ell\ell\nu_\ell$ symbol is the summary of events where the leptons ℓ could either be electrons, muons or taus (decaying either in e/μ or in hadrons). The W pairs (CC03) in this class are strongly polluted by many four-fermion-background graphs, such that the total number of graphs that have to be considered is 56 (CC56). The signal fraction can be enriched by implying the following phase space cuts.

$$|\cos\theta_{\ell/\ell'}| < 0.96$$
$$\max(E_\ell, E_{\ell'}) > 15 \text{ GeV}$$
$$\min(E_\ell, E_{\ell'}) > 5 \text{ GeV}$$

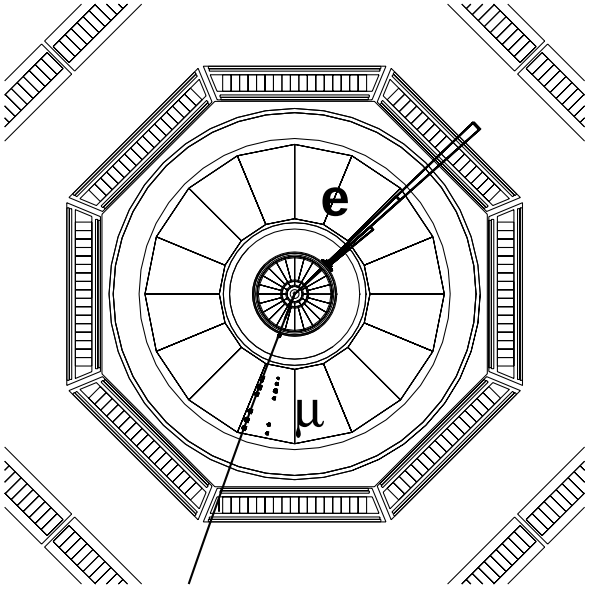

Figure 5.6: *The event was selected as $\ell\nu_\ell\ell\nu_\ell$ event. Selection criteria are quoted in the text.*

The selection is then optimised for a MC where those phase space cuts are applied and quoted efficiencies and expected signal events always refer to these phase space cuts.
On detector level one can distinguish the classes with two identified leptons (e/μ), with one identified lepton and a jet and with two jets, where the jets result from hadronic τ-decays. The leptons are identified as outlined earlier. The list of the selection cuts applied to each of the classes is listed in appendix C. Figure 5.7-a shows the distribution of the lepton energy, peaking for the signal as expected at about half the beam energy and for the background at lower energy values.
Applying all cuts one finds 54 events, 26 identified in the two-lepton class, 25 in the lepton-jet class and 3 in the two-jet class.

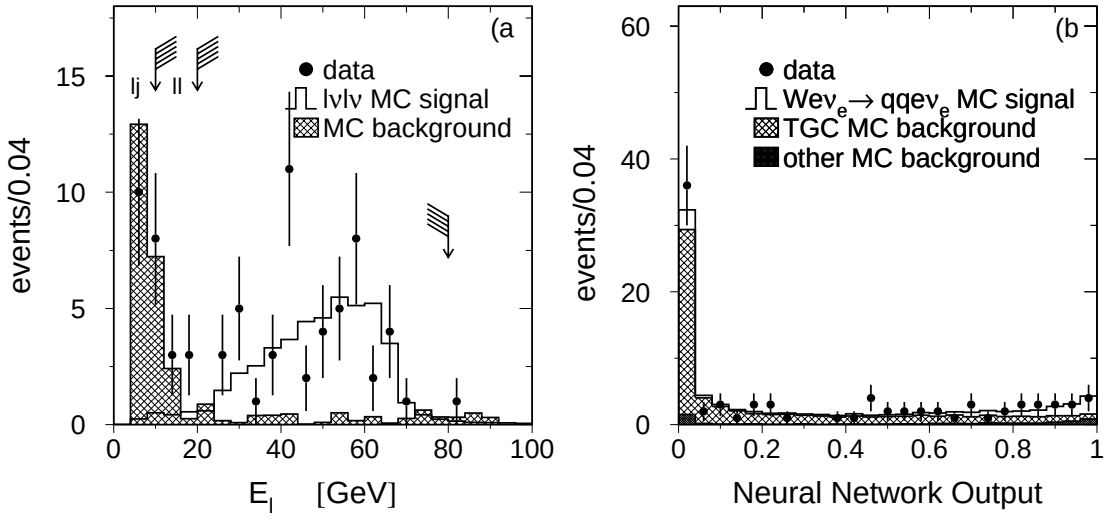

Figure 5.7: *The distribution of the lepton energy E_ℓ for the selection of* $\mathrm{W^+W^-} \to \ell\nu_\ell\ell\nu_\ell$ *(a) showing the cuts for the two-lepton (ll) and the lepton-jet (lj) configuration. The cut at high energies is the same for both classes. All other cuts are already applied. Secondly, the distribution of neural net output for single* W *production, where the* W *decays hadronically (b) after application of all cuts.*

5.2 Selection of single Ws

The production of a single W occurs via $\mathrm{W}\gamma$ fusion in the t-channel. The name single W relates to the $\mathrm{e^+}\nu_e W^-$ and $\mathrm{e^-}\bar{\nu}_e W^+$ final states. The W decays afterwards either in two quarks ($\mathrm{q\bar{q}'}$), in the following called the hadronic final state, or in leptons ($\ell\nu_\ell$), called the leptonic final state. Since the four fermion final state is strongly polluted by background diagrams one needs a strict signal definition on generator level. One requires

$$|\cos\theta_e| > 0.997 \tag{5.1}$$

and for the W side

$$\min(E_f, E_{f'}) > 15 \ \text{GeV} \tag{5.2}$$

$$|\cos\theta_e| < 0.75 \ \text{ if } \mathrm{W} \to \mathrm{e}\nu_e. \tag{5.3}$$

The selection of the single W final states at $\sqrt{s} = 183$ GeV [?, ?, ?] is discussed in the following paragraphs. The selections at other centre-of-mass energies [?, ?] are based on the same principles.

5.2.1 Hadronic final state

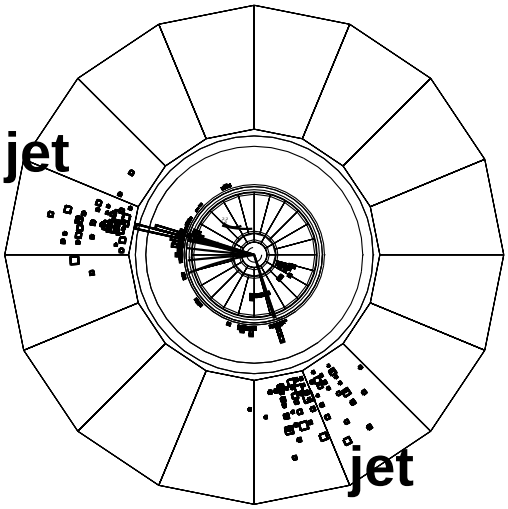

Figure 5.8: *A single* W *event where the* W *decays hadronically is characterised by two well separated jets with a high invariant mass.*

The selection of hadronic W decays focuses on the requirements of two acoplanar jets and large missing momentum. Since the final state electron goes along the beam pipe one does not allow particles identified as leptons in the detector. The two jets should have at least five charged tracks to separate against low multiplicity τ decays, and at least 10 GeV energy deposition in the electromagnetic and 60 GeV in both calorimeters. Since the jets come from the decay of a W one requires a high invariant mass of at least 40 GeV but it should also not exceed 120 GeV. The sum of energies of the ALR and the luminosity monitor should not be greater than 60 GeV. Since the high energetic neutrino leaves the detector with transverse momentum, one asks for at least 15 GeV momentum imbalance perpendicular to the beam axis. The neutrino direction should point far away from the beam axis to avoid background from qq(γ) events. So one requires that the missing momentum vector points at least 0.3 rad away from the beam axis. A list of all cuts can be found in appendix C. After all these cuts are applied one ends up with 86 events found in data, while from MC studies one expects 12 events from signal and 73 events from background. One has to apply a neural net to distinguish between these two classes. The distribution of the output of the neural network which uses the nine input variables spherocity, visible mass, ratio of missing momentum and visible energy, the sum of the masses of the jets and their maximum width when the event is forced to be a two jet event, the Durham clustering parameters y_{23} and y_{34}, the ratio of mass and energy of the third jet if the event is assumed to be a three jet event and the stereo angle of these three jets, is shown in figure 5.7-b. It can be seen , that the neural net is capable of distinguishing signal and

background. Nevertheless, cutting on the neural network output would mean to disregard a significant fraction of signal events, which ended up at low values of the NN-output. The overwhelming fraction of the background is TGC dependent. These are mostly $W^+W^- \to qq\tau\nu_\tau$ events, where the τ decay products are identified as part of the quark jets or were lost due to detector imperfections. For these reasons no further cut on the neural net output is applied. Thus the cross section as well as the TGCs (as will be discussed later) are obtained by fitting the distribution in figure 5.7-b.

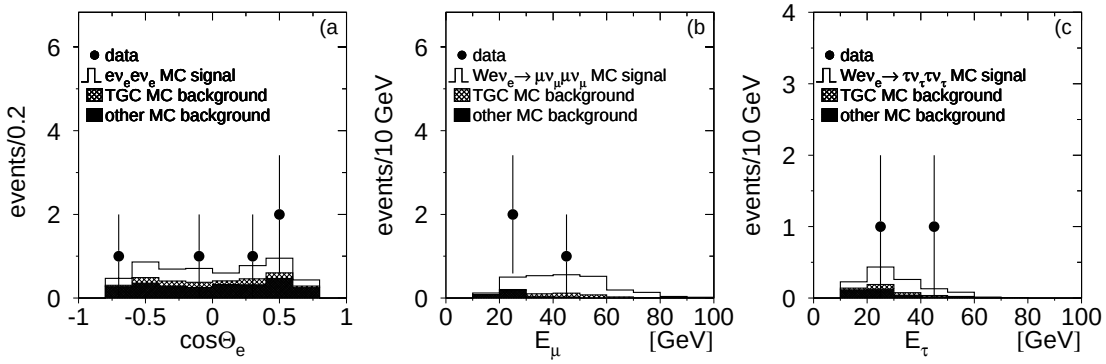

Figure 5.9: *The distribution of the polar angle of electrons from* $We\nu_e \to e\nu_e e\nu_e$ *events and the energy distribution of the* μ *or of the visible* τ*-decay products from events with* $We\nu_e$ *where the* W *decays in* $\mu\nu_\mu$ *or* $\tau\nu_\tau$*. All cuts are applied.*

5.2.2 The leptonic final state

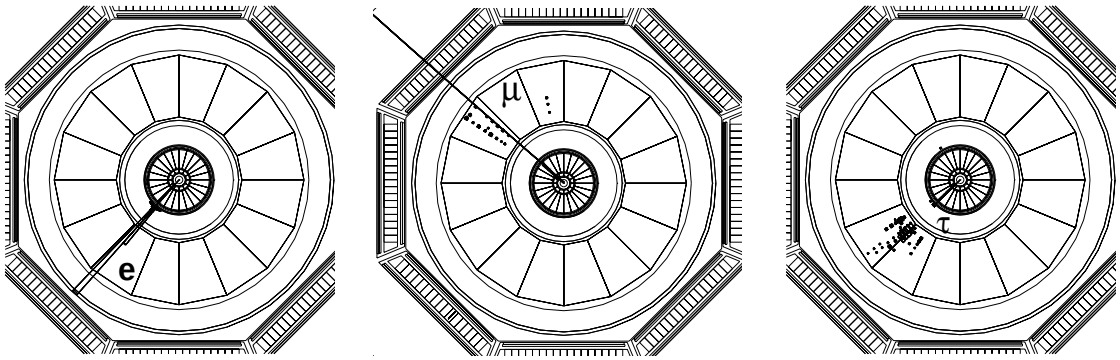

Figure 5.10: *Candidates for single* Ws *in the final states* $e\nu_e e\nu_e$*,* $\mu\nu_\mu e\nu_e$ *and* $\tau\nu_\tau e\nu_e$*.*

The selection of the leptonic W decays is based on the identification of a single highly energetic lepton in the detector. The lepton candidate is required to have at least an energy of 15 GeV. In the case it is an electron 20 GeV energy is needed. The lepton identification proceeds along the lines described earlier. Only the lepton track is allowed in the tracking chamber. The lepton must be responsible for 92 percent of the total visible energy of a selected event. A list with all cuts can be found in appendix C. Three candidate events are displayed in figure 5.10 and the distributions of electron polar angle, μ and τ energy in the 183 GeVdata are shown in figure 5.9. The electron polar angle has a flat distribution and one finds good agreement between MC prediction and data. The lepton energies peak as expected at about half of the W mass. The number of selected events in data and MC agree.

5.3 Selection of $\nu\bar{\nu}\gamma(\gamma)$ events

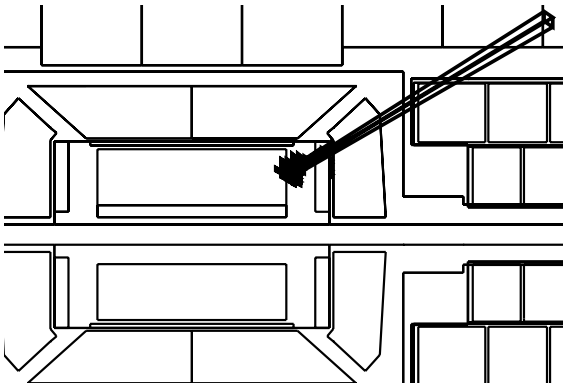

Figure 5.11: *A single photon event leaves a high energy deposition in the electromagnetic calorimeter. None of the other detector components show any response.*

$\nu\bar{\nu}\gamma(\gamma)$ events are only visible due to the identification of photons. A photon in the detector is identified by its electromagnetic shower in the BGO with no associated track. The track criterion is the only one distinguishing the photon from an electron. The energy deposition in the BGO should exceed 1 GeV while the energy seen by the HCAL due to possible energy leakage is required to be less than 20 GeV. Also the energy in forward direction, seen by the luminosity monitor (ALR) is expected to be less than 20 GeV(10 GeV), to suppress Bhabha background. Cosmics background is rejected by the requirements of at least one scintillator hit within 5 ns after the beam crossing and the absence of muons in the muon chamber. To account for photon conversion into two electrons, one allows apart from a single identified photon also for events with two tracks, which are found very close together in the tracking chamber ($\Delta\phi \leq 0.2$ rad). The

list with all applied selection cuts can be found in appendix C. The photon energy spectrum can be seen in figure 5.12. The radiative return peak, where the s-channel Z^0 exchange goes through its resonance is clearly visible. The agreement between MC simulation and data is excellent. The selection for the data collected at 183 GeV [?, ?] is identical to those at 161 and 172 GeV [?, ?].

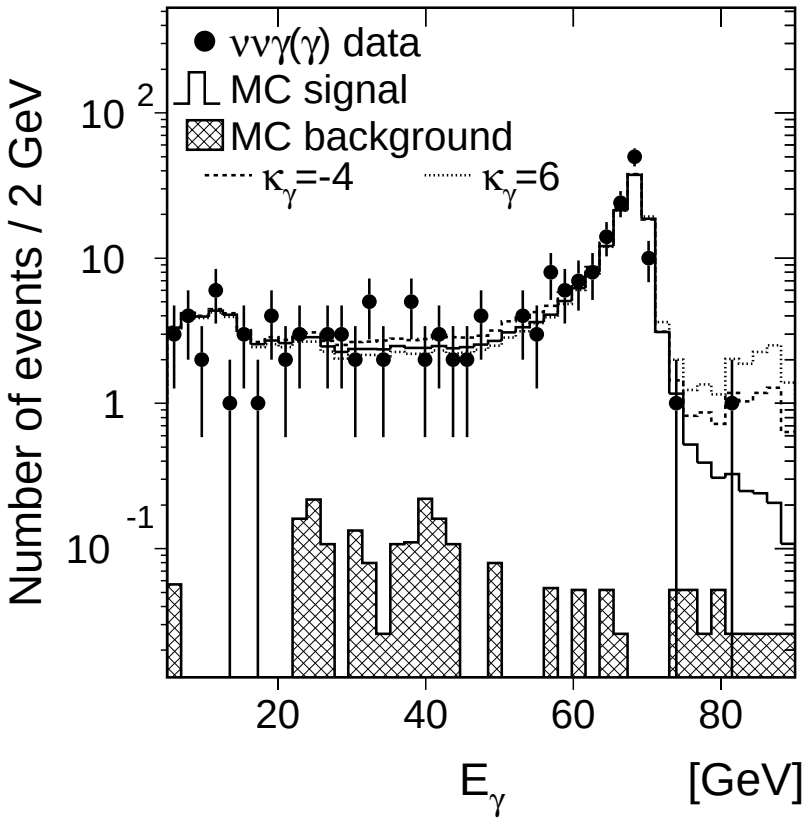

Figure 5.12: *The energy spectrum of single photon events peaks at the radiative return energy, where the s-channel Z^0 decay into two neutrinos has its resonance. Predictions of alternative coupling models (κ_γ=-4,+6) are displayed next to the SM prediction.*

5.4 Summary of selections

The results of the selections which where outlined in the last sections are condensed in table 5.1. The selection cuts are summarised in appendix C.

Process/Energy	ϵ [%]	N_{bg}	N_{data}	ϵ [%]	N_{bg}	N_{data}	ϵ [%]	N_{bg}	N_{data}
	183 GeV			172 GeV			161 GeV		
$\ell\nu_\ell\ell\nu_\ell$	55.8	9.7	54	45.1	0.6	19	39.8	0.4	2
$\mathrm{qqe}\nu_e$	85.4	6.7	112	79.3	0.4	9	76.3	0.2	4
$\mathrm{qq}\mu\nu_\mu$	77.0	5.7	108	74.1	2.1	12	66.0	0.2	4
$\mathrm{qq}\tau\nu_\tau$	50.1	10.6	77	46.6	0.3	9	37.5	1.6	3
qqqq	87.5	81.2	473	84.1	12.6	61	[1]	[1]	8.9[1]
$\mathrm{e}\nu_e(\mathrm{W}\to\mathrm{qq})$	62.5	72.6	86	55.2	10.1	15	49.5	5.5	7
$\mathrm{e}\nu_e(\mathrm{W}\to\ell\nu_\ell)$	53.8	3.1	10	55.1	0.4	1	49.5	0.4	1
$\nu\bar{\nu}\gamma(\gamma)$	197.3[2]	2.1	198	44.4[2]	0.3	52	53.7[2]	0.6	59

Table 5.1: *Selection efficiency, background expectation and number of selected data events for the centre-of-mass energies of 161, 172 and 183 GeV.*

All described selections show good agreement between MC description and selected data events. Since the data-MC comparison is done on the basis of MC samples generated at SM values of the couplings, the good agreement is a sign that the TGC values that are realised in nature do not largely differ from their SM expectations. The results of the computation of the W pair and single W cross sections from values displayed in table 5.1 are presented in figures 5.13 and 5.14. The W pair cross section expectations for the SM, for the absence of the ZWW vertex (g_1^Z=0, κ_γ=0) and the absence of ZWW and γWW vertex (g_1^Z=0, κ_Z=0, g_1^γ=0, κ_γ=0) are shown next the measured cross section. These extreme coupling models are already excluded from the total cross section measurement as displayed in figure 5.14. The same accounts for the single W cross section. Figure 5.13 reveals that this measurement favours strongly the SM values of κ_γ. The sensitivity to λ_γ is not as high. After these first qualitative statements about TGCs as inferred from the total cross section measurement, in the next chapter it will be discussed how the phase

[1] The hadronic WW cross section at 161 GeV is measured by a fit to the neural network output.

[2] The efficiency depends very strongly on the chosen phase space cuts, such that quoting the number of expected events is more meaningful

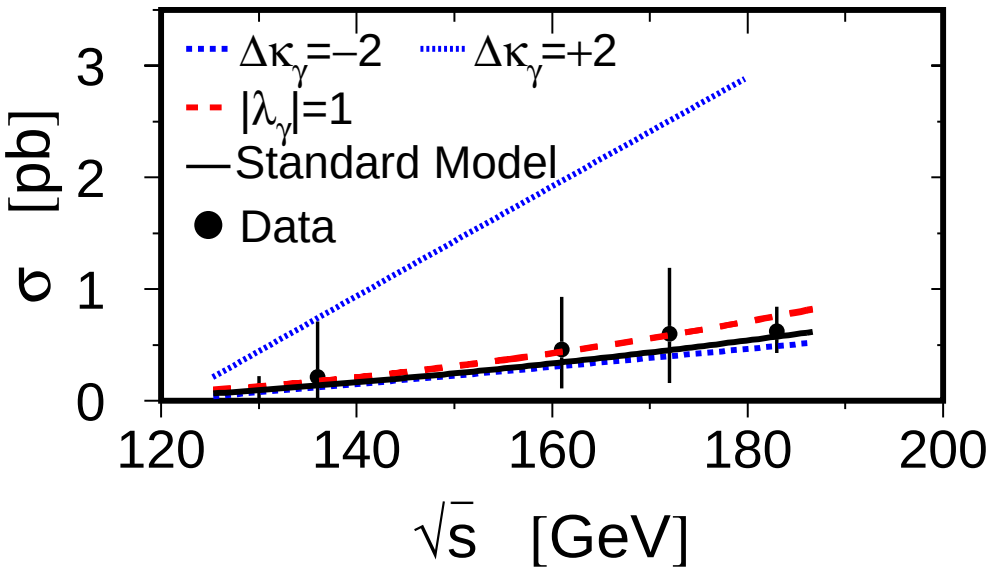

Figure 5.13: *The single* W *cross section was measured at centre-of-mass energies between 130 and 183 GeV [?, ?].*

space of the data events can be exploited to extract more detailed information about TGCs.

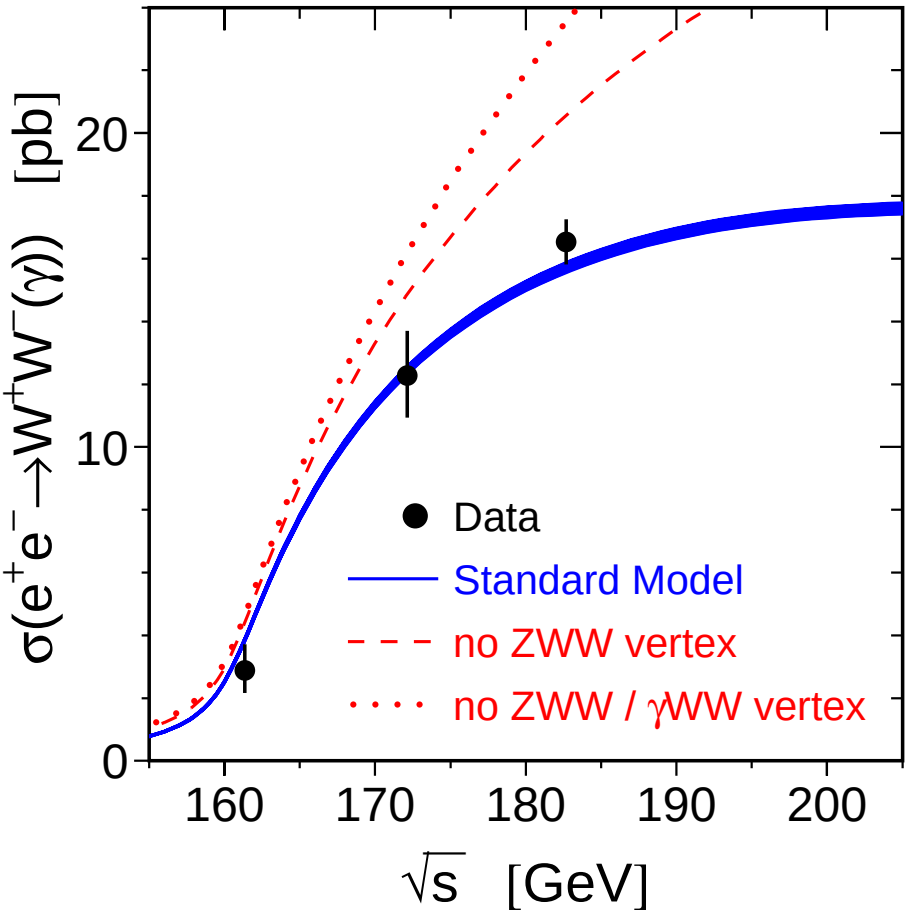

Figure 5.14: *The W pair cross section as measured at 161, 172 and 183 GeV [?, ?, ?]. This measurement already excludes models in which no* Z^0WW *or* γWW *vertex is realised. The thickness of the SM line indicates the theoretical error of the cross section prediction.*

Nothing is impossible for the man who doesn't have to do the work.
Weiler's Law

VI

From selected events to physics parameters

The coupling measurement involves two things; the measurement of the total cross section as described in the last chapter and the analysis of differential and total cross sections with respect to couplings which will be discussed in the following. The wish to extract physics parameters from differential cross sections, results immediately in the question which distributions are the most sensitive ones and how much of the available information do they contain. This question will be addressed in the first section. The second section addresses shortly the question whether one can find distributions, that can display the data in a model- and detector independent way, conserving their information are conserved for later analysis. Hereafter the more technical aspects of how changes in the TGCs can be propagated most efficiently into changes of differential cross sections and on which basis the differential cross sections found in data can be compared to the TGC-dependent predictions, are addressed. The fit results for several combinations of TGCs are presented in section 6.5, followed by a comparison with fit results of an alternative method. The limitations of the fit method are discussed in terms of systematic errors in section 6.7.

6.1 Choice of observables

The event reconstruction yields typically energies and directions of the final state particles. However, the nature of the interaction correlates some of them. In W pair events the number of independent observables is reduced from 16 to five as is displayed in table 6.1. Thus at maximum five independent observables can be

four four-momentum vectors	4×4
four-momentum conservation	$-\ 4$
masses of final state fermions	$-\ 4$
W masses	$-\ 2$
azimuthal independence	$-\ 1$
number of independent parameters	$=\ 5$

Table 6.1: *The number of independent variables in* W *pair events*

identified in the case of the coupling measurement in W pair events. In section 2.6 it was discussed extensively, that linearly independent linear-combinations of the TGCs, as displayed in table 2.2, are multipliers of the contributions from the different helicity combinations of the two Ws. Thus the five variables have to be chosen such, that they separate best between those helicity combinations. From figure 2.5 it was concluded that the two decay angles, $\cos\theta^*$ and ϕ^*, of each W, are excellent W polarisation analysers. A polarisation analysis is not only possible due to the W decay, but also at the production, as is displayed in figure 2.7. Since the Ws are produced back-to-back, their production is characterised only by the forward-backward asymmetry of the W^-, $\cos\theta_{\mathrm{W}}$ and by ϕ_{W}. However, at LEP physics is independent from the azimuth angle, such that only $\cos\theta_{\mathrm{W}}$ is a useful observable. Thus the idea to separate the W helicity states, delivered, not surprisingly, five independent observables. Although this is the case for all W pair decays the unambiguous measurement of all five observables is not possible for W pair events. In the case of hadronic W pair decays the W^- direction is identified via the jet charge method (see figure 4.15-b). Both sets of W decay angles have a twofold ambiguity. Therefore only $\cos\theta_{\mathrm{W}}$ is used in the coupling measurement in the qqqq channel. The distribution is shown in figure 6.1-a for the 183 GeV data set, showing good agreement between data and MC prediction. Next to the

SM prediction, predictions for g_1^Z of zero and two are displayed, demonstrating the coupling sensitivity of this variable. Wrong assignment of the W charge, moves an event from $\cos\theta_{\mathrm{W}}$ to $-\cos\theta_{\mathrm{W}}$. Thus the slightly increasing cross section at $\cos\theta_{\mathrm{W}} = -1$, completely different from the expected theoretical distribution as displayed in figure 2.8, results from events with $\cos\theta_{\mathrm{W}} \approx 1$. Therefore an excellent W charge determination is crucial for measuring TGCs in hadronic W pair events [**?**]. As outlined in section 4.4.5 the W^- direction can only be identified with a twofold ambiguity in $\ell\nu_\ell\ell\nu_\ell$ events. Thus $\ell\nu_\ell\ell\nu_\ell$ events have two entries of weight 0.5 in the distribution of $\cos\theta_w$ as visualised in figure 6.1-b. The loss in TGC sensitivity due to the ambiguity is clearly visible, *e.g.* by comparison with figure 6.1-a. Data and MC expectation agree well.

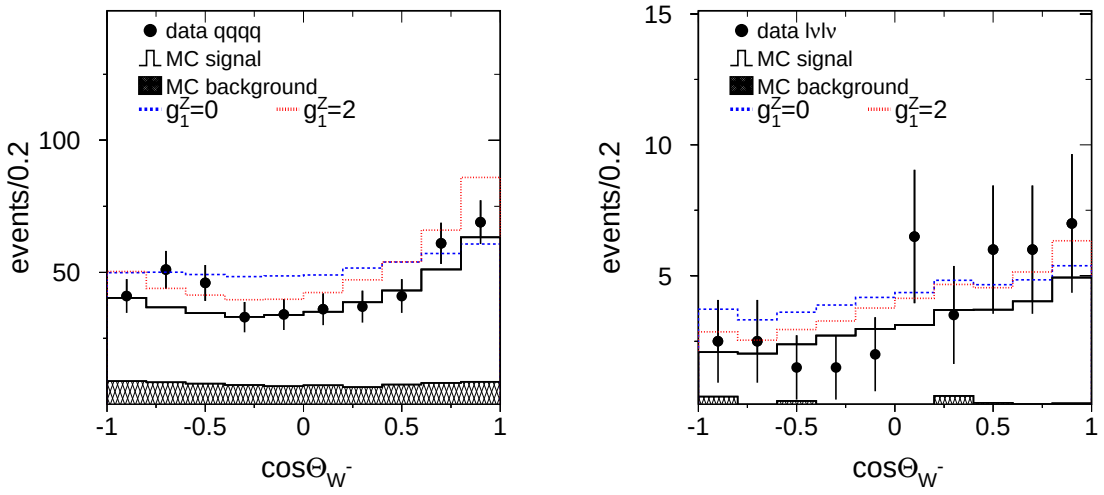

Figure 6.1: *The phase space variables which are used for the coupling fit of hadronic and leptonic* W *pair events are compared to coupling models where* g_1^Z *equals zero or two. Each leptonic event enters twice in the distribution (with weight 0.5), reflecting the twofold ambiguity of the* $\cos\theta_{\mathrm{W}}$ *reconstruction in* $\ell\nu_\ell\ell\nu_\ell$ *events.*

The most complete reconstruction can be undergone in the case of semileptonic W pair decays where one can identify easily the W^- direction and the W^- or W^+ decay angles. However, since the quarks cannot be distinguished (c.f. figure 4.13) from the anti-quarks, the decay angle of the other W can only be identified with a twofold ambiguity. Thus a reduced set of observables, namely $\cos\theta_{\mathrm{W}}$, $\cos\theta_\ell^*$, ϕ_ℓ^*, is used for $\mathrm{qq}\ell\nu_\ell$ events, since the inclusion of the of the W decay angles from the hadronic side

has only negligible impact on the result. The one-dimensional projections of this three-dimensional phase space for data collected at $\sqrt{s} = 183$ GeV are displayed in figure 6.2. The distributions of the MC predictions agree very well with the one from the data. The coupling sensitivity of $\cos\theta_w$ is clearly visible, whereas the one-dimensional projections of $\cos\theta^*_\ell$ and ϕ^*_ℓ show only little sensitivity. However, the three-dimensional distributions are used in the data-MC comparison to measure couplings, as will be explained in the successive sections, thus correlation among the observables will play a crucial role. Since the three-dimensional distributions imply a large number of MC events to fill all the space in the three-dimensional phase space one tries to reduce the dimensionality without reducing the sensitivity. The method of optimal observables (OO) provides this functionality.
The base of this method is the Taylor-expansion of the differential cross section in the fit parameter. This implies that the approximate position of the fit value is known, such that an expansion around this approximate value converges rapidly.

$$\frac{d\sigma}{d\Omega}(\Omega,\omega) - \frac{d\sigma}{d\Omega}(\Omega,\omega_0) = \frac{d^2\sigma}{d\Omega d\omega}(\Omega,\omega_0)(\omega-\omega_0) + \frac{d^3\sigma}{d\Omega d\omega^2}(\Omega,\omega_0)(\omega-\omega_0)^2 + \ldots \tag{6.1}$$

In the case of the TGC estimation ω_0 is chosen to be identical to the SM expectation, thus one finds :

$$\begin{aligned}\frac{\frac{d\sigma}{d\Omega}(\Omega,\omega)}{\frac{d\sigma}{d\Omega}(\Omega,\omega_0)} - 1 &= \frac{\frac{d^2\sigma}{d\Omega d\omega}}{\frac{d\sigma}{d\Omega}}(\Omega,\omega_0)\Delta\omega + \frac{\frac{d^3\sigma}{d\Omega d\omega^2}}{\frac{d\sigma}{d\Omega}}(\Omega,\omega_0)\Delta\omega^2 + \ldots \\ &= O_1\Delta\omega + O_2\Delta\omega^2 + \ldots \quad . \end{aligned} \tag{6.2}$$

The complete phase space is now contracted into O_i. In case of the measurement of only one TGC - only O_1 and O_2 differ from zero, since the couplings enter only linearly into the Matrix element, thus quadratically in the cross section. It can be shown [?, ?] (c.f. appendix D) that for the case of one fit parameter ω two O_i are sufficient to contain the complete sensitivity of the phase space. Assuming that the observed coupling parameters are close to the SM expectation, O_2 can be omitted. This means that one can estimate the coupling constants from a one-dimensional distribution O_1 only, having approximately conserved the sensitivity of the complete phase space. Figure 6.2-d shows the O_1 distribution for g_1^Z. The coupling sensitivity is clearly visible. The data distribution is close to that from the MC with SM couplings. The OO-distributions of the couplings λ_γ, κ_γ and g_5^Z are

displayed in figure 6.4 in appendix F. Also they show good MC-data agreement. Phase space reduction is not obtained in the evaluation of multiple couplings ω_j, $(j = 1 \ldots n)$, since the expansion has at first order n elements and already the second order has in total $2n + n\,(n-1)/2$ variables to fit. Therefore the advantage of the optimal observable method, namely the reduction of the dimensionality of the phase space, reduces with the number of parameters to estimate.
In the case of single γ production one has only two observables assuming azimuthal independence, namely the photon energy E_γ and the photon polar angle $\cos\theta_\gamma$. This two-dimensional distribution is taken for the TGC measurement.
The choice of the observables in the case of single W production can be analogous to the one for the single γ channel extended by the W decay angles as polarisation analysers. For leptonic W decays non of these variables can be obtained, since only the lepton momentum is measured. The W direction and its energy can be reconstructed in hadronic W decays, however, the reconstruction of the W decay angles is only possible with a two-fold ambiguity, since a quark cannot be distinguished from the anti-quark. On the other hand it was already noted in the last chapter that separation between signal and background, which is mostly TGC dependent, is hardly achievable in the single W selection. Thus it would be desirable to use a distribution with good signal-to-background separation and containing nevertheless coupling sensitive information. Careful studies of the sensitivity of several distributions have been undertaken. The sensitivity of a variable is estimated on the basis of the power to distinguish a reweighted[1] MC sample from itself, according to

$$\chi^2 = \sum_{i=\text{bins}} \frac{(N_i(\omega) - N_i(\omega_0))^2}{N_i(\omega)} = \sum_{i=\text{bins}} \frac{(\langle w(\omega)\rangle_i - 1)^2}{\langle w(\omega)\rangle_i^2}\, N_i(\omega_0), \qquad (6.3)$$

where $w(\omega)$ is the weight factor for the coupling value ω and will be explained in detail in section 6.3. The result is displayed for the output of the neural net, already explained in section 5.2, and the W polar angle $\cos\theta_{\mathrm{W}}$ in figure 6.3-a/b. Since it was found that the neural net distribution, that was already used in the selection, is the most sensitive observable, this distribution was used to measure TGCs in the single W channel, where the W decays hadronically.
In the selection of hadronic single W events a large background from W pair events was accepted, most of them being $\mathrm{qq}\tau\nu_\tau$ events. Some of these events were also

[1] c.f. section 6.3 for explanation

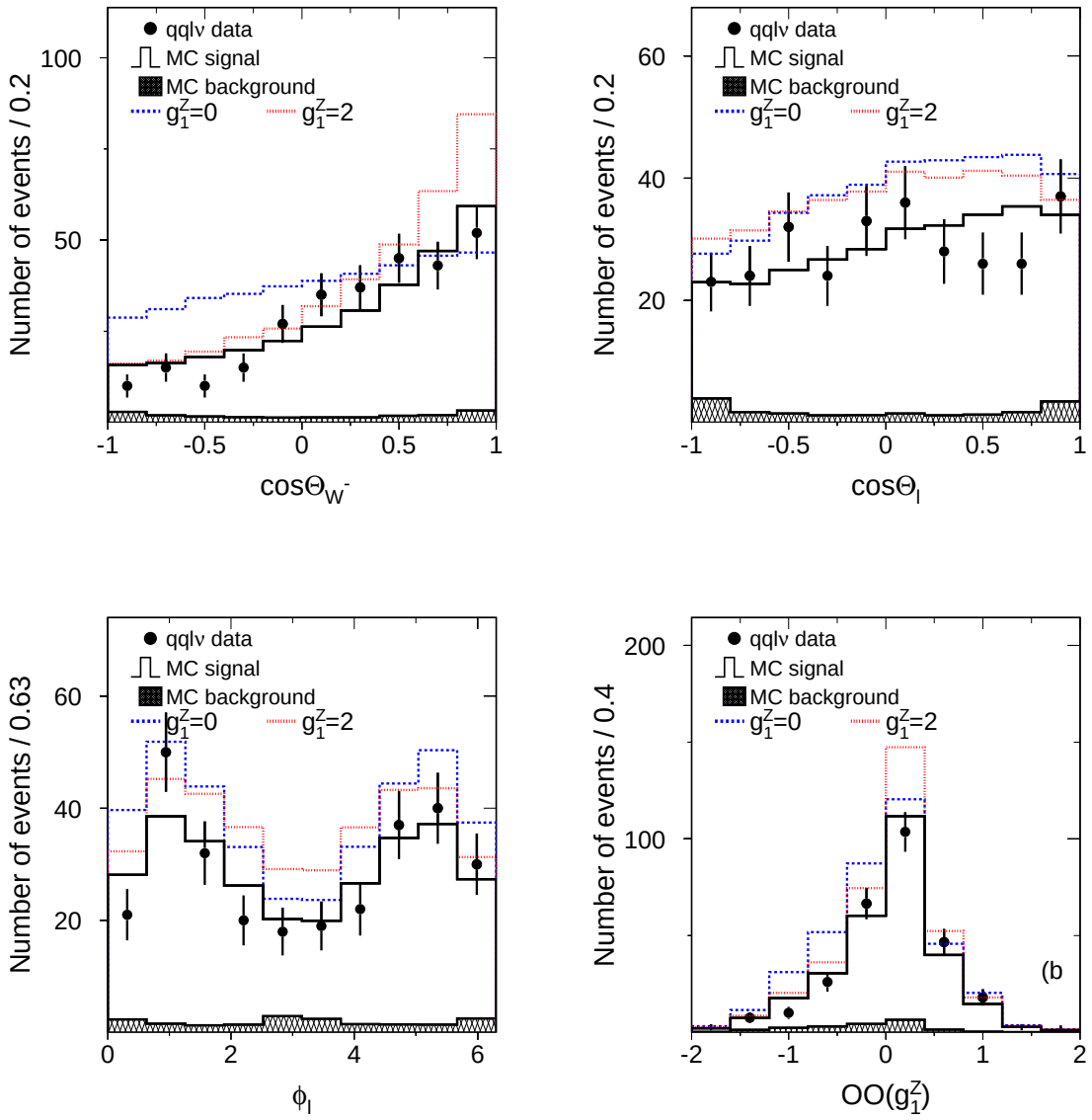

Figure 6.2: *The phase space variables which are used for the coupling fit of semileptonic* W *pair events are compared to coupling models where* g_1^Z *is equal to zero or two. For the case* $W^+ \to \ell^+\nu$ *the value of* ϕ_l *is shifted by* π *to be able to present* W^+ *and* W^- *in the same plot.* $OO(g_1^Z)$ *is the optimal observable* $\mathcal{O}_1$ *with respect to the coupling* g_1^Z*, the optimal observables for* κ_γ*,* λ_γ *and* g_5^Z *are displayed in figure 6.4 in appendix F.*

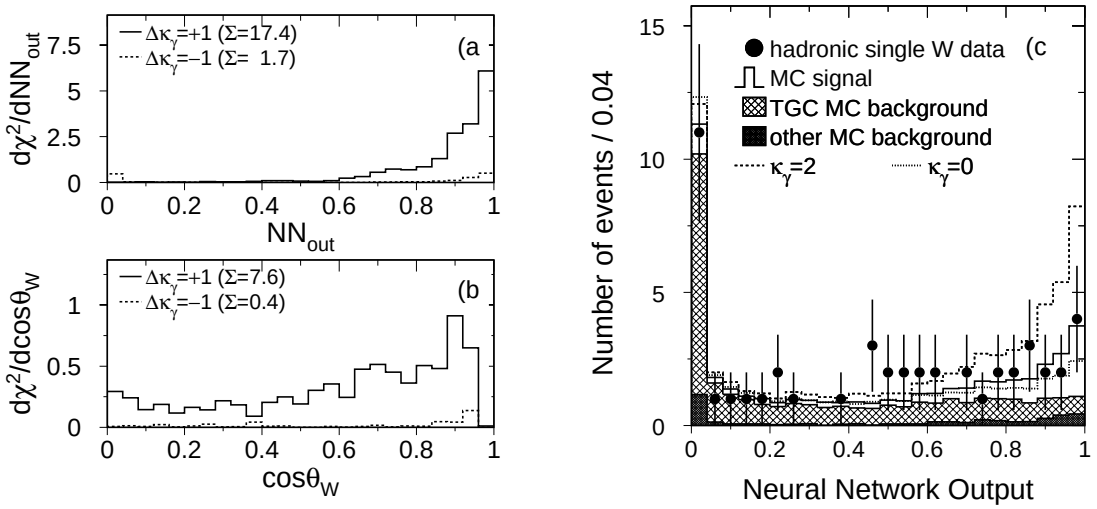

Figure 6.3: *The estimation of the sensitivity of a variable to TGCs is important for selecting it for the fit. The sensitivity of the neural network output* NN_{out} *(a) and* $\cos\theta_{\mathrm{W}}$ *(b) in* $\mathrm{e}\nu_e(\mathrm{W} \to \mathrm{qq})$ *is shown. The sensitivity is the contribution to the total* χ^2 *by comparing a SM-MC with its reweighted distribution. The* $\mathrm{W}^+\mathrm{W}^-$ *overlap is already removed from the sample. The neural network output distribution (c) changes with respect to figure 5.7 due to overlap removal.*

selected in the dedicated W pair selections as displayed in table 6.2, thus using them in the coupling measurement of both channels would lead to a correlation, which must be respected in the combination of the measurement. A more easy treatment is the removal of the overlap, which is done on the basis of run and event numbers in data and MC.

6.2 Model independent presentation of data

Until now the data were presented either in a detector dependent or in a model dependent way. Optimal observables account only for particular coupling constants (since it is only optimal for a particular coupling) and are thus very model dependent. The same holds for the multidimensional distributions, as these distributions involve detector dependent effects and multi-dimensional distributions are not easily presentable. As the view to coupling models may change with time

$\sqrt{s}$	sample	overlap to					final sample
		qqqq	qqeν_e	qq$\mu\nu_\mu$	qq$\tau\nu_\tau$	$\ell\nu_\ell\ell\nu_\ell$	
161 GeV	7	–	–	–	–	–	7
172 GeV	15	–	1	–	3	–	11
183 GeV	86	–	2	9	27	–	48

Table 6.2: *The overlap between selected hadronic single* W*s and the* W *pair events is removed from the single* W *data and MC sample before the fit, reducing the statistics by about a factor of two.*

it is desirable to find distributions which are model and detector independent, involve no correlations and are presentable. Density matrix elements $\rho_{\lambda\lambda'}$ (DME) are thought to have this potential. They correspond to the relative contribution of a helicity state to the cross section, according to

$$\rho_{\lambda,\lambda,\bar{\lambda},\bar{\lambda}} = \frac{\frac{d\,\sigma}{d\,\cos\theta}(\mathrm{e^+e^-} \to \mathrm{W^+_\lambda W^-_{\bar{\lambda}}})}{\frac{d\,\sigma}{d\,\cos\theta}(\mathrm{e^+e^-} \to \mathrm{W^+W^-})} \tag{6.4}$$

for the $\mathrm{W^+W^-}$ helicity state $\lambda\bar{\lambda}$. Interference terms between W pair helicity states have also to be considered, as was already displayed in equation 2.37. If only the helicity of one W can be analysed the 81 W pair DMEs reduce to 2×9 single $\mathrm{W^\pm}$ DMEs

$$\rho^{\mathrm{W^-}}_{\lambda\lambda'} = \sum_{\bar{\lambda},\bar{\lambda}'} \rho_{\lambda,\lambda',\bar{\lambda},\bar{\lambda}'} \tag{6.5}$$

However, the DMEs are constructed in a way that $\rho_{\lambda\lambda'} = \rho_{\lambda'\,\lambda}$, thus reducing the number of independent DMEs to 2×6. Additional constrains are involved if CPT invariance

$$\rho^{\mathrm{W^-}}_{\lambda\lambda'} = (\rho^{\mathrm{W^+}}_{-\lambda\,-\lambda'})^* \tag{6.6}$$

and CP-conservation

$$\rho^{\mathrm{W^-}}_{\lambda\lambda'} = \rho^{\mathrm{W^+}}_{-\lambda\,-\lambda'} \tag{6.7}$$

are required, reducing the number of independent DMEs to six. While the off-diagonal DMEs have real and imaginary parts, the diagonal one have only real

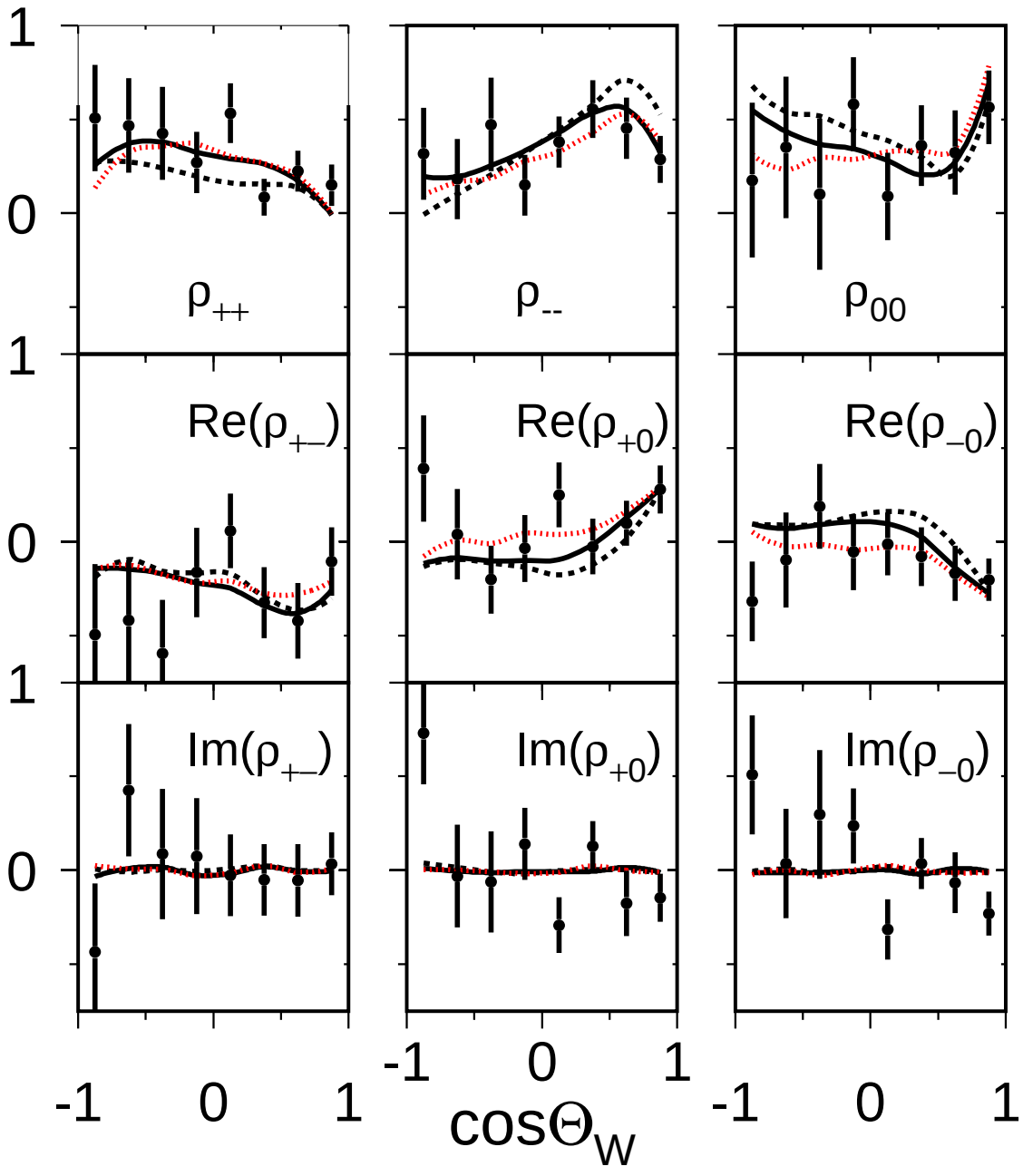

Figure 6.4: *The spin density matrices of the* W *compared to the SM-MC expectation (solid line) and to the of coupling values of* $\Delta g_1^Z = (-1, +1)$ *(dashed,dotted). The matrices are computed on detector level, with the background contribution statistically removed from the data(see figure 6.5 and the text for explanation).*

parts, as they result from a squared matrix element. Thus the complete helicity decomposition is displayed in form of nine (six real + three imaginary) observables. The DMEs must be projected from the measured data. For this the orthogonality of the decay amplitudes, as displayed in equation 2.36, is used, to construct projection operators $\Lambda_{\lambda\lambda'}(\theta_\ell, \phi_\ell)$, such that

$$\rho_{\lambda\lambda'}\frac{d\sigma}{d\cos\theta_W} = \frac{1}{B(\mathrm{W^+W^-} \to \mathrm{qq}\ell\nu_\ell)}\int \frac{d\sigma(\mathrm{W^+W^-} \to \mathrm{qq}\ell\nu_\ell)}{d\cos\theta_\mathrm{W} d\cos\theta_\ell d\phi_\ell}\Lambda_{\lambda\lambda'}(\theta_\ell, \phi_\ell) d\cos\theta_\ell d\phi_\ell. \tag{6.8}$$

A set of normalised projection operators are computed [?] from equations 2.36 and 2.37

$$\Lambda^{\mathrm{W^+}}_{\mp\mp} = \Lambda^{\mathrm{W^-}}_{\pm\pm} = \frac{1}{2}(5\cos^2\theta_\ell \mp 2\cos\theta_\ell - 1) \tag{6.9}$$

$$\Lambda^{\mathrm{W^+}}_{00} = \Lambda^{\mathrm{W^-}}_{00} = 2 - 5\cos^2\theta_\ell \tag{6.10}$$

$$\Lambda^{\mathrm{W^+}}_{+-} = \Lambda^{\mathrm{W^-}}_{+-} = 2\exp[-2i\phi_\ell] \tag{6.11}$$

$$\left(\Lambda^{W^+}_{\mp 0}\right)^* = -\Lambda^{W^-}_{\pm 0} = \frac{8}{3\pi\sqrt{2}}(1 \mp 4\cos\theta_\ell)\exp[\mp i\phi_\ell]. \tag{6.12}$$

Since the DMEs parametrise the contributions of several helicity states and the couplings modify the contributions of those as was discussed in the last section, deviations in the DMEs give a hint of physics beyond the ones described by the SM. The density matrix elements (DME) $\rho_{\lambda\lambda'}$ as computed from data taken at $\sqrt{s} =$ 183 GeV are shown in figure 6.4. They are compared to a computation of DMEs from MC and good agreement is found. The subtraction of the background from the data has almost no effect on the distribution as the background contribution after the selection of semileptonic W pair events is very small.

The computation uses the angular information as found on detector level. This means the detector resolution and its imperfections are included in this distribution of the DMEs. Unfolding of detector effects either on the level of the angles or on the level of DMEs introduces correlations among different bins of the distributions, thus the complete detector independent information is only obtained if in addition to the GL-DME distributions also their correlation matrices are given. If instead of complete unfolding a bin-wise correction of the data distribution is intended, thus the correlation among bins is omitted, the correction factors might become large, as can be seen in figure 6.5. While for ρ_{++} the correction factor varies only between 0.8 and 1.5, thus DL values correspond almost to GL values of the DME, the

correction factors for Im(ρ_{-0}) becomes as large as 13, thus large corrections have to be applied. Such large corrections are not acceptable, especially in distributions that scatter around zero.
This means that DMEs do not fulfil the goal of presenting the data in an easy (one-dimensional and detector independent) way, but are only useful if apart from the nine simple GL-DME distributions the complete set of nine correlation matrices are supplied.

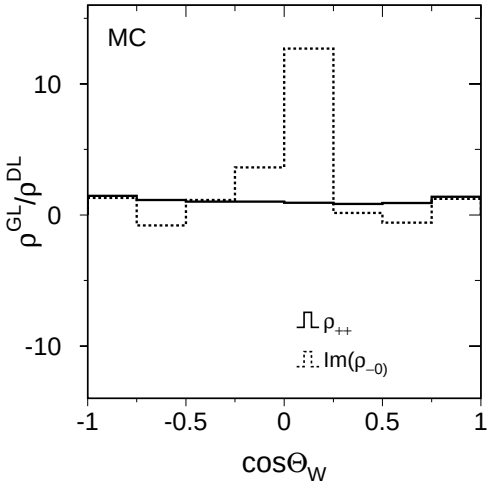

Figure 6.5: *One possibility of correction of detector effects is the bin-wise correction of the distributions. For DMEs large correction factors for the elements ρ_{+-}, ρ_{+0} and ρ_{-0} are found, while for ρ_{++}, ρ_{--} and ρ_{00} the correction factor is flat and close to one.*

6.3 Theory prediction

The measurement of the TGCs is the comparison of the (multi-dimensional) distributions of the discussed coupling sensitive observables of theory and data. Theory in this respect means MC event distributions. Finding the best matching distribution, would thus imply to generate MC samples at various TGC values. Since full MC event simulations are very resource-consuming (time, computer power) it is, from the technical point of view, not the favoured solution. The reweighting mechanism instead uses only one MC sample - the baseline MC - which is generated at a particular choice of the physics parameter values ω_{MC}, such as the SM (*e.g.*

$\omega_{MC} = g_1^Z = 1$). The other samples are constructed by giving each event from the baseline MC a weight w_i, corresponding to the ratio of the probabilities P_i, that a particular event occurs at ω_{MC} or at different values ω (*e.g.* $\omega = g_1^Z \neq 1$))

$$w_i = \frac{P_i(\omega)}{P_i(\omega_{MC})}. \tag{6.13}$$

Thus the weight w_i of an event specifies how much more or less probable it is to find this event at ω than at ω_{MC}.
This weight factor can now be used in a MC-method to produce a sample which is consistent with ω using the weights w_i to accept or reject events generated at ω_{MC}. The distributions can then be compared to data to extract the parameter value set that is best suitable to describe the data. The probability P_i is the normalised differential cross section at the phase space point Ω_i where the MC event was generated

$$P_i(\omega) = \frac{1}{\sigma(\omega)} \frac{d\sigma}{d\Omega}(\Omega_i, \omega). \tag{6.14}$$

The differential cross section can be split into the matrix element $\mathcal{M}(\Omega_i^{GL}, \omega)$ and the phase space part $\Xi(\Omega)$, which is independent of the TGCs (c.f. equation 2.37). The weight definition can thus be written as

$$w_i(\Omega_j^{GL}, \omega) = \frac{|\mathcal{M}|^2(\Omega_i^{GL}, \omega)}{|\mathcal{M}|^2(\Omega_i^{GL}, \omega_{MC})}, \tag{6.15}$$

where GL denotes the fact that the matrix element is computed from the generator level phase space, including *e.g.* effects of initial and final state radiation. The weight distribution for the reweighting of a qqeν_e MC sample, selected in the $W^+W^- \to$ qqeν_e selection, from only considering W pair production (CC03) to considering all relevant processes (c.f. figure 2.10) is shown in figure 6.6-a. The weights are all close to one, thus the differential cross sections are not strongly changed due to the inclusion of the additional processes. In addition the events are reweighted to $\Delta g_1^Z = 0.5$. The $\cos\theta_W$ distribution of the weights is visualised in figure 6.6-b. A clear $\cos\theta_W$ dependence of the average weight is observable, manifest of the fact that the $\cos\theta_W$ distribution becomes steeper with increasing Δg_1^Z. The averaged weight is also displayed for the case of selected $\nu\bar{\nu}\gamma(\gamma)$ events in figures 6.6-c and 6.6-d. The coupling sensitivity of E_γ is clearly visible, whereas $\cos\theta_\gamma$ shows only little sensitivity.

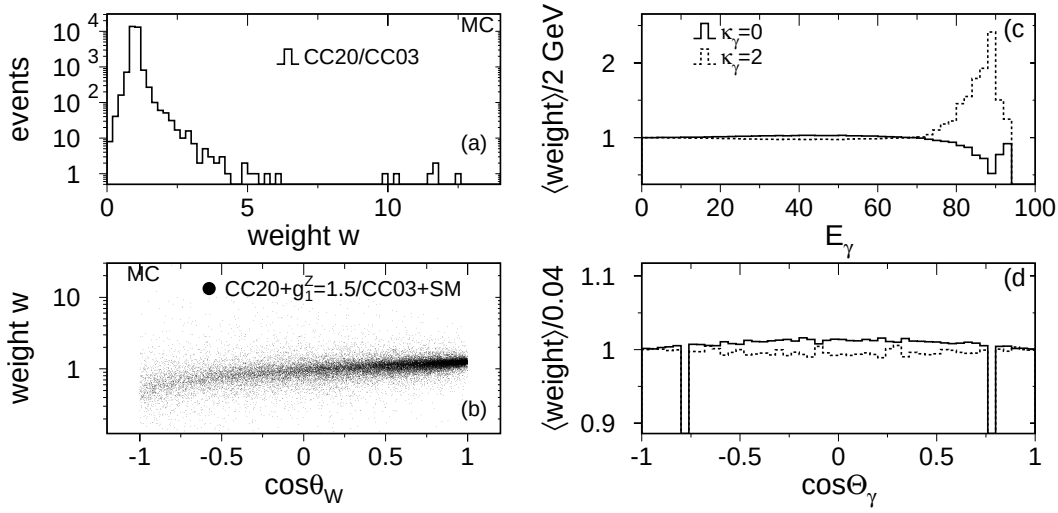

Figure 6.6: *Weights to reach a) CC20 from a CC03 baseline for the* $\mathrm{qqe}\nu_e$ *sample , b) a* $\cos\theta_{\mathrm{W}}$ *distribution corresponding to a coupling value of* g_1^Z *=1.5 for* $\mathrm{qqe}\nu_e$ *MC events, c) the photon energy and d) the* $\cos\theta_\gamma$ *distribution corresponding to* $\kappa_\gamma = 0, 2$*. The weights are computed for selected* $\mathrm{qqe}\nu_e$ *and* $\nu\bar{\nu}\gamma(\gamma)$ *events.*

Disadvantages of the event reweighting come into play if ω_{MC} and ω are largely different. Phase space regions which are poorly populated at ω_{MC} start to become important, resulting in large weights for the baseline events. However, the MC statistics error is given by the number of events in this region and is thus large. This property of the reweighting procedure is visualised in figure 6.7, showing the number of effective MC events

$$N_{\mathrm{MC}}^{\mathrm{eff}} = \frac{(\sum_i w_i)^2}{\sum_i w_i^2}. \tag{6.16}$$

The effective number of MC events decreases quite dramatically at large values of the couplings. However, it will become clear that the effect is not as dramatic, as coupling values found in data are close to zero having also a relatively small error, such that the variation of $N_{\mathrm{MC}}^{\mathrm{eff}}$ in the region of interest is less than ten percent. An almost flat distribution of the number of effective MC events can be obtained, if several baseline MCs at different values of TGCs are considered or if a sample is generated which contains events at critical regions of the phase space. The second method is applied for the $\nu\bar{\nu}\gamma(\gamma)$ baseline, where a sample of events

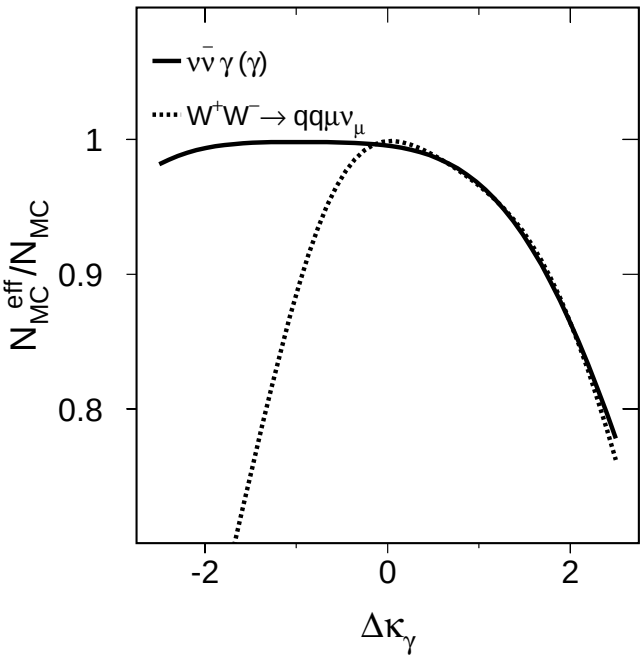

Figure 6.7: *The effective number of MC events for the reweighting of* $\nu\bar{\nu}\gamma(\gamma)$ *and* $W^+W^- \to qqe\nu_e$ *events.*

with large photon energies (larger than the radiative return energy) is considered in addition to the SM MC sample. This allows to populate an energy region, where one finds very little events in the SM (c.f. figure 5.12), but which is very sensitive to couplings (c.f. figure 6.6-c). The importance of large numbers of effective MC baseline events will be stressed again in the next section.

The last paragraphs focused on the reweighting of single events. However, the task can be simplified by reweighting distributions [**?**]. This is particularly interesting in the case of TGCs, as the differential cross sections depend always quadratically on the couplings. Thus for changing one (four) coupling(s) three (14) MC samples need to be simulated to find a second order polynomial describing the dependence of the differential cross section on the TGCs. These polynomials can be computed with great accuracy if large amounts of MC events are considered. Since full event simulation is a resource consuming process, generator level events are used to determine the polynomials, leaving the task of propagation to the detector level (DL). The folding of the detector effects to the reweighted distribution can be

done either by smearing of the GL-distribution or more correctly by considering the matrix method, exploiting the knowledge about DL-GL interconnection from a baseline MC and its independence on the couplings.

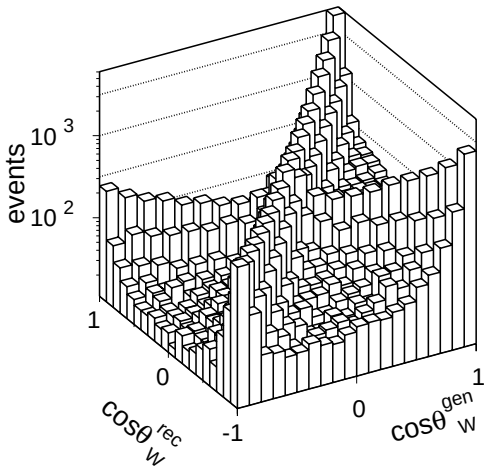

Figure 6.8: *Matrix for the conversion of observed values for* $\cos\theta_{\mathrm{W}}$ *in* qqqq *events into the true ones. The size of charge confusion can be obtained by comparing diagonal with off-diagonal bins.*

In the case of hadronic W pair events the forward backward asymmetry of the W is the coupling sensitive observable and is thus used as distribution $\mathcal{D}_{GL}(\omega)$ to be reweighted

$$\mathcal{D}_{GL}(\omega) = \mathcal{D}_{GL}(0) + \mathcal{B}\omega + \mathcal{C}\omega^2, \quad (6.17)$$

where $\mathcal{B}$ and $\mathcal{C}$ are the matrices of the polynomial coefficients. The propagation of the effect to DL is performed as

$$\mathcal{D}_{DL} = \mathcal{S}\,\mathcal{D}_{GL}, \quad (6.18)$$

where $\mathcal{S}$ denotes the propagation matrix. The matrix $\mathcal{S}$ is obtained by histogramming of GL and DL values of MC events, as displayed in figure 6.8. and normalisation according to

$$(\mathcal{S})_{ij} = \frac{(\mathcal{N})_{ij}}{\sum_i (\mathcal{N})_{ij} + N_i}, \quad (6.19)$$

where $(\mathcal{N})_{ij}$ is the number of entries in the histogram bin ij and N_i are those events which were generated in bin i but which were not selected, thus the efficiency can be expressed as

$$\epsilon = \sum_j \epsilon_j = \sum_j \sum_i (\mathcal{S})_{ij}. \quad (6.20)$$

The reweighting of distributions can easily be extended to the multi-dimensional case. However, one has to consider that the propagation matrix elements have MC statistics errors of $1/\sqrt{(\mathcal{N})_{ij}}$, assuming that $\sum_i (\mathcal{N})_{ij}$ is large. Thus a balance between bin size and bin content of the propagation matrix has to be found in such a way that good resolution on the observables and small MC statistics errors, that result in biases in the data-MC comparison, are achieved. This is especially

complicated in the case of multi-dimensional distributions, where the ideal binning in each dimension has to be chosen.
In summary the strength of the distribution reweighting is the simple reweighting polynomial, which is obtained by generating some generator level samples at different TGC values, whereas the event reweighting is more demanding since it requires the computation of the matrix element of each event at different TGC values. The strength of the event reweighting is the propagation from GL to DL, since its provides events with full phase space information, while the distribution reweighting delivers only some distributions on DL. Theses reasons suggest that event reweighting is to be preferred in the case of multi-dimensional distributions, whereas the distribution reweighting is an excellent method for one-dimensional observables. Thus event reweighting is used in the case of phase space variables and distribution reweighting in the case of optimal observables.

6.4 Principle of measurement

After the coupling sensitive observables are identified as well as methods to quickly supply MC event samples at various TGC values one task remains, namely the method on which basis MC samples and data are compared and the best fitting MC sample, *i.e.* the TGC value, is found.
Two different methods have been considered - comparing the differential cross section of predefined phase space volumes, and the box method, using the differential cross section at the data phase space point as probability estimator for having the data event at this point.
The first method is closely connected to the matrix method, as its results are differential cross section predictions at predefined phase space volumes, namely the folded bins of the reweighted MC histogram. The data are binned in the same manner as the MC. The probability to find N_i^{data} events in bin i of the distribution is expressed with Poisson probability as

$$P_i = \frac{N_i^{\mathrm{exp}\,N_i^{\mathrm{data}}}(\omega)\; e^{-N_i^{\mathrm{exp}}(\omega)}}{N_i^{\mathrm{data}}!}, \tag{6.21}$$

where N_i^{exp} is the theoretically expected number of events in bin i for a coupling value of ω. The comparison is based on the joined probability or likelihood L [**?**]

of all data events according to

$$\ln L = \sum_{i=bins} P_i = \ln L_{\text{diff}} + \ln L_{\text{tot}}\,, \tag{6.22}$$

which is split into the contribution from the normalised differential cross section and from the total cross section, according to

$$\ln L_{\text{diff}} = \sum_{i=bins} N_i^{\text{data}} \ln \frac{N_i^{\text{exp}}(\omega)}{N_{tot}^{\text{exp}}(\omega)} = \sum_{i=bins} N_i^{\text{data}} \ln \frac{(\mathcal{S}(\mathcal{D}_{GL}(0) + \mathcal{B}\omega + \mathcal{C}\omega^2))_i}{\sum_{j=\text{bins}} \epsilon_j (\mathcal{D}_{GL}(0) + \mathcal{B}\omega + \mathcal{C}\omega^2)_j} \tag{6.23}$$

and

$$\begin{aligned}\ln L_{\text{tot}} &= N_{tot}^{\text{data}} \ln N_{tot}^{\text{exp}}(\omega) - N_{tot}^{\text{exp}}(\omega) \\ &= n_{tot}^{\text{data}} \ln \left(\sum_{j=\text{bins}} \epsilon_j (\mathcal{D}_{GL}(0) + \mathcal{B}\omega + \mathcal{C}\omega^2)_j \right) - \mathcal{L} \sum_{j=\text{bins}} \epsilon_j (\mathcal{D}_{GL}(0) + \mathcal{B}\omega + \mathcal{C}\omega^2)_j,\end{aligned} \tag{6.24}$$

where the variables denoted with subscript *tot* correspond to the total sample instead as for bin i. Although, this likelihood construction goes natural together with the matrix method, event reweighting is also capable to supply the distributions, if the events are binned in the coupling sensitive observables. Reweighted events are however more flexible, and it would be more valuable to use methods that are based on this flexibility, such as the box method [**?**, **?**].
The intention in the usage of flexible methods for MC-data comparison is that no prejudices and definitions previous to the data analysis have influence on the result of the comparison and that the available MC event samples are used most efficiently in the comparison [**?**]. Starting point for the box method is the assumption that the differential cross section around the data point is well-behaved, *i.e.* no sudden peaks occur. Thus the differential cross section at any point in phase space can be obtained by interpolating the differential cross sections of neighbouring events in phase space. Thus if the expected differential cross section at the data event phase space point is the subject of interest, MC events close in phase space are collected and are used to interpolate. Its obvious by construction, that the best result can be obtained if the MC events are very close, thus the distance to interpolate is small. Therefore the density of MC events, *i.e.* their amount, must be large. After

this introduction to the box method two questions remain, how to interpolate and what means close in phase space ?
Simple averaging of the cross sections of the MC events is used to predict the cross section at the data phase space point. Real interpolation is not possible in this case, as the interpolation is not done in the full phase space but in the one of the sensitive observables. Thus one has to integrate over those components of the full phase space that are not measured, which is done by averaging the cross sections of those events only close in the observable. However, this requires that the events are well scattered around the data phase space point in all variables, thus many events that are close to the data should be used in the averaging. The assignment in the one dimensional case seems rather obvious, however the requirement of well scattering around the data event and the requirement of closest events, cannot be fulfilled both in all cases. Thus three different strategies have been considered

I. $|\cos\theta_{\mathrm{W}}^{\mathrm{MC}} - \cos\theta_{\mathrm{W}}^{\mathrm{data}}| < \Delta$

II. $N_{\mathrm{events}}(-\Delta_1 < \cos\theta_{\mathrm{W}}^{\mathrm{MC}} - \cos\theta_{\mathrm{W}}^{\mathrm{data}} < 0) = N_{\mathrm{events}}(0 < \cos\theta_{\mathrm{W}}^{\mathrm{MC}} - \cos\theta_{\mathrm{W}}^{\mathrm{data}} < \Delta_2)$

III. $\langle\cos\theta_{\mathrm{W}}^{\mathrm{MC}}\rangle \approx \cos\theta_{\mathrm{W}}^{\mathrm{data}}$.

The first one just uses the distance to the data event as criteria to select the closest events, thus all events that are closer to the data event than Δ are considered in the averaging. These are indeed the closest events, however, if the density of MC events changes with $\cos\theta_{\mathrm{W}}$ there are not equal amounts of events on the negative and one the positive side of the data event. This is the case for the second strategy. It actually requires, that these amounts are equal sacrificing the requirement of closeness, as the distances Δ_1, Δ_2 on both sides of the data event could be largely different. The third construction does in general not fulfil both requirements. However, it seems natural to request that the average of the observable in the MC events should be equal to the one of the data event, if it desired that the average of the differential cross sections of MC events is equal to that at the data phase space point. The three strategies are extendible to the multi-dimensional case. The implementation of strategy I requires the introduction of a metric in the space of the observables, for which the most natural choice are the resolutions in these observables, as displayed figure 4.15 for semileptonic W pair decays and in figure 6.9 for the polar angle in qqqq-events, leading in the three-dimensional case to

I*. $\sqrt{\frac{(\cos\theta_{\rm W}^{\rm MC}-\cos\theta_{\rm W}^{\rm data})^2}{\sigma(\cos\theta_{\rm W})^2}+\frac{(\cos\theta_\ell^{\rm MC}-\cos\theta_\ell^{\rm data})^2}{\sigma(\cos\theta_\ell)^2}+\frac{(\phi_\ell^{\rm MC}-\phi_\ell^{\rm data})^2}{\sigma(\phi_\ell)^2}}<\Delta.$

This forms an ellipsoid in the three-dimensional observable space, having half-axis that are proportional to the resolutions σ. The more easier case is to construct boxes according to strategy I, with extension Δ_i in the dimension of observable i

I** $$\begin{aligned}&|\cos\theta_{\rm W}^{\rm MC}-\cos\theta_{\rm W}^{\rm data}|<\Delta_1\\&|\cos\theta_\ell^{\rm MC}-\cos\theta_\ell^{\rm data}|<\Delta_2\\&|\phi_\ell^{\rm MC}-\phi_\ell^{\rm data}|<\Delta_3.\end{aligned}$$

The multi-dimensional case requests detailed tests of the method, since it requires that not only single detector effects but also their correlations are well described in the MC, such as angular and energy resolutions of the detector.
The predicted differential cross section in this box is

$$\frac{d\sigma}{d\Omega}=\frac{N_{MC}^{\Delta\Omega_i^{DL}}}{\mathcal{L}\Delta\Omega_i^{DL}}=\frac{\sigma_{MC}}{N_{MC}}\frac{N_{MC}^{\Delta\Omega_i^{DL}}}{\Delta\Omega_i^{DL}}, \tag{6.25}$$

where N_{MC} and σ_{MC} are the number of events and the total cross section of the selected MC sample and $N_{MC}^{\Delta\Omega_i^{DL}}$ is the number of selected events in the DL-phase space volume $\Delta\Omega_i^{DL}$ which is assigned to the data event i. The number of events in the box is changed due to the reweighting procedure to

$$N_{MC}^{\Delta\Omega_i^{DL}}\rightarrow\sum_{j\epsilon\Delta\Omega_i^{DL}}w_j(\Omega_j^{GL},\omega). \tag{6.26}$$

Therefore the probability to find the data event i at its phase space point is according to equation 6.14

$$P_i(\omega)=\frac{1}{\sum_{j=\rm all}w_j(\Omega_j^{GL},\omega)}\,\frac{1}{\Delta\Omega_i^{DL}}\sum_{j\epsilon\Delta\Omega_i^{DL}}w_j(\Omega_j^{GL},\omega), \tag{6.27}$$

where the total cross section is obtained due to reweighting of all selected MC events. Thus the likelihood $L=\prod_i P_i(\omega)$ is maximised ($-\ln L$ is minimised) with respect to ω to find the best description of the data. This definition of the likelihood does only exploit the differential distribution of the data events. In the case that also the total number of expected events depends on TGCs the likelihood is completed by the likelihood of the total cross section measurement,

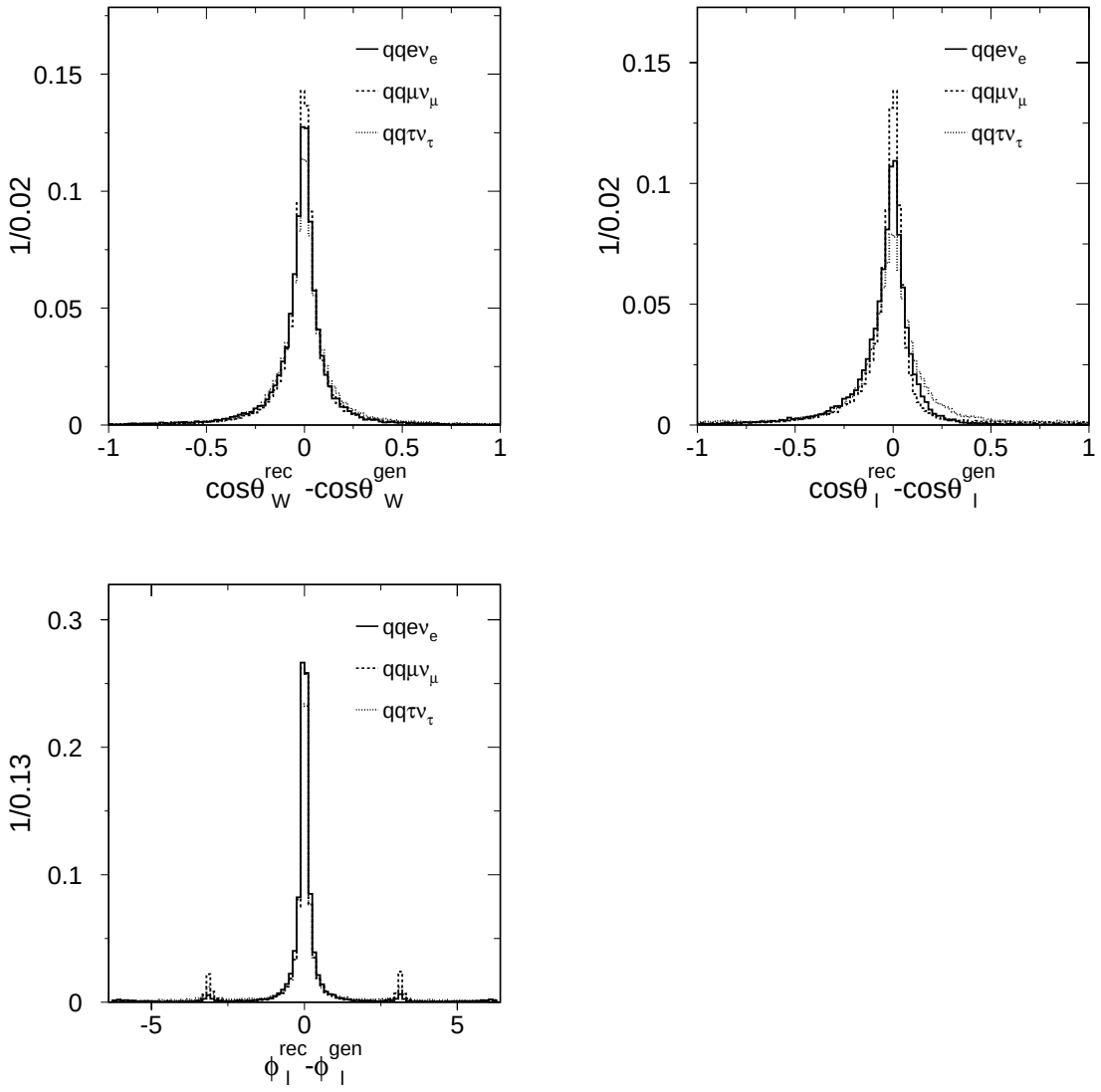

Figure 6.9: *Resolution of* $\cos\theta_{\mathrm{W}}$, $\cos\theta_\ell$ *and* ϕ_ℓ *in* $\mathrm{qqe}\nu_e$, $\mathrm{qq}\mu\nu_\mu$ *and* $\mathrm{qq}\tau\nu_\tau$ *-events. The resolutions of the phase space variables are best for* $\mathrm{qq}\mu\nu_\mu$*-events.*

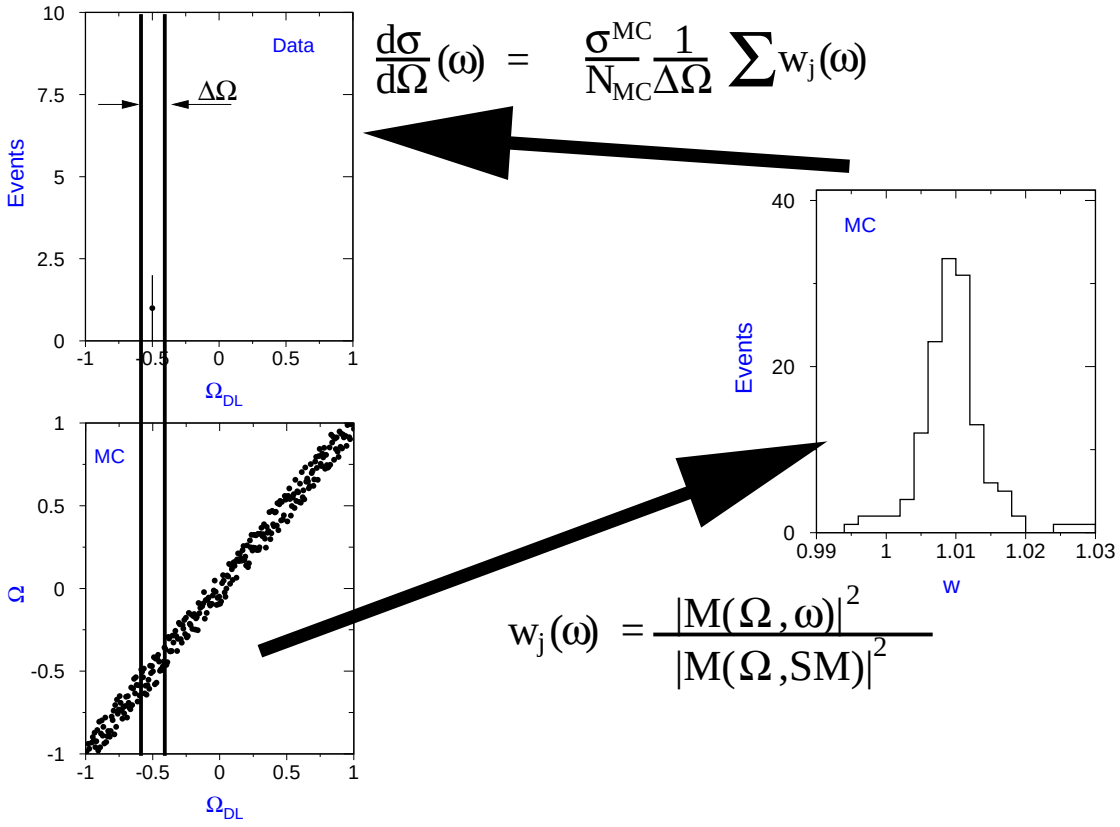

Figure 6.10: *The analysis consists of reweighting of MC events and comparison of differential cross sections between data and MC.*

using equation 6.21. The number of expected events is computed by reweighting of the complete MC sample. The total (extended) log-likelihood has the form

$$-\ln L = -\sum_{i=1}^{N_{\text{data}}} \ln\left\{ \frac{1}{\Delta\Omega_i^{DL}} \sum_{j}^{j\epsilon\Delta\Omega_i^{DL}} \frac{|\mathcal{M}|^2(\Omega_j^{GL},\omega)}{|\mathcal{M}|^2(\Omega_j^{GL},\omega_{MC})} \right\} + \sum_{j=\text{all}} \frac{|\mathcal{M}|^2(\Omega_j^{GL},\omega)}{|\mathcal{M}|^2(\Omega_j^{GL},\omega_{MC})}. \tag{6.28}$$

After the discussion of the complete analysis chain, which is pictured in figure 6.10, the box method is now applied to data.

6.5 Measuring the couplings

The dependence of the likelihood on the TGCs is computed for each channel according to equation 6.28 taking total and differential cross section terms into account. Ten coupling models have been selected for the measurement. These are the evaluation of g_1^Z, κ_γ, λ_γ, and g_5^Z taking the constraints coming from $SU(2) \times U(1)$

$$\Delta\kappa_\gamma = \frac{\cos^2\theta_w}{\sin^2\theta_w}(\Delta\kappa_Z - \Delta g_1^Z) \quad \text{and} \tag{6.29}$$

$$lg = \lambda_Z \tag{6.30}$$

into account. All other couplings are set to their SM value. The functional dependences of the negative log-likelihood for these four one-dimensional coupling measurements are displayed in figure 6.11. The results from the W pair production, single W production and from the $\nu\bar{\nu}\gamma(\gamma)$ channel are displayed next to the total log-likelihood resulting from the combination of all channels. Thus the sensitivity of the single channels to TGCs is very well visible. The inclusion of the $\nu\bar{\nu}\gamma(\gamma)$ channel adds only little information to the total coupling measurement, whereas the consideration of the single W channel is very valuable in the case of the measurement of κ_γ. The measurement of the coupling at the ZWW vertex, *i.e.* g_1^Z and g_5^Z, relies completely on the W pair production channel. The position of the minimum of the likelihood for each single channel is displayed in table 6.3. The combination of all results, which is technically obtained by a fit to the summed likelihood curves, leads to

$$g_1^Z = 1.11^{+0.19}_{-0.18}$$

$$\kappa_\gamma = 1.11^{+0.25}_{-0.25}$$

$$\lambda_\gamma = 0.10^{+0.22}_{-0.20} \qquad \text{and}$$

$$g_5^Z = -0.44^{+0.23}_{-0.22}$$

where the error is the statistical error only. It is obtained by inspection of the coupling value at which the negative log-likelihood is by 0.5 larger than at its minimum. The systematic errors will be evaluated in the next section.

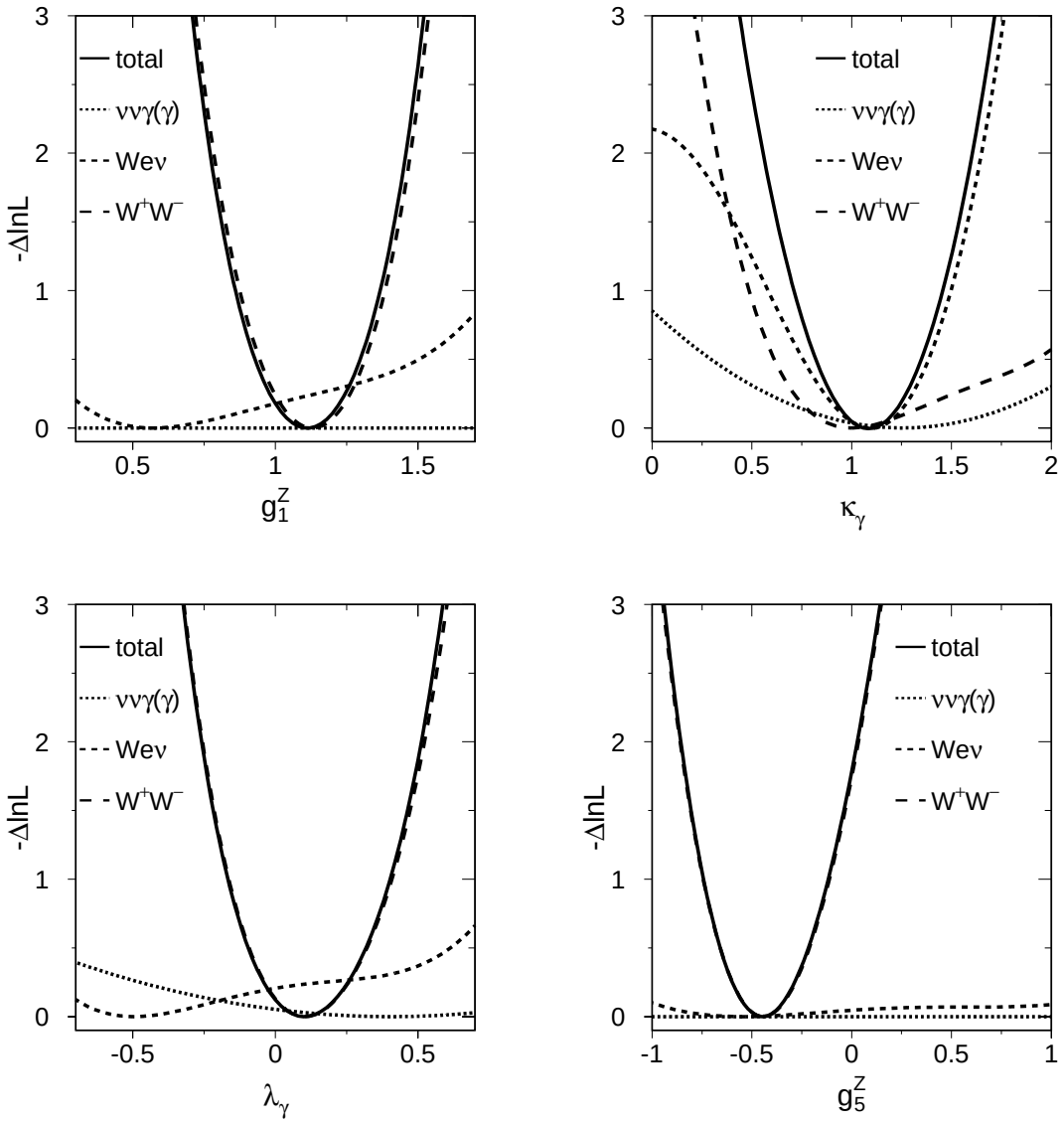

Figure 6.11: *The likelihood curves for a fit to the phase space variables of* W *pair, single* W *and* $\nu\bar{\nu}\gamma(\gamma)$ *events estimating the TGCs* g_1^Z, κ_γ *and* λ_γ. *The sensitivity of the* $\mathrm{W^+W^-}$ *channel is highest for* g_1^Z *and* λ_γ , *while for* κ_γ *the single* W *production is the most sensitive channel.*

Process	Δg_1^Z data	(exp)	$\Delta\kappa_\gamma$ data	(exp)	λ_γ data	(exp)
$e^+e^-\to qqqq$	$0.54^{+0.17}_{-0.26}$ [a]	(±0.19)	$-0.75^{+0.47}_{-0.35}$	(±0.49)	$-0.35^{+0.35}_{-0.21}$	(±0.21)
$e^+e^-\to qqe\nu_e$	$-0.06^{+0.34}_{-0.28}$	(±0.26)	$0.58^{+0.88}_{-1.06}$	(±0.70)	$0.09^{+0.43}_{-0.37}$	(±0.30)
$e^+e^-\to qq\mu\nu_\mu$	$0.19^{+0.27}_{-0.28}$	(±0.26)	$1.26^{+0.62}_{-1.57}$	(±0.73)	$0.13^{+0.32}_{-0.29}$	(±0.31)
$e^+e^-\to qq\tau\nu_\tau$	$-0.06^{+0.30}_{-0.27}$	(±0.32)	$0.18^{+0.68}_{-0.60}$	(±0.50)	$-0.06^{+0.37}_{-0.31}$	(±0.35)
$e^+e^-\to\ell\nu_\ell\ell\nu_\ell$	$0.34^{+0.32}_{-0.37}$	(±0.43)	$0.28^{+0.92}_{-0.86}$	(±0.93)	$0.33^{+0.34}_{-0.36}$	(±0.42)
$e^+e^-\to W^+W^-$	$0.13^{+0.18}_{-0.18}$	(±0.13)	$0.00^{+0.93}_{-0.39}$	(±0.27)	$0.10^{+0.22}_{-0.20}$	(±0.14)
$e^+e^-\to e\nu_e(W\to qq)$	$-0.43^{+0.93}_{-0.40}$	(±0.65)	$0.01^{+0.35}_{-0.48}$	(±0.45)	$-0.47^{+1.01}_{-0.38}$	(±0.72)
$e^+e^-\to e\nu_e(W\to\ell\nu_\ell)$	–		$0.30^{+0.43}_{-0.48}$		$0.94^{+0.7}_{-2.84}$	
$e^+e^-\to We\nu_e$	$-0.43^{+0.93}_{-0.40}$	(±0.65)	$0.12^{+0.27}_{-0.31}$	(±0.34)	$-0.52^{+1.16}_{-0.36}$	(±0.54)
$e^+e^-\to\nu\bar{\nu}\gamma(\gamma)$	–		$0.26^{+0.96}_{-0.96}$	(±1.19)	$0.41^{+1.26}_{-1.25}$	(±1.49)
total	$0.11^{+0.19}_{-0.18}$	(±0.12)	$0.11^{+0.25}_{-0.25}$	(±0.23)	$0.10^{+0.22}_{-0.20}$	(±0.13)

Table 6.3: *Results of fits to the phase space variables of* W *pair, single* W *and* $\nu\bar{\nu}\gamma(\gamma)$ *events estimating one TGC only , while fixing all other to their SM value. The displayed errors are statistical only. The expected error from fitting many MC samples is displayed in brackets.*

[a] The quoted numbers correspond to an up value of 0.5 and not to the 68 % CL, see appendix E for the right treatment.

So far only one coupling was freely varied during the fit procedure. The most general case would be that none of the 14 coupling constants is fixed to its SM value or is correlated to another coupling constant. First step to this goal is to increase the number of fit parameters until the errors are too large to distinguish the case of the SM from the non-existence of the coupling. Thus firstly the fit is extended to two fit parameters, for which always two of the three couplings g_1^Z, κ_γ and λ_γ are varied, while the third and the remaining ones are either set to their SM value or assumed to be correlated by $SU(2) \times U(1)$ symmetry, as stated for the one-dimensional case. The contour curves in the plane of the two varied couplings are displayed in figure 6.12. These curves correspond to parameter sets where the negative log-likelihood exceeds its minimum value by 1.15 (68 % confidence level (C.L.))and 3 (95 % C.L.). The search for the minimum of the likelihood leads to

$$
\begin{array}{lll}
g_1^Z = 1.11^{+0.18}_{-0.20} & \kappa_\gamma = 1.07^{+0.29}_{-0.27} & \rho = -0.24 \\
g_1^Z = 1.18^{+0.23}_{-0.43} & \lambda_\gamma = -0.08^{+0.48}_{-0.24} & \rho = -0.78 \\
\kappa_\gamma = 1.02^{+0.30}_{-0.30} & \lambda_\gamma = 0.09^{+0.23}_{-0.21} & \rho = -0.35
\end{array}
$$

Since on the basis of the statistical error the SM and the non-existence of the ZWW and/or γWW vertex are still distinguishable, fits with the variation of three and four couplings have been performed. For the three dimensional case the three parameters g_1^Z, κ_γ and λ_γ are varied respecting the constraint from $SU(2) \times U(1)$ symmetry. A second set of parameters is also measured, which is g_1^Z, κ_γ and κ_Z, setting λ_γ and λ_Z to their SM values of zero. The two scenarios correspond to the linear and the non-linear extension of the SM as discussed in section 2.6. Combining the information of all coupling sensitive channels values of

$$
\begin{array}{lll}
g_1^Z = 1.11^{+0.18}_{-0.20} & \kappa_\gamma = 1.07^{+0.29}_{-0.27} & \lambda_\gamma = -0.08^{+0.48}_{-0.24} \\
\rho(g_1^Z, \kappa_\gamma) = -0.21 & \rho(g_1^Z, \lambda_\gamma) = -0.80 & \rho(\kappa_\gamma, \lambda_\gamma) = 0.04
\end{array}
$$

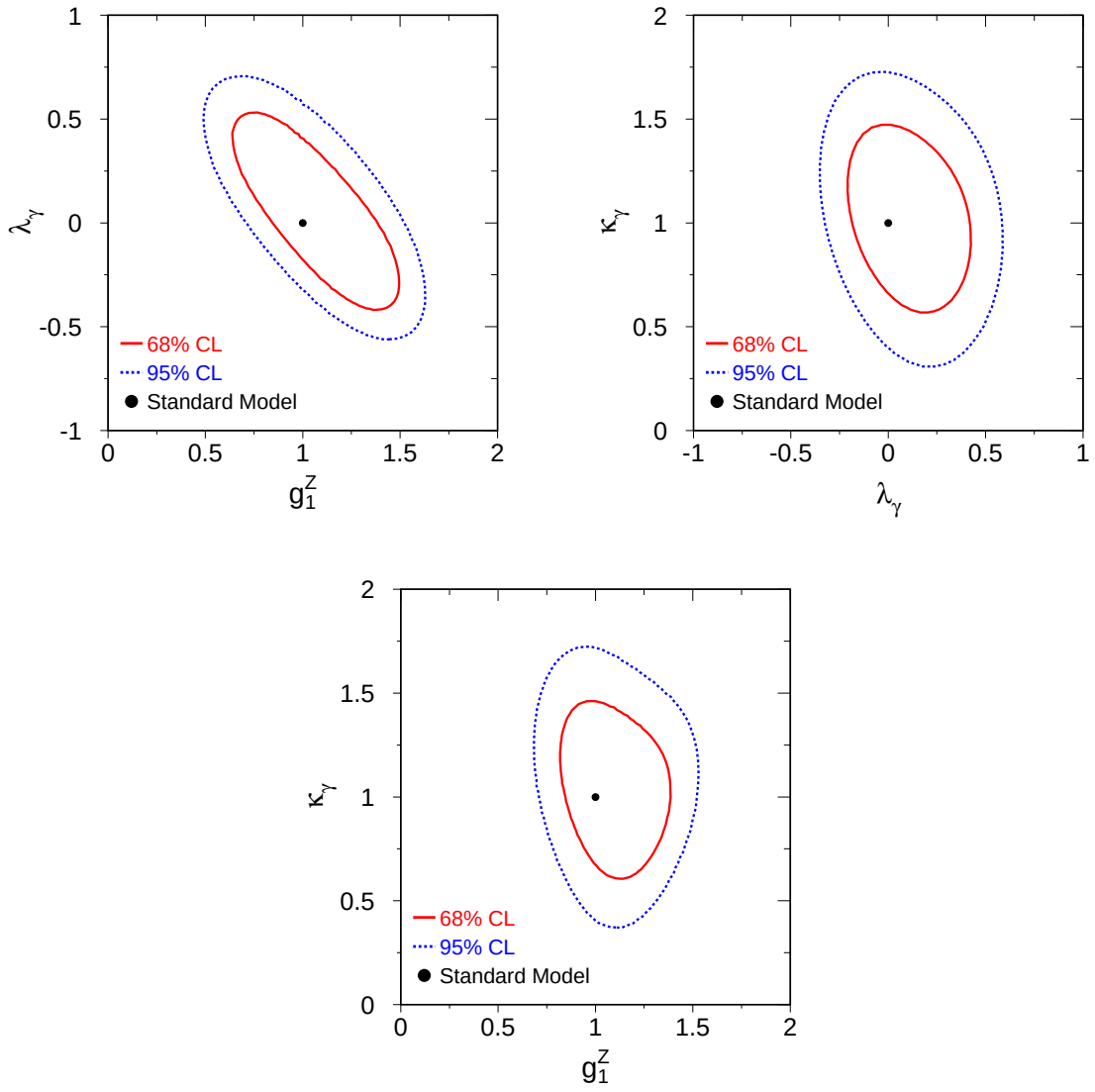

Figure 6.12: *The contour curves for a fit to the phase space variables of* W *pair, single* W *and* $\nu\bar{\nu}\gamma(\gamma)$ *events estimating the TGCs* g_1^Z-κ_γ , λ_γ-κ_γ *and* g_1^Z-λ_γ. *All other couplings are set to their SM value or are varied according to SU(2)×U(1) invariance.*

and

$$g_1^Z = 1.80^{+0.45}_{-1.23} \qquad \kappa_\gamma = 1.07^{+0.23}_{-0.24} \qquad \kappa_Z = 0.41^{+1.16}_{-0.53}$$

$$\rho(g_1^Z, \kappa_\gamma) = 0.07 \qquad \rho(g_1^Z, \kappa_Z) = -0.57 \qquad \rho(\kappa_\gamma, \kappa_Z) = -0.29$$

are obtained. The contour curves in the planes of each two couplings are displayed in figure 6.1 in appendix F. In the last step the scenario is extended to a variation of four couplings. In this scenario, the "weak charge" g_1^Z is fixed to its SM value, as it is always done with the electric charge, and only C and P invariance is required, thus the couplings κ_γ, κ_Z, λ_γ, and λ_Z are measured. Information of all three coupling sensitive channels are used to determine

$$\kappa_\gamma = 1.20^{+0.37}_{-0.26} \qquad \kappa_Z = 1.23^{+0.40}_{-0.42}$$

$$\lambda_\gamma = 0.42^{+0.34}_{-0.57} \qquad \lambda_Z = -0.46^{+0.26}_{-0.34}$$

with

$$\rho(\kappa_\gamma, \kappa_Z) = +0.29 \qquad \rho(\lambda_\gamma, \lambda_Z) = -0.05$$

$$\rho(\kappa_\gamma, \lambda_\gamma) = -0.35 \qquad \rho(\kappa_Z, \lambda_Z) = -0.26$$

$$\rho(\kappa_\gamma, \lambda_Z) = -0.30 \qquad \rho(\kappa_Z, \lambda_\gamma) = -0.10$$

Contour curves of the projections in two-dimensional planes of two couplings are displayed in figure 6.3 in appendix F. A further increase of the number of free couplings is not considered, as the sensitivity of this fit with the available data, prohibits the distinction between the SM and the non-existence of the ZWW or γWW vertex. The result of the measurement and its principle are matter of discussion of the next two section.

6.6 Test of fit result

The results of the last section were obtained using the box method and a fit to the phase space, which was *e.g.* in the case of semileptonic events three-dimensional. Thus a cross check of this method using an easy and straightforward method is very desirable. For this purpose optimal observables as presented in section 6.1 are used. The likelihood curve is obtained by comparing the bin content of the binned OO-distribution in MC and in data as displayed in figure 6.2-d. The coupling dependence of the bin content was obtained by reweighting the SM-MC sample to two coupling values and the computation of the second-order polynomials for each bin. Thus the likelihood reads as

$$-\ln L = \frac{1}{2} \sum_{k=\text{energies}} \sum_{i=\text{qqe}\nu_e}^{\text{qq}\mu\nu_\mu,\text{qq}\tau\nu_\tau} \sum_{j=1}^{N_{bins}} \left(\frac{(N^{k,i,j}_{\text{data}} - N^{k,i,j}_{\text{exp}}(\omega))^2}{N^{k,i,j}_{\text{exp}}(\omega)} \right) \tag{6.31}$$

The dependence of the negative log-likelihood on the coupling g_1^Z for the optimal observable for g_1^Z is displayed in figure 6.13. The results of fits to the OO for

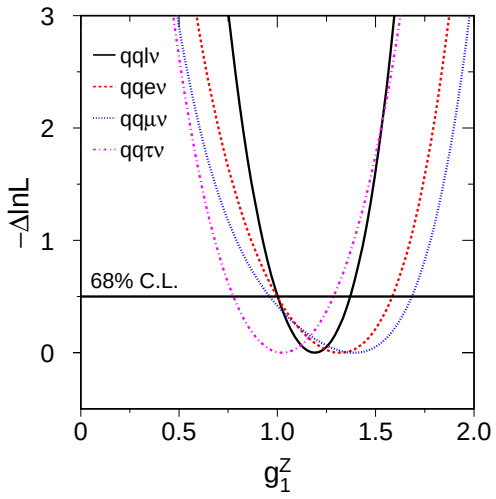

Figure 6.13: *The likelihood curves of the fit to OO(Δg_1^Z) using the channels* qqeν_e, qq$\mu\nu_\mu$ *and* qq$\tau\nu_\tau$. *The* qq$\ell\nu_\ell$ *curve (solid) is the sum of the three single likelihood curves*

the semileptonic W pair decays are listed in table 6.4. The errors and the central values are compatible with those displayed in table 6.3, which were obtained with the box method. A combination of the information of all three semileptonic W pair channels delivers

$$g_1^Z = 1.19^{+0.18}_{-0.19}$$

$$\kappa_\gamma = 1.16^{+0.32}_{-0.33} \qquad \text{and}$$

$$\lambda_\gamma = 0.08^{+0.17}_{-0.16}.$$

Since these two methods use a different approach to measure couplings, confidence about the results and errors of the box method is gained by this cross check.

model	channel			
	$\mathrm{qqe}\nu_e$	$\mathrm{qq}\mu\nu_\mu$	$\mathrm{qq}\tau\nu_\tau$	$\mathrm{qq}\ell\nu_\ell$
Δg_1^Z	$1.32^{+0.26}_{-0.32}$	$1.39^{+0.29}_{-0.43}$	$1.02^{+0.26}_{-0.24}$	$1.19^{+0.18}_{-0.19}$
$\Delta\kappa_\gamma$	$1.62^{+0.64}_{-0.78}$	$2.11^{+0.77}_{-1.39}$	$0.98^{+0.39}_{-0.42}$	$1.16^{+0.32}_{-0.33}$
λ_γ	$0.18^{+0.27}_{-0.36}$	$0.16^{+0.15}_{-0.29}$	$0.00^{+0.24}_{-0.23}$	$0.08^{+0.17}_{-0.16}$

Table 6.4: *The optimal observables for g_1^Z, κ_γ and λ_γ are fitted for semileptonic* W *pair decays. The combined* $\mathrm{qq}\ell\nu_\ell$ *fit value results from adding the three likelihood curves from* $\mathrm{qqe}\nu_e$, $\mathrm{qq}\mu\nu_\mu$ *and* $\mathrm{qq}\tau\nu_\tau$.

A second test of the fit result concerns its statistical error. For this purpose MC samples are generated according to the SM expectation of signal and background. These samples are fitted in the same manner as data. Thus the comparison of the size of the errors as obtained by fitting MC is compared to that by fitting data. The expected error, identical to the mean of the distribution of MC fit errors, is displayed next to the data statistical error in table 6.3. The combined statistical error on data is much larger than the expected one. This results mainly from the fact, that the hadronic W pair cross section is measured more than two sigmas larger than the SM expectation, in turn leading to a topological likelihood curve with two minima and a local maximum at the SM expectation for hadronic W pair events. Thus the combined likelihood curve is more flat, then the one which

is obtained if the cross section of hadronic W pairs would coincide with the SM prediction. The agreement between expected and obtained statistical error in the case of κ_γ is good, as the κ_γ measurement relies more on the single W channel.
Since the MC samples are statistically uncorrelated the scatter of the fit result gives also an indication of the size of the statistical error. Thus the agreement of the two, the mean of the fit error distribution and the width of the fit result distribution tests whether the fit method delivers biased statistical errors. The agreement is good, as is shown for the case of $qq\mu\nu_\mu$ events in figure 6.14. More tests of the fit method will be discussed in the next section.

6.7 Tests of fit method

Incomplete understanding of detector effects and incomplete theoretical descriptions of the physics processes are possible source for significant systematic errors. Sources of systematic errors will be discussed in the following. A summary of all systematic errors will be given in table 6.5.

Linearity

The ability of the fit to reproduce the TGC value of a MC sample which is generated at SM and non-SM TGC values is called linearity. It is the basic test of the fit procedure. However non-linear or biased behaviour of the fit does not imply the uselessness of the fit procedure but makes a calibration of the final fit result necessary.
Since the fitting procedure is equal for all channels only two W pair channels were selected to test the linearity of the box-reweighting. These are the $qq\mu\nu_\mu$ and the $qqe\nu_e$ channel.
Large samples of MC events were generated at 5 (3) TGC values. These events are passed through the complete simulation chain of **L3**. The GL events are fitted and the outcome is compared to the value at which the samples were generated. The result for the TGC λ_γ is displayed in figure 6.14 for the $qq\mu\nu_\mu$ channel. The fit uses only the differential distributions but not the total cross section. Thus if the linearity is expressed as

$$\omega_{\text{true}} = A + B\,\omega_{\text{fitted}} \tag{6.32}$$

the systematic error derived from calibration is

$$\sigma_{sys} = \sqrt{\sigma^2(A) + \omega^2_{\text{fitted}}\sigma^2(B) + (B^2-1)\sigma^2(\omega_{\text{fitted}})}, \tag{6.33}$$

where $\sigma(x)$ denotes the statistical error of variable x and ω_{fitted} denotes the fit result of a fit to the differential cross section only. It is assumed that this error is fully correlated among channels, as this systematic error comes from the fit method which is equal for all channels.

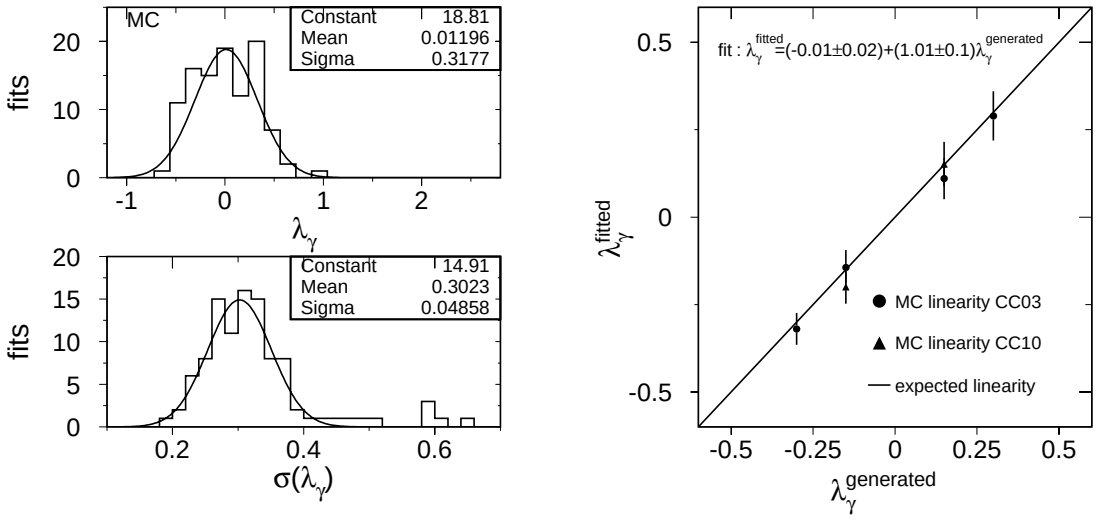

Figure 6.14: **Left:** *The determination of the errors from fitting large numbers of MC samples allows to evaluate the trustworthiness of the error obtained from the data.* **Right:** *The ability of the fit to reproduce the coupling value of MC samples is an important check of the bias of the fit. One expects no biases from a good box fit.*

Four fermions and CC03

Important is also to test whether the irreducible four-fermion background effects the fit results and to which extend. The reweighting procedure for qqqq, qq$\mu\nu_\mu$and qq$\tau\nu_\tau$events uses a CC03 baseline MC which is reweighted properly to the four-fermion configuration (CCn/CC03 reweighting, n denotes the number of graphs that are contributing), as was described earlier in detail. However phase space regions where the CC03 cross section differs largely from the CCn cross section are problematic in this treatment. On the other hand the event selection is tuned

to select mainly CC03 events such that these problematic phase space regions are mainly not included in the final selected data sample. To test the capability to fit CCn samples and to determine the difference to fit CC03 samples, the linearity test outlined in the last paragraph was carried out for CC10 and CC03 samples for $qq\mu\nu_\mu$. The difference of the fit results between these samples is shown in figure 6.14.

The difference in *e.g.* the $qqe\nu_e$ channel is expected to be larger than the difference in the $qq\mu\nu_\mu$ channel since the contributions from the non-CC03 diagrams are much larger. Thus baseline samples having full CCn information are considered for the coupling measurement in the $qqe\nu_e$, $\ell\nu_\ell\ell\nu_\ell$ and single W channel.

Box occupancies and box volumes

The box-reweighting method is performed such that the occupancy per box is kept almost constant. This is done by requiring that the number of MC events per box is a fixed number. This number has to be chosen such that the statistical fluctuation coming from the MC is small. The working point is determined by fitting a large SM-MC sample for different numbers of box occupancies. The fit result as a function of the number of the events in the box is displayed in figure 6.15. It is biased towards the TGC value of the baseline (which is zero in figure 6.15) if the box occupancy is to low, whereas the statistical error increases with box occupancy. Both effects are understood in terms of limited MC statistics. Because of limited baseline MC statistics in the box the differential cross section or the probability density function P_i fluctuates. Since with sufficient statistics the fluctuation is symmetric, it leads to an upward shift in the $-\log(P_i)$ accordingly. Thus higher values of the likelihood are obtained with increasing fluctuation of the pdf. Since the fluctuation increase with departure from the coupling value of the MC baseline, as displayed in figure 6.7, the likelihood curves get steepened, leading to smaller errors. The same effect leads of course also to a bias of the minimum of the likelihood to the coupling value of the baseline. However, this does not mean that TGC information is lost by taking to few MC events, but it results that the linearity curve shown in figure 6.14 has a slope which is less than one and a calibration has to be performed to obtain the right coupling with its true error. Since the true error stays more or less constant, the fit error decreases as the slope gets smaller.

Thus the working point is chosen to be 200 events per box, since the sum of bias and statistical error approaches approximately its minimum at this box occupancy.

Since changing the working point has a small effect on the fit result, the difference is taken as systematic error. A fixed number of events per box requires different box sizes in different phase space regions. The distribution of the box size versus the emission angle of the W^- is shown in 6.15. As systematic error the change of the fit result due to variation of the box content by 50 MC events (150-250) is taken.

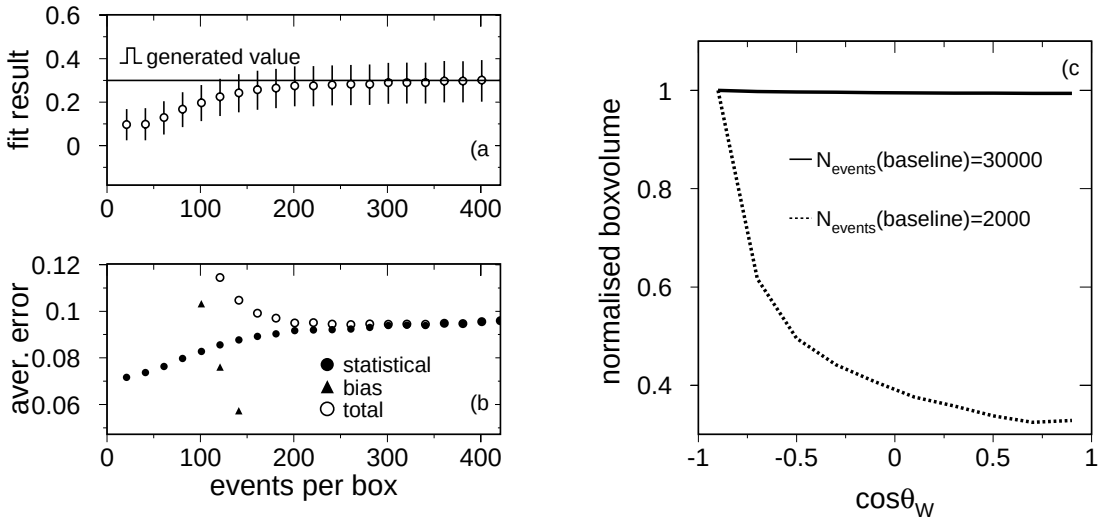

Figure 6.15: *(a+b) The number of events which must lie in the box is chosen such that the statistical error is small and the total error approaches its minimum. The relative change of the box size with* $\cos\theta_W$ *(c) is less dramatic if the number of MC events in the baseline* N_{events}*(baseline) is large.*

MC statistics

The MC fluctuation of the differential cross section required that a large number of MC events is collected in the box. However, this means that either the boxes are large or a large total number of MC events is needed. This is displayed in figure 6.15-c. As the $\cos\theta_W$ distribution increases with $\cos\theta_W$ the density of SM MC events increases as well. This is reflected in the fact that the box size can be small, whereas at $\cos\theta_W \approx -1$ the MC event density is small and the box size has to be larger. The relative change of this box size between $\cos\theta_W \approx -1$ and

$\cos\theta_W \approx +1$ is made less pronounced if larger amounts of MC events are involved in the boxing. Thus the total amount of MC events might influence the fit result. The size of this effect is tested by splitting the MC into N subsamples á k events and observing the scatter of the fit results. The scatter indicates the size of the systematic error if the MC baseline has only k events, while the systematic error at N×k MC events is to be estimated. Therefore the scatter is divided by $\sqrt{N-1}$ to obtain the systematic error on the fit result.

Background description

The non-W pair background does not carry information on TGCs. Thus inexact description of the background gives a bias to the TGC determination. This systematic error is estimated by varying the background cross section according to its error from the cross section measurement. In addition to this, the background shape is varied in $\cos\theta_W$ according to $1 \pm 0.05(\cos\theta_W \langle\cos\theta_W\rangle)$. Thus this worst case scenario assumes that the background is wrongly described in the TGC sensitive variable. Since the background is flat in the distributions of $\cos\theta_W$ this effect makes its distribution forward or backward peaked, exactly the effect of non-SM TGCs on data. Only $\cos\theta_W$ is selected as the effect of the background shape in the other variables is not as large. The same functional dependence is also used for the neural net output in hadronic single W events and the energy in $\nu\bar{\nu}\gamma(\gamma)$ events.

Final state interaction and hadronisation effects

The final state interactions colour reconnection (CR) [**?**] and Bose-Einstein effect (BE) [**?**] have influences on the final state momentum configuration. CR accounts for momentum exchange of the final state quarks of different Ws during the fragmentation process due to soft gluons. This happens since the Ws decay so fast that they are still in the interaction range of the strong force of about 1 fm, when they decay. A change of the initial momentum configuration occurs also after the fragmentation, as the BE-effect brings bosons, such as pions, closer in phase space. Both effects are non-perturbative and as such hard to compute in the SM and thus their description in the MC is assumed to be inaccurate. Since wrong modelling of CR and BE in the MC leads to differences in the distribution of the phase space variables, biases in the TGC measurement can occur. In order to test the effect of CR MC events have been simulated according to today's most attractive models [?]. The couplings were set to their SM values. TGC fits are performed in

the four-jet channel using the CR-MC events as data and the usual baseline MC sample which has no CR modelled at all. In a second test the data were fitted with the standard baseline MC and with a baseline MC which included CR. The change of the fit result was taken as systematic error. Effects of BE-correlation are estimated by fitting samples with BE correlation among particles from the same and from different Ws with samples which have only correlations between particles from the same W. As second test the data were fitted with a baseline MC which included BE among different jets. The fit result was compared to the one obtained using the standard baseline. Analogous effects on the final state four momentum configuration can occur due to wrong modelling of the fragmentation process. The standard fragmentation which is used in this analysis is the string fragmentation [?]. Concurrent to this modelling is the cluster fragmentation [?]. Measurements at the Z^0 peak [**?**] prefer the string model. Thus four-jet events are simulated using the cluster fragmentation scheme and fitted with the standard baseline which was generated with string fragmentation.

Initial and final state radiation

The modelling of initial state radiation is quite different for the MC generators (EXCALIBUR, KORALW) that are used. Approaches to include ISR/FSR in the computation of the W pair cross section were discussed in chapter II. Tests of the influence of these effects are the fit of an EXCALIBUR sample with the standard KORALW baseline MC. As the linearity and CCn tests are done this way, the systematic error from ISR is correlated to those two systematic errors. The effect of final state radiation is tested by fitting the data with a baseline in which all FSR photons were removed. The importance of a correct photon energy spectrum for the spectrum of the observables is shown in figure 6.16. Disregarding events with photon energies larger than 1 GeV, changes largely the $\cos\theta_\ell$ distribution, expression of the fact that $\cos\theta_\ell$ is strongly correlated with the lepton energy. Since four-momentum conservation is imposed in a kinematic fit, the momenta of lost photons are assigned to the W decay products. The assignment respects the resolution on the measured fermion energies, which is excellent for muons measured with the **L3** detector and less good for the jet energy measurement. The main share of the photon energy is therefore assigned to the jets and to the neutrino. Thus the relative contribution of the muon energy to the total event energy is less in $qq\mu\nu_\mu$ events with large ISR, leading to less events at low $\cos\theta_\ell$ values if those events are

disregarded.

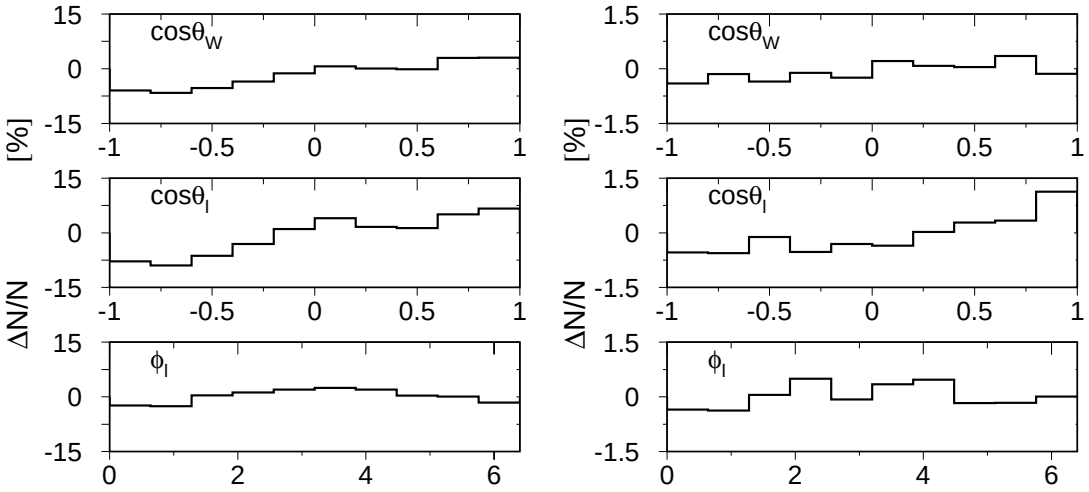

Figure 6.16: *The relative change of the differential cross section in the observables due to disregarding events with more than 1 GeV ISR and FSR photon energies (left) and due to scaling the lepton energy up by +10 percent (right). The effect is shown for the baseline MC of the coupling measurement in the* $\mathrm{qq}\mu\nu_\mu$ *channel.*

Energy and angle measurements

The agreement of the description of the jet four-momentum reconstruction between MC and data is vital for determining the couplings. The quality of this agreement can be checked by comparing data and MC distributions at the Z^0 pole. The agreement between MC and data is better than 0.2 GeV for the energy scale, five percent for the energy resolution and 0.5° for the jet angle. In the case of semileptonic W pair decays the measurement of the lepton four-momentum becomes important. Again data were collected at the Z^0 peak and MC-data agreement is checked with this control sample. The agreement of the energy scale is better than $0.1\sigma_\mathrm{E}$, of the energy resolution better than $0.25\sigma_\mathrm{E}$ and of the angular resolution is better than $0.25\sigma_{cos\theta,\phi}$ for electrons or muons. Thus the MC baseline is smeared with the obtained differences between MC and data, and the change of the measured coupling values is quoted as systematic error The change of the observable distributions if the energy of the lepton is scaled up by ten percent is displayed in figure 6.16.

The influence is strongest for the $\cos\theta_\ell$ distribution. Larger lepton energies lead to larger values of the decay angle $\cos\theta_\ell$ since the emission of the lepton in the direction of the W gives the lepton an additional boost leading to larger energies. The influence on the other observables is small and comes through the application of the kinematic fit imposing four-momentum conservation.

Charge confusion

The capability of **L3** to measure lepton and quark (jet) charges was already discussed in chapter IV. Since the phase space distributions depend crucially on the identification of the W^- charge, a wrong description of the charge confusion in the MC introduces a bias of the coupling determination. The charge confusion in the baseline MC was changed according to the difference of MC and data shown in figure 4.11 for the leptons. The charge determination in hadronic W^+W^- events as obtained by the jet charge method could not be tested in a MC independent way. Thus a disagreement in charge confusion of two percent was assumed.
Additional charge confusion according to the found MC-data differences is introduced to the MC baseline and the change of the fit result is quoted as systematic error.

Energy scale and W mass

The computation of the matrix elements in the reweighting process uses the centre-of-mass energy and the W mass. Big efforts as described in chapter IV have lead to a very precise energy measurement, as listed in table 4.1. However, the inaccuracy of the centre-of-mass energy leads to a systematic error on the coupling measurement coming mainly through the information from the total cross section measurement. This has been evaluated by fitting MC samples which where generated at centre-of-mass energies of 181.72-184.00 GeV. The difference between the generated and fitted coupling is then scaled down by the ratio of the LEP energy error and the difference of the MC sample energy and the energy which was used in the reweighting procedure. The same formalism was used to determine the systematic error coming from the W mass. The W mass was assumed to be 80.448 ± 0.062 GeV, corresponding to a measurement of the W mass at the TEVATRON [**?**], which is assumed to be uncorrelated with this TGC measurement, while this is not valid for the LEP 2 measurement of the W mass of 80.350 ± 0.056 GeV
.

Theory and selection

The measurement of the couplings relies heavily on theoretical predictions of total and differential cross sections and how they change with the couplings. However, so far only tree level computations with incomplete treatment of ISR are available in the case of W pair production. The description of single W production is even more problematic, as it includes electron emission under low angles, such that fermion masses have to be included in the computation. The theoretical description of the $\nu\bar{\nu}\gamma(\gamma)$ channel lacks on the inclusion of higher-order corrections. For these reasons the overall theoretical error on the cross sections is assumed to be two percent [?, **?**, ?, ?]. A further error on the accepted cross section prediction is introduced due to error of the selection efficiencies introduced due to inaccurate MC-modelling of the detector response in the selection variables and due to the limited MC statistics with which this efficiency is computed. The errors on the efficiencies are in the order of two percent [?, ?, ?, ?, ?, ?, ?, ?, ?, ?].

Combination of systematics

Systematic errors on the measured TGCs are summarised in table 6.5, table 6.6 and table 6.7. They are combined taking correlation among channels into account. In the combination, the likelihood curve of each channel which includes only the statistical error σ_{stat} is modified with a scale factor

$$f = \frac{\sigma^2_{\text{stat}}}{\sigma^2_{\text{stat}} + \sigma^2_{\text{sys}}} \tag{6.34}$$

in order to incorporate systematic effects of size σ_{sys}. In cases where the error is non-symmetric, the average of positive and negative error is taken as σ_{stat}. These modified likelihood curves are used in a combined fit to the couplings. The change of the combined result between using likelihood curves with statistical information only and those with incorporated systematic errors is used as combined systematic error. The change is expressed in terms of loss of sensitivity σ_{loss}, resulting in changed errors, and biases $sigma_{\text{bias}}$, resulting in changed fit results. Both errors are summed in quadrature to find the total systematics.

The values in tables 6.5 and 6.6 are obtained from one-dimensional fits to the listed couplings implying the SU(2)×U(1) constrained as displayed in equations 2.57 and 2.58, while the values in table 6.7 are obtained by setting all couplings except the fitted one to their SM value.

channels	Selection/ theory	Charge confusion	Background	ISR/ FSR	MC statistics	LEP-energy m_W-mass/width	Jet measurement	Fragmentation	Fitting method	CR/ BE	Lepton measurement
					g_1^Z						
qqqq	0.23	0.04	0.10	0.07	0.10	0.04	0.14	0.07	0.10	0.04	–
qqeν_e	0.12	0.12	0.03	0.03	0.08	0.04	0.03	0.01	0.06	–	0.06
qq$\mu\nu_\mu$	0.20	0.09	0.02	0.13	0.14	0.03	0.02	0.02	0.07	–	0.07
qq$\tau\nu_\tau$	0.10	0.06	0.02	0.05	0.10	0.03	0.03	0.01	0.05	–	0.05
$\ell\nu_\ell\ell\nu_\ell$	0.15	0.00	0.02	0.11	0.08	0.02	–	–	0.06	–	0.07
eν_e(W $\to$ qq)	0.23	–	0.12	0.09	0.13	0.02	–	–	0.10	–	–
					κ_γ						
qqqq	0.62	0.10	0.14	0.06	0.15	0.06	0.14	0.15	0.15	0.05	–
qqeν_e	0.54	0.27	0.09	0.03	0.20	0.03	0.08	0.07	0.06	–	0.07
qq$\mu\nu_\mu$	0.87	0.15	0.17	0.09	0.31	0.04	0.07	0.05	0.08	–	0.11
qq$\tau\nu_\tau$	0.23	0.08	0.05	0.05	0.16	0.03	0.06	0.04	0.06	–	0.05
$\ell\nu_\ell\ell\nu_\ell$	0.39	0.00	0.09	0.04	0.21	0.03	–	–	0.07	–	0.05
eν_e(W $\to$ qq)	0.25	–	0.16	0.06	0.10	0.03	–	–	0.10	–	–
eν_e(W $\to \ell\nu_\ell$)	0.43	–	0.38	0.08	0.10	0.03	–	–	–	–	–
$\nu\bar{\nu}\gamma(\gamma)$	0.22	–	0.16	–	0.82	0.10	–	–	0.24	–	–
					λ_γ						
qqqq	0.20	0.03	0.13	0.04	0.12	0.04	0.13	0.08	0.10	0.05	–
qqeν_e	0.30	0.21	0.03	0.12	0.08	0.05	0.04	0.01	0.06	–	0.05
qq$\mu\nu_\mu$	0.12	0.04	0.03	0.06	0.09	0.06	0.02	0.02	0.08	–	0.06
qq$\tau\nu_\tau$	0.14	0.08	0.03	0.01	0.11	0.04	0.04	0.01	0.06	–	0.05
$\ell\nu_\ell\ell\nu_\ell$	0.14	0.00	0.02	0.11	0.07	0.04	–	–	0.06	–	0.06
eν_e(W $\to$ qq)	0.27	–	0.15	0.00	0.12	0.02	–	–	0.09	–	–
eν_e(W $\to \ell\nu_\ell$)	0.93	–	0.72	0.64	0.26	0.02	–	–	–	–	–
$\nu\bar{\nu}\gamma(\gamma)$	0.34	–	0.26	–	0.86	0.05	–	–	0.25	–	–
					g_5^Z						
qqqq	0.28	0.04	0.13	0.10	0.12	0.05	0.26	0.07	0.12	0.06	–
qqeν_e	0.14	0.15	0.05	0.03	0.10	0.05	0.03	0.02	0.07	–	0.06
qq$\mu\nu_\mu$	0.24	0.11	0.03	0.16	0.16	0.05	0.02	0.02	0.08	–	0.07
qq$\tau\nu_\tau$	0.12	0.07	0.02	0.06	0.11	0.03	0.04	0.02	0.07	–	0.06
$\ell\nu_\ell\ell\nu_\ell$	0.18	0.00	0.03	0.13	0.09	0.03	–	–	0.07	–	0.08

Table 6.5: *The list of systematic errors split into the different channels and sources.*

channels	Selection/ theory	Charge confusion	Background	ISR/ FSR	MC statistics	LEP-energy m_W-mass/width	Jet measurement	Fragmentation	Fitting method	CR/ BE	Lepton measurement	total
g_1^Z												
W^+W^-	0.04	0.05	0.03	0.05	0.07	0.04	0.06	0.04	0.03	0.02	0.04	0.10
$We\nu_e$	0.23	–	0.12	0.09	0.13	0.02	–	–	0.10	–	–	0.33
all	0.05	0.08	0.05	0.04	0.06	0.01	0.06	0.04	0.02	0.02	0.05	0.10
κ_γ												
W^+W^-	0.37	0.25	0.22	0.24	0.26	0.24	0.22	0.21	0.21	0.23	0.14	0.39
$We\nu_e$	0.19	—	0.14	0.05	0.07	0.02	—	—	0.07	—	—	0.26
$\nu\bar{\nu}\gamma(\gamma)$	0.22	—	0.16	—	0.82	0.10	—	—	0.24	—	—	0.90
all	0.12	0.02	0.10	0.03	0.09	0.02	0.03	0.04	0.06	0.01	0.01	0.17
λ_γ												
W^+W^-	0.05	0.06	0.06	0.04	0.01	0.03	0.06	0.04	0.02	0.02	0.04	0.08
$We\nu_e$	0.26	—	0.12	0.10	0.14	0.06	—	—	0.15	—	—	0.32
$\nu\bar{\nu}\gamma(\gamma)$	0.34	—	0.26	—	0.86	0.05	—	—	0.25	—	—	0.99
all	0.03	0.04	0.08	0.05	0.04	0.01	0.07	0.06	0.05	0.04	0.03	0.10
g_5^Z												
W^+W^-	0.08	0.05	0.01	0.05	0.06	0.04	0.03	0.02	0.04	0.02	0.04	0.12
$We\nu_e$	0.70	–	0.28	0.18	0.28	0.04	–	–	0.25	–	–	0.86
all	0.08	0.04	0.01	0.05	0.06	0.04	0.03	0.02	0.05	0.02	0.04	0.12

Table 6.6: *The list of systematic errors split into the different channels and sources. Decay modes of the* W *are already combined. See text for combination procedure. Other couplings then the one evaluated are set to their SM value or are constrained by SU(2)×U(1).*

channels	Selection/ theory	Charge confusion	Background	ISR/ FSR	MC statistics	LEP-energy m_W-mass/width	Jet measurement	Fragmentation	Fitting method	CR/ BE	Lepton measurement	total
g_1^Z												
W^+W^-	0.04	0.04	0.03	0.04	0.07	0.03	0.07	0.03	0.03	0.02	0.03	0.09
$We\nu_e$	0.24	–	0.15	0.08	0.12	0.02	–	–	0.12	–	–	0.35
all	0.05	0.06	0.05	0.04	0.06	0.02	0.07	0.03	0.03	0.02	0.04	0.10
κ_γ												
W^+W^-	0.35	0.29	0.20	0.24	0.29	0.25	0.22	0.22	0.21	0.21	0.20	0.46
$We\nu_e$	0.25	—	0.18	0.08	0.10	0.05	—	—	0.10	—	—	0.32
$\nu\bar{\nu}\gamma(\gamma)$	0.22	—	0.16	—	0.82	0.10	—	—	0.24	—	—	0.90
all	0.18	0.02	0.14	0.04	0.11	0.05	0.05	0.05	0.08	0.03	0.02	0.28
λ_γ												
W^+W^-	0.07	0.06	0.07	0.05	0.01	0.03	0.07	0.04	0.02	0.03	0.05	0.10
$We\nu_e$	0.39	—	0.21	0.20	0.29	0.10	—	—	0.20	—	—	0.50
$\nu\bar{\nu}\gamma(\gamma)$	0.34	—	0.26	—	0.86	0.05	—	—	0.25	—	—	0.99
all	0.03	0.04	0.08	0.05	0.04	0.01	0.07	0.06	0.05	0.04	0.03	0.10
κ_Z												
W^+W^-	0.20	0.15	0.16	0.16	0.13	0.11	0.10	0.12	0.10	0.11	0.05	0.25
$We\nu_e$	0.47	—	0.20	0.15	0.20	0.10	—	—	0.10	—	—	0.50
all	0.19	0.12	0.16	0.16	0.14	0.10	0.09	0.05	0.07	0.07	0.05	0.23
λ_Z												
W^+W^-	0.08	0.06	0.04	0.04	0.02	0.03	0.06	0.05	0.02	0.04	0.03	0.10
$We\nu_e$	0.56	—	0.31	0.30	0.34	0.26	—	—	0.37	—	—	0.63
all	0.08	0.05	0.04	0.04	0.03	0.02	0.07	0.05	0.03	0.04	0.02	0.11

Table 6.7: *The list of systematic errors split into the different channels and sources. Decay modes of the* W *are already combined. See text for combination procedure. All except the evaluated coupling are set to their SM expectation.*

6.8 Fit result

Summarising the last sections the couplings were measured to be

$$g_1^Z = 1.11^{+0.19}_{-0.18} \pm 0.10 \qquad g_1^Z(\mathrm{SM}) = 1$$

$$\kappa_\gamma = 1.11^{+0.25}_{-0.25} \pm 0.17 \qquad \kappa_\gamma(\mathrm{SM}) = 1$$

$$\lambda_\gamma = 0.10^{+0.22}_{-0.20} \pm 0.10 \qquad \lambda_\gamma(\mathrm{SM}) = 0 \qquad \text{and}$$

$$g_5^Z = -0.44^{+0.23}_{-0.22} \pm 0.12 \qquad g_5^Z(\mathrm{SM}) = 0$$

where the first error is statistical and the second systematic. The SM prediction displayed at the right side is in good agreement with this measurement. Higher dimensional fits revealed also good agreement of SM and this measurement. The next chapter will elaborate on how these values can be exploited in terms of extensions of the SM and how the understanding of the W can be improved by this measurement.

How do you know, it was a success? You don't know.
S.C.C. Ting

VII

From numbers to model comparison

The measurement of the TGCs gives for the first time access to a fundamental property of nature - the self-coupling of the weak bosons and adds valuable information to the knowledge of electroweak bosons. This gain in information can now be used to test whether the predictions of models that intend to describe the electroweak sector are confirmed by this measurement or not.

7.1 Standard Model and W substructure

As already pointed out in the last chapter, the predictions of the SM are consistent with this measurement. Even more so the measurement of g_1^Z of

$$g_1^Z = 1.11^{+0.19}_{-0.18} \pm 0.10$$

proofs the existence of the ZWW coupling on the level of five standard deviations. The first error denotes the statistical and the second the systematic error. The significance of the measurement of κ_γ,

$$\kappa_\gamma = 1.11^{+0.25}_{-0.25} \pm 0.17,$$

is about four standard deviations. No C or P violation in the WWZ^0 interaction has been seen in measuring g_5^Z

$$g_5^Z = -0.44^{+0.23}_{-0.22} \pm 0.12.$$

The static properties of the W are obtained from the two dimensional fit to κ_γ and λ_γ, and lead to

$$\mu_W = (1.3^{+0.19}_{-0.18}) \times 10^{-5} \ \mu_B \qquad\qquad q_W = (-5.7^{+2.5}_{-2.4}) \times 10^{-36} \ \mathrm{m}^2$$

assuming that the Q^2 dependence is small compared to the errors. The Q^2 dependence is obtained by comparing the combined W pair result, giving a coupling measurement at $Q^2 = s$, with the coupling measurement in the single W channel at $Q^2 = m_W^2$ and the single photon channel $Q^2 = 0$. No functional dependence is found as displayed in figure 7.1.

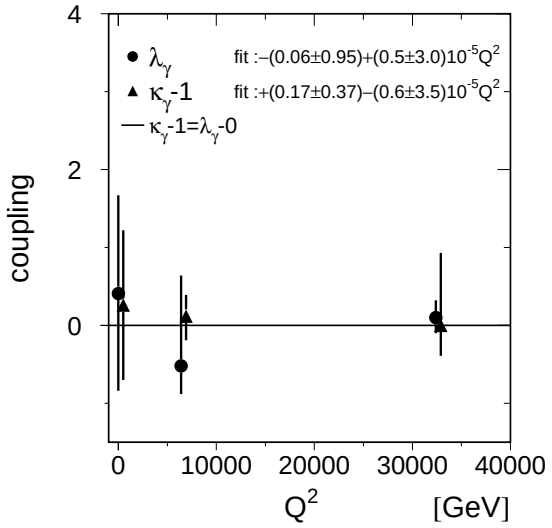

Figure 7.1: *The Q^2 dependence of the measurements of κ_γ and λ_γ. The result of a line fit to the data, gives no indication of a change of the coupling constants with energy (running).*

The measurement of the magnetic dipole and the electric quadrupole moment give information on the size and the geometrical form of W. Comparing the measured

dipole moment with the one expected from SM, an "anomalous" component $\Delta\mu$, coming from W substructure, can be postulated. Assuming that the particles of the substructure have charge of order one, the relative change is [?]

$$\frac{\Delta\mu}{\mu_W} \approx \frac{m_{\mathrm{W}}}{\mathrm{m}^*} = m_{\mathrm{W}} R_{\mathrm{W}}, \tag{7.1}$$

where m^* is the mass of the particles of the substructure and R_{W} is thus the size at which these subparticles play a role, thus the size of the W. Thus R_{W} is

$$R_{\mathrm{W}} = \frac{\Delta\kappa_\gamma + \lambda_\gamma}{m_{\mathrm{W}}}. \tag{7.2}$$

The magnetic quadrupole moment gives information on the shape of the physics object according to

$$\Delta q_{\mathrm{W}} = \frac{4}{5}\delta \cdot R_{\mathrm{W}}^2, \tag{7.3}$$

where δ indicates the deformation of the W shape if it is assumed to be an ellipsoid [?, ?, ?]. This contribution from the W geometry would add on top of the contribution from the W bosonic quadrupole moment as described in the SM, thus the deformation parameter is

$$\delta \cdot R_{\mathrm{W}}^2 = -\frac{5}{4}\,\frac{\kappa_\gamma - \lambda_\gamma - 1}{m_{\mathrm{W}}^2}. \tag{7.4}$$

A combined fit to κ_γ and λ_γ is performed to measure the radius and δR_{W}^2, resulting into

$$R_{\mathrm{W}} = (3.3^{+9.5}_{-9.9}) \times 10^{-19}\ \mathrm{m} \qquad \delta \cdot R_{\mathrm{W}}^2 = (3.3^{+30}_{-31}) \times 10^{-37}\ \mathrm{m}^2. \tag{7.5}$$

Thus this measurement sets an upper limit on the substructure of the W at 2×10^{-18} m. The shape of the W can not be extracted, as long as R_{W} is not established. The precision of this measurement did not give access to measure the effects of SM radiative corrections to the WWZ^0 and $\mathrm{WW}\gamma$ vertices. A gain in significance of more than a factor of 20 must be achieved to test this correction. This is beyond the scope of the LEP 2 program. Additional corrections resulting from SUSY, TECHNICOLOUR or a potential fourth generation fermion family are of the same size and therefore this measurement is insensitive to them.

7.2 Non-standard models

The formulation of a theory of unified matter and forces by Klein [?, ?] predicts $\kappa_\gamma = -2$. The vector fields of this theory, the "mesotons" are here identified as the W bosons. The measurement of

$$\kappa_\gamma = 1.11^{+0.26}_{-0.25} \pm 0.17$$

rules out this theory by more than ten standard deviations.

In models that extent the SM linearly (see equation 2.65) a connection of the WWZ^0 and $WW\gamma$ couplings to $H\gamma\gamma$, HZ^0Z^0 and $HZ^0\gamma$ couplings is established. Thus the TGC measurement allows to restrict the $HH\gamma$ couplings.

$$|g^{(1)}_{HZ^0\gamma}| < 0.006.$$

The additional couplings $g^{(1)}_{H\gamma\gamma}$ and $g^{(2)}_{HZ^0\gamma}$ cannot be restricted by this measurement, making direct searches for the Higgs-photon coupling necessary [?].

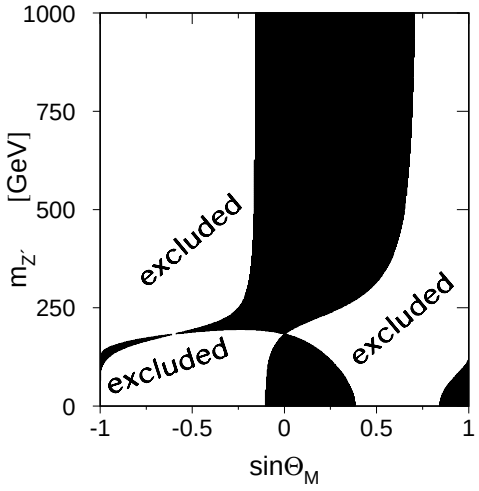

Figure 7.2: *Exclusion regions in the mixing angle,* $\sin\Theta_M$*,* Z′ *mass plane. The most recent mass limits from fermion pair production are* $\sin\theta_M$ *independent and exclude masses below 779 GeV [?, ?]*

An additional sequential Z′ boson will influence the W pair production and therefore will lead to non-SM TGC. The effect of the Z′ depends crucially on the Z′-mass and its mixing angle to the SM-Z^0, as stated in equation 2.68. Thus limits on these parameters can be inferred from non-observation of a difference of the measured g_1^Z from its SM expectation. The excluded region in the $m_{Z'}$-$\sin\theta_M$ plane is shown in figure 7.2. For the most of the Z′ mass region values of the mixing angle are only allowed in the range

$$-0.16 \leq \sin\Theta_M \leq 0.71. \tag{7.6}$$

Thus the Standard Model was again successful in predicting the result of a measurement, whereas other models could be ruled out, their parameter space was restricted or they predict such tiny effects that this measurement was insensitive to them.

There is something fascinating about science. One gets such wholesale returns of conjecture out of such a trifling investment of fact.
Mark Twain

VIII

From this measurement to the world

During the LEP data taking at 161-183 GeV not only **L3** was collecting events and analysed them with respect to TGCs, but also the other three LEP experiments, ALEPH [**?**, **?**, **?**], DELPHI [**?**, **?**, **?**] and OPAL [**?**, **?**, **?**]. Each of these experiments collected about 75 pb^{-1} corresponding to about 1000 W pair events. All coupling measurements so far are statistics limited, thus combining them will increase the accuracy of the coupling information. The sensitivity of all four experiments is almost equal, thus a factor two decrease of the error is expected by combining their results.

Interesting measurements from the TEVATRON experiments, DØ [?] and CDF [?], became also available, resulting from the analysis of the processes $q\bar{q}' \rightarrow \mathrm{W} \rightarrow \mathrm{W}\gamma/\mathrm{WZ}^0$ and $q\bar{q} \rightarrow \mathrm{Z}^0/\gamma \rightarrow \mathrm{W}^+\mathrm{W}^-$ [**?**, **?**] in the data taken in 1994-1995 at $\sqrt{s} = 1.8$ TeV. DØ and CDF have collected about 100 pb^{-1} per experiment.

All experiments have independently analysed their data sets, resulting in full negative log-likelihood curves as a function of the TGCs. These likelihood-curves are provided such that they contain statistical and systematic effects. Since they are not parabolic it is not possible to combine them in terms of weighted averages. Thus the likelihood curves are added together and the combined coupling value is obtained by identifying the minimum and the values at which the log-likelihood

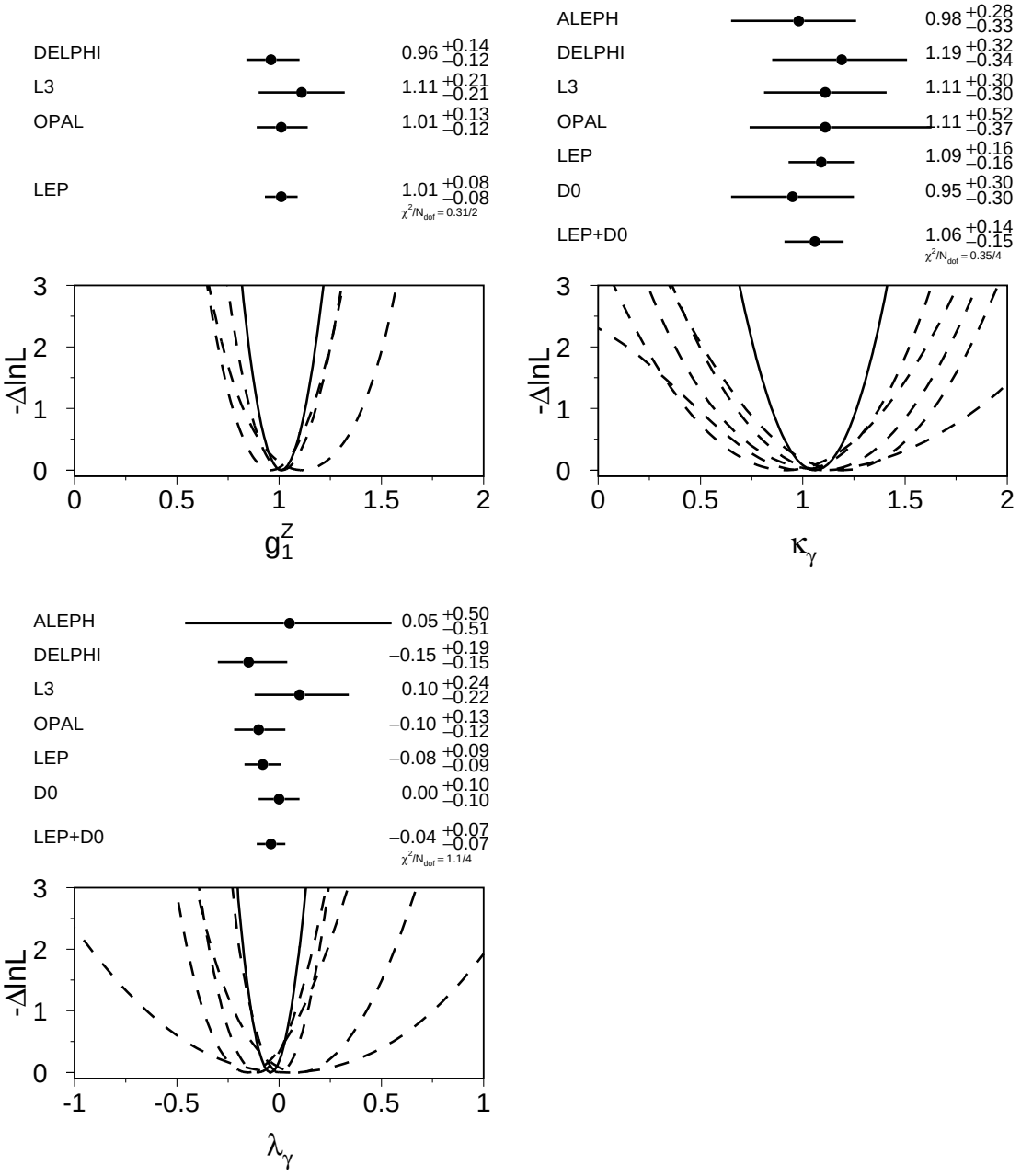

Figure 8.1: *The status of the world average using the 161-183 GeV LEP TGC measurements [?] and data from DØ.*

exceeds its minimum by 0.5.
In principle there are some common systematic effects which should be included in a correlated way. These include the uncertainties of the W mass, and some effects estimated by varying MC generators. Among the LEP experiments also the systematic error from the uncertainty of the LEP beam energy is correlated. However, in the combination this correlation is not considered as it has a negligible effect. The systematic errors are typical small compared to the statistical errors. The main contributions come from background to the selected W pair sample, detector resolutions, fitting methods and limited Monte Carlo statistics. The order of their importance varies.
The individual log-likelihood curves for each parameter and the sum of the curves for the one parameter case are shown in figure 8.1 where each curve is plotted relative to its minimum value. The combined coupling values are also displayed in figure 8.1.
More recently preliminary results from the 1998 data taking at 189 GeV became available [?, ?, ?, ?]. Each of the LEP experiments collected at this centre-of-mass energy about 170 pb^{-1}, thus increasing the total statistics by a factor of 3. The same procedure of combining experiments was applied for this preliminary data set. The result of this combination is displayed in figure 8.2. This combination reduced the errors on the couplings, as expected, by a factor of two. The SM expectation agrees also well with this combined coupling measurement. However, it must be pointed out that all χ^2/Ndf of the combinations are very low, resulting in χ^2-probabilities between 85 and 98 percent for the 183 GeV combination and between 72 and 99.8 percent for 189 GeV. This is usually a sign for overestimated systematic errors but not for the coupling measurement as it is statistically limited. Essentially three scenarios are possible; a statistical fluctuation (although it is disturbing that this applies to 183 and 189 GeV), an unnoticed correlation among the coupling results of the experiments or new physics which effects the coupling sensitive channels orthogonal to what is possible by the measured couplings (*e.g.* if the W pair cross section is measured lower than the SM expectation a measurement of g_1^Z will always lead to the SM coupling values, as g_1^Z only increases the cross section). The identification of the real source needs further study. Future experiments for TGC measurements are therefore discussed in the next chapter.

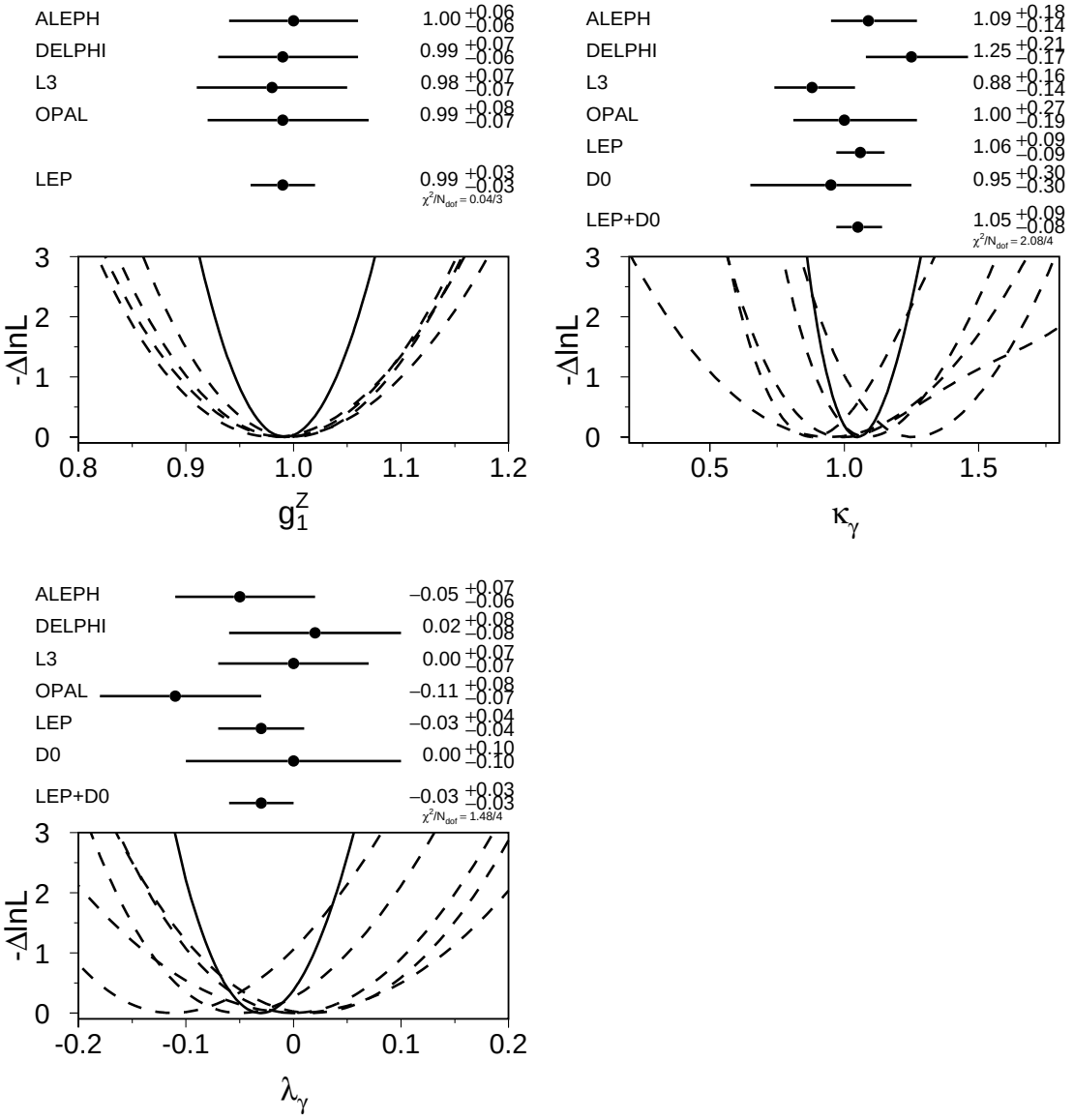

Figure 8.2: *The status of the world average after including also preliminary 189 GeV LEP results [?].*

I have seen the future and it is just like the present, only longer.
Kehlog Albran, "The Profit"

IX

From present to future studies of TGCs

9.1 TGCs from electroweak precision data

The measurement of TGCs from electroweak precision data was discussed in chapter III. Slight improvements of the indirect determination of the TGCs are expected with decreased errors on m_{W} and $\mathrm{m_{top}}$ which will be available at the end of the LEP II and TEVATRON-run II.

9.2 Rare B and K decays

Recent measurements of rare decays of B [**?**, **?**] and K-hadrons allow also to measure TGCs [**?**]. The deviation from the SM expectation can be observed at best if the SM decay rate is small. In the case of B-decays the electromagnetic penguin graphs for $\mathrm{b} \to \mathrm{s}\gamma$ and $\mathrm{b} \to \mathrm{s}\ell^+\ell^-$ as shown in figure 9.1 a) and b) are suited to measure the couplings $\Delta\kappa_\gamma$ and λ_γ. The measured $\mathrm{b} \to \mathrm{s}\gamma$ branching fraction of $\mathrm{B}(\mathrm{b} \to \mathrm{s}\gamma) = (2.50 \pm 0.47 \pm 0.39) \times 10^{-4}$ [?] ($(3.11 \pm 0.80 \pm 0.72) \times 10^{-4}$ [?]) can be combined and turned into a measurement of $\Delta\kappa_\gamma$ ($|\Delta\kappa_\gamma| < 0.20$ at 68 % C.L.) [?]. Future measurements at the BaBar and Belle detectors will allow to measure this branching fraction with an error better than 2×10^{-5} and replace the upper limits

on the branching fraction of $b \to s\ell^+\ell^-$ with a measurement, thus one can expect to measure $\Delta\kappa_\gamma$ with much higher precision. As the branching fraction reach of the B-factories goes down to 10^{-7}, one can also expect to measure $b \to d\gamma$ which will add another channel constraining the WWγ couplings. Although the channel $b \to s\ell^+\ell^-$ is not very sensitive to the WWγ coupling it is very sensitive to the coupling Δg_1^Z. A 30% measurement of $B(b \to s\ell^+\ell^-)$ would allow to measure Δg_1^Z with a precision of 0.1 [?].

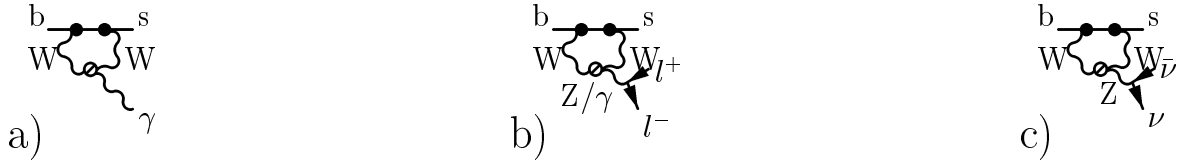

Figure 9.1: *The electromagnetic and weak penguin decays of B- or K-hadrons are sensitive to TGCs. The* WWZ^0 *and the* WWγ *couplings can be measured independently by measuring the branching fraction of* $b \to s\gamma$ *(*$s \to d\gamma$*) (a) and* $b \to s\nu\bar{\nu}$ *(*$s \to d\nu\bar{\nu}$*) (c). The measurement of* $b \to s\ell^+\ell^-$ *(*$s \to d\ell^+\ell^-$*) (b) measures a mixture of* WWZ^0 *and* WWγ *couplings.*

Similarly to the B-penguin diagrams also penguin decays of K-mesons show sensitivity to TGCs. Especially the ZWW coupling constants can be constraint by the decays $K^+ \to \pi^+\nu\bar{\nu}$ and $K_L \to \pi^0\nu\bar{\nu}$. Today's measurements of these branching fractions like $B(\pi^+\nu\bar{\nu}) = (4.2^{+9.7}_{-3.5}) \times 10^{-10}$ [**?**] determine only upper limits on the branching fractions. The current run of the KTEV experiment at FERMILAB is likely to give access to this branching fraction.

9.3 Direct measurements of TGCs

After completion of the LEP II program TGCs will be directly tested at the TEVATRON, at LHC and at a possible future linear collider.

The TEVATRON-run II is expected to deliver 2 fb^{-1} to the DØ [?] and CDF [?] experiments, increasing their current statistics by a factor of ten. Thus it is expected that these experiments will measure $\Delta\kappa_\gamma$ with a precision of 0.3 and λ_γ with 0.1 [**?**] .

Even higher luminosities are expected at the Large Hadron Collider (LHC) cur-

rently built at CERN. Also here TGCs can be measured via the bremsstrahlung process of photons and Z^0s. The expected spectra of the transverse momentum are displayed in figure 9.2. One expects to reach accuracies [**?**] of

0.07 for $\Delta\kappa_Z$ 0.04 for $\Delta\kappa_\gamma$ 0.005 for λ_Z 0.0025 for λ_γ

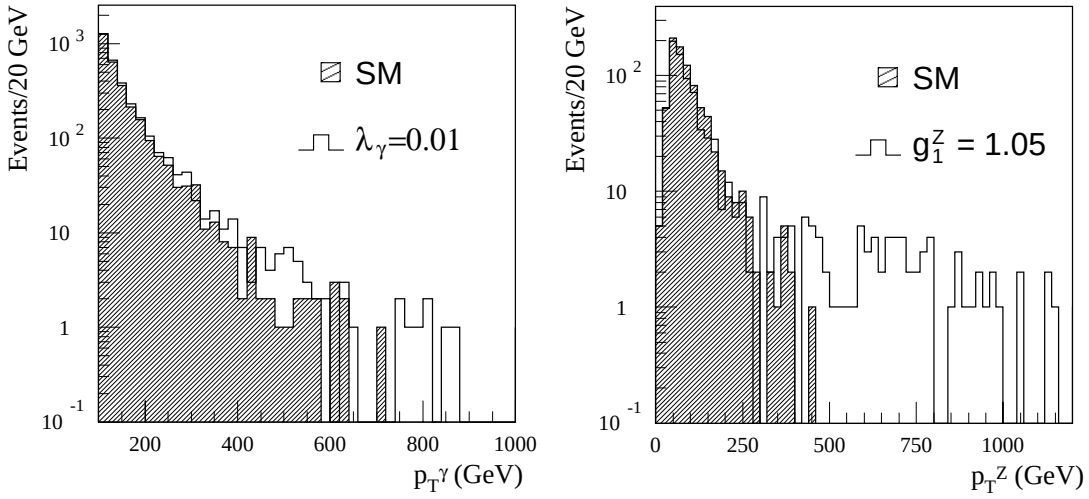

Figure 9.2: *Distribution of transverse γ (left) and Z^0 (right) momentum in $W\gamma$ and WZ^0 final states at the LHC for a total luminosity of 30 fb^{-1}. The expectation from SM is displayed next to expectations for λ_γ=0.01 (left) and g_1^Z=1.05 (right) [?].*

The natural successor of LEP will be a future e^+e^- linear collider (LC) currently planned at particles physics laboratories in Japan (KEK), in the USA (SLAC) and in Germany (DESY). This collider will run at energies between the top quark pair production threshold of 350 GeV and 2000 GeV at luminosities of about $5 \times 10^{34}\text{cm}^{-2}\text{s}^{-1}$. With these parameters one estimates a sensitivity of $\mathcal{O}(10^{-4})$ [**?**] for the CP-conserving coupling constants and a sensitivity of $\mathcal{O}(10^{-3})$ for the CP-violating ones if one measures the differential cross section of the W pair production at these energies.

Nobody cares about your method. People remember only your last number.
S.C.C. Ting

X

From beginning to end

The charged weak boson W couples to the neutral weak boson Z^0 and to the photon.

A new window for precise measurements of particle physics properties was opened in 1996 by crossing the W pair production threshold of 161 GeV. Whereas the couplings of the W boson to fermions are very well known to be [**?**, ?, **?**]

$$G_F = (1.16639 \pm 0.00001) \times 10^{-5}\ \mathrm{GeV}^2$$

$$V_{\mathrm{CKM}} = \begin{pmatrix} 0.9740 \pm 0.0005 & 0.2205 \pm 0.0018 & 0.00325 \pm 0.00058 \\ 0.224 \pm 0.016 & 1.01 \pm 0.18 & 0.0401 \pm 0.0029 \\ 0.0113^{+0.0060}_{-0.0029} & 0.045^{+0.022}_{-0.010} & 0.77^{+0.18}_{-0.24} \end{pmatrix}$$

its coupling to the other electroweak bosons was until then not precisely determined.

The details of a measurement of couplings between the electroweak bosons in data collected in the years 1996 and 1997 at 161, 172 and 183 GeV centre-of-mass energy corresponding to an integrated luminosity of 77 pb^{-1} have been discussed in the recent chapters. The couplings were determined in one, two, three and four-dimensional fits using total and differential cross sections of W pair, $\mathrm{e^+e^-} \to \mathrm{W^+W^-}$, single-resonant W, $\mathrm{e^+e^-} \to \mathrm{We}\nu_\mathrm{e}$, and single photon production, $\mathrm{e^+e^-} \to \nu\bar{\nu}\gamma(\gamma)$ as collected with the **L3** detector. Standard Model predictions agree well

with this measurement. In particular one-dimensional coupling values of

$$g_1^Z = 1.11^{+0.19}_{-0.18} \pm 0.10 \qquad \kappa_\gamma = 1.11^{+0.26}_{-0.25} \pm 0.17 \qquad \text{and}$$
$$\lambda_\gamma = 0.10^{+0.22}_{-0.20} \pm 0.10, \qquad g_5^Z = -0.44^{+0.23}_{-0.22} \pm 0.12.$$

have been obtained, where the first error is statistical and the second systematic. The Standard Model predicts one for g_1^Z and κ_γ and zero for λ_γ and g_5^Z. The consistency of the g_5^Z measurement with the Standard Model expectation limits the size of possible C- or P-violating but CP-conserving effects at the ZWW vertex. The accuracy of the coupling determination of this analysis alone reaches already the precision to which quark-W boson couplings have been measured. A significant increase in statistical accuracy is obtained by averaging results from all four LEP experiments and DØ, leading to

$$g_1^Z = 1.01 \pm 0.08 \qquad \kappa_\gamma = 1.06^{+0.14}_{-0.15} \qquad \text{and}$$
$$\lambda_\gamma = -0.04 \pm 0.07$$

The three channels that have been analysed correspond to coupling measurements at three different values of momentum transfer of about 180 ($e^+e^- \rightarrow W^+W^-$), 80 ($e^+e^- \rightarrow We\nu_e$) and 0 GeV($e^+e^- \rightarrow \nu\bar{\nu}\gamma(\gamma)$). No dependence of the couplings on the momentum transfer is found.
This direct measurement agrees well with results obtained by analysing electroweak precision data which were evaluated with respect to the influence of triple gauge boson couplings to the radiative corrections, leading to

$$g_1^Z = 0.983 \pm 0.018^{+0.018}_{-0.003} \quad \text{and} \quad \kappa_\gamma = 1.016 \pm 0.019^{+0.009}_{-0.013},$$

where the first error represents statistical and systematic uncertainties and the second results from varying the Higgs mass between 90 and 1000 GeV. However, the indirect measurement is only valid in a model where non-Standard Model couplings arise from a linear extension of the Standard Model and under the assumption that no other physics beyond the Standard Model contributes significantly to the radiative corrections, whereas the direct measurement is valid without these assumptions.
The direct measurement is exploited further to limit the size of the W, by computing its radius from the magnetic dipole moment μ_W and the electric quadrupole

moment q_{W} to be

$$R_{\mathrm{W}} = (3.3^{+9.5}_{-9.9}) \times 10^{-19}\ \mathrm{m}.$$

Thus this measurement limits the size of the W to be smaller than 2×10^{-18} m. No sign of compositeness has been found.

The sector of triple gauge boson couplings will gain attention much beyond the time at which LEP shuts down. At this time the coupling values will be known as precise as 0.2 for g_1^Z and λ_γ and 0.6 for κ_γ. However the analysis of the data that will be taken at LHC and a possible future linear collider will bring the sensitivity down to 10^{-4}. The accuracy of these measurements will make the test of radiative corrections to the ZWW and γWW vertex possible and will allow to study physics beyond the Standard Model.

The fact that it works is immaterial.
L. Ogborn

Appendix A

Boson self-coupling in the SM

The SM describes the interaction of three electroweak bosons. Although in the most general terminology assuming only charge conservation one would expect six such vertices, the SM includes only two of them. The structure of the SM Lagrangian which forbids the other four vertices is derived and discussed.
The SM Lagrangian includes the boson self-interaction in the terms

$$L = -\frac{1}{4}W_{\mu\nu} \cdot W^{\mu\nu} - \frac{1}{4}B_{\mu\nu}B^{\mu\nu} \tag{1.1}$$

The field strength tensors in the SM are defined as

$$W_{\mu\nu} = \partial_\mu \vec{W}_\nu - \partial_\nu \vec{W}_\mu - g\vec{W}_\mu \times \vec{W}_\nu \tag{1.2}$$

and

$$B_{\mu\nu} = \partial_\mu B_\nu - \partial_\nu B_\mu. \tag{1.3}$$

If these definitions are substituted in equation 1.1 one finds

$$\begin{aligned} L = & -\frac{1}{2}(\partial_\mu \vec{W}_\nu - \partial_\nu \vec{W}_\mu) \cdot \partial^\mu \vec{W}^\nu + g(\vec{W}_\mu \times \vec{W}_\nu) \cdot \partial^\mu \vec{W}^\nu \\ & - \frac{1}{2}g^2 \left[(\vec{W}^\mu \cdot \vec{W}^\nu)^2 - (\vec{W}^\mu \cdot \vec{W}^\nu)(\vec{W}_\mu \cdot \vec{W}_\nu) \right] \\ & + (\partial_\mu B_\nu - \partial_\nu B_\mu)(\partial^\mu B^\nu - \partial^\nu B^\mu) \end{aligned} \tag{1.4}$$

Here one can easily identify the TGC piece which comes with g while the four boson part comes with g^2. Since $\vec{W}_\mu$ is an isotriplet of the vector fields $(\vec{W}_\mu)_i$ one

can split the TGC piece in six pieces containing all combinations of the isotriplet field.

$$g(\vec{W}_\mu \times \vec{W}_\nu) \cdot \partial^\mu \vec{W}^\nu = g \sum_{ijk} ((\vec{W}_\mu)_i (\vec{W}_\nu)_j \partial^\mu (\vec{W}^\nu)_k \tag{1.5}$$

Terms with two identical field indices i vanish since the isotriplet fields are orthogonal, leading to

$$g(\vec{W}_\mu \times \vec{W}_\nu) \cdot \partial^\mu \vec{W}^\nu = g\epsilon^{ijk} (\vec{W}_\mu)_i (\vec{W}_\nu)_j \partial^\mu (\vec{W}^\nu)_k \tag{1.6}$$

with $\epsilon^{ijk} = 0$ except if $i \neq j \neq k$ where $\epsilon^{ijk} = 1$. Therefore one has only terms with a field combination of 123. Using the SM relations

$$(\vec{W}_\mu)_1 = \frac{1}{\sqrt{2}}(W_\mu^- + W_\mu^+), \tag{1.7}$$

$$(\vec{W}_\mu)_2 = \frac{\imath}{\sqrt{2}}(W_\mu^- + W_\mu^+) \qquad \text{and} \tag{1.8}$$

$$(\vec{W}_\mu)_3 = \sin\theta_w \, A^\mu + \cos\theta_w \, Z^\mu \tag{1.9}$$

in equation 1.6 one finds, *e.g.* ,

$$e \, W_\mu^- W_\nu^+ \partial^\mu A^\nu \qquad \text{or} \tag{1.10}$$

$$e \cot\theta_w \, W_\mu^- W_\nu^+ \partial^\mu Z^\nu. \tag{1.11}$$

Thus $\gamma \mathrm{W^+W^-}$ and $\mathrm{ZW^+W^-}$ interactions are present in the SM, while no other three boson vertex evolves from the structure of the Lagrangian of the electroweak SM.

For those who like this sort of thing, this is the sort of thing they like.
Abraham Lincoln

Appendix B

The linear extension

This appendix displays a list of all eleven independent bosonic dimension 6 operators

$$\mathcal{O}_{DW} = tr[D_\mu, \hat{W}_{\nu\rho}][D^\mu, \hat{W}^{\nu\rho}] \tag{2.1}$$

$$\mathcal{O}_{DW} = -\frac{g'^2}{2}(\partial_\mu B_{\nu\rho})(\partial^\mu B^{\nu\rho}) \tag{2.2}$$

$$\mathcal{O}_{BW} = \Phi^+ \hat{B}_{\mu\nu}\hat{W}_{\mu\nu}\Phi \tag{2.3}$$

$$\mathcal{O}_{\Phi} = (D_\mu\Phi)^+\Phi\Phi^+(D^\mu\Phi) \tag{2.4}$$

$$\mathcal{O}_{\Phi,2} = \frac{1}{2}\partial_\mu(\Phi^+\Phi)\partial^\mu(\Phi^+\Phi) \tag{2.5}$$

$$\mathcal{O}_{\Phi,3} = \frac{1}{3}(\Phi^+\Phi)^3 \tag{2.6}$$

$$\mathcal{O}_{W} = tr(\hat{W}_\nu^\mu \hat{W}_\rho^\nu \hat{W}_\mu^\rho) \tag{2.7}$$

$$\mathcal{O}_{W\phi} = (D_\mu\Phi)^+\hat{W}^{\mu\nu}(D_\nu\Phi) \tag{2.8}$$

$$\mathcal{O}_{B\phi} = (D_\mu\Phi)^+\hat{B}^{\mu\nu}(D_\nu\Phi) \tag{2.9}$$

$$\mathcal{O}_{WW} = \Phi^+\hat{W}^{\mu\nu}\hat{W}_{\mu\nu}\Phi \tag{2.10}$$

$$\mathcal{O}_{BB} = \Phi^+\hat{B}^{\mu\nu}\hat{B}_{\mu\nu}\Phi, \tag{2.11}$$

where

$$\hat{W}_{\mu\nu} = \imath g \frac{\sigma^a}{2}(\partial_\mu W^a_\nu - \partial_\nu W^a_\mu - g\epsilon^{abc} W^b_\mu W^c_\nu) \tag{2.12}$$

$$\hat{B}_{\mu\nu} = \imath g \frac{\sigma^a}{2}(\partial_\mu B^a_\nu - \partial_\nu B^a_\mu) \tag{2.13}$$

All other variables are explained in chapter II.

If you steal from one author, it's plagiarism; if you steal from many, it's research.
Wilson Mizner

Appendix C

The selection cuts

The major selection cuts of the single channels are listed for the centre-of-mass energies of 161, 172 and 183 GeV. Please consult the text for the explanation of single variables.

channel	cut	$\sqrt{s}$ [GeV]		
		161	172	183
$W^+W^- \to$				
qqqq	N_{tracks}	> 5	–	–
	N_{SRC}	> 30	> 30	> 30
	$E_{\text{vis}}/\sqrt{s}$	> 0.65	> 0.7	> 0.7
	$\lvert\sum p_{\parallel}\rvert/E_{\text{vis}}$	< 0.25	< 0.25	< 0.25
	E_γ [GeV]	< 30	< 40	< 40
	E_γ/E_{jet}	–	< 0.5	< 0.8
	y_{34}	> 0.0025	> 0.0025	> 0.0015
	Neural Network Output	fit	> 0.72	> 0.67
qqeν_e	$\lvert\cos\theta_e\rvert$	< 0.90	< 0.95	< 0.95
	E_e [GeV]	> 25	> 25	> 20
	$\Delta\phi$(bump,track) [mrad]	< 10	< 10[1]	< 40 (< 100[2])
	$E_e/E_e^{15^\circ}$	> 0.7	> 0.7	> 0.73
	$E_e^{\text{BGO}} - E_e^{\text{TEC}}$ [GeV]	–	–	< 61 (< 38)
	$E_e^{\text{HCAL, }7^\circ}$	–	–	–(< 8)

[1] Cut changes to 42 mrad in the forward region to account for the worse resolution

[2] Numbers in brackets account for the case where the electron is identified as bump in the SPACAL

channel	cut	$\sqrt{s}$ [GeV]		
		161	172	183
	E_{miss} [GeV]	> 25	> 20	–
	$\lvert\cos\theta_{\mathrm{miss}}\rvert$	< 0.90	< 0.95	< 0.94 (< 0.91)
	$\angle$(jet, jet, e) if $\lvert cos\theta_e\rvert > 0.9$	–	–	< 5.4
	$\lvert\vec{p}_\mu \cdot \vec{n}_{\mathrm{jet}}\rvert$ [GeV]	–	–	< 17 (< 14)
	N_{SRC}	> 15	> 15	> 12 (> 17)
	N_{jets}	$= 2$	$= 2$	$= 2$
	$M_{e\nu}$ [GeV]	> 50	> 55	> 60
	M_{qq} [GeV]	> 50	> 45	> 33 (> 48)
$\mathrm{qq}\mu\nu_\mu$	E_μ [GeV]	> 20	> 15	> 15
	$\alpha(\mathrm{jet}, \mu)$ [°]	> 15	> 10	–
	$\lvert\cos\theta_{\mathrm{miss}}\rvert$	< 0.95	< 0.95	–
	$\alpha_{\mathrm{min}}(\mathrm{jet}, \mu)\sin\theta_{\mathrm{miss}}$ [°]	–	–	> 4
	E_μ^2 [GeV]	< 20	–	–
	N_{SRC}	> 15	> 15	> 10
	N_{tracks}	> 5	> 5	> 5
	$M_{\mu\nu}$ [GeV]	> 55	> 55 (> 20[1])	> 45
	M_{qq} [GeV]	$\epsilon[40, 120]$	$\epsilon[30, 120]$ ([40, 110])	$\epsilon[20, 120]$
μ=MIP	$\alpha(\mathrm{jet}, \mathrm{HCAL\text{-}MIP})$ [°]	–	> 15	
	$\alpha(\mathrm{jet}, \mathrm{BGO\text{-}MIP})$ [°]	–	> 20	
	$\lvert p_{\mathrm{track}}(\mathrm{MIP})\rvert$ [GeV]	–	–	> 20
	$E_{\mathrm{BGO}}(\mathrm{MIP})$ [GeV]	–	–	$\epsilon[0.2, 2]$
	$E_{\mathrm{MIP}}^{15°} - E_{\mathrm{MIP}}$ [GeV]	–	–	< 7
$\mathrm{qq}\tau\nu_\tau$	N_{SRC}	> 15	> 15	> 14
	N_{tracks}	–	–	> 5
	$E_{\mathrm{vis}} - \lvert p_{\mathrm{miss}}\rvert$ [GeV]	< 120	< 130	< 140
	$\lvert p_{\mathrm{miss}}\rvert$ [GeV]	–	> 10	$--$
	$\lvert\sum p_{\lvert\rvert}\rvert$ [GeV]	< 30	< 40	< 40
	$\lvert\sum p_\perp\rvert$ [GeV]	> 5	> 5	> 10
$\tau \to \mathrm{e}, \mu$	E_ℓ [GeV]	> 5	> 5	> 5
	$E_\ell + \lvert p_{\mathrm{miss}}\rvert$ [GeV] ($\ell = \mathrm{e}/\mu$)	< 65	$< 70/65$	–
	$\lvert\cos\theta_{\mathrm{miss}}\rvert$	–	–	< 0.95
	$M_{\ell\nu}$ [GeV] ($\ell = \mathrm{e}/\mu$)	–	–	$< 60/45$
$\tau \to$hadrons[2]	$N_{\mathrm{jets}}(E_{\mathrm{jet}} > 10$ GeV)	≥ 3	≥ 3	≥ 3
	N_τ^{SRC}	–	< 5	NN
	$\angle(\tau)$ [°]	–	< 8	NN

[1] The numbers in brackets account for cuts which are changed in the case that the μ is identified by its MIP signature

[2] τ-jets are clustered using the cone algorithm with a 15° half-opening angle

channel	cut	$\sqrt{s}$ [GeV]		
		161	172	183
	E_τ^{BGO} [GeV]	> 35	> 25	NN & < 35
	E_τ^{HCAL} [GeV]	> 3	> 5	> 2
	M_τ [GeV]	–	< 2	NN
	N_τ^{tracks}	$\epsilon[1,3]$	$\epsilon[1,3]$	NN
	$\alpha(\tau, jet)$ [°]	> 25		
	$M_{\tau\nu}$ [GeV]	> 55	$\epsilon[50,110]$	$\epsilon[40,120]$
	M_{qq} [GeV]	$\epsilon[60,100]$	$\epsilon[60,100]$	$\epsilon[50,110]$
$\ell\nu_\ell\ell\nu_\ell$	N_{tracks}	$\epsilon[1,6]$	$\epsilon[1,6]$	$\epsilon[1,6]$
	N_{SRC}	< 15	< 15	$\epsilon[1,15]$
	$E_{\mathrm{vis}}/\sqrt{s}$	$\epsilon[0.02,0.8]$	$\epsilon[0.02,0.8]$	$\epsilon[0.02,0.8]$
	$\lvert\cos\theta_{\ell,\mathrm{jet}}\rvert$	< 0.92	< 0.92	< 0.96
$N_\ell = 2$	E_ℓ^2 [GeV]	$\epsilon[8,70]$	$\epsilon[8,70]$	$\epsilon[5,80]$
	acoplanarity$(\ell^+\ell^-)$ [°]	> 8	> 8	> 8
	N_{tracks}	$= 2$	$= 2$	$= 2$
	$\lvert\sum p_\perp\rvert$ [GeV]	≥ 8	≥ 10	≥ 8
	$\lvert\sum p_\perp\rvert/E_{\mathrm{vis}}$	≥ 0.1	≥ 0.1	≥ 0.1
	$\lvert\cos\theta_{\mathrm{miss}}\rvert$	< 0.96	< 0.96	–
	$E_{\mathrm{BGO+HCAL}} - E_\ell^1 - E_\ell^2$ [GeV]	< 10	< 10	< 10
	E_ℓ^1 [GeV]	–	–	$\epsilon[20,80]$
$\ell = \mathrm{e}$	$\lvert\cos\theta_e\rvert$	–	–	< 0.92
$N_\ell = 1$	E_{jet} [GeV]	> 8	> 8	> 8
	E_ℓ [GeV]	–	–	$\epsilon[10,80]$
	acoplanarity (ℓ,jet) [°]	> 8	> 8	> 8
	E_{track} [GeV]	> 2	> 2	> 2
	$\lvert\sum p_\perp\rvert/E_{\mathrm{vis}}$	–	–	> 0.1
	$\lvert\cos\theta_{\mathrm{miss}}\rvert$	–	–	< 0.98
	$E_{\mathrm{miss}}/E_{\mathrm{vis}}$	> 0.2	> 0.2	–
	E_γ [GeV]	< 10	< 10	< 10
$N_\ell = 0$	$\lvert\cos\theta_{\mathrm{jet}}\rvert$	–	–	< 0.92
	E_{jet_1} [GeV]	–	–	> 10
	E_{jet_2} [GeV]	–	–	> 6
	$\lvert\sum p_\perp\rvert/E_{\mathrm{vis}}$	–	–	> 0.1
	$\lvert\cos\theta_{\mathrm{miss}}\rvert$	–	–	< 0.98
	E_{track_1} [GeV]	–	–	> 5
	E_{track_2} [GeV]	–	–	> 1
	E_γ [GeV]	–	–	< 50
	E_{FB} [GeV]	–	–	< 20
	acoplanarity (track,track) [°]	–	–	> 14
W$e\nu \to$				

channel	cut	$\sqrt{s}$ [GeV]		
		161	172	183
qqeν_e	N_{track}	> 4	> 4	> 5
	E_{BGO} [GeV]	> 15	> 15	> 10
	E_{vis} [GeV]	–	–	> 60
	M_{vis} [GeV]	–	–	$\epsilon[40, 120]$
	$y_{23}(JADE^1)$	–	–	< 0.06
	$y_{34}(JADE)$	–	–	< 0.015
	E_{FB} [GeV]	< 50	< 50	< 60
	$\lvert\sum p_\perp\rvert$ [GeV]	> 10	> 10	> 15
	$\lvert\cos\theta_{\text{miss}}\rvert$	< 0.955	< 0.955	< 0.955
	$E^{25^\circ}_{\text{miss}} - E_{\text{miss}}$ [GeV]	< 10	< 10	< 20
	$\angle$(jet,jet) [rad]	< 3	< 3	< 3
	$E^{40^\circ}(-\vec{n}_{\text{jet}_1} - \vec{n}_{\text{jet}_2})$ [GeV]	< 15	< 15	–
	E_ℓ [GeV]	< 15	< 15	–
	Ω(jet, jet, jet) [rad]	< 3	< 3	< 5.5
	Neural Network Output			
$\ell\nu_\ell$eν_e	E_ℓ [GeV]	> 15	> 15	> 15
	N_{tracks}	$= 1$	$= 1$	$= 1$
	E_ℓ / E_{vis}	> 0.9	> 0.9	> 0.92
	$E^{25^\circ,miss}$ [GeV]	< 1	< 1	< 1
	E_{FB} [GeV]	< 15	< 15	< 60
ℓ = e	$\lvert\cos\theta_e\rvert$	< 0.72	< 0.72	< 0.7
	E_e [GeV]	–	–	> 20
$\nu\bar{\nu}\gamma(\gamma)$	E_γ [GeV]	> 5	> 5	> 5
	$\lvert\sum p_\perp\rvert$ [GeV]	> 5	> 5	> 5
	$\phi_{\gamma-\text{HCAL}}$ [$^\circ$]	< 15	< 15	< 15
	$\Delta\phi_{\text{jet,jet}}$ [rad]	< 3.1	< 3.1	< 3.1
	E_{HCAL} [GeV]	< 20	< 20	< 20
	E_{LUMI} [GeV]	< 20	< 20	< 20
	E_{ALR} [GeV]	< 10	< 10	< 10
	E_{SPACAL} [GeV]	< 7	< 7	< 7
	$E_{\text{vis}} - E_\gamma$ [GeV]	< 10	< 10	< 10
	$N_{\text{bumps}} - N^\gamma_{\text{bumps}}$	< 2	< 2	< 2
	N_μ	< 1	< 1	< 1
	N_{SRC}	< 14	< 14	< 14
	N_{tracks}	< 7	< 7	< 7
	$N_{\text{tracks},20^\circ}$	$= 0/2$	$= 0/2$	$= 0/2$
	N_{scint}	≥ 1	≥ 1	≥ 1
γ-Id	E_9/E_{25}	> 0.94	> 0.94	> 0.94

[1] DURHAM is the default clustering algorithm that is used, except for this selection.

channel	cut	$\sqrt{s}$ [GeV]		
		161	172	183
	E_{bump} [GeV]	> 5	> 5	> 5
	χ^2_{em}(Barrel)	< 10	< 10	< 10
	χ^2_{em}(Endcap)	< 25	< 25	< 25
	$E_{\mathrm{HCAL}}/E_{\mathrm{bump}}$	< 0.2	< 0.2	< 0.2
	Skewness	> 0.2	> 0.2	> 0.2

Table 3.1: *Selection cuts of channels used in the analysis [?, ?, ?, ?, ?, ?, ?, ?]. The variables are explained in the previous chapters*

I was gratified to be able to answer promptly, and I did. I said I didn't know.
Mark Twain

Appendix D

Optimalness of optimal observables

The reduction of dimensionality of distributions that are used in fits without losing sensitivity, as outlined in chapter V, section 6.1, is very desirable. The mathematical prove of this property of optimal observables is outlined in the following for the case of one fit parameter ω only. Starting point is the Taylor expansion of the differential cross section at a fit parameter value ω_0

$$\begin{aligned}\frac{\frac{d\sigma}{d\Omega}(\Omega,\omega)}{\frac{d\sigma}{d\Omega}(\Omega,\omega_0)} - 1 &= \frac{\frac{d^2\sigma}{d\Omega d\omega}}{\frac{d\sigma}{d\Omega}}(\Omega,\omega_0)\Delta\omega + \frac{\frac{d^3\sigma}{d\Omega d\omega^2}}{\frac{d\sigma}{d\Omega}}(\Omega,\omega_0)\Delta\omega^2 + \ldots \\ &= O_1\Delta\omega + O_2\Delta\omega^2 + \ldots \quad . \end{aligned} \tag{4.1}$$

This differential cross section is to be normalised to find the probability density function (pdf) $f(\Omega,\omega)$ at the phase space point Ω. The normalisation factor is the inverse of the total cross section which can be obtained by integrating equation 4.1

$$\begin{aligned}\frac{\sigma(\omega)}{\sigma(\omega_0)} - 1 &= \frac{1}{\sigma(\omega_0)}\,\frac{d\sigma}{d\omega}(\omega_0)\Delta\omega + \frac{1}{\sigma(\omega_0)}\,\frac{d^2\sigma}{d\omega^2}(\omega_0)\Delta\omega^2 + \ldots \\ &= S_1\Delta\omega + S_2\Delta\omega^2 + \ldots \quad . \end{aligned} \tag{4.2}$$

The likelihood for N observed data events can then be expressed as

$$\begin{aligned} L(\omega) &= \prod_{i=1}^{N} f(\Omega_i, \omega) \\ &= \prod_{i=1}^{N} \frac{\frac{d\sigma}{d\Omega}(\Omega, \omega_0)}{\sigma(\omega_0)} \quad \frac{1 + O_1\Delta\omega + O_2\Delta\omega^2 + \ldots}{1 + S_1\Delta\omega + S_2\Delta\omega^2 + \ldots}. \end{aligned} \tag{4.3}$$

The O_i are functions of the full phase space and therefore is the function f the pdf of the complete phase space.
The estimator $\hat{\omega}$ of ω is found by maximising the log-likelihood

$$\frac{d\ln L}{d\omega}(\omega)|_{\omega=\hat{\omega}} = \sum_{i=1}^{N} \frac{d\ln f(\Omega_i, \omega)}{d\omega}|_{\omega=\hat{\omega}} = 0 \tag{4.4}$$

The variance of $\hat{\omega}$ is

$$\begin{aligned} V(\hat{\omega}) &= -\frac{1}{E(\frac{d^2L}{d\omega^2}\ |_{\omega=\hat{\omega}})} \\ &= -\frac{1}{N}\frac{1}{\int \frac{d^2f}{d\omega^2}\ |_{\omega=\hat{\omega}}\ f(\omega_{\text{true}})d\Omega}. \end{aligned} \tag{4.5}$$

Equation 4.5 is derived from the Cramer-Rao bound [**?**]. If f is substituted by its definition one finds

$$\begin{aligned} V^{-1}(\hat{\omega}) &= N\frac{2S_2(1 - 2S_1\hat{\omega} - 2S_2\hat{\omega}^2) - S_1^2}{(1 + S_1\hat{\omega} + S_2\hat{\omega}^2)^2} \\ &\quad - N\int \frac{2O_2(1 - 2O_1\hat{\omega} - 2O_2\hat{\omega}^2) - O_1^2}{(1 + O_1\hat{\omega} + O_2\hat{\omega}^2)^2} f(\omega_{\text{true}})d\Omega \end{aligned} \tag{4.6}$$

If one constructs now a pdf g of a reduced phase space $\tilde{\Omega}$ of dimensionality n

$$g(\tilde{\Omega}, \omega) = \int f(\Omega, \omega)\delta(\tilde{\Omega}_1 - \Omega_1)\ldots\delta(\tilde{\Omega}_n - \Omega_n)d\Omega_1\ldots d\Omega_n \tag{4.7}$$

one finds a different likelihood function

$$\tilde{L}(\omega) = \prod_{i=1}^{N} g(\tilde{\Omega}_i, \omega) \tag{4.8}$$

Also this likelihood is maximised in order to find $\hat{\omega}$. The variance of $\hat{\omega}$ coming from the pdf g for the reduced phase space $\tilde{\Omega}$ is

$$\tilde{V}^{-1}(\hat{\omega}) = N\frac{2S_2(1-2S_1\hat{\omega}-2S_2\hat{\omega}^2)-S_1^2}{(1+S_1\hat{\omega}+S_2\hat{\omega}^2)^2}$$
$$-N\int\int\int\frac{2\tilde{\Omega}_2(1-2\tilde{\Omega}_1\hat{\omega}-2\tilde{\Omega}_2\hat{\omega}^2)-\tilde{\Omega}_1^2}{(1+\tilde{\Omega}_1\hat{\omega}+\tilde{\Omega}_2\hat{\omega}^2)^2}f(\omega_{\text{true}})\delta(\tilde{\Omega}_1-\Omega_1)\delta(\tilde{\Omega}_2-\Omega_2)d\Omega d\tilde{\Omega}_1 d\tilde{\Omega}_2. \tag{4.9}$$

if a two-dimensional reduced phase space is assumed. The definition of g has already been substituted. The reduced phase space has the same sensitivity as the full phase space if the variance in equation 4.9 is equal to that in equation 4.6. This can be achieved if

$$\tilde{\Omega}_1 = O_1 \tag{4.10}$$

and

$$\tilde{\Omega}_2 = O_2. \tag{4.11}$$

reversing the order of the integration in equation 4.9. Thus the two dimensional phase space of O_1 and O_2 has the same sensitivity as the full phase space.

As far as the laws of mathematics refer to reality, they are not certain; and as far as they are certain, they do not refer to reality.
Albert Einstein

Appendix E

Some words about likelihood curves and statistics

Likelihood curves are the most general way to express the probability of a certain set of physics variables. However a numerical representation of a measurement is most desirable. Thus the likelihood curve has to be turned into its numerical counterpart. The most common known method is the identification of the global minimum of the likelihood curve L_0 at the value of the physics variables x_0 and to find the values x_1 and x_2 where the likelihood exceed L_0 by 0.5 (1.95 for 95% C.L.). Although this way of finding the numerical representation is used most often, it assumes that the likelihood curve behaves properly, *i.e.* it does not have other local minima. Nevertheless this case can occur in measuring the TGCs at LEP. Since the cross section dependence on the TGCs is quadratic, always two values of couplings can lead to a measured cross section, thus the total cross section contribution has two minima if the measured cross section exceeds the minimal predicted cross section. In this case alternative methods for finding the numerical representation have to be used. The one which is used in this theses, turns the log-likelihood curve into a probability $\mathcal{P} = e^{\ln L}$. The probability is then integrated to find the 68% and the 95% C.L. The range of integration is found by scanning the probability distribution from the high probabilities to the low ones. The correct ranges are found if the integral corresponds to 68 (95) percent of the total integral.

This method can give disjunct intervals of errors, but which have the highest probability to be the true physics parameter. The method is pictured in figure 5.1.

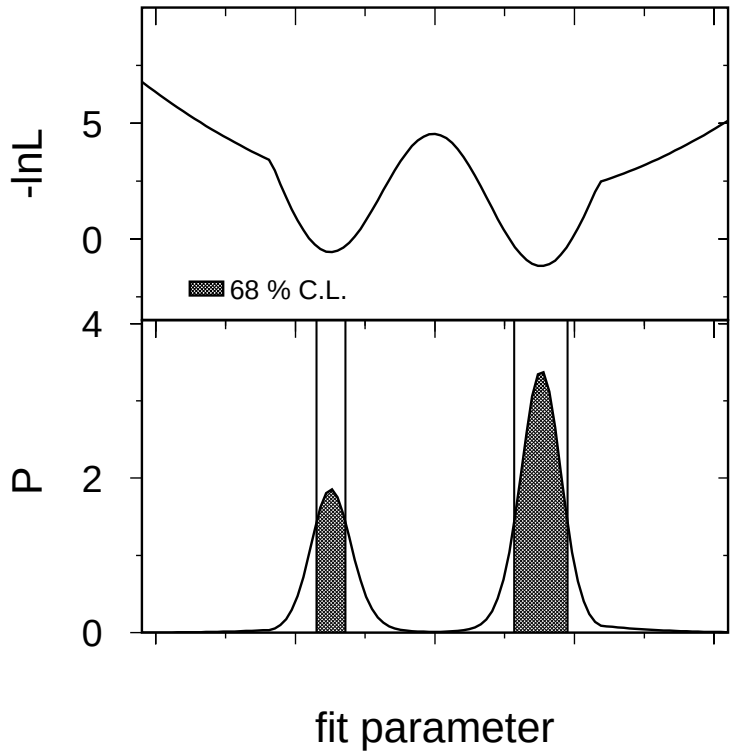

Figure 5.1: *The most probable regions are used for the 68% C.L interval, by computing the probability and integrating over the intervals which are obtained by scanning through the probability from the high side.*

The trouble with doing something right the first time is that nobody appreciates how difficult it was.

Appendix F

Contour curves and distributions

This appendix collects the two dimensional contour curves of the fit to three or four TGCs and the distributions for the optimal observables of κ_γ, λ_γ and g_5^Z.

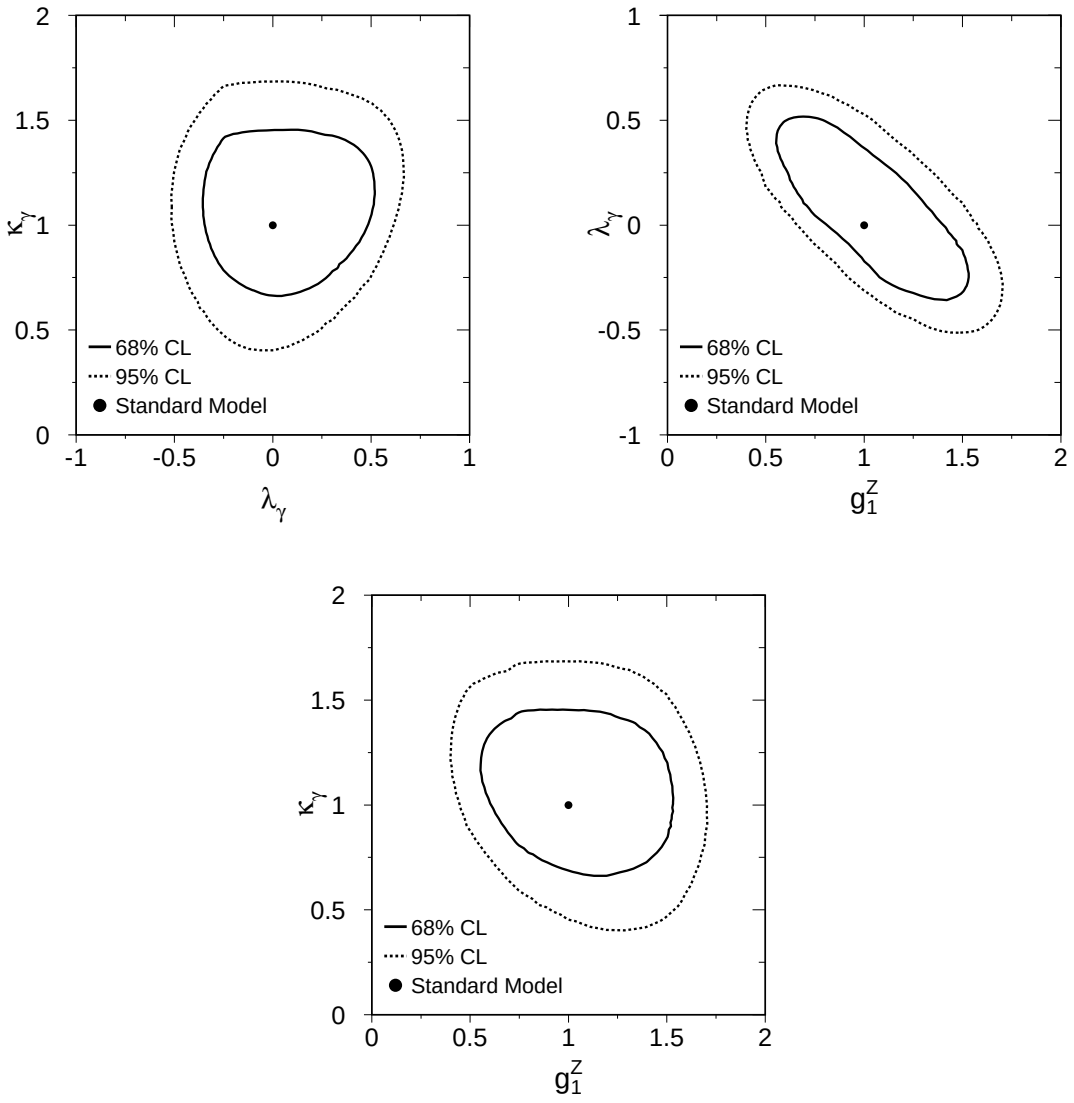

Figure 6.1: *The contour curves from a fit to the phase space variables of* W *pair, single* W *and* $\nu\bar{\nu}\gamma(\gamma)$ *events estimating the TGCs* Δg_1^Z-$\Delta\kappa_\gamma$-λ_γ. *All other couplings are set to their SM value or are varied according to SU(2)*$\times$*U(1) invariance.*

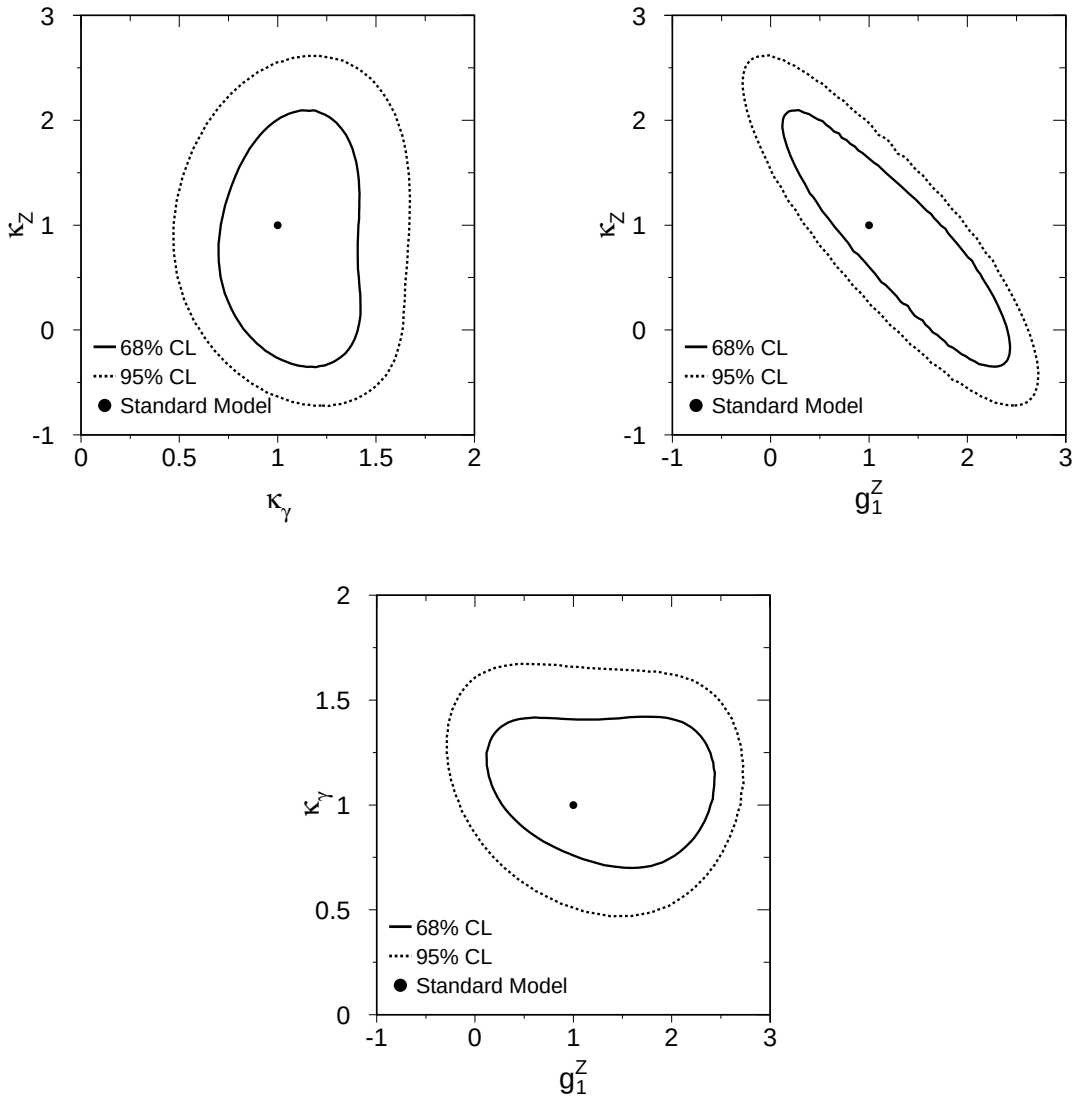

Figure 6.2: *The contour curves from a fit to the phase space variables of* W *pair, single* W *and* $\nu\bar{\nu}\gamma(\gamma)$ *events estimating the TGCs* Δg_1^Z-$\Delta\kappa_\gamma$-κ_Z. *All other couplings are set to their SM value or are varied according to SU(2)×U(1) invariance.*

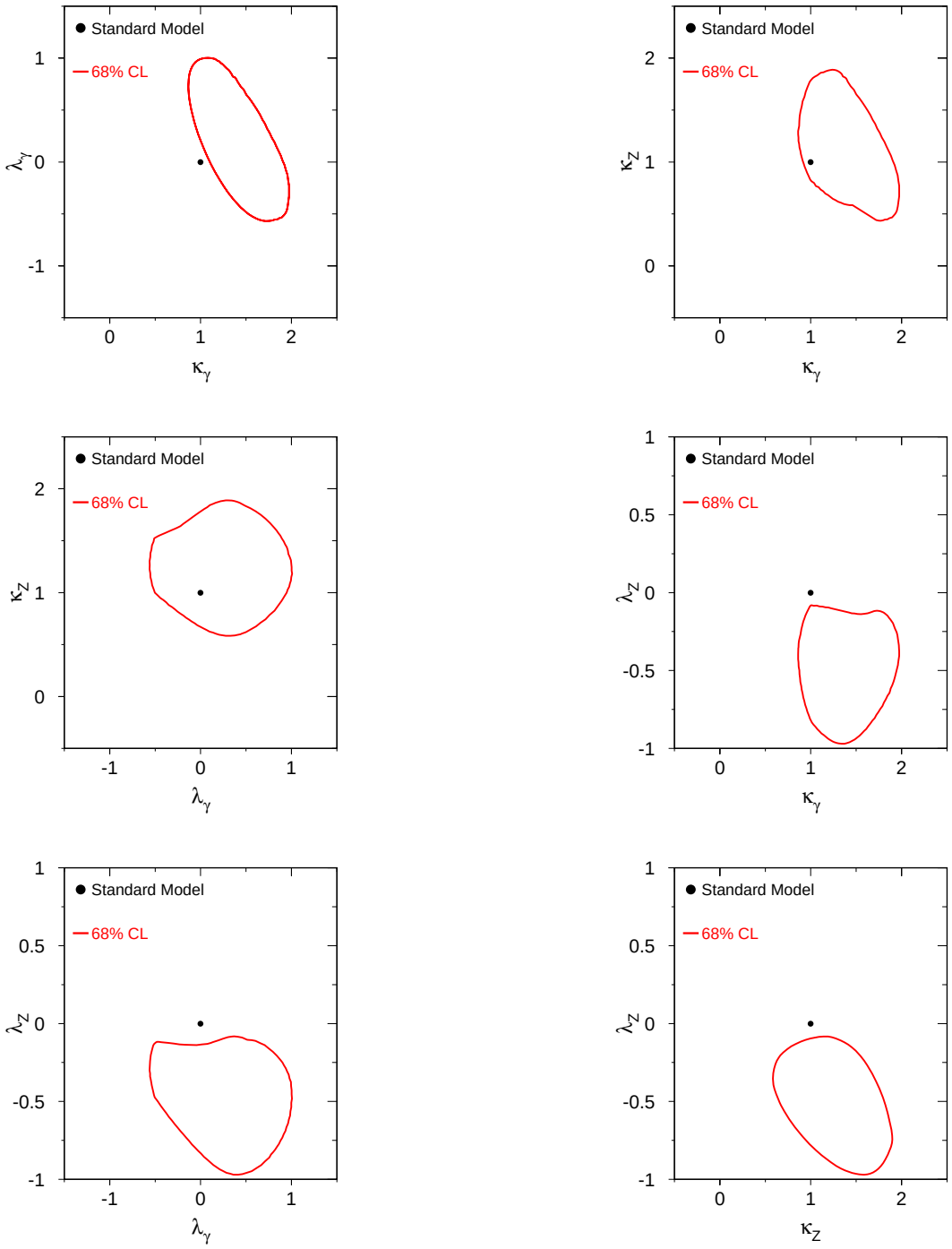

Figure 6.3: *The contour curves from a fit to the phase space variables of* W *pair, single* W *and* $\nu\bar{\nu}\gamma(\gamma)$ *events estimating the TGCs* $\Delta\kappa_\gamma$-λ_γ-$\Delta\kappa_Z$-λ_Z. *All other couplings are set to their SM value.*

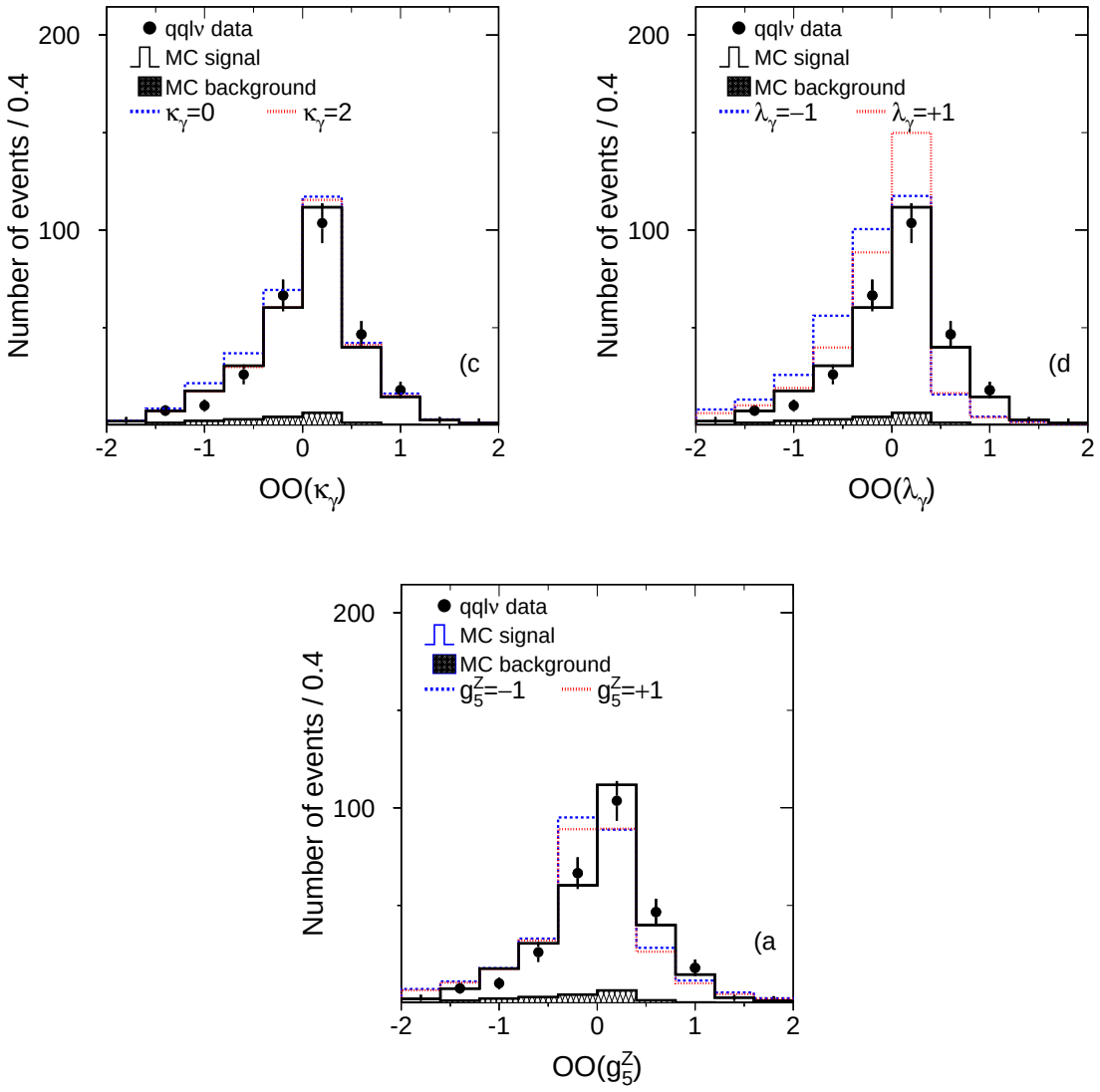

Figure 6.4: *Optimal observables for the couplings κ_γ, λ_γ and g_5^Z.*

Acknowledgement

It is a pleasure to acknowledge the support of my supervisor Thomas Hebbeker. Apart from making this thesis possible, he always helped me coming back to the important questions if I was lost in the details of the analysis.

I have greatly benefited from working together with Martin W. Grünewald. Although many of our discussions left me back puzzled about some interesting details of particle physics and statistics, I have enjoyed our extended discussions about physics very much. Many inspirations for this thesis originated from them.

This thesis is build on the work of many people from **L3** and LEP - physicists, engineers and technicians who have constructed LEP and the **L3** detector and keep it running. As this analysis is only the last of so many steps to extract physics I want to express my appreciation of their work, without which this thesis would be impossible. In particular I want to express my gratitude to the WW-physics analysis group, especially to Doris Kim, Tania Moulik, Sonia Natale, Alan Button, Andrej Kunin, Luca Malgeri, Aleandro Nisati, Alex Shvorob, Georgi Sultanov and Alfons Weber for doing the selections. I enjoyed very much discussing about fitting methods with Alan Button, Arno Strässner and Paul de Jong.

I have appreciated many discussions with Daniel Ruschmeier about photons as such and their importance to particle physics and the world in general. Especially the time in which we did "valuable" physics studies gave me a lot of fun.

During conference preparation I enjoyed the work in the LEP-electroweak working group. The TGC-subgroup meetings were always very entertaining and I profited a lot from discussions with Clara Mateuzzi, Gideon Bella and Peter Clarke.

I am very grateful to Sabine Riemann for suggesting the LEP 1 analysis to me. In the same context I have benefited from discussions with Tord Riemann and technical advise by Christoph M.E. Paus.

My lack of theoretical understanding of physics in the W- and Z-physics sector were always cured by discussion with Jochen Biebel and I am very thankful to him for answering all questions.

I have enjoyed the CERN-Cafeteria discussions with Andreas Kopp which have fasten many problem solutions.

A final thanks goes to those which did not particularly work with me but who kept my spirit up, gave me encouragement and tried to keep me sane.

Lebenslauf

Persönliche Daten

Name	: Peter Molnár	Geburtsdatum	: 15. Mai 1973
		Geburtsort	: Zossen
Wohnort	: Mahlow (15831)	Straße	: Virchowstraße 28

Akademische Laufbahn

Zeitraum	**akademische Einrichtung**
1979-1987	Polytechnische Oberschule Mahlow
1987-1991	Erweiterte Spezialoberschule mathematisch-naturwissenschaftlicher und technischer Richtung Kleinmachnow
1991	Abitur mit Durchschnittsnote 1.4
1991-	Technische Universität Berlin
1993	Vordiplom in Physik (sehr gut)
1993-1994	University of Manchester (UMIST)
1994	BSc (First Class Honours Degree)
1996	Diplom in Physik (sehr gut)
1996-1999	Graduiertenkolleg "Strukturuntersuchungen, Präzisionstests und Erweiterungen des Standardmodells der Elementarteilchenphysik"
1999	Wissenschaftlicher Mitarbeiter der Humboldt-Universität zu Berlin

Praktika/Tätigkeiten

Jahr	**Einrichtung**	**Tätigkeit**
1991	CvO Teltow	Untersuchung von Cu-Keramik Verbindungen
1994	KfA Jülich	Bau eines Vetozählersystems, Fit von pp$\rightarrow d\pi$ Wirkungsquerschnitts
1995	CERN Genf	Monte-Carlo Generatoren für hadronische Ereignisse
1995-1996	HU Berlin	Betreuung von Übungen und Fortgeschrittenenpraktika zur Teilchenphysik

Selbständigkeitserklärung

Hiermit versicher ich, die vorliegende Arbeit selbständig angefertigt und keine weiteren als die angegebenen Hilfsmittel verwendet zu haben.

Peter Molnár